Coupled Finite Element Modelling and Transduction Analysis of a Novel EMAT Configuration Operating on Pipe Steel Materials.

By

Evans Chinemezu Ashigwuike

A thesis submitted for the degree

of

Doctor of Philosophy

Brunel University London

Department of Electronics and Computer Engineering

College of Engineering, Design and Physical Sciences

September 2014

Dedication

This piece of research is dedicated to the Almighty God for his Kindness and mercy throughout my studies, and to my beloved wife (Assumpta) and children (Adaeze and Ozioma) for their patience and encouragement throughout my stay in the UK.

Acknowledgement

There are many people whose support and assistance played a very important role in the realisation of this piece of research. First and foremost, a huge thanks to Prof. Wamadeva Balachandran, who I am really grateful to. He was not just my supervisor, but also a great mentor and friend. He has believed in me from day one, motivated me to excel and always provides all the resource and guidance to keep me going. Also I greatly appreciate the time and dedication of my second supervisor Dr. Rajagopal Nilavalan.

Furthermore, my special appreciation goes Dr. Ruth Mackay, Dr. Nadaraja Manivanan, Dr.Sadiq Thomas and the members of Doc Lab for their advice, support and encouragement during my time as a PhD student.

Finally, I would to acknowledge the support of the staff and members of Brunel Innovation Centre (BIC) and The Welding Institute (TWI), especially Dr. Alex Haig, Dr. Mathew Legg, Mr. S Lowe and Mr. Abbas Mohimi. Their hand-on experience and knowledge base was very useful in setting-up and troubleshooting my model validation experiments.

This Thesis was supported by the Petroleum Technology Development Fund (PTDF) Nigeria, under the PTDF Oversees Scholarship Scheme (OSS) 2011.

Abstract

Electromagnetic Acoustic Transducers (EMATs) are advanced ultrasonic transducers that generate and detect acoustic waves in an electrically conducting material without making physical contact with the material unlike its counterpart, the piezoelectric transducers (PZT). The conventional EMAT consists of copper coil that generates the dynamic field when excited with a sinusoidal current, a permanent or electromagnet that provides the bias field and the conducting material specimen. The complex interaction between the bias field and the Eddy current induced within the skin depth of the conducting material by the dynamic field gives rise to the acoustic wave that then propagates within the surface of the material.

Within the research a finite element EMAT model was developed using commercial software Comsol Multiphysics, to study and compare the Eddy current density and Lorentz force density generated by three EMAT configurations: The Meander-line, Spiral and Key Type EMAT configuration respectively. It was observed that apart from the ease of fabrication and simplicity of connectivity when stacked in layers, the Key Type coil EMAT showed a high tendency to generate higher amplitude of Eddy current and Lorentz force test materials especially when stacked in layers. Also, the effect of varying some key EMAT parameters was investigated to determine the optimal performance of Key Type EMAT configuration on CS70 pipe steel plate.

The research further developed a coupled finite element model using the same software, Comsol Multiphysics to account for the generation, propagation and detection of acoustic wave by the Key Type EMAT configuration on CS70 grade of pipe steel. The model can solve the magnetostatic, electrodynamic and elastic equations that give rise to acoustic wave generation, propagation and detection on the test material. The developed coupled finite element model was validated both analytically and experimentally to establish the validity of the finite element model. The analytical and experimental results obtained were consistent with the numerical result with an average discrepancy less than 9 % percent.

Finally, the research developed a novel modelling strategy to decouple and quantify the various transduction forces in operation when normally-biased EMAT and magnetostrictive EMAT configurations are used on various grades of pipe steel materials. The strategy established the value of the critical excitation current beyond which acoustic wave is generated solely by the dynamic Lorentz force mechanism. The critical excitation currents when Magnetostrictive EMAT configurations are used to generate acoustic wave was found to be; 268A, 274A, 279A, 290A and 305A for CS70, L80SS, L80A, TN80Cr3 and J55 respectively. While for Normally-Biased EMAT configurations, the critical excitation current was found to be 190A, 205A, 240A, 160A and 200A respectively. This work also compared the critical excitation current of the two EMAT configurations studied and established that normally-biased EMATs are more efficient in the generation of acoustic waves than their magnetostrictive counterpart due to their lower value of critical excitation current.

Contents

LIST OF FIGURES

List of Tables

Abbreviations

AC/DC	Alternating Current/Direct Current
CFD	Computational Fluid Dynamics
CT	Computed Tomography
CEC	Critical Excitation Current
DLF	Dynamic Lorentz Force
DMF	Dynamic Magnetic Field
DLKT EMAT	Double Layer Key Type Coil Electromagnetic Acoustic Transducer
ECT	Eddy Current Testing
EMAT	Electromagnetic Acoustic Transducer
ECD	Eddy Current Density
FEM	Finite Element Method
FVM	Finite Volume Method
FDM	Finite Difference Method
KT EMAT	Key Type Coil Electromagnetic Acoustic Transducer
LPT	Liquid Penetrant Testing
LRUT	Long Range Ultrasonic Testing
LFD	Lorentz Force Density
LF-EMAT	Line Focussing Electromagnetic Acoustic Transducer
MPT	Magnetic Particle Testing
MFL	Magnetic Flux Leakage
MF	Magnetostrictive Force

MS-EMAT	Magnetostrictive Electromagnetic Acoustic Transducer
mf	Magnetic field
mfnc	Magnetic Field No Current
ML EMAT	Meander-Line Coil Electromagnetic Acoustic Transducer
MVP	Magnetic Vector Potential
NDT	Non-Destructive Testing
NB-EMAT	Normally Biases Electromagnetic Acoustic Transducer
NdFeB	Neodymium Iron Boron
PPM-EMAT	Periodic Permanent Magnet
PDA	Particle Displacement Amplitude
PVA	Particle Velocity Amplitude
PZT	Piezoelectric Transducer
P-P	Peak to peak value
RT	Radiographic Testing
SLF	Static Lorentz Force
sm	Structural Mechanics
SLKT EMAT	Single Layer Key Type Coil Electromagnetic Acoustic Transducer
SP EMAT	Spiral coil Electromagnetic Acoustic Transducer
SH-WAVE	Shear Horizontal Wave
SV- WAVE	Shear Vertical Wave
SNR	Signal to noise ratio
SCD	Source Current Density

TLF	Total Lorentz Force
UT	Ultrasonic Testing
VOT	Visual/Optical Testing

Nomenclature

$\vec{B}_{\mathrm{T}}$	Total magnetic field vector
$\vec{B}_0$	Static magnetic field vector
$\vec{B}_d$	Dynamic magnetic field vector
$\vec{E}$	Electric field intensity vector
$\vec{H}_d$	Dynamic magnetic field intensity vector
$\vec{D}$	Electric flux density vector
$\vec{J}$	Total current density vector
ϵ	Permitivity
ρ_{υ}	Volume electric charge density
$\mu_{2\times2}$	Differential magnetic permeability matrix
σ	Conductivity
$\vec{M}_0$	Bias Magnetisation vector
$\vec{u}$	Displacement vector
$\vec{B}_{MS}$	Magnetostrictive field vector
B_{MS}	Magnetostrictive field
$e_{3\times1}$	Magnetostrictive matrix
$S_{6\times1}$	Column matrix of strain
K^T	Transpose of the column matrix K
v	Inverse of the permeability matrix
$\vec{J}_s$	source current density

$\vec{J}_L$	Lorentz current density
$\vec{J}_M$	Magnetisation current density
$\vec{J}_{MS}$	Magnetostrictive current density
$\vec{J}_e$	Eddy current density
$\vec{H}_{MS}$	Magnetostrictive field intensity vector
$\vec{A}$	Magnetic vector potential
I_p	Amplitude of excitation current
w_0	Current angular frequency
n	Number of cycles per tone burst
$\vec{f}_{total}$	Total force per unit volume
ρ	density
$\vec{f}_{traction}$	Surface traction
$\vec{f}_{body}$	Body force
$\vec{f}_L$	Lorentz force density
$\vec{f}_M$	Magnetisation force density
$\vec{f}_{MS}$	Magnetostrictive force density
f_0	Centre frequency of electromagnetic wave
μ_0	Permeability of free space
μ_r	Relative permeability
δ	Electromagnetic skin depth
$\vec{F}_{Ls}$	Lorentz force density due to the static magnetic field

$\vec{F}_{Ld}$	Lorentz force density due to the dynamic magnetic field
$\tilde{S}_{IJ}^{H}$	components of compliance matrix at a constant field
$\tilde{\sigma}_{J}$	Component of stress
c_{KI}^{H}	Elastic stiffness coefficient at a constant magnetic field
$\tilde{\sigma}_{K}$	Stress field
S_I	Strain field
$i_k(t)$	Total current of the K^{th} coil conductor
s_k	Cross-sectional area of the K^{th} conductor
J_{exc}	Transient excitation current
I_0	the excitation current amplitude
ϑ	Particle velocity
$V_R(t)$	Induced voltage at the receiver coil
V_{rec}	Received signal of individual coil layers
d_c	Coil spacing
V_0	Amplitude of the received voltage
B_r	Remnant magnetic flux
V_m	Scalar magnetic potential
$j_{\emptyset}^{e}$	External current density
J_0	Bessel function of the first order
J_1	Bessel function of the second order
T	maxwell's stress tensor
F	Force density

$\mathbf{C}$	Speed of light
$\frac{S}{C^2}$	Momentum density
$\boldsymbol{J_m}$	Magnetic source density
$\boldsymbol{J_f}$	Total free conducting current density
$\boldsymbol{T_k}$	Negative kinetic stress tensor
$\boldsymbol{G_m}$	Material momentum density
$\boldsymbol{G_k}$	Kinetic momentum density
$\boldsymbol{G_e}$	Electromagnetic momentum density
$\boldsymbol{T_m}$	Material tensor
$\boldsymbol{T_e}$	Negative Maxwell's stress tensor
$\boldsymbol{f_k}$	Source term due to the magnetic field distribution
$\boldsymbol{f_m}$	Material dependence force
$\boldsymbol{\sigma_0}$	Effective initial stress
$\boldsymbol{C_{mod}}$	Effective stiffness coefficient
$\boldsymbol{\beta}$	Piezomagnetic stress coefficient
D	Piezomagnetic strain coefficient
s	compliance matrix
$-\boldsymbol{e^T}$	Third rank magnetostrictive tensor

CHAPTER 1

INTRODUCTION

1.1 Background

In the last decade, Non-destructive testing (NDT) has proven to be the primary method employed in addressing key maintenance challenges. This is because the method is non-invasive and does not compromise the integrity of the material under assessment; hence it provides a very good balance between quality control and cost value.

The utmost goal of any industry is to maximise profits. A way of achieving this is by extending the life span of its plants, equipment and final product, through implementing different maintenance strategies such as making repairs when there is a break-down (corrective maintenance) or by performing scheduled maintenance servicing (preventive maintenance) [1]. To choose a maintenance strategy, many factors that depend on the particular case need to be taken into consideration.

One of the main objectives of NDT is to predict the performance and service life of a component or a system [2]. It is employed for quality control of facilities and products and to evaluate the remaining operational life of a plant component for example processing line, pipes, machines parts and vessels. The importance of applying NDT techniques is seen in the inspection of industrial equipment and engineering structures, especially power generation plants, petroleum and chemical processing industries, nuclear plants and transportation sectors. It provides important data needed to develop strategic plans for plant life extension and assessment services in the area of [1]:

(a) Equipment integrity analysis

(b) Corrosion monitoring in structures and equipment

(c) Corrosion damage evaluation

(d) Fatigue and creep damage prediction

(e) Fitness for service evaluation.

The field of NDT is very dynamic and diverse; there is no specific technique that suits all environments or the varieties of specimen encountered in the field. In some cases, multiple NDT methods are combined to assess a particular specimen or structure. In the next section (1.2) a brief review of some established techniques will be presented.

1.2 Review of Non-destructive testing methods

There are several NDT techniques available for use in industries. This section will give a brief description of the commonly used techniques in conjunction with details of typical applications, advantages and disadvantages. Some of the most common methods discussed include: Radiographic testing (RT), Ultrasonic testing (UT), Liquid penetrant testing (LPT), magnetic particle testing (MPT), magnetic flux leakage, Eddy current testing (ECT), visual/optical testing and EMAT, which is the subject of this research (see section 1.2.2.2).

1.2.1 Radiographic testing (RT)

Radiographic inspection technique is one of the foremost NDT techniques in use for the detection of discontinuities such as cracks, voids and missing constituent during manufacturing processes and condition monitoring. This technique makes use of the ability of high energy photons to penetrate various materials as illustrated in Fig.1.1. There are three common methods of radiographic inspection; X-ray, Gamma-ray and Neutron radiography respectively and they differ from one another by their source of radiation.

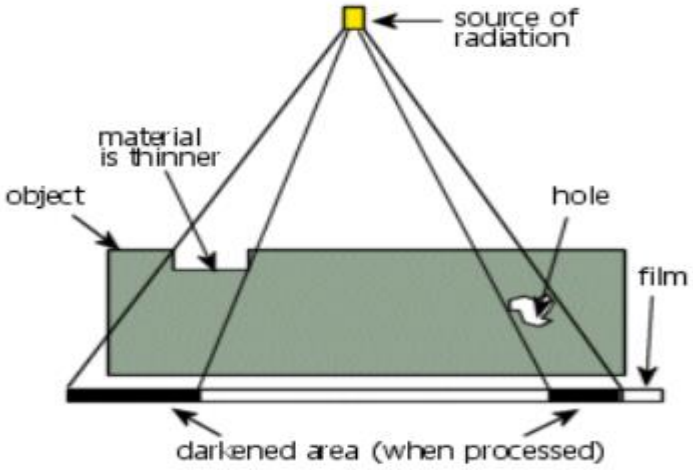

Fig.1.1: Schematic representation of radiographic testing technique showing the radiation source, photographic film and the test material [3].

1.2.1.1 X-ray radiography

Data can be obtained from X-rays in one dimension (gage measurement), two-dimensions (radiograph), or three dimensions (computed tomography). The most widely employed imaging method in NDT is the two dimensional radiography, mainly because it is applied in detecting cracks, inclusions and voids. However, the introduction of computers made it possible to acquire a large number radiographic data at different angular orientations to the object, and made computed tomography a serious competitor especially when information is required in three dimensions. One of the numerous advantages of using X-ray is that complex shapes can be easily assessed, it is suitable for sensing changes in elemental composition (that is mass, density or thickness), it does not usually require expert skills to analyse and interpret the data. Disadvantages are that it poses a serious safety concern due to radiation, high voltage are required to generate the X-rays, access to the opposite side of the test specimen is required, closed cracks are not detectable and flaws must be oriented parallel to the direction of radiation travel. Finally, X-ray machines especially the CT systems are quite expensive and measurement can be time-consuming depending on the computational capabilities. More details about the basic theories, general equipment and procedures can be found in [4-10].

1.2.1.2 Gamma ray radiography

The major difference between Gamma ray and X-ray is the source and penetrating power. While X-rays are produced electrically, Gamma rays are product of radioactive decay of unstable atomic nuclei; consequently, there is a continuous reduction in the intensity of emitted radiation with time. Thus, the selection of a radioisotope for a specific task is very important and is based on the radiation energy, the source size, and the output. Since very limited source of radioisotopes have the required properties (Iridium 192, Celsium137 or Cobalt 60, amongst others), there is much less diversity in application than for X-rays. However, when compared with X-ray sources for NDT, Gamma ray sources have the advantage of compactness, freedom from electrical power supplies, transportability and high penetrating power. Cobalt 60 emits gamma rays at 1.17 and 1.33 MeV, which may appear to be comparable to the output of a 1-MV X-ray unit; however this is not correct, in fact a 2-MV X-ray unit would be required to generate X-ray having the same penetrating power as Cobalt 60 [11]. There are also some disadvantages which include: the need to routinely change the radioisotopes due to constant decay cost of replenishing the radioisotopes when the dose rate falls below practical levels, special safety considerations are required due to constant emission of radiation, and licensing and personal training requirements. More information about the basic concepts, penetration capability and of recent applications of gamma rays for NDT can be found in [12-15].

1.2.1.3 Neutron adiography

Neutron radiography assesses the physical integrity of selected materials in a similar way to X-ray radiography. Their effectiveness depends on the relative attenuation of the incident radiation intensity in the test specimen. However, while the attenuation of X-rays increases with the atomic number that of neutron radiography is more complicated [11]. Neutron radiography compliment conventional x-ray radiography by having the capability of detecting flaws that cannot be effectively detected with x-ray. The unique capability of neutrons is because they do not interact with orbiting electrons in the atoms of the test specimen. The main disadvantages of neutron

radiography are that practical neutron sources are very expensive; it makes use of large and heavy shielding materials, it requires more complex film exposure procedures and safety issues must be considered paramount in order to protect personnel from radiation. See [8, 9, 16-20] for detailed information on different neutron sources, equipment and state of the art on the application neutron radiography for NDT.

1.2.2 Ultrasonic testing (UT)

Ultrasonic inspection consists of the generation, propagation and detection of sound waves (typically greater than 20 kHz) through a material to measure either or both the time of travel (velocity) and change of intensity (attenuation) for a given propagation distance (see Fig.1.2). Using these features in ultrasonic waves, the elastic constants (Young modulus and Poisson's ratio, etc.), density, and geometry of a material can be determined. The position, shape and size of a flaw can also be resolved using ultrasonic testing [21]. Some advantages of ultrasonic methods are that they can be deployed for almost all type of materials including biological, metals, and ceramics. UT method offers contact as well as non-contact approaches, and only single-surface accessibility is required. Conversely, the disadvantages are: there can be difficulty in coupling to rough surfaces when contacting transducers are used and may require extensive surface preparation. The sensitivity is frequency dependent; special scanning systems may be required for inspecting large surfaces. More information on the application of ultrasonic waves can be found in chapter 2, as well as [8, 10, 19, 22-27].

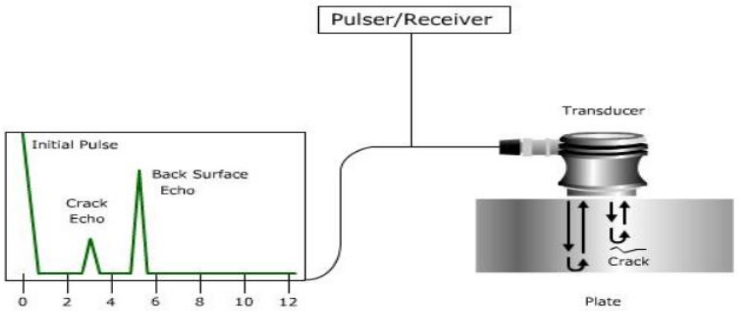

Fig.1.2: Basic principle of operation of an ultrasonic transducer [28]

1.2.2.1 Long range ultrasonic testing (LRUT)

In LRUT, low frequency ultrasonic guided wave (UGW), typically from 10 - 100 kHz is used. This range of frequencies has low attenuation and can propagate in tens of meters along the length of the material such as pipelines. This testing method employs an array of transducers to generate a tone burst signal with a certain wave mode rather than generating a pulse wave at the resonant frequency as in conventional UT. In order to maximally reduce dispersion, LRUT can generate a particular wave mode and suppress other modes by selecting a frequency according to the geometry and property of the test material. Fig.1.3 (A and B) a shows a Teletest® LRUT setup and a typical scan display for flaw detection on a pipeline. The setup consists of an array of transducer segments arranged in ring with approximately equal spacing between them to allow the axial symmetric wave modes generated by a tone burst signal to propagate in one direction [29]. One major disadvantage of the LRUT system is that it has a very complicated design, unlike the conventional UT systems. More information on LRUT can be obtained in [29-31].

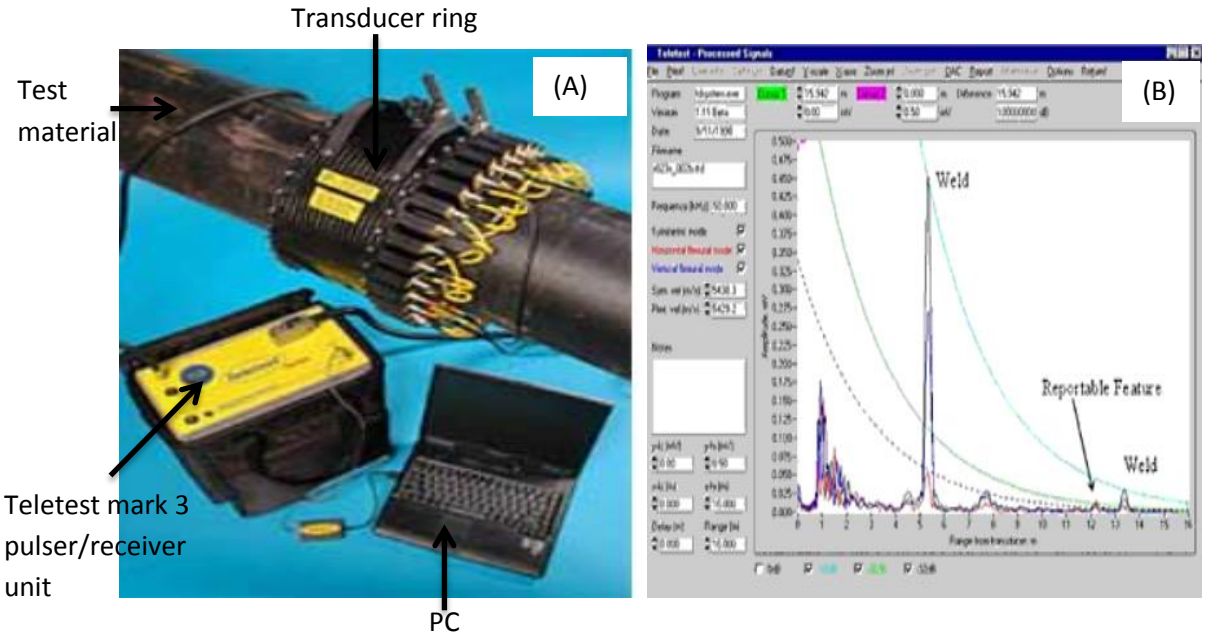

Fig.1.3: (A) Teletest® LRUT equipment setup, (B) A typical A-scan display from the Teletest equipment showing an echo from a corrosion defect of 3% cross sectional area located 12 m from the transducers and 1 m in front of a weld [32].

1.2.2.2 Electromagnetic acoustic transducers (EMAT)

This section describes briefly electromagnetic acoustic transducers (EMATs) which is the main subject of this research. EMATs are advanced ultrasonic transducers that can generate and detect acoustic waves in an electrically conducting material without making physical contact with the material under test. As depicted in Fig.1.4, a conventional EMAT consists of copper coils and permanent or electromagnet in proximity to the test material. The coils are excited with a high-frequency tone burst pulse that creates a dynamic magnetic field and consequently generates a high-frequency Eddy current on the conducting material. The permanent or electromagnet magnet provides the static or bias magnetic field which interacts with the Eddy current to produce mechanical strain on the test material. This mechanical strain gives rise to the ultrasonic wave that propagates through the test material and can be used to detect discontinuities in the test material [33-35]. The main advantage of EMAT is that no couplant is required for it to function, hence does not have to make contact with the material making EMAT suitable for automated, high speed and in-line inspection. The main drawback of EMAT is its low transduction efficiency (i.e. low signal to noise ratio (SNR)) which has affected its widespread used since a complicated and costly electronic system is required to reduce the effect of the low SNR.

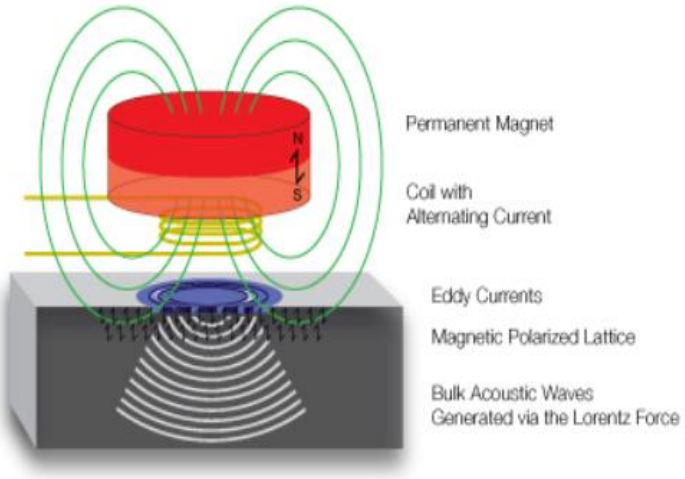

Fig.1.4: Schematic of the basic principle of operation of an EMAT [36].

1.2.3 Liquid penetrant testing (LPT)

This is an NDT method that applies the principle of capillary action to detect surface discontinuities in a wide range of materials. It involves the use of liquids with high surface wetting and contrasting colours that can penetrate into extremely fine surface discontinuities (e.g. cracks or pitting) to reveal the outline of the discontinuities [1, 2]. In order to obtain reliable inspection results using this method, strict procedure (such as surface preparation, application of penetrant, removal of excess penetrant, developer application and post-cleaning) and specifications related to the materials being tested must be carried out as shown in Fig.1.5. The main advantages of LPT are that they are simple and inexpensive to perform and can be applied to materials with complex geometry. On the other hand, its disadvantages are that it is limited to detecting surface discontinuities, it cannot be applied to materials that are porous, it requires access to the material for surface preparation and excess penetrant removal before inspection, erroneous result can be obtained as a result of irregular material surface and finally, environmental and safety issue must be considered prior to applying this method as some of the inspection material may be corrosive. More information about some applications, advantages and limitations of this method can be obtained in [11, 37-41].

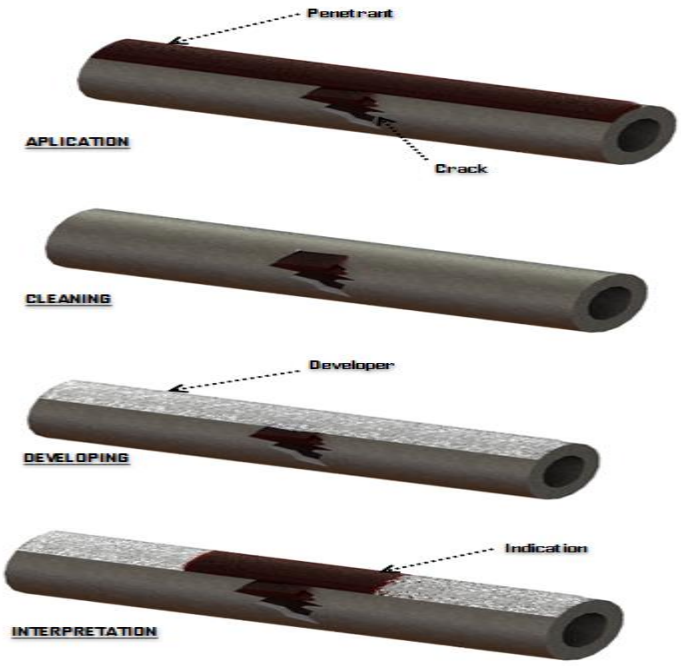

Fig.1.5: Principle of operation of Liquid penetrant inspection technique [42].

1.2.4 Magnetic particle testing (MPT)

This is an NDT method that employs the principle of magnetism. The sample is magnetised using a permanent magnet, electromagnet or an electrical current through a conductor. It involves the introduction of a dye impregnated with finely milled magnetic particles around the surface of the magnetised specimen. As depicted in Fig.1.6, a discontinuity or inclusions within the specimen under test will produce magnetic flux leakage field which attracts the magnetic particle to form clusters and patterns around the discontinuities or flaws [1, 2, 43, 44]. These patterns can be visibly detected by the inspector under good lighting condition. The MPT method is most suited for detecting surface flaws or discontinuities (e.g. cracks) on ferromagnetic materials. Some advantages of this method include: the method is low cost, the equipment are portable and easy to operate, and the method provide rapid results and is sensitive to surface and subsurface flaws and discontinuities. The disadvantages include; the application of the method is limited to ferromagnetic materials alone, it is not sensitive to internal defects, it requires power supply for magnetization, the material may be burned during magnetization and coating of the material can mask flaws or discontinuities. More information on some equipment and applications of this method can be found in [43-45].

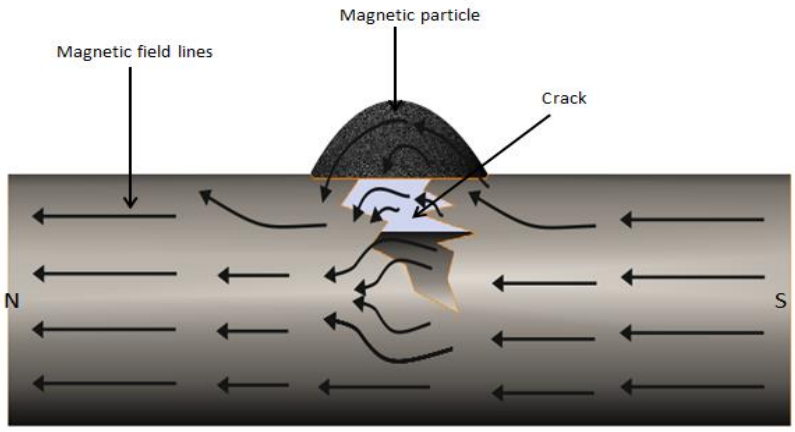

Fig.1.6: Magnetic field lines and magnetic particles influenced by a crack [46].

1.2.5 **Magnetic flux leakage (MFL)**

Another method closely related to the MPT is the magnetic flux leakage (MFL) method. The method involves detecting flaws or discontinuities in a magnetised material by scanning the surface for magnetic leakage fields (magnetic perturbations produced by non-magnetic flaws, discontinuities or inclusions) using a magnetic flux sensor or sensors (e.g. coils, C-core yokes or solid state magnetic sensors) as shown in Fig.1.7. This method is ideally suited for detecting of surface flaws, discontinuities and wall thinning in ferromagnetic materials. The advantages of MFL method are: no contact with sample and no specific surface preparation are required. The disadvantage of MFL is that its sensitivity is limited by ambient noise and background magnetic field, it can only be deployed on ferromagnetic and magnetically permeable materials, only surface and near surface flaws and discontinuities can be detected and access to the test surface is required. More details on the application of this method can be found in [45, 47-49].

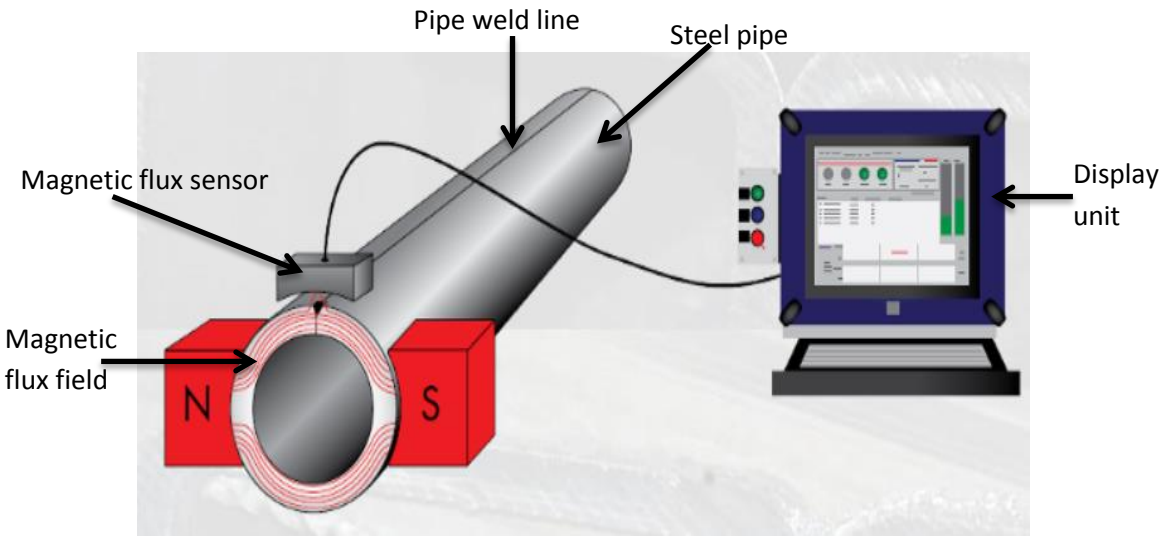

Fig.1.7: In-line flux leakage test showing how the leaked flux due to a weld is detected by a magnetic flux sensor [50]

1.2.6 Eddy current testing (ECT)

Fig.1.8 shows the principle of operation of the Eddy current (EC) testing method, which operates on the principles of electromagnetism. It measures the response of

materials to electromagnetic fields over a specific frequency range (typically from a few kHz to several MHz). From this response, material conditions such as thickness, presence of corrosion, hardness or defects (porosity and cracks) can be revealed. Primarily, Eddy current probes operate on electrically conducting materials, although some low conductivity materials such as graphite-epoxy composites can also be examined. Some advantages of this method are; the method can be automated and high speed scanning can be accomplished due to its noncontact nature, it is not expensive as surface preparation is not often required, depth of inspection can be controlled by adjusting the frequency of the exciting current, and finally, this is one of the few inspection methods used successfully in high temperature applications. The inspection method suffers from a number of draw backs which includes: depth of penetration is limited and is determined by the skin depth of the material, the sensitivity of the probe is affected by the lift-off distance and also special operator training is required to be able to interpret the result correctly.

Recently significant progress regarding pulse Eddy current testing (PEC) method has been made. The main advantages of PEC over conventional EC methods are that it has a relatively simple circuitry when compared to that needed for broad band alternating current testing and a single transient response contains as much information as an entire spectrum of frequency domain excitation. However, data analysis is still a challenge and new methods to extract dominant features are been developed. Detailed information regarding the basic concept on generation and detection of EC and PEC, together with equipment requirement can be found in [47, 49, 51-55].

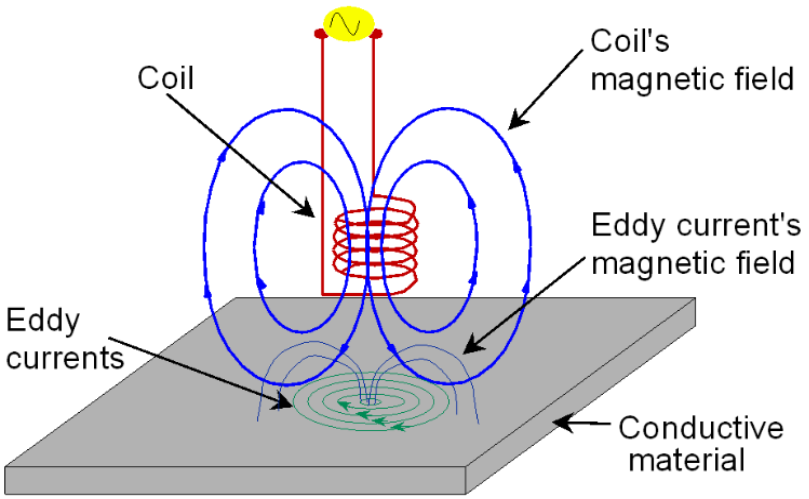

Fig.1.8: Principle of operation of Eddy current testing technique [56].

1.2.7 Visual and optical testing

This is a process of examination and evaluation of system components by use of human systems (e.g. eyes) and by mechanical enhancement (e.g. magnifiers, dental picks, statoscope, borescope etc.) [57], as shown in Fig.1.9. The visual testing method is the oldest and the most common NDT method available, it is the initial step in the examination of any part or specimen. Many NDT methods require visual intervention to interpret results, for example the penetrant, magnetic particle, radiographic methods all rely on the inspector's ability to visually identify surface and subsurface flaws [58]. The main advantages of visual inspection method are its speed, simplicity, size of system to be inspected is not a hindrance and relatively low cost of inspection. On the other hand, its main disadvantages are that surface preparation is required in some cases and some internal and inaccessible areas cannot be inspected with this method [59].

In the case of optical inspection, various techniques are available for flaw detection and determining the stress condition of components, for example: holographic and speckle interferometer [60] as shown in Fig.1.10 and more recently, shearography (developed to address the limitations of holographic interferometer) [61, 62] and digital shearography [63]. The main advantage of interferometer method lies in its ability to examine an object at two different times and conditions. The advantage of these methods lies in the fact that the regenerated image can be used like a 3D

template of which any deviation in shape or dimensions of the object under investigation can be measured. The main disadvantage is that the method is relatively expensive since lasers are involved and requires great caution during operation.

A detail discussion on the theories, applications equipment and state of the art of these techniques can be found in [60-69].

Fig.1.9: Advanced video borescope used for remote visual inspection [70].

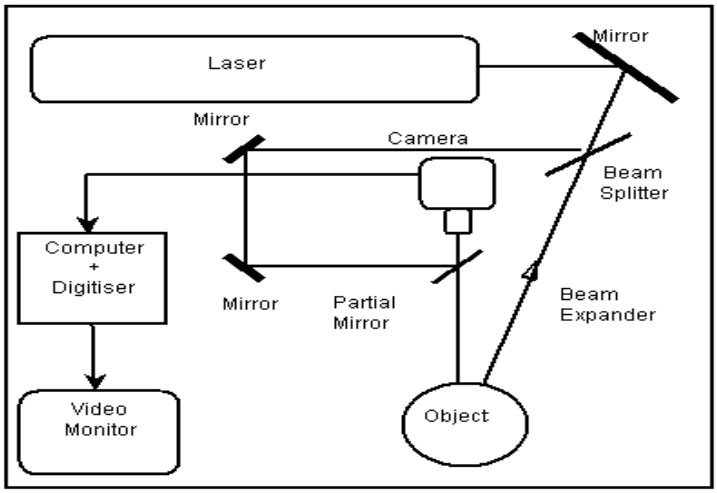

Fig.1.10: Basic principle of operation of an out of plane electronic speckle pattern interferometer [71].

1.3 MOTIVATION

Ultrasonic non-destructive testing technique (briefly described in section 1.2.2) is a well-known method used in modern industries. The need for early and prompt detection of flaws in critical components such as pipe lines (employed by oil and gas industries), power generation plants, aerospace industries etc., is very important. An undetected flaw in such components can lead to catastrophic failure resulting in fatalities, environmental pollution and great cost to the industries involved. Hence, the ability to detect, locate and size flaws in a component can guarantee their safety and allows the estimation of remnant life, thereby reducing the cost and unnecessary replacement of safe parts.

The dominant technology in ultrasonic sensors is piezoelectric transducers. These transducers have some positive characteristics which include: high signal to noise ratio, linear behaviour, simplicity of hardware, ease of use and relatively low cost [72-75]. However, piezoelectric transducers require contact between the sensors and the materials. This contact is enhanced using a fluid couplant or high pressure coupling, implying that the transducers cannot be deployed for measurement in a lot of situations such as: high temperature environments and moving parts of machines etc. Errors can also be introduced in the measurement due to the coupling fluid [74-77].

Given these draw backs, a non-contact ultrasonic method has become imperatively more attractive. The main non-contact ultrasonic methods employed in NDT are the laser based techniques and the Electromagnetic Acoustic Transducers Systems (EMATS) [33, 35, 75, 78], the later will be the main subject of this work.

Although EMATs present several advantages for ultrasonic non-destructive testing, two key problems that affects their deployment on ferromagnetic materials do exist: a good understanding of the mechanical coupling between the transducer and the specimen, which has given rise to low transduction efficiency (i.e. how efficiently EMAT converts electromagnetic energy to acoustic energy) and the undesired requirement of incorporating permanent (rare earth) magnetic in EMAT design.

EMATs as a transducer exploit the phenomenon of electromagnetic induction during operation; they consist essentially of a copper coil, permanent magnet and a conducting test specimen. The coil is excited with a high frequency tone burst pulse, which induces a high frequency Eddy current on the material. The interaction of the Eddy current and the bias field from the permanent magnet gives rise to ultrasonic wave on the material. One major way of minimising the poor transduction efficiency is by increasing the number of turns of the EMAT coil. This can be easily achieved by stacking the coils in layers. Due to connectivity problems it is practically impossible to stack spiral and elongated spiral coils which are some of the commercially available coils structure used in EMATs. A KT coil produced using PCB technology (which has the structural configuration of a spiral coil and current part of a meander line coil) can be stacked easily in layers to generate higher Eddy current on the material.

Furthermore, to improve the performance and better understand the principle of operation of EMAT on ferromagnetic materials; researchers have developed several numerical models [79-87]. These researchers merely created simple models that were able to calculate the magnetostrictive and Lorentz force mechanism, implying that the effect of the DLF and SLF were lumped together as Lorentz force. Creating a numerical model to account for the three major transduction mechanism (static Lorentz force, dynamic Lorentz force and magnetostriction) exploited by EMAT has been a challenge to researchers. Analytical work carried out in [88, 89], accounted for the magnetostriction and Lorentz force in MS EMAT operating in ferromagnetic media and concluded that magnetostriction is the dominant mechanism. Ribichini [90], evaluated numerically and experimentally the magnetostrictive and Lorentz force density in an NB EMAT operating on various grades of structural steel with a conclusion that Lorentz force is dominant. Ludwig [91, 92], pioneered the research that established theoretically the three main transduction mechanisms exploited by EMAT on ferromagnetic material. A more recent work by Wang [82], on NB EMAT operating on an aluminium specimen, established numerically the presence of dynamic and static Lorentz.

The work presented in this thesis, developed and studied a novel EMAT coil configuration with a view of improving the SNR by increasing the Eddy current density induced on the material. It also investigates comprehensively the three major transduction mechanisms that both magnetostrictive (MS) and normally biased (NB) EMAT exploit when operating on ferromagnetic material with a view to better understanding and design of EMAT for better performance.

1.4 AIMS AND OBJECTIVES

The overall aim of this piece of research is to embark on an in-depth study of the operational mechanisms (by means of numerical modelling) of electromagnetic acoustic transducer systems and to develop a technique to mitigate the low SNR inherent in EMAT operation. The objectives of the study are as follows:

- To develop a novel KT Type EMAT configuration that has the capacity to combine the characteristics of the conventional meanderline and spiral coil EMAT for optimal generation of sound wave
- To conduct a comprehensive comparative study of a novel (KT) coil and conventional EMAT coils with focus on the generated dynamic magnetic field Eddy current and Lorentz force density.
- To investigate the performance of novel KT EMAT configuration with a view of improving the Eddy current and Lorentz force densities respectively.
- To experimentally determine the magnetostrictive parameters of pipe steel material and incorporate them in to a comprehensive EMAT model to account for magnetostrictive effects when EMAT are used of pipe steel materials.
- To develop a comprehensive modelling strategy to decouple and evaluate the transduction forces that exist when EMAT are used on pipe steel material, and to determine the CEC required for MS and NB EMAT configuration respectively to generate acoustic wave more efficiently using the DLF mechanism only.
- To compare the critical excitation current (CEC) of both MS and NB EMAT configuration respectively to determine the configuration that is more efficient in generating acoustic wave on pipe steel materials.

- To experimentally and analytically validate the developed coupled finite element EMAT model (referred to in this thesis as coupled mechanical model).

1.5 PROGRAM OF WORK

The study started with an extensive review of relevant and related literature. The main focus of the literature review is to identify the gaps in knowledge in the area of modelling of EMAT transduction mechanisms. Four knowledge gaps were recognised after substantial literature search, namely:

- Researchers have not been able to conclusively find a way around the low transduction efficiency inherent in EMAT.
- There is a need to carry out comprehensive evaluation of the transduction mechanism as there is discrepancy as to which transduction force dominates when EMATs are used on ferromagnetic materials.
- There is need to experimentally determine the magnetostrictive parameters of pipe steel materials and incorporate them to achieve a realistic model of EMATs behaviour on pipe steel materials.
- There is a need to study the effect of increase of excitation current on the profile of the transduction mechanisms of both MS and NB EMATs.

These four identified gaps formed the integral part of the studies carried out in the body of work reported in this thesis. The methodology employed in this study involved developing a 2D axisymmetric model implemented in Comsol multiphysic® software version 4.2. Three distinct model were created to the aforementioned concerns:

(a) The magnetostic model which employs the magnetic field no current (mfnc) interface of Comsol, was use to study the static magnetic field generated by the permanent magnet in the stationary domain.
(b) The electrodynamic model which employs the magnetic field (mf) interface of Comsol, was used to study the transient phenomenon in time domain which

includes the dynamic magnetic field and the Eddy current induced in the material by a time varying tone burst pulse signal.

The coupling of the magnetostatic and electrodynamic model gave rise to the Lorentz force model, used to study the Eddy current and Lorentz body force generated with the skin depth of the material.

(c) The structural mechanics model employs the solid mechanics (solid) interface of Comsol in time domain to study the vibration and deformation due to a body force in the material. When couple to the Lorentz force model, it gives rise to the coupled mechanical model that was used to study the generation, propagation and detection of acoustic wave by th novel EMAT configuration.

To obtain the true picture of EMAT operation on pipe steel material, a comprehensive model was created by introducing the magnetostrictive parameters of pipe steel material into the coupled mechanical model. This gave rise to the coupled magnetostrictive model, which accounted for the magnetostrictive phenomenon that occurs when EMAT is used on ferromagnetic materials. The coupled magnetostrictive model was used to study comprehensively, the transduction forces that causes the generation of acoustic wave when EMAT is used on pipe steel materials.

Finally, the structural mechanics model was validated both analytical and experimentally. The analytical solution made use of classical electromagnetic equations to validate single bench mark models such as the Eddy current, static field and ultrasonic field models respectively. While the multiphysics model was validated experimentally due to the complexity of EMAT operation. The experimental validation was achieved by varying some key EMAT parameters (such as excitation current, excitation frequency and bias field) and comparing their results with their numerical counterpart from Comsol multiphysics. The comprehensive program of work is presented in Fig. 1.11.

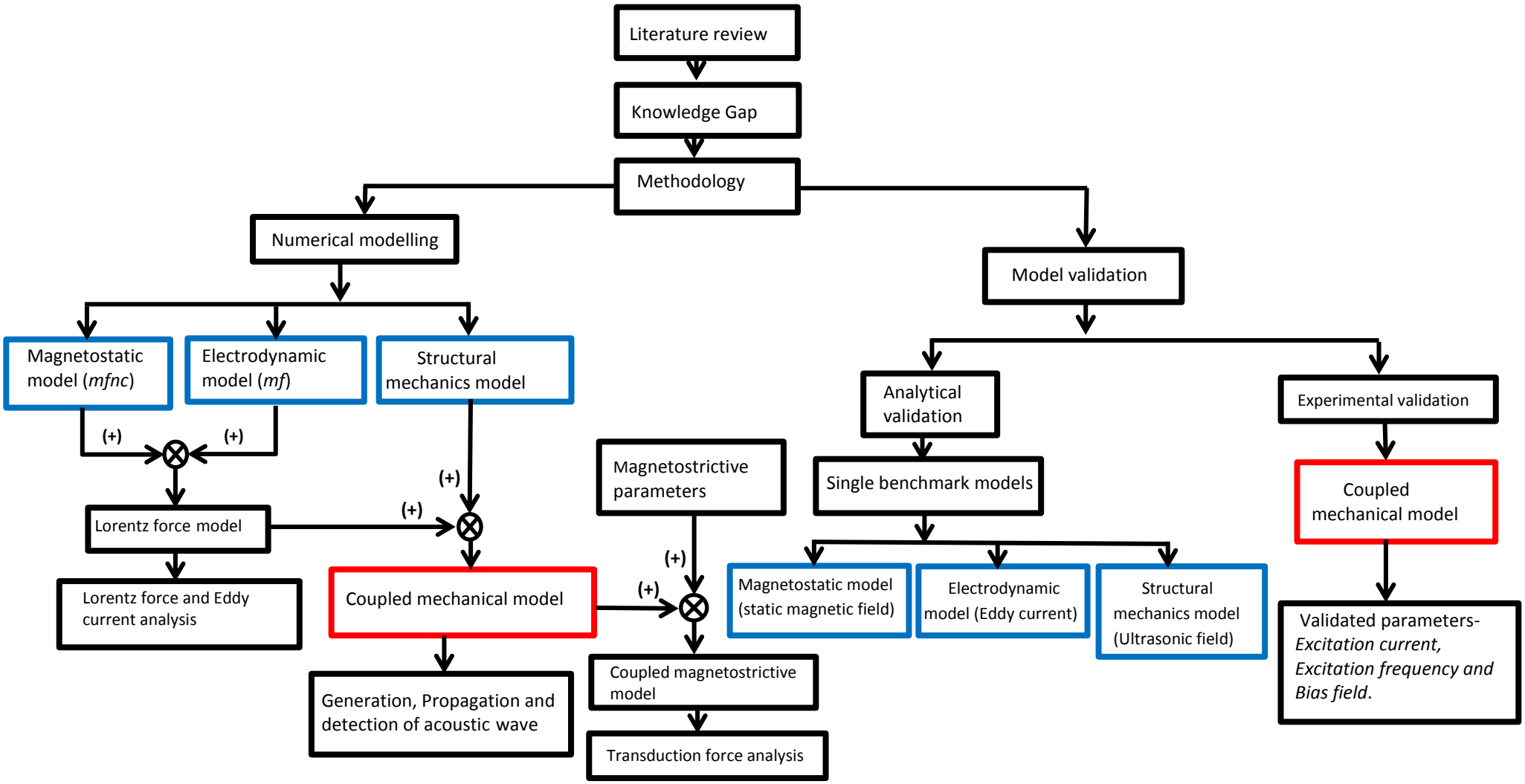

Fig 1.11 Chart showing the program of work carried out in this thesis

1.6 THESIS OVERVIEW

This thesis contains seven chapters. Briefly, the content of each chapter is described below:

Chapter 2, a review of electromagnetic acoustic transducer is presented. The discussion will include its operation mechanisms, types of EMAT available for different purposes and their comparative advantages and limitations. The chapter will give further insight in to the historical development of EMAT including the state of the art in modelling and design.

Chapter3 describes the underlying equation governing both the generation and detection mechanism in EMAT operation. The transduction mechanisms involved when EMATs operate on pipe steel materials are discussed, including the analysis of the dynamic and static components of magnetostriction.

In Chapter 4, a 2D axisymmetric Lorentz force model is presented which was developed in Comsol multiphysics to study and compare the Lorentz force and Eddy current densities respectively generated by various conventional EMAT coil structures (i.e. the spiral and the meanderline coils) in one hand and a novel KT EMAT coil structure. Using the developed Lorentz force model, the chapter further investigated the performance of the KT EMAT structure on pipe steel material when certain EMAT parameters varied, with a view to improving the performance of the novel KT EMAT. This chapter is the basis for the published articles [93-96].

Chapter 5 describes the development of a coupled mechanical model which is made up of the Lorentz force model coupled to the structural mechanics module in Comsol multiphysics. The coupled mechanical model was used to study the generation, transmission and detection of acoustic wave by the novel KT EMAT structure. presents the validation of the finite element model used in this study. Furthermore, the coupled mechanical model was validated in two stages; the first stage of the validation involves splitting the EMATs model into its constituent modules (i.e. the magnetostatic, electrodynamic and acoustic modules respectively) and benchmarking them against known analytical solutions for simple configuration. The second stage involves validating the full multiphysics EMAT model (i.e. the coupled mechanical

model) against experimental results. Some of the results from this chapter and part of chapter five are the basis for the published article [98].

In Chapter 6, The coupled mechanical model was modified to study the transduction mechanisms of NB EMAT and MS EMAT respectively by incorporating the magnetostrictive parameters of some pipe steel materials. The chapter further highlighted some experimental procedures undertaken to determine the magnetostrictive parameters used in the aforementioned model to determine the effect of magnetostriction on acoustic wave generation. Finally, a novel algorithm was developed to decouple and quantify the transduction forces that lead to the generation of acoustic waves when NB and MS EMAT are respectively used on pipe steel materials. This chapter is the basis for the published articled [97, 98].

Chapter 7 presents the summaries of the main results of this study including suggestions for future work.

1.7 CONTRIBUTION TO KNOWLEDGE

To the best of my knowledge and since most of the concepts have been published, many findings from this work are considered significant and the following contributions to knowledge have been shown:

- A novel KT EMAT coil configuration was designed and developed to be able to generate radially polarised surface and bulk wave modes by combining the structural characteristic of the spiral coil EMAT and current part of a meander line coil EMAT. The novel EMAT coil has the advantage of being easy and cheap and easy to manufacture using PCB technology and can be stacked easily to generate stronger Lorentz force density which leads to higher amplitude of acoustic and reduction of SNR.
- It was observed in this work that there is a linear relationship between the Lorentz force density and the period number of the tone burst excitation current signal. This linear relationship was observed to peak around eleven periods per burst, beyond which no significant change was observed. This implies that the number of periods of

an excitation current signal determines the quantity of energy transferred from the power source to the coil.

- The research showed that the novel KT-EMAT configuration has better lift-off characteristics up to 5mm. This is significant because conventional EMAT have a lift off limit of 3mm. It further implies that the hybrid coil when fully deployed can be used on insulated and rough surface with greater success compared to other coil configurations.
- It was observed that the thickness of the insulation layer (Z1258 silicon baffle paint) between the stacked coils affects the density of the Lorentz force generated on the pipe steel material. The Lorentz force density decreases almost exponentially as the thickness of the insulation layer is increased. For optimal performance, an insulation layer of less than 1mm is recommended.
- The research developed a novel numerical modelling technique that accounted for the magnetostrictive phenomenon in both MS and NB EMATs respectively. The model was able to decouple and quantify the three major transduction mechanisms (SLF, DLF and MF) that exist at any given excitation current when EMATs are used on pipes steel materials. This modelling method can also be extended to other ferromagnetic materials.
- Hirao et al. [33], Ogi et al. [99], Thompson [88, 100] and more recently Ribichini et al [90, 101] in their respective works claimed that the Lorentz force mechanism due to the influence of static magnetic field is the dominant transduction mechanism in normally biased EMAT configuration, while magnetostriction is dominant in magnetostrictive EMAT. It is established in this research that the claim by these researchers is true as far as EMATs (both MS and NB) are operated below the critical excitation current (CEC) which is a function of the electrical and magnetic properties of the test material. When operated beyond the CEC, the dynamic Lorentz force becomes the dominant transduction force due to the saturation of the permanent magnet and an increase in the density of the dynamic magnetic field and induced Eddy current. This observation is a major departure from earlier knowledge on the operation of various EMATs configuration.

- The research has shown that because EMAT generates DLF more efficiently than other transduction mechanisms, and when driven with current above the excitation current the DLF becomes the major transduction mechanism it is possible to harness this great attribute to develop a coil only EMAT. This kind of EMAT will operate based on the dynamic Lorentz force mechanism alone, thereby eliminating the undesirable effect of incorporating a permanent magnet in the construction of EMAT. With proper insulation of the coils, this benefit can be extended to developing miniaturised and robust EMAT that can operate in temperatures well above the Curie temperature of permanent magnet (NdFeB) which is about 400^0C

1.8 LIST OF PUBLICATIONS

Three Journal papers (two published [93, 95] and one submitted for publication) and five conference papers [94, 96-98, 102] have been published from the research presented in this Thesis. There are other recent publications by the author in the course of this PhD research. They include two journal papers (one published [103] and the other accepted for publication) and three conference papers (two published [104, 105] and one accepted for publication). The highlights of the publications are:

Journals:

(1) **E.C. Ashigwuike**, W. Balachandran, S. Thomas, R. Mackay, "Numerical Study of EMATS Coil Structure based on Finite Element Method", *Petroleum Technology Development Journal*, Vol. 1, Jan 13.

(2) S.Thomas, S.S.A Obayya, **E.C. Ashigwuike**, W. Balachandran, "Characterization of Defects in Non-ferromagnetic material using an Electromagnetic Acoustic Transducer", *Sensors & Transducers Journal,* April 2013.

(3) **E.C. Ashigwuike**, S.Thomas, Ruth Mackay, Nadaraja Manivalan, W. Balachandran. 'Improving the Lorentz force Amplitude of a Novel EMAT using stacked coil onfiguration', *Sensors & Transducers Journal,* August 2013.

(4) Thomas S, **Ashigwuike E.C**. 'Defect characterisation in ferromagnetic and non-ferromagnetic aircraft plate material using electromagnetic acoustic transducers',

Int. Journal of Microstructure and Material properties. Vol.9, Nos. 3/3/4, Pp.401-412, October 2014.

(5) **Evans Ashigwuike**, James Ushie, Ruth Mackey, Alex Haig, Sadiq Thomas, Rajagopal Nilavalan, Wamadeva Balachandran. ' A new study of the transduction mechanisms of Normally Biased and Magnetostrictive EMATs configuration operating on Ferromagnetic pipe steel materials', Sensors and actuators A: Physical (Accepted January 2015).

Conferences:

(1) **Evans Chinemezu Ashigwuike**, Rajagopal Nilavalan, Wamadeva balachandran: Non-Destructive Testing of pipeline corrosion using Electro-magnetic acoustic transducer system (EMATS); RESCON 2012 poster conference, 2012, School of Engineering and Design, Brunel University.

(2) **E.C. Ashigwuike**, W.Balachandran, S.Thomas: Simulation based comparative study of EMATS coil structure for long range ultrasonic testing; BINDT conference and exhibition proceedings, Sept. 2012, Northamptonshire, UK.

(3) S.Thomas, W.Balachandran, **E.C. Ashigwuike**: Characterization of Electromagnetic acoustic transducer using finite element method.
BINDT conference and exhibition proceedings, Sept. 2012, Northamptonshire, UK.

(4) S.Thomas, **E.C. Ashigwuike**, O.Ubadike, "Comparison of defect detection in Aluminum and Steel plates using an Electromagnetic Acoustic Transducer", International Conference Application of Contemporary Non-destructive testing in Engineering˝, Slovenia, September 2013.

(5) **E.C. Ashigwuike**, S.Thomas, W. Balachandran, "Comparative study of KT-EMAT and SP-EMAT based on Lorentz force mechanism", International Conference Application of Contemporary Non-destructive testing in Engineering˝, Slovenia, September 2013.

(6) **Evans Chinemezu Ashigwuike**, Waamadeva Balachandran, Rajagopal Nilavalan, ''Study of the transduction mechanisms of a Magnetostrictive EMAT on pipe steel''. RESCON 2014.

(7) **Evans Chinemezu Ashigwuike**, Wamadeva Balachandran, Sadiq Thomas, Rajagopal Nilavalan. 'Comprehensive study of the Transduction mechanism of Normally-Biased –EMATS configuration operating on ferromagnetic materials'. European Conference on Non-destructive Testing. Prague-Czech Republic, October 2014.

(8) S. Thomas, O. Ubadike, **E.C. Ashigwuike**. 'Defect detection in Ferromagnetic Aircraft parts using hybrid EMAT and Eddy current sensor. BINDT conference and proceedings. September 2014, Manchester. UK.

CHAPTER 2

REVIEW OF RELEVANT LITERATURES

2.1 Introduction

In this Chapter, EMATs and the principles of operation are introduced, a brief review of the historical development are discussed. Classification of various EMAT configurations and their different applications to industrial and scientific measurements, with their advantages and limitations are outlined.

2.2 Principle of operation of EMAT

An electromagnetic acoustic transducer is a non-contact technique used for non-destructive testing of conductive materials. Basically, EMAT consists of a coil to induce a dynamic electromagnetic field at the surface of a conductive material when fed by a large dynamic current; usually a pulse or a tone burst current signal, a permanent or electromagnet to provide the static (bias) magnetic field and a conducting material as shown in Figure 2.1. To induce an Eddy current density, $\mathbf{J_e}$ within the skin depth surface of the conducting material, the coil of the EMAT sensor is excited with a high dynamic pulse or a tone burst current, typically of the range of (40-50)A and placed underneath the magnet close to the surface of the conductive material [33, 35, 78, 88]. The interaction of the Eddy current density and the static magnetic flux density or bias field introduced by a permanent magnet or an electromagnet gives rise to a body force known as ''Lorentz force'' on the conducting material. This force impacts motion on the surface of the material and launches acoustic vibration at the same frequency as the current in the coil. The principle involved in the generation of acoustic wave can also work in the inverse sense by converting acoustic vibrations into electrical signal [106], thus allowing EMAT to operate as an acoustic wave detector. The motion of the metallic surface in the magnetic field generates an Eddy current in the surface that is detected by the coil in close proximity to the material through the mechanism of electromagnetic induction across the air gap between the coil and the material.

The constitutive equation for Lorentz force is linear and is given as;

$$\mathbf{F_L = J_e \times B_0} \qquad (2.1)$$

Where J_e and B_0 are induced Eddy current and bias magnetic flux respectively.

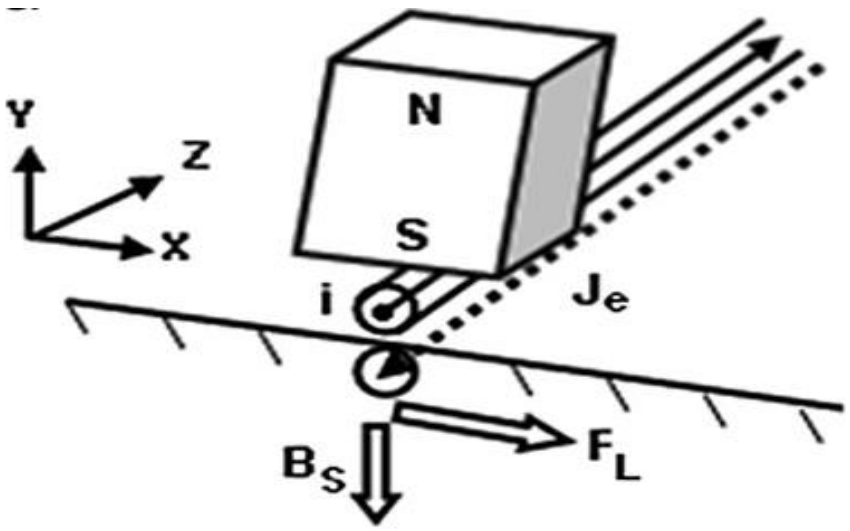

Fig.2.1 Schematic of the basic operating principle of a Lorentz force EMAT consisting of a single wire and a magnet leading to the generation of Lorentz force. Diagram adapted from [107].

The Lorentz force created within the skin depth of the conducting material excites the material and generates acoustic wave, which propagates along the surface of the material, however, if the material is ferromagnetic, a further principle known as magnetostriction contributes to the generation of acoustic wave. The constitutive equation for magnetostriction is nonlinear and is given as [108];

$$\begin{cases} S = f(\tilde{\sigma}, H) \\ B_0 = g(\tilde{\sigma}, H) \end{cases} \qquad (2.2)$$

Where S and $\tilde{\sigma}$ are the strain and stress tensors and B_0 and H are the magnetic flux density and the magnetic field strength respectively.

These phenomenona are utilised in non-destructive testing (NDT) [33, 35, 87, 100, 109].

2.3 Coupling mechanism

In the study of EMATs, understanding the mechanism by which electromagnetic energy is converted to acoustic energy is of paramount importance. Previous studies reveal that the operation of EMATs is characterised by three major coupling mechanisms, namely; the magnetization force, the magnetostriction force and the Lorentz force [35, 78, 100]. It is very important in the study of EMAT to know which transduction mechanism dominates the operation of a given EMAT configuration and in a given sample, since this affect the performance of the transducer when used on different materials. Studies carried out on this subject revealed that the Lorentz, magnetisation and magnetostrictive forces respectively are the three major coupling mechanisms in EMATs operating in a ferromagnetic media [78, 87, 88, 100, 110-112], whilst the Lorentz force mechanism is the only transduction mechanism that operates on non-Ferro-magnetic media [33].

Further research also established that in a ferromagnetic medium, the Magnetisation force and the Magnetostriction force mechanism are the main transduction mechanisms in EMATs with a bias magnetic field parallel to the surface of the sample (see Fig.2.2) [78]. However, there are divergent opinions when the static bias field is normal to the surface of the sample, especially when Lamb waves are to be generated in ferromagnetic plate-like structures. Some researchers claimed that Lorentz force is the dominant mechanism [78, 110, 113], while some others claimed otherwise [99]. A more recent research by Ribichini et al [101] convincingly came to the conclusion that the Lorentz force mechanism has a much more significant effect on normal biased EMAT configuration on ferromagnetic material Fig.2.3). This is in line with claims made earlier by [78, 110, 113].

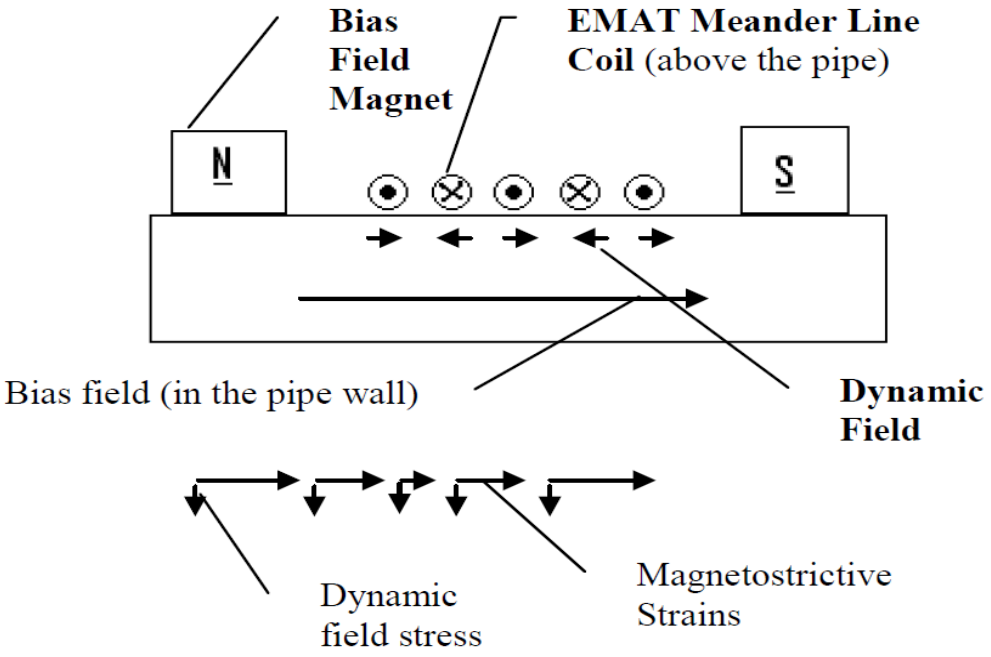

Fig.2.2 Schematic of the basic operating principle of a magnetostrictive EMAT consisting of a meander line coil and a magnet leading to the generation of magnetostrictive strain, adapted from [111].

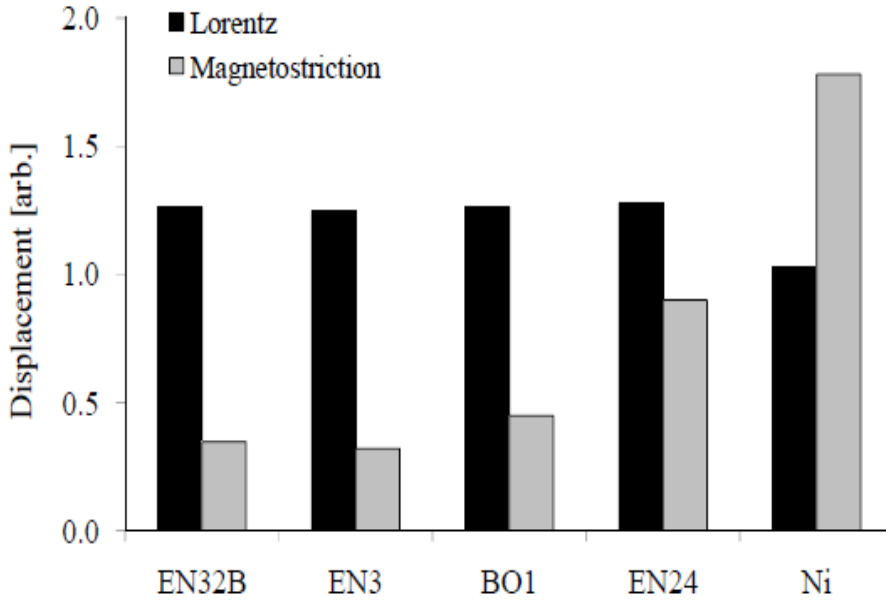

Fig.2.3 Simulated displacement as a result of the Lorentz force and magnetostriction in four steel grades and nickel as adapted from [90].

2.3.1 Lorentz force mechanism

The Lorentz force mechanism is as a result of the interaction between the static magnetic flux and the Eddy current as stated in equation (2.1). From the microscopic point of view and as presented by [35, 78, 87], the Lorentz force $\mathbf{ev_e \times B_0}$ is generated when an electric field **E** created by the excitation current on the conducting material produces a coulomb force **–eE** on individual electrons and interact with a static magnetic flux density $\mathbf{B_0}$. Here, $\mathbf{v_e}$ and **e** denotes respectively the mean velocity of electron and the charge of the electron [33]. Considering the above report, the equation of motion of an electron is given as:

$$mv_e = -e\,(E + v_e \times B_0) - \frac{mv_e}{\tau} \tag{2.3}$$

where *m, e and* τ denotes the mass of the electron, the charge of electron and the mean time of electron-ion collision respectively.

Assuming that the harmonic oscillation is much slower than the mean frequency of electron, that is; $\omega\tau \ll 1$, the equation of electron motion in (2.3) reduces to

$$n_e \frac{mv_e}{\tau} = -n_e e(E + v_e \times B_0) \tag{2.4}$$

Where n_e is the electron density.

When the electrons collide with the ions of the metal, they transfer their momentum to the ions and the body force generated within the ions is written as;

$$f = NZ_e(E + \phi \times B_0) + n_e \frac{mv_e}{\tau} \tag{2.5}$$

Where *N*, Z_e and ϕ denote ion density, charge and displacement respectively.

Assuming that ion displacement is insignificant when compared to the mean electron velocity, and that $n_e e = NZ_e$, equations (2.4) and (2.5) reduces to [33];

$$f = -n_e e v_e \times B_0 \tag{2.6}$$

Equation (2.6) is analogous to (2.1) as the term $-n_e e v_e$ is the electron Eddy current density.

2.3.2 Magnetisation mechanism

The Magnetisation force mechanism is as a result of the oscillating magnetic field and the magnetisation of the fero-magnetic material. Researchers have revealed both experimentally [100, 111, 114] and theoretically [33] that in EMATs configurations with the bias field tangential to the material field, the Lorentz force component and the magnetization force in the direction normal to the sample tend to cancel out each other. This is because the two forces have similar amplitude but are out of phase to each other. For this reason, the magnetisation mechanisms are not able to generate significant acoustic wave in fero-magnetic material.

It has also been shown in [33, 100], that the contribution of the magnetisation force to shear wave generation is very small. Therefore, researchers neglect its effect in the calculation of acoustic wave generation in fero- magnetic materials.

2.3.3 Magnotostrictive mechanism

The magnectostrictive mechanism is due to the piezomagnetic effect of the ferro-magnetic material as shown in Fig.2.4.

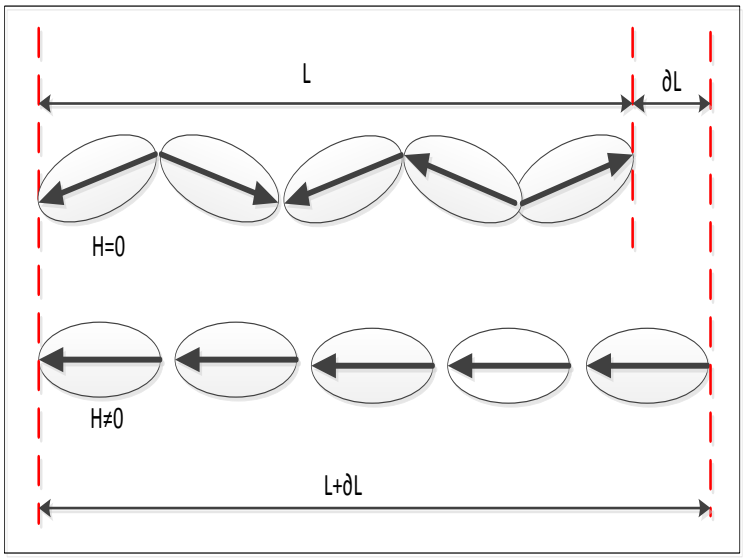

Fig.2.4 Microscopic process of magnetostriction. magnetic field causes the magnectostrictive material to change shape. Here two phenomena occur; (i) the

migration of the domain walls within the magnetic material in response to external magnetic field H. (ii) The domains rotate in response to an external magnetic field H, adapted from [115].

Research has shown that there are two types of magnetostriction, namely spontaneous and induced magnetostriction [48]. Within the Currie temperature, if a magnetic field is applied to a ferromagnetic material, a preferred direction arises towards which the magnetic domains tend to align. The result is a net strain in the direction of the applied field. This is because a large number of close-by magnetic dipoles aligns to a given directions forming the magnetic domains. The alignment of the magnetic diploes within a domain results in a spontaneous magnetisation of the domain along a certain direction and this is associated with a spontaneous strain. The average deformation of the whole ferromagnetic material is the average of the deformation of the single domains, and is known as spontaneous magnetostriction. If the material is isotropic, this causes a change in the volume of the solid but not in the shape of the specimen. Above the Curie temperature, the magnetic dipoles are randomly aligned due to the thermal excitation. The second type of magnetostriction, that is, the field induced magnetostriction, causes pure strain with no change in volume below the Curie temperature [48, 116]. This is the operational mechanism employed by magnetostrictive EMAT.

2.4 History of EMAT development

This section presents a historical overview and background of the major steps in the development of EMATs. Numerous researchers in the field of non-destructive testing have proposed theoretical and analytical models to improve the understanding of the physics behind EMAT operation. Also, apart from the numerical studies, some experimental researches have been carried out on EMAT. This has led to a significant improvement in the design, signal to noise ratio and deployment of EMATs.

The physical principles underlying the operation of EMATs were known since the early studies of fundamental electromagnetism. In 1847, Joule [117] reported the phenomenon of magnetostriction on steel and iron. While in 1861, Maxwell

incorporated the Lorentz force phenomenon into the electromagnetic equation [118].

The first recorded study and application of EMAT for non-destructive evaluation was in 1939 by Randall et al. [119] who designed an experiment to detect the contribution of intercrystalline thermal currents to the internal friction of polycrystalline metals as shown in Fig.2.5. Here the specimen is supported by silk thread at the nodes of vibration. The driving force is obtained when the magnetic force produced by the permanent magnet (M) interacts with the Eddy current induced by the sinusoidal current in the driver coil. At the other end of the bar, an alternating electromotive force is observed in the detector coil as a result of the Eddy current created by the vibration of the atomic particles of the bar immersed in the magnetic field of a second permanent magnet (M'). This was followed in 1956 by Thompson et al. [120], when they used a similar magnet and coil configuration as used by Randall to study the effect of neutron radiation on single crystals of copper to determine the effect of radiation damage on the mechanical properties of metals. Grimes et al [121], in 1964 investigated the interaction between helicon wave and sound waves in potassium, this study gave rise to further studies on the behaviour of electromagnetic waves on materials. In the wake of this work, Gaerttner and his team examined quantitatively the ultrasonic wave generated by magnetic body forces on the Eddy currents in the skin depth of metals [122]. Further to this work, Dobbs in the early seventies, began an investigation in the ultrasonic wave generated by electromagnetic mechanism, in the cause of his work, he found out that the Lorentz forces was the main factor inducing ultrasonic wave on conducting material, and proposed the use of the ultrasonic signal generated for non-destructive testing [109].

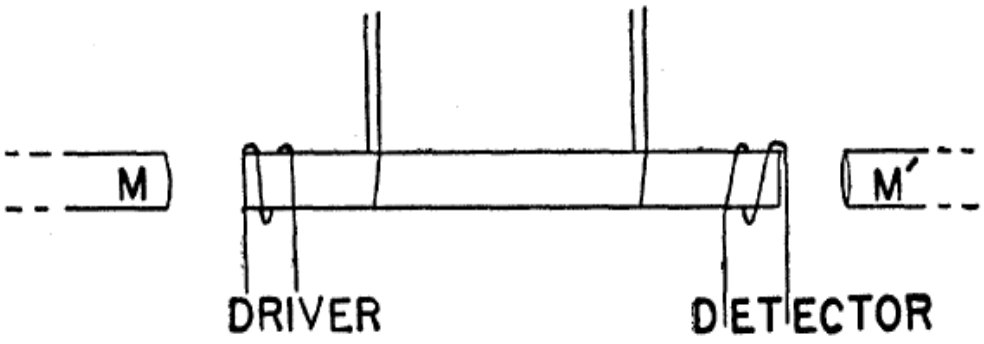

Fig.2.5 Early use of electromagnetic induction to excite and detect longitudinal resonant vibration in a metal sample for measurement of Young's modulus and the damping capacity of the sample. This is adapted from [119].

Thompson [89] in his work also in the early period of 1973 developed an analytical model of a meander-line coil EMAT and used it to generate and measure the efficiencies of Rayleigh and Lamb wave on both aluminium and steel plates. The research also formulated an analytical expression to predict the performance of both the transmitting and receiving EMATs. The classical electrodynamics equation describing the Eddy current induced on a metal surface by an infinite current-carrying wire was used to model a single wire of the coil. Then, he adopted a special Fourier analysis to model a two dimensional meander line coil. He later concentrated his research on the study of the effect of magnetostriction and addressed the efficiency of the transduction mechanism on various ferromagnetic materials [88]. Furthermore, he investigated the effect of variation of the applied magnetic field on the generated wave amplitude and concluded that, for low magnetic field when the static magnetic field is parallel to the surface of the sample, the magnetostrictive mechanism is the dominant transduction mechanism and the relationship between the acoustic wave amplitude and the static magnetic field is highly non-linear and dependent on the test material. On the other hand as the magnetic field progressively increases, magnectostriction saturates and no longer contribute meaningfully to the elastodynamic force generation within the material. However, the elastodynamic force due to Lorentz force mechanism increases linearly with the magnetic field as seen in Fig.2.6. In this manner, he introduced a general equation

governing the operation of EMAT [100]. The equation highlighted a third transduction mechanism, the Magnetisation force which he showed to be very small when compared to the other two mechanism and can be neglected in the study of EMATs. Furthermore, in 1979 Vasile and Thompson [123] developed novel periodic permanent magnets (PPM) EMAT. This kind of EMAT differ from the previous configuration in the sense that it is made up of an axially wound coil and a number of permanent magnet arranged in such a way that the polarity alternates, establishing a periodic magnetic bias field. The axially wound coil and the periodic permanent magnet combines to produce a shear horizontal (SH) surface waves in plate-like structures. Experimental work in the area of guided wave EMATs for pipe inspection was first carried out by Mohr et al. in 1975 [124]. They used longitudinal and torsional modes to study the reflection characteristics of flaws in feritic and austenitic pipes.

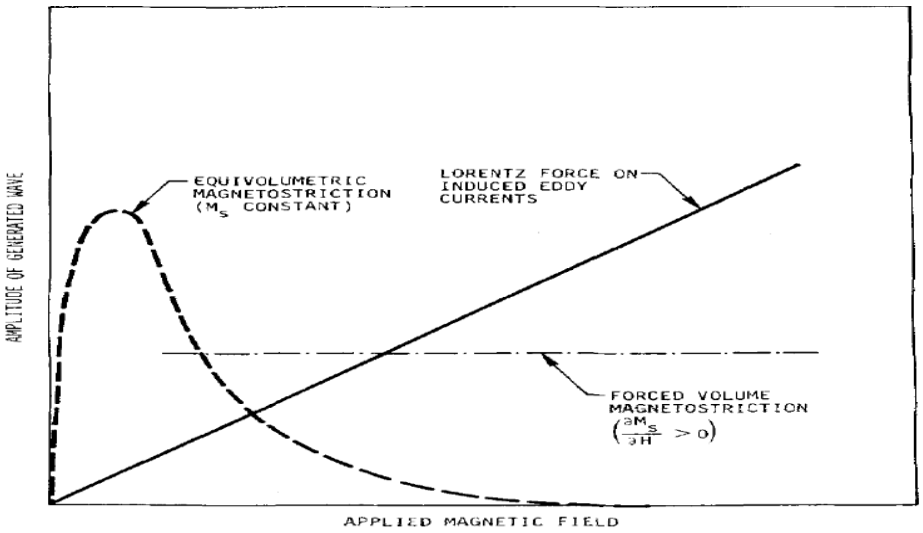

Fig.2.6 Schematic of the field dependence of the amplitude of the generated acoustic wave on applied magnetic field, adapted from [88].

In 1976, Kawashima [87], made a key improvement in the numerical study of spiral coil EMATs operating in ferromagnetic media. He modelled the coil as the superposition of several circular loops lying in planes parallel to the surface of the sample at a specific distance. This assumption allowed him to use the classical Dodd and Deeds model [125] proposed in 1968 to solve the electrodynamic equations in steady state conditions, using a magnetic vector potential formulation, together with

an axisymmetric geometry. Kawashima applied this relationship together with the experimentally measured magnetic flux density to predict the Lorentz force generated by a spiral coil EMAT. He further assumed that the forces acting on the specimen could be superficial rather than body forces as they are concentrated within the skin depth of the material, which is usually smaller than the wavelength of the electromagnetic wave. This made it possible for the piston source model to be used [126, 127]. Kawashima in 1984 [128], extended his analysis to transient excitation using Fourier analysis. Qualitatively, his predicted result showed good agreement with the experimental result, but the discrepancy was between 30% and 50% when viewed quantitatively. This is as a result of the number of approximations he made in the theoretical analysis. Another important study was made by Mirkhani et al. [129], in the early eighties. Their study was based on a three part finite element model which was able to simulate the profile of the static magnetic flux, the profile of the Eddy current distribution and propagation of the ultrasonic pulse through an aluminium specimen. They were the first to compare a numerical model of an EMAT with absolute measurement of ultrasonic pulse magnitude and carried out a detailed calculation of the magnetic flux. This calculation is very important in the optimisation of EMAT design. Also, in the 1980s Wilbrand [110, 113] developed a magnetostrictive model to study the magnetostrictive effect in terms of elastic and electromagnetic constitutive equations linked by coupling terms accounting for the magneto-mechanical transduction, in analogy with piezoelectric equations. Similarly, Doniavi and Eskandarzade [111] developed a new analytical magnostrictive EMAT model for wave propagation based on the momentum conservation forms of Maxwell's field equation. The model took into account the effect of the dynamic Lorentz force in a magnetostrictive environment.

Further work on planar spiral coil EMAT was carried out by Wilcox et al [130], to investigate the excitation and detection of Lamb wave using an aluminium plate acting as the wave guide. They developed a model that could calculate the modal content of the radiated Lamb wave field from a transmitting EMAT as well as predict the output voltage from a receiving EMAT when a Lamb wave is incident on it. The different effects and conditions that contribute to the generation of Lamb waves was

also studied within the model. Jian et. al. [131] developed a model of a spiral and a linear coil EMAT operating on the principle of Lorentz force. The model combines analytical solution with numerical calculation to predict the transient displacement of Rayleigh waves of arbitrary forces and also demonstrate how the orientation of the bias field can constructively and destructively affect the Lorentz force due to static and dynamic magnetic fields.

Javier et.al. [132] theoretically modelled and simulated the performance of an n-turn, two layer planar rectangular spiral coil located on a semi-infinite, isotropic, non-ferromagnetic conductor and fed with a sinusoidal current (see Fig.2.7) .

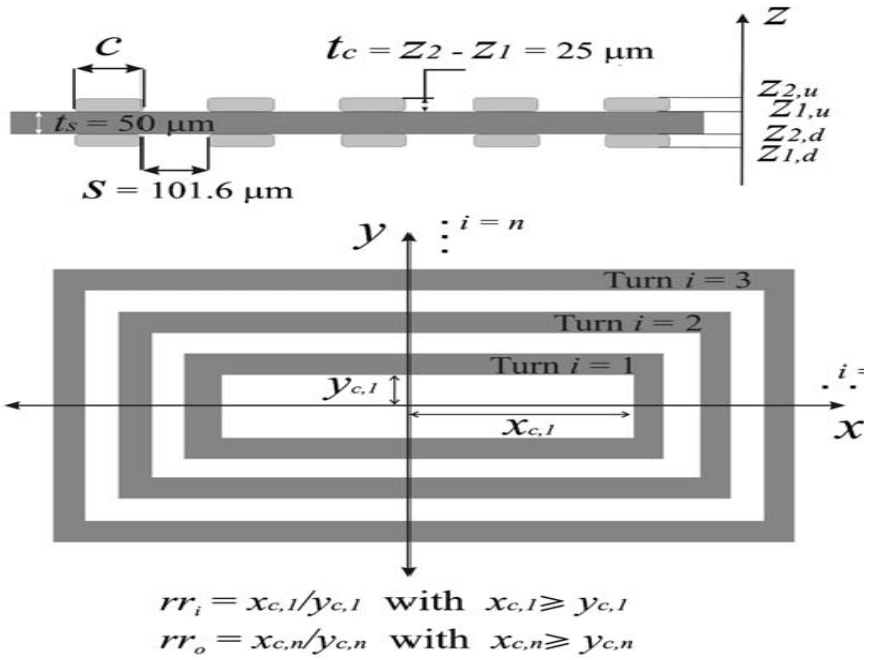

Fig. 2.7 Features of planner spiral rectangular coil modelled in [132]

The second order vector potential approximation was employed to determine the influence of coil shape and size on the sensitivity to electrical conductivity of the material for the three modelling scenarios: the inductance of a coil as function of number of turns and width of the coil in free space for different coil inner shape factor; the impedance change, as a function of the product of the frequency and conductivity of the substrate for different shape factors; coil sensitivity to small changes in electrical conductivity of the substrate. They observed that inductance of the coil increases as expected with coil area (i.e. the number of turns and width of

coil), while the shape factor decreases with coil area. Also strong dependence on the sensitivity to change in the number of turns was observed when compared with the outer shape factor. They concluded that for better sensitivity and larger inductance in Eddy current tests, coils with larger number of turns and narrower coil width and spacing should be employed.

An important parameter to be considered in the design of EMATs is the acoustic radiation pattern due to the coil configuration. Meander line coil configurations generate waves with broad radiation pattern with the consequence of reducing the sensitivity of the EMAT system and restrict its use in flaw detection. To mitigate against this draw-back, Wang et al. [133] with the insight from work done by Ogi et al. [112, 134, 135] (on line focusing EMATs), proposed a coil system able to generate acoustic wave in one direction using two meander-line coils driven by two burst pulse signals of equal amplitude and a phase shift of 90^0. This was achieved by re-adjusting the spacing of the two meander-line coils and making the driving pulse signal in one of the coils to be out of phase with the other by 90^0. Thus, causing the generated wave to be suppressed in one direction and enhanced in the other direction. A numerical model was developed and used to calculate the directivity of the Rayleigh wave generated by the EMAT. The model was implemented in two separate parts: The Lorentz force phenomenon was implemented in Comsol multiphysics®, while the acoustic phenomenon was modelled using Abacus software®.

2.5 State of the art in EMAT modelling

In the past seven years, most developments in the modelling of EMAT were due to the effort of Dixon et. al. [85, 85, 131, 136-139] and Cawley et.al. [90, 101, 140, 141]. The work of Dixon et. al. focussed mainly on the Lorentz force mechanism due the dynamic field produced by the EMAT coils. In one study [137], they introduced a concept of generating ultrasonic waves in metals with a coil, pulse generator and the sample without a permanent magnet. A simplified equivalent coil circuit was introduced (which includes an internal electrical resistance, an equivalent inductance and an equivalent capacitance) to calculate the excitation current. The work

demonstrated that due to the Eddy current and magnetisation mechanisms, the equivalent inductance is dependent on the magnetic susceptibility, the electrical conductivity of the metal sample and the configuration of the coil. Also, the sensitivity of the lift-off is related to coil shape, size and number of turns. Furthermore, taking advantage of the dynamic magnetic field interacting with the induced Eddy current, the researchers generated acoustic waves without requiring a permanent magnet. This was achieved by enhancing the induced Eddy current generated by the coil using a ferrite back plate [85].

In another work [131], a finite element model that combines analytical and numerical methods to compute Rayleigh waves generated by EMAT was developed. The model computes the transient force distribution and further decomposes it into several force components that can be solved analytically. They observed that the contribution of the Lorentz force due to the dynamic magnetic field is greater than that due to static field especially in the generation of Rayleigh waves. This is a major deviation from previous reports [134, 135] which claimed otherwise.

More recent works on modelling of EMATs transduction mechanisms was carried out by Cawley [90, 101, 140, 141]. The different transduction phenomena are influenced in different ways by the material properties (such as the conductivity and relative permeability) and operational conditions (e.g. the bias field and the driving frequency). For example, the Lorentz force mechanisms is very sensitive to electromagnetic properties, while magnetostriction is non-linear and its contribution to wave generation and reception depends highly on the bias magnetic field and the physical properties of the material under test. Their works established that the Lorentz force mechanism is the dominant transduction mechanism in operation when EMATs are used on non-oxidised structural steel material. This agrees with earlier claims made by [78, 110, 113], but contradicts claims by Ogi et al. [112, 142]. An experimental assessment of the performance of some EMATs configuration (magnetostrictive EMATs and periodic permanent magnet EMATs) in terms of shear and torsional wave generation on some grades of structural steel plates (EN24, EN3, EN32B and BO1) was carried out by [143] and observed that the magnetostrictive EMAT performed poorly comparatively with low wave amplitude, while the periodic

permanent magnet EMAT generated intermediate wave amplitude. The poor performance of magnetostrictive EMAT was shown to improve when a layer of highly magnetostrictive material is attached on the structural steel, however this contradicts the main benefit of EMAT as contact with the material under investigation is requires. The work was extended to include magnetostriction in the finite element code to assess the effect of magnetostriction when magnetostrictive EMATs (normal and nickel bonded) and periodic permanent magnet EMAT are used on various grades of structural steel.

2.6 Types of EMAT

Various types of EMATs configurations have been proposed for different applications depending on the type of wave mode required [33, 35, 78, 144]. This section will discuss some of the more popular and useful types of EMATs commonly found in the industry.

2.6.1 Bulk wave EMATs

These EMATs can generate and detect simultaneously shear and longitudinal waves, propagating perpendicular to the surface of the material. The shear wave has a polarisation parallel to the surface of the material. Bulk wave EMATs are popular in practical and scientific applications due to their compact structure, broad bandwidth between 0.1 to 50MHz and high transfer efficiency. In these EMATs the permanent magnet produce a bias field normal to the surface under the unidirectional coil elements and the tangential fields around the centre and edges of coil elements. Due to the Lorentz force mechanism discussed earlier, this EMAT configuration excites only shear and longitudinal waves in a non-ferromagnetic material (Fig 2.8A). However, only shear waves are excited on ferromagnetic materials (Fig 2.8B), as the longitudinal wave is too small to be observed [33] . This phenomenon is due to the large difference in magnitude of the various components of the magnetostrictive force mentioned earlier in this chapter.

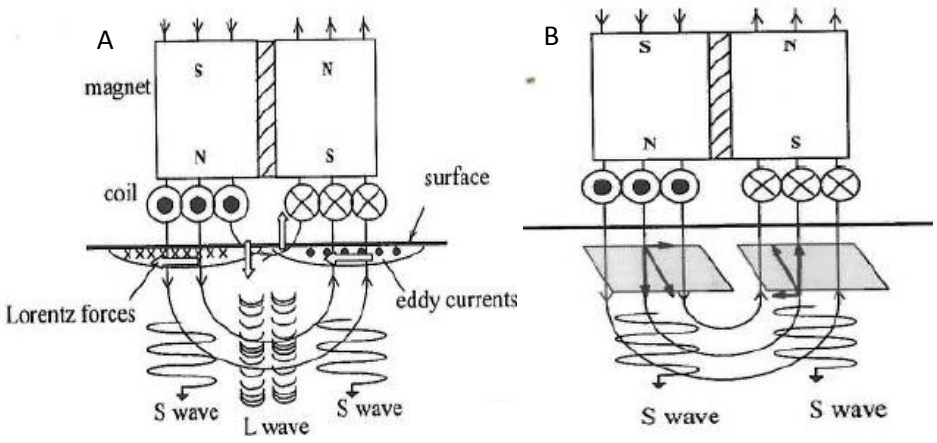

Fig.2.8: Mechanisms for the bulk wave generation by the Lorentz force in (A) and tmagnetostriction force in (B) [33].

Another configuration of bulk wave EMAT consists of a single permanent magnet and a planner spiral coil as shown in Fig. 2.9. The static field produced by the magnet has the radial and normal components, which interact with the Eddy current to produce the Lorentz force along the normal and radial directions ($f_z^{(L)}$ and $f_r^{(L)}$) respectively. The Lorentz force generates longitudinal and radially-polarised shear waves along the thickness of the material simultaneously.

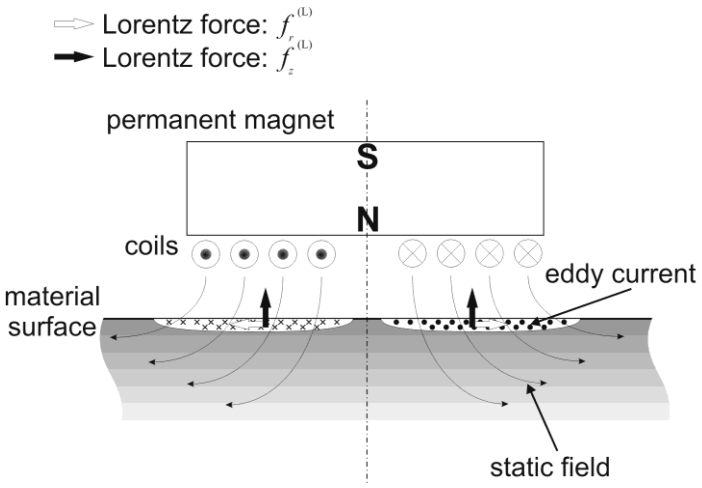

Fig.2.9: The Lorentz force mechanism for the generation of radially-polarised shear wave and longitudinal wave using a single permanent magnet and a planar spiral coil. The white arrow indicates the Lorentz for in the radial direction, while the dark arrow indicates the Lorentz force in the normal direction [33].

2.6.2 Periodic permanent magnet EMAT (PPM-EMAT)

Periodic permanent magnet EMAT (PPM-EMAT) generates shear horizontal waves with polarization parallel to the surface of the material on both sides. It consists of several permanent magnets placed in alternate magnetization directions over an elongated spiral coil (see Fig.2.10). The shear waves are launched simultaneously along the surface and deep into the material with a traction parallel to the surface and alternating with a period equal to twice the width of the magnets [35, 78, 123]. These EMATs generates shear horizontal (SH) wave by exploiting the Lorentz force mechanism and are particularly useful as they can be used to excite shear horizontal waves, which are generally difficult to excite with conventional piezoelectric transducers. Thinner magnets generates higher frequency SH waves which are more useful in detecting surface flaws. However, the efficiency decreases drastically if magnets are too thin and magnets with thickness greater than 1 mm are normally employed in the design of these EMATs. A similar concept has been applied successfully to detect surface flaws in gas pipelines [145].

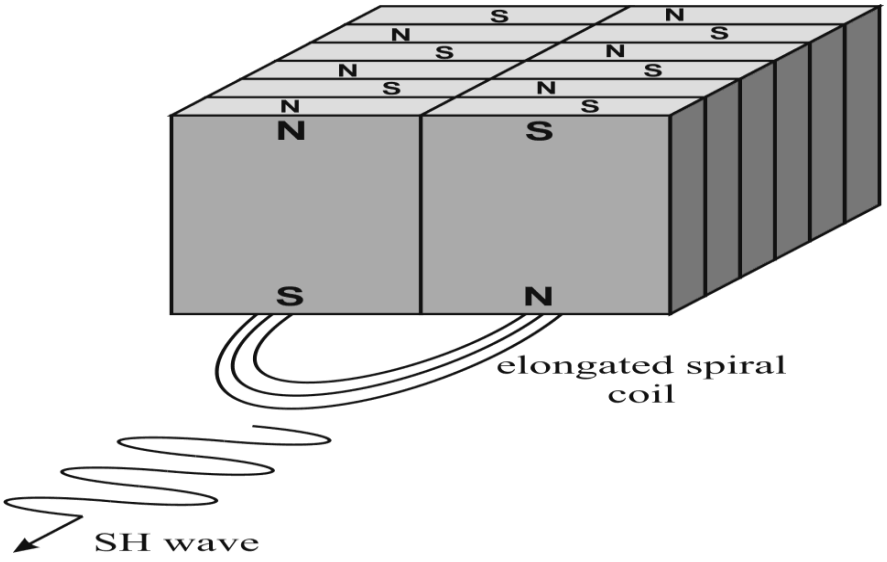

Fig.2.10: A typical structure of a periodic permanent magnet EMAT used for the generation of shear horizontal wave on conducting materials. This is diagram adapted from [33].

2.6.3 Meander-Line coil shear horizontal wave EMAT

The design in Fig.2.11 is adapted for the generation of shear wave on ferromagnetic materials and consists of a meander-line coil placed within a tangential magnetic field. This EMAT configuration relies purely on the principle of magnetostriction for its operation [142, 146]. The SH-wave frequency is governed by the meander-line period, which can be controlled by fabricating the coil using a printed circuit technique [33]. The advantage of this EMAT is its ability to generate surface SH waves of higher frequencies. A major drawback of this EMAT is the requirement of very large biasing magnetic field when the static magnetic field is applied along the straight lines of the meander-line coil. However, using an oblique biasing magnetic field, the efficiency can be improved as demonstrated in [142].

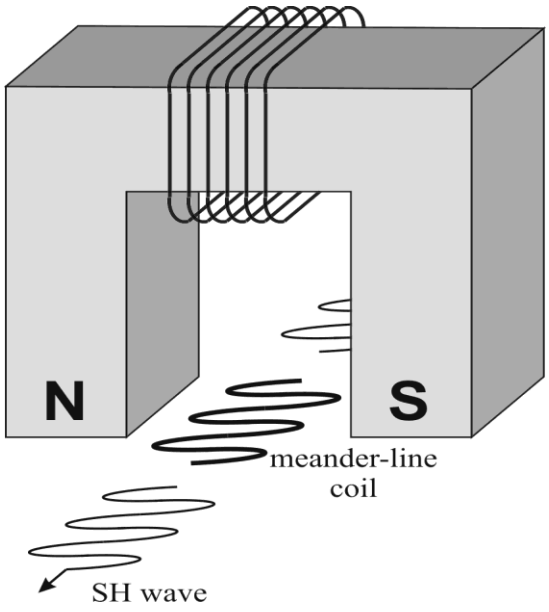

Fig.2.11: Typical structure of a meander-line coil shear horizontal wave EMAT. Diagram adapted from [142].

2.6.4 Axial-Shear-Wave EMAT

These EMAT configurations are designed to excite axially polarised shear wave propagating in the circumferential direction along a cylindrical surface of a circular

rod or pipe material. It can be designed to exploit either the magnetostrictive mechanism or Lorentz force mechanism on ferromagnetic and non-ferromagnetic material respectively [33]. The former consist of a solenoid coil that supply the biasing field along the axial direction and a meander-line coil surrounding the cylindrical surface (Fig. 2.12), whilst the latter consists of numerous permanent magnets arranged with radial polarity of alternating signs and a solenoid coil wrapped around the cylindrical surface [33, 147] (see Fig. 2.13).

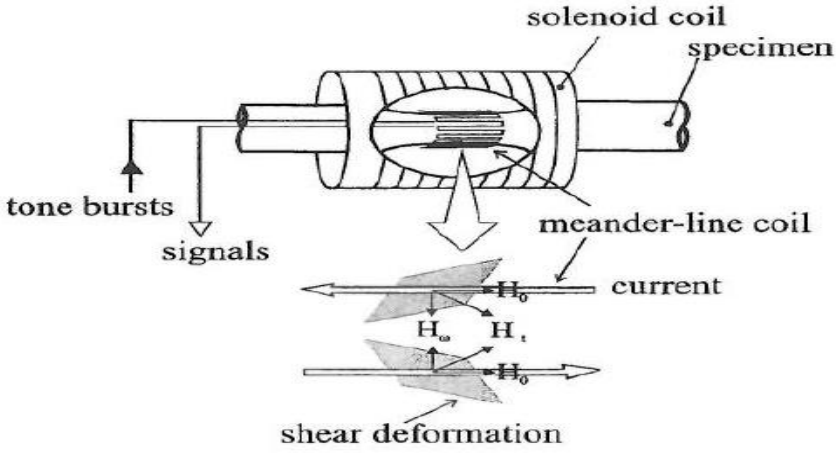

Fig.2.12: Structure of Axial-shear-wave EMAT consisting of a solenoid coil and a meander-line coil surrounding the cylindrical surface. The magnetostriction force mechanism causes an axial surface wave [148]

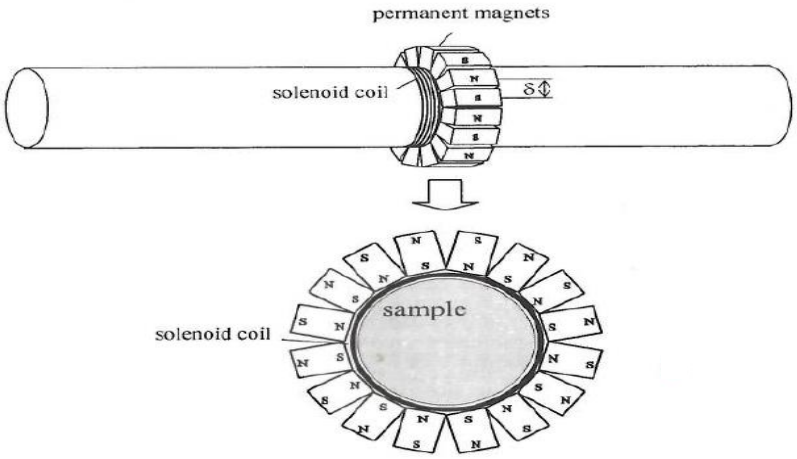

Fig.2.13 (B): Structure of axial-shear-wave EMAT consisting of periodic permanent magnets with the alternating radial polarity and a solenoid coil surrounding the

cylindrical surface. The Lorentz force mechanism causes an axial surface wave. Diagram adapted from [147].

In the two forms of axial-shear-wave EMAT, the total fields oscillates about the axial direction at the same frequency as the driving currents and creates a shearing vibration resulting in the excitation of an axial shear wave. The application of this configuration is seen in the area of resonance frequency measurement focussed on the outer region of a cylinder [147, 149]

2.6.5 Rayleigh- Wave EMAT

The structure of this configuration of EMAT consists of a permanent magnet and a meander-line coil. The permanent magnet is positioned to produce a normal biasing field which interacts with the Eddy current induced by the meander-line coil to create the body forces (Lorentz force and magnetostrictive force), parallel to the surface as shown in Fig. 2.14. The orientation of the Rayleigh wave changes alternately with the period of the meander-line coil [33]. The body forces generate simultaneously the Rayleigh wave, longitudinal wave and the shear vertical wave. The Rayleigh wave propagates along the surface of the material, while the shear vertical and longitudinal waves propagate obliquely into the material. A major drawback experienced with this configuration is the difficulty in identifying the wave mode propagating at any time.

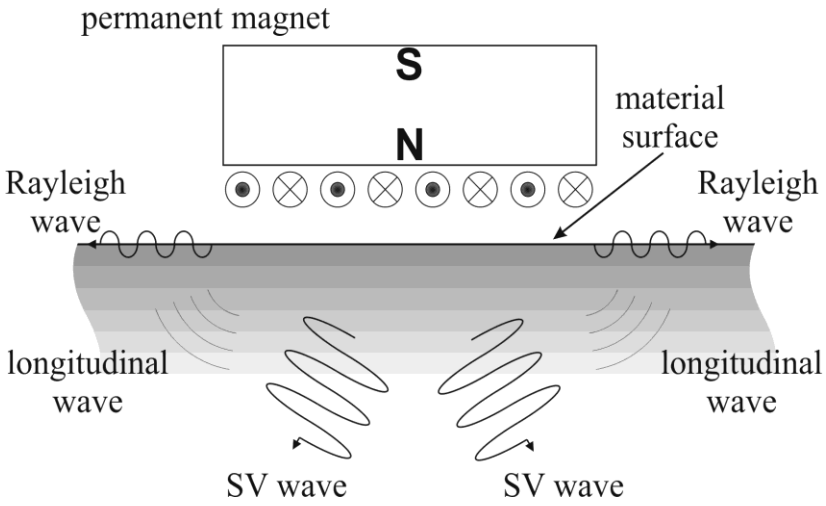

Fig. 2.14: Rayleigh wave EMAT consisting of a permanent magnet and a meander-line coil. Diagram adapted from [135].

2.6.6 Line focusing EMAT

The elastic wave generated by most EMATs propagate in nearly all directions generating a broad radiation, which decreases the ultrasonic energy and it is often difficult to distinguish the flaw signals from other signals [135]. To mitigate these drawbacks, a special design array of the meander-line coil allows concentration of the shear vertical wave within a line inside the material. This special EMAT design is termed the line focusing EMAT (LF-EMAT), and consists of a permanent magnet block and a meander-line coil, whose spacing is continually varied so that the excited shear vertical wave is consistent on a focal line after propagating in oblique paths (Fig.2.15)[112, 134].

In this design, the non-uniformity of the meander-line coil spacing coupled with the effect of the transduction mechanisms associated with the materials creates shearing forces parallel to the surface of the coil segment. These forces in turn generate the shear vertical wave directed on a line inside the material.

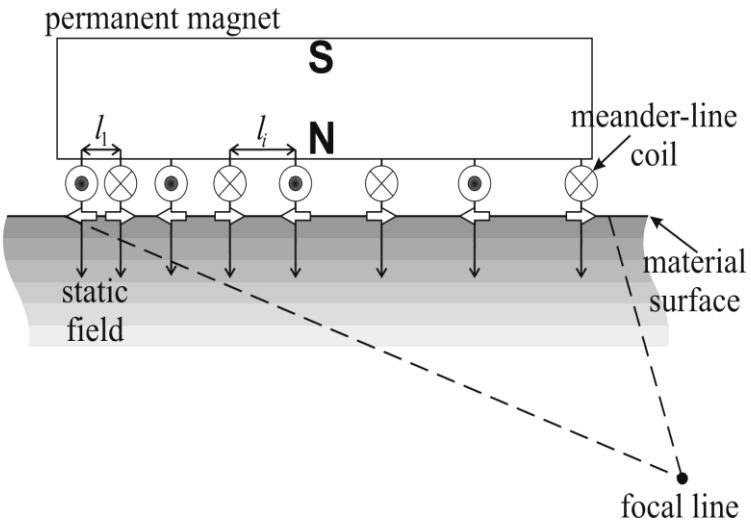

Fig.2.15: Shear Vertical wave focusing with a permanent magnet block and a meander-line coil with the changing spaces [135].

2.6.7 Longitudinal –Guided wave EMAT for wires and pipes

The EMAT configuration described in Fig.2.16 is used to excite and detect longitudinal guided waves on rods and pipes [33, 150-152]. It operates primary on the principle of magnetostriction and consists of an electromagnet or permanent magnet to create the biasing field along the material axis and a solenoid coil to cause the dynamic field to superimpose on the biasing field. Long range inspection up to 100m, is possible with this type of EMAT configuration due to low damping rates which occur due to the low operating frequencies in the sub-megahertz range and also the guided wave energy generated is confirmed within the rod or wire [33]. However, this EMAT generates the longitudinal wave symmetrically in both directions in the material, which makes the signal interpretation complicated. Unidirectional generation with amplification is possible by arranging an array of generation coils with prescribed spaces as proposed in [144].

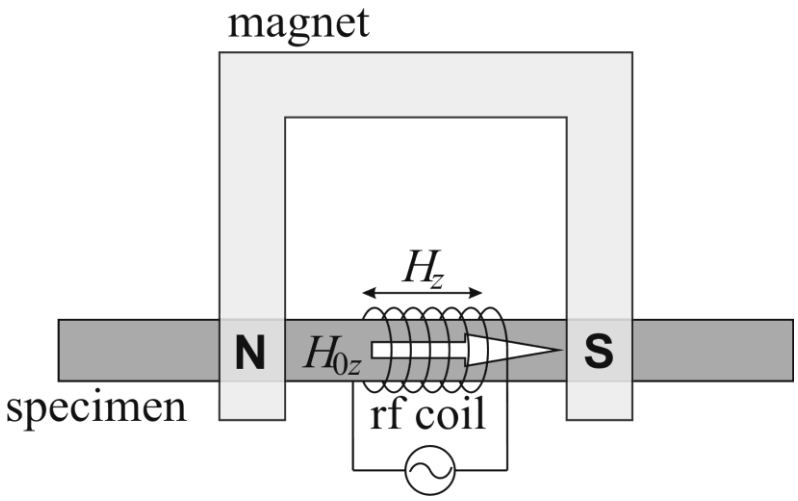

Fig.2.16: A typical structure of magnetostrictive EMAT for generation of longitudinal waves in pipes. This diagram was adapted from [33].

2.6.8 EMATs for high temperature measurement

The structure of an EMAT configured to measure the elastic constant and internal friction of small specimens at elevated temperature is shown in Fig.2.17. It consists of a solenoid coil made with a Nickel-alloy wire and held by ceramic cement to enable it operate at elevated temperature typically above 1000^0C [33]. The specimen is inserted within the solenoid coil located within a stainless steel cylindrical chamber; a central line heater supplies the heat to the coil and specimen. The static magnetic field required for the electromagnetic excitation and detection of acoustic wave is provided by a pair of permanent magnets. This type of EMAT generates acoustic waves either by the Lorentz force mechanism or the magnetostrictive mechanism depending on the orientation of the biasing field and nature of the specimen.

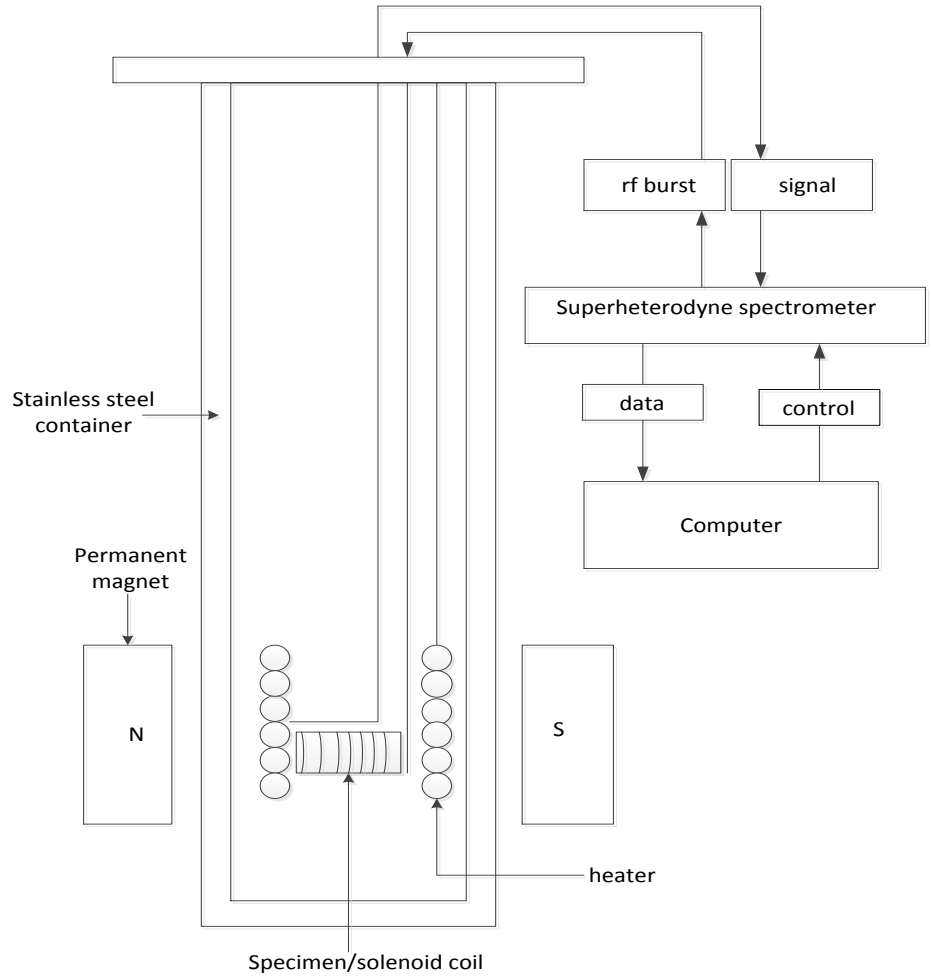

Fig.2.17: Detailed structure of an EMAT for high temperature measurement [33].

2.7 Advantages and limitations of EMAT

The mechanism of operation of EMATs does not require the transducer to make direct contact with the material under test. This great advantage is exploited in high temperature measurement as well as measurement of moving samples. Since no contact is needed, couplant fluids are not required; this advantage minimises the cost associated with surface preparation and simplifies the operation of the transducer. Also, more reliable and accurate measurement can be achieved since errors due to the couplant are eliminated. EMATs as a transducer have been successfully deployed in different industrial applications. High temperature thickness gaging of seamless steel pipes have been achieved during manufacturing process using water cooled permanent magnet [33]. Furthermore, specially designed EMATs have been employed in steel rolling mills to detect anisotropy in the elastic and

electromagnetic properties of steel materials. The non-contact nature of EMAT can be harnessed to measure the speed of sound at different angles from the rolling direction, yielding important information on the formability of the metal sheet [153, 154]. A major advantage of EMAT over other ultrasonic transducers is its ability to generate a wide variety of wave modes. Careful design of the geometry of the EMAT coil and magnet and their relative position allows the excitation and detection of complex wave modes, such as bulk longitudinal and shear waves, Lamb and shear horizontal waves in plate-like structures as well as torsional, flexural and longitudinal modes in pipes and wires [33, 35, 78, 150].

A major limitation of EMAT stems from the fact that due to the non-contact nature and the operating principle, the transducer is extremely inefficient in generating acoustic wave when compare to other traditional ultrasonic transducers, for example, the piezoelectric transducers. The signal to noise ratio is very poor and they require special electronics and careful design for them to be deployed for measurements [155]. Another disadvantage of EMAT is the variation of their performance with the electromagnetic properties of the sample under test. Also, the transducers can only function properly when used on a good electrical conducting material. Table 2.1 summarises the applications, advantages and limitations of various configurations of EMATs used in NDT.

Table 2.1 Summary of EMAT types and their typical applications in NDT.

Types of EMAT	Advantages	Disadvantages	Application
Bulk Wave EMAT	Simultaneously generates shear and longitudinal wave	Does not generate surface waves.	Measurements of in plane anisotropy in rolled sheets
Longitudinal Guided Wave EMAT	Detect flaws in wires of 100m or more	Not ideal for flat metal sheets and irregular shapes	Long range inspection of wires and pipes
Periodic-Permanent EMAT	Generate and lunches shear waves along the surface and inside the material	Operates at low frequencies	Surface flaw detection
Meander-Line Coil SH-Wave EMAT	Generating surface SH wave of higher frequencies.	A large biasing magnetic field is needed when the static field is applied along the straight line of the meander line coil	Surface flaw detection
Axial Shear Wave EMAT	Resonance measurements focused on outer regions of cylinders	Not suitable for non-cylindrical materials shapes	Cylindrical surface of circular rod, pipes and bolt heads.
Rayleigh Wave EMAT	Simultaneously generates surface, longitude and SV waves	It is difficult to identify the mode from the observed echoes	Surface defects and defects inside the material
Line Focusing EMAT	Specially designed array of the meander-line elements allow focusing of the shear vertical waves on a line inside the martial	It is difficult to defect faults deep inside. The shear vertical wave amplitude drops rapidly beyond certain angles	Surface flaw detection
EMAT for High Temperature Measurements	Works at elevated temperature. Up to 1000^{o}C can be achieved	Not ideal for testing of materials below certain temperatures	For welds and high temperature scenarios

2.8 Summary

This chapter presents a general introduction to EMATs, describing in detail their principle of operation and history of development. Various configurations of EMATs including their applications, advantages as well as their limitations in the field of NDT were discussed. Also in the course of the review some and challenges and gaps in knowledge were observed such as:

(a) The signal to noise ration of the output signal of EMAT is still a major souce of concern in the field of EMAT and researchers have not been able to conclusively develop a method to mitigate it.
(b) There is still the problem of decoupling and quantifying the transduction forces that generate acoustic wave when EMATs are used on ferromagnetic materials.
(c) Researchers in the field of EMAT have not been able to develop a numerical model that can account for the magnetostatic, electrodynamic and acoustic phenomenon together. Current models are able to couple the magnetostatic and electrodymic phenomenon while the acoustic phenomenon is treated separated using the piston source model.
(d) Incoporating the effect of magnetostriction has been a problem in the numerical modelling of EMAT. The first attempt was made by Remo Ribichini at Imperial College, but the model did not decouple and quantify the static and the dynamic Lorentz which plays a major role in the generation of acoustic wave in EMAT.

These gaps formed the bases for the study carried out in Chapters 4, 5 and 6.

CHAPTER 3

FUNDAMENTAL THEORY OF EMATs OPERATION

3.1 Introduction

This chapter presents the theoretical background for the governing electrodynamic equations of EMATs. The equations are further extended to account for the derivation of magnetic and acoustic field equations in terms of the magnetic vector potential (MVP) and the displacement vector respectively. Furthermore, the study of EMATs is divided into the transmitting and the receiving mode. In the transmitting mode, three forces; the Lorentz force, magnetization and magnetostriction mechanism are formulated as a function of the MVP for ferromagnetic materials. Whilst, the induced voltage in a receiving coil, is computed as a function of the MVP in the receiving mode.

3.2 Governing equations

The governing electrodynamic equations are presented in terms of the magnetic fields, electric fields and the strain as stated in [33, 99, 110, 113, 156]. These equations will be stated in terms of the MVP and the displacement vector so that the finite element methods can be applied to the equations. In general, the total magnetic field vector $\vec{\boldsymbol{B}}_T$ can be stated in terms of the static magnetic field vector, $\vec{\boldsymbol{B}}_0$ and the dynamic magnetic field vector, $\vec{\boldsymbol{B}}_d$ as:

$$\vec{\boldsymbol{B}}_{\mathbf{T}} = \vec{\boldsymbol{B}}_0 + \vec{\boldsymbol{B}}_{\boldsymbol{d}} \qquad (3.1)$$

The dynamic field has a high frequency and small amplitude (i.e. $\left|\vec{\boldsymbol{B}}_{\boldsymbol{d}}\right| \ll \left|\vec{\boldsymbol{B}}_{\boldsymbol{0}}\right|$). Here it is assumed that the dynamic magnetic field for ferromagnetic material is linear and the losses due to hysteresis effect are negligible, hence they are not included in the formulation. The electromagnetic phenomena leading to the generation of elastic wave by EMATs can be described by Maxwell's equation [33, 48, 99] as:

$$\nabla \times \vec{E} = -\frac{\partial \vec{\boldsymbol{B}}_{\boldsymbol{d}}}{\partial t} \qquad (3.2)$$

$$\nabla \times \vec{H}_d = \vec{J} + \epsilon \frac{\partial \vec{E}}{\partial t} \quad (3.3)$$

$$\nabla . \vec{B}_d = 0 \quad (3.4)$$

$$\nabla . \vec{D} = \rho_\upsilon \quad (3.5)$$

Where $\vec{E}$ is the electric field intensity vector, $\vec{H}_d$is the dynamic magnetic field intensity vector, $\vec{D}$ is the electric flux density vector, $\vec{J}$ is the total current density vector, ϵ is the permittivity and ρ_υ is the volume electric charge density.

Assuming that $\rho_\upsilon = 0$, since the excitation frequency of a typical EMAT does not exceed 10 MHz and neglecting the time derivative in equation (3.3), equations (3.3) and (3.5) can be given as:

$$\nabla \times \vec{H}_d = \vec{J} \quad (3.6)$$

$$\nabla . \vec{D} = 0 \quad (3.7)$$

The coupling between the dynamic fields in EMAT is described by the following constitutive equations [110, 156]:

$$\vec{J} = \sigma\vec{E} + \sigma\frac{\partial \vec{u}}{\partial t} \times \vec{B}_0 \quad (3.8)$$

$$\vec{B}_d = \mu_{2\times2} (\vec{H}_d - \vec{M}_0 \nabla . \vec{u}) + \vec{B}_{MS} \quad (3.9)$$

Where σ and $\mu_{2\times2}$ are the conductivity and the differential magnetic permeability matrix of the material respectively. $\vec{M}_0$ and $\vec{u}$ are the bias magnetisation and particle displacement vectors. The components of the magnetostrictive field vector, $\vec{B}_{MS}$, are determined by:

$$B_{MS} = e_{3\times1} S_{6\times1} \quad (3.10)$$

Where $e_{3\times1}$ and $S_{6\times1}$ are the magnetostrictive matrix, and the column matrix of strain respectively, caused by the ultrasonic waves. The vector $\vec{B}_{MS}$ is computed from its components as:

$$\vec{B}_{MS} = K^T B_{MS} \quad (3.11)$$

Where K^T is the transposed column matrix K containing the basic unit vectors,

$$K = \begin{bmatrix} a_x \\ a_y \\ a_z \end{bmatrix} \tag{3.12}$$

The components e and μ depend on the static magnetic field $\overrightarrow{B_0}$. The terms involving $\vec{u}$ and S are small with respect to other terms in (3.8) and (3.9) and are considered only in the receiving mode [99].

The strain column matrix expressed as a function of the displacement vector, $\vec{u}$, in an xyz Cartesian co-ordinate system, can be stated as

$$S = \nabla_u u \tag{3.13}$$

Where u is a column matrix containing the components of the displacement vector ($\vec{u} = u_x a_x + u_y a_y + u_z a_z$) and operator ∇_u is the displacement gradient matrix given as:

$$\nabla_u = \begin{bmatrix} \frac{\partial}{\partial x} & 0 & 0 \\ 0 & \frac{\partial}{\partial y} & 0 \\ 0 & 0 & \frac{\partial}{\partial z} \\ 0 & \frac{\partial}{\partial z} & \frac{\partial}{\partial y} \\ \frac{\partial}{\partial z} & 0 & \frac{\partial}{\partial x} \\ \frac{\partial}{\partial y} & \frac{\partial}{\partial x} & 0 \end{bmatrix} \tag{3.14}$$

The relationship between the dynamic magnetic field flux ($\vec{B}_d$) and the MVP ($\vec{A}$) is given by

$$\vec{B}_d = \nabla \times \vec{A} \tag{3.15}$$

3.3 Magnetic field equation

To derive the transient magnetic field equations for a two dimensional EMAT model, equation (3.15) is substituted into (3.2) and (3.9) to obtain a comprehensive equation in terms of the MVP [157] (see appendix (A.1) for more detail):

$$\nabla \times (v\nabla \times \vec{A}) = -\sigma\frac{\partial \vec{A}}{\partial t} + \vec{J}_S + \vec{J}_L + \vec{J}_M + \vec{J}_{MS} \quad (3.16)$$

$$\vec{J}_e = -\sigma\frac{\partial \vec{A}}{\partial t} \quad (3.17)$$

Where v is the inverse of the permeability matrix, $\vec{J}_S$ is the source current density (SCD) vector, $\vec{J}_e$ is the Eddy current density, $\vec{J}_L$ is the Lorentz current density, $\vec{J}_M$ is the magnetisation current density and $\vec{J}_{MS}$ is the magnetostrictive current density.

3.3.1 Lorentz current density (J_L)

This phenomenon occurs in both ferromagnetic and non-ferromagnetic materials. It is as a result of the interaction between the time dependent particle displacement vector and the static bias field. The direction and intensity of the Lorentz current density is determined by equation (3.18) [157].

$$\vec{J}_L = \sigma \frac{\partial \vec{u}}{\partial t} \times \vec{B}_0 \quad (3.18)$$

3.3.2 Magnetisation current density (J_M)

The magnetisation current density is found only in ferromagnetic materials. It is due to the unequal dislodgement of the positive and negative charges that constitute the magnetic dipoles. The dislodgement is created by the interactions between the spatial variation of the particle displacement vector and the magnetisation vector. The intensity ($\vec{J}_M$) can be determined by equation (3.19) [157]

$$\vec{J}_M = -\nabla \times (\vec{M}_0 \nabla . \vec{u}) \quad (3.19)$$

3.3.3 Magnetostrictive current density (J_{MS})

This is due to the interaction between the static magnetic field and the spatial variation of the particle displacement vector. The individual domains of ferromagnetic material experiences physical deformation under the influence of static magnetic field. The intensity of J_{MS} is calculated from equation (3.20).

$$\vec{J}_{MS} = \nabla \times \vec{H}_{MS} \tag{3.20}$$

The magnetostrictive field intensity vector $\vec{H}_{MS}$ is given as

$$\vec{H}_{MS} = v\,\vec{B}_{MS} \tag{3.21}$$

In a 2D model of EMAT, the MVP has only z-orientation given as

$$\vec{A} = A_z\,a_z \tag{3.22}$$

This implies that $\vec{J}_L, \vec{J}_M$ and $\vec{J}_{MS}$ have only the z component respectively. Substituting equation (3.22) into (3.16) the MVP becomes

$$- v\nabla^2 A_z + \sigma\frac{\partial A_z}{\partial t} = J_{sz} + J_{Lz} + J_{Mz} + J_{MSz} \tag{3.23}$$

More details on equations (3.16 to 3.21) are given in Appendix A.1.

3.4 Elastic wave generation

In the generation of acoustic wave by EMAT, a current carrying coil placed in close proximity with the material creates the dynamic magnetic field flux. The sinusoidal excitation current flowing inside the coil gives rise to the source current density (SCD) in the z direction (J_{sz}). In equations (3.8) and (3.9), the term $\vec{u}$ and S are small compared to other terms in the equations and are not considered in wave generation. Since the current densities (J_{Lz}, J_{Mz} and J_{MSz}) contain terms in u and S , they are ignored in the equation for SCD. Therefore, the SCD in terms of total current of the K^{th} conductor $i_k(t)$ and the z component of the MVP (A_z) is expressed as

$$J_{sz}(t) = \frac{i_k(t)}{S_k} + \frac{\sigma}{S_k}\frac{\partial}{\partial t}\iint_{R_k} A_z ds \tag{3.24}$$

Where J_{sz} and $S_k = \iint_{R_k} ds$ are the constant SCD of the K^{th} conductor in the z direction and the cross-sectional area of the K^{th} conductor respectively.

To obtain a complete equation for the SCD, equation (3.23) is substituted into equation (3.24) to give

$$- v\nabla^2 A_z + \sigma\frac{\partial A_z}{\partial t} - \frac{\sigma}{S_k}\frac{\partial}{\partial t}\iint_{R_k} A_z ds = \frac{i_k(t)}{S_k} \tag{3.25}$$

To excite EMATs a tone burst signal is required, the transient current of the K^{th} conductor ($i_k(t)$) can be described as a tone burst signal by

$$i_k(t) = \begin{cases} (-1)^k I_p sin^2\left\{\frac{w_0 t}{(2n)}\right\}\cos(w_0 t) \\ \quad for\ 0 \le t \le \frac{(2n\pi)}{w_0} \\ 0 \quad for\ t \le 0\ and\ t \ge \frac{(2n\pi)}{w_0} \end{cases} \tag{3.26}$$

Where I_p, w_0=2πf_0 and *n* are the amplitude of excitation current, current angular frequency and the number of cycles per tone burst signal.

If the material is assumed to be an isotropic solid with electrodynamic force density, the inhomogeneous elastic equation according to Newton's law is stated as

$$\vec{f}_{total} = \rho\frac{\partial^2 \vec{u}}{\partial t^2} \tag{3.27}$$

Where $\vec{f}_{total}$, ρ and $\vec{u}$ are total force per unit volume, material density and particle displacement vector respectively.

The total force density can also be expressed as

$$\vec{f}_{total} = \vec{f}_{traction} + \vec{f}_{body} \tag{3.28}$$

Where $\vec{f}_{traction}$ and $\vec{f}_{body}$ are surface traction and body force respectively.

The body force density is also stated as

$$\vec{f}_{body} = \vec{f}_L + \vec{f}_M + \vec{f}_{MS} \tag{3.29}$$

Where $\vec{f}_L$, $\vec{f}_M$ and $\vec{f}_{MS}$ are Lorentz, magnetisation and magnetostrictive force densities respectively and are explain as follows:

3.4.1 Lorentz force density ($\vec{F}_L$)

The time variable SCD, $J_{sz}(t)$, flowing in the EMATs coil induces an Eddy current density J_e , in the conducting material, opposing the original current in accordance to Faraday's law (see equation 3.2). The induced current is confined in a superficial portion of the material known as the electromagnetic skin depth (δ). For a sinusoidal plane electromagnetic wave of frequency f_0, impacting on a material with conductivity (σ) and permeability ($\mu_0\mu_r$), the electromagnetic skin depth is given as [48].

$$\delta = \frac{1}{\sqrt{\pi f_0 \sigma \mu_0 \mu_r}} \tag{3.30}$$

The Eddy current interacts with both the static magnetic and dynamic magnetic field to yield a body force known as the Lorentz force. The direction and intensity of the Lorentz force is given as

$$\vec{F}_L = \vec{J}_e \times (\vec{B}_0 + \vec{B}_d) \tag{3.31}$$

$$\vec{F}_L = \vec{F}_{Ls} + \vec{F}_{Ld} = (\vec{J}_e \times \vec{B}_0) + (\vec{J}_e \times \vec{B}_d) \tag{3.32}$$

$$\vec{F}_{Ls} = \vec{J}_e \times \vec{B}_0 \tag{3.33}$$

$$\vec{F}_{Ld} = \vec{J}_e \times \vec{B}_d \tag{3.34}$$

Where $\vec{F}_{Ls}$ and $\vec{F}_{Ld}$ are the Lorentz force density due to the static magnetic field flux and the dynamic magnetic field flux respectively.

3.4.2 Magnetisation force density ($\vec{f}_M$)

The interaction between the dynamic magnetic field $\vec{B}_d$ and the bias magnetization vector $\vec{M}_0$ in a ferromagnetic material creates a reorientation of the magnetic dipoles, which give rise to the magnetisation force. The intensity of $\vec{f}_M$ is described as [78]

$$\vec{f}_M = (\vec{M}_0 \,.\, \nabla)\, \vec{B}_d \tag{3.35}$$

When the bias magnetic field of EMAT is tangentially oriented (i.e. $\vec{B}_{0z}$ = 0), the z component of the Lorentz and the magnetization forces respectively act in opposite direction hence the z component of magnetization force cancels a large part of the Lorentz force. Thus, the Lorentz and the magnetisation forces are not effective in generating longitudinal wave mode in ferromagnetic materials [33, 100] .

3.4.3 Magnetostrictive force density

This phenomenon is due to the physical deformation of the magnetic domain in ferromagnetic materials when immersed in an external magnetic field. The individual magnetic domains are spontaneously deformed by their internal magnetization [78, 113].

Coupling between the elastic and magnetic fields for a ferromagnetic material can be assumed to take a similar form as that for a piezoelectric material [33]:

$$S_I = P_{Ij}^{(MS)} H_J + \tilde{S}_{IJ}^{H}\, \tilde{\sigma}_J \text{. } (I, J = 1, 2, \ldots\ldots, 6;\ j = x, y, z) \tag{3.36}$$

Where S_I, $\tilde{S}_{IJ}^{H}$ and $\tilde{\sigma}_J$ are component of strain, component of the compliance matrix at a constant field and component of stress respectively. $P^{(MS)}$ is the piezomagnetic strain coefficient and can be described as [22]:

$$P_{Ij}^{(MS)} = \left(\frac{\partial S_I}{\partial H_j}\right)_{|\tilde{\sigma}} \tag{3.36}$$

With reference to (3.36), the strain field can be written in terms of the stress component and the magnetic field as:

$$S_I = P_{Ij}^{(MS)} \times H_j \tag{3.37}$$

When H = 0, the relationship between the strain and stress field is given as

$$\tilde{\sigma}_K = c_{KI}^{H}\, S_I \tag{3.38}$$

Where c_{KI}^{H} is the elastic stiffness coefficient at a constant field, $\tilde{\sigma}_K$ is the stress field and S_I is the strain field.

Substituting equation (3.37) into equation (3.38) yields the magnitude of stress required to cause magnetostriction in a ferromagnetic material

$$\tilde{\sigma}_K = c_{KI}^H \, P_{Ij}^{(MS)} \, H_j \tag{3.39}$$

If the magnetic field changes with time or vibrate with a high frequency, a negative stress field component ($-\tilde{\sigma}_K$) known as magnetostrictive stress will be created in the material and can be described as

$$\tilde{\sigma}_I^{(MS)} = - c_{IJ}^H \, P_{Jj}^{(MS)} \, H_j = - e_{Ij}^{(MS)} H_j, \tag{3.40}$$

With the converse piezomagnetic stress coefficients as

$$e_{Ij}^{(MS)} = c_{IJ}^H \, P_{Jj}^{(MS)} = - \left(\frac{\partial \tilde{\sigma}_I^{(MS)}}{\partial H_j} \right)_{|S} \tag{3.41}$$

The constitutive equation accounting for stress, strain and the magnetic field can be stated as

$$\tilde{\sigma}_I = - e_{Ij}^{(MS)} H_j + c_{IJ}^H \, S_J \tag{3.42}$$

Equation (3.42) is analogous to the piezoelectric stress equation. The body forces due to magnetostrictive stress can be given as [33]

$$\begin{cases} f_x^{(MS)} = \dfrac{\partial \tilde{\sigma}_1^{(MS)}}{\partial x} + \dfrac{\partial \tilde{\sigma}_6^{(MS)}}{\partial y} + \dfrac{\partial \tilde{\sigma}_5^{(MS)}}{\partial z} \\ f_y^{(MS)} = \dfrac{\partial \tilde{\sigma}_6^{(MS)}}{\partial x} + \dfrac{\partial \tilde{\sigma}_2^{(MS)}}{\partial y} + \dfrac{\partial \tilde{\sigma}_4^{(MS)}}{\partial z} \\ f_z^{(MS)} = \dfrac{\partial \tilde{\sigma}_5^{(MS)}}{\partial x} + \dfrac{\partial \tilde{\sigma}_4^{(MS)}}{\partial y} + \dfrac{\partial \tilde{\sigma}_3^{(MS)}}{\partial z} \end{cases} \tag{3.43}$$

A combination of equations (3.27) and (3.43) yields the acoustic field generated by magnetostrictive forces when the piezomagnetic coefficients ($P^{(MS)}$ and $e^{(MS)}$) are known. The piezomagnetic constants depend highly on the magnitude and the direction of the applied field. However, they can be estimated from the magnetostriction curve.

3.5 Elastic wave detection

In the acoustic wave detection mode of EMAT, a dynamic deformation caused by an acoustic wave creates dynamic magnetic field in a conducting material subjected to a steady magnetic field. The dynamic magnetic fields will pass through the material/ vacuum boundary and induce a voltage in a pickup coil above the material. Therefore, the analysis of the detection mechanisms of EMAT must include three main factors [33], [156]:

(i) The electromagnetic fields within the material due to the elastic wave

(ii) Moving boundary at the material surface, through which the fields pass into a vacuum.

(iii) The electromagnetic fields in vacuum where the fields are located, where the pickup coil is located.

Since the pickup coil is modelled as an open circuit coil, the total current in the coil conductors ($i_k(t)$), is taken to be zero. Therefore, equation (3.24) is resolved to become

$$J_{sz} = \frac{\sigma}{S_k}\frac{\partial}{\partial t}\iint_{R_k} A_z ds \tag{3.44}$$

Substituting equation (3.44) to the MVP equation in (3.23) yields

$$-\nu\nabla^2 A_z + \sigma\frac{\partial A_z}{\partial t} - \frac{\sigma}{S_k}\frac{\partial}{\partial t}\iint_{R_k} A_z ds = J_{zE} \tag{3.45}$$

Where $J_{zE} = J_{Ls} + J_{Mz} + J_{MSz}$ (3.46)

Solving equation (3.46) for $\vec{A} = A_z a_z$ in the space above the specimen based on Faraday's law and Stoke's theorem, the induced voltage in the pickup coil is given as [158]:

$$\text{Emf} = -\frac{d\emptyset}{dt} = -\frac{\partial}{\partial t}\iint_S B_d . ds = \oint_C \overrightarrow{E} . \vec{d}l \tag{3.47}$$

Where $\vec{E}$ can be computed by $\vec{A}$ and $\vec{J}_s$ as

$$\vec{E} = -\frac{\partial \vec{A}}{\partial t} + \frac{1}{\sigma}\vec{J}_s \quad \text{(details in Appendix A)} \tag{3.48}$$

3.6 Summary

This chapter presents the physical principles that governs the magnetostatics, electrodynamic and acoustic equations of EMATs. It also extends these equations to the derivation of the magnetic and acoustic field equations in terms of the magnetic vector potential and the displacement vector respectively. The formula for calculating current and force densities were also presented. The analysis of EMAT is separated into the transmitting and the detection mode. The expression for force and current densities were obtained based on the Lorentz, magnetisation and magnetostriction mechanisms. The equations and the formulations are the basis for the finite element model created in Chapters 4 and 6 respectively.

CHAPTER 4[1]

DEVELOPMENT AND EVALUATION OF A NOVEL KT- EMAT CONFIGURATION BASED ON LORENTZ FORCE MECHANISM.

4.1 Introduction

The purpose of this chapter is to develop a Lorentz force finite element EMAT model (see Fig.1.11) using a commercial software (Comsol Multiphysics®), to study and compare the eddy current and Lorentz force densities generated by two commercially available EMAT coil configurations (meanderline and spiral coil configurations), and a novel KT coil configuration operating on CS70 grade of pipe steel. The model will couple the magnetostatic and electrodynamic phenomenon to generate Eddy current and Lorentz for on the surface of CS70 grade of pipe steel material. The Model will be used to compare the Eddy current and Lorentz force densities generated in order to ascertain the configuration that generates greater density under any given condition. Finally, the performance of the novel EMAT configuration will be investigated by studying how some EMAT design parameters influence the density of Lorentz force generated. The parameters investigated includes: coil dimension, static magnetic field, coil internal diameter, excitation frequency, lift-off, coil stacking, insulation layer thickness and the number of cycles per burst of excitation current.

4.2 Numerical simulation

The core of EMATs operational mechanisms consist of body forces created in the material by the interaction of the static and dynamic fields with the Eddy current induced in the material. As described in section (2.2), the Eddy current is produced by the time varying excitation current while the bias field is produced by a permanent or an electromagnet. The body forces cause the generation of acoustic wave in the conducting material. Therefore, the modelling process of EMAT is split into the magnetostatics, electrodynamics and the mechanical/elastic part.

[1] The bulk of this chapter has been published by the author in [93-96]

The most accurate method to solve the electrodynamic and elastic problem is to invoke the differential form of Maxwell's equations (Ampere's law and Faraday's law of induction) with the appropriate boundary conditions taken into account (see section 3.2). The most suitable solution to these problems is to use numerical techniques to find an approximate solution to the partial differential equations (PDE). The three commonly used techniques to solve PDE's are: the finite element method (FEM), the finite volume method (FVM) and the finite difference method (FDM) [159]. Amongst the three methods, FEM is often regarded as the most common and most accurate approximation technique employed in solid based simulations and structural mechanics. FVM and FDM employs slightly different method of finding solutions to PDE's, by discretising the problem to large number of grids and are widely used in computational fluid dynamics (CFD). In FEM, the geometry and the domains are discretised into a set of finite elements (mesh generation) and the final solution is the sum of the discrete solutions in each discrete element, hence the accuracy of the solution can be increased by increasing the number of discrete elements in the domain.

For a 2D geometry, the subdomains are partitioned into triangular or quadrilateral mesh elements. In a curved boundary, the elements represent only an approximation of the original geometry. Similarly, in the 3D geometry the subdomains are partitioned into hexahedral or prism and tetrahedral elements. The geometry edges are partitioned into edge elements [159]. There are several commercial simulation software based on FEM modelling techniques for solution of PDE's such as Comsol multiphysics, ANSYS, Abacus, ADINA and ALGOR. Comsol multiphysic is used in this research because of the following fetures:

(i) Comsol multiphysics is very robust and versatile in the coupling of different physics which gives room for modelling of the actual phenomenon that take place in the operation of EMAT (i.e. the conversion of electromagnetic energy into acoustic energy and vice versa).

(ii) The software makes use of Maxwell's equation in FE approximation method to solve electrodynamic problems. A unique feature of Comsol multiphysics is that the underlying equations for electromagnetics are automatically

available in all other application modes, making coupling of different physics much easier between different application modes.

(iii) The software has predefined physics interfaces which gives room for the control over the definition of constants, the use of the material properties and the boundary conditions.

(iv) Comsol multiphysics give room for models to take advantage of symmetry where possible to reduce computation time and exploit available memory.

4.2.1 Model implementation in Comsol multiphysics

The design of the model in Comsol multiphysics started with the selection of appropriate modules related to the physics involved in EMAT operation. The AC/DC module and the structural mechanics module where used to solve the magnetostatics, electrodynamics and the elastic problems respectively. Figure 4.1 shows the block diagram of the processes involved in modelling EMAT for the generation of Eddy current and Lorentz force.

The simulation carried out in this chapter involves different shapes/structures of copper coil (i.e. meander-line coil, spiral coil and KT coil). The spiral and KT coil were simulated in 2D axisymmetric mode, while the meander-line coil was simulated in 2D mode. The 2D axial symmetric application mode is not suitable for the simulation of non- circular coil structure, hence the meander-line coil was model in the x and z plane with some appropriate assumptions.

The application mode used for the simulation is the magnetic field (mf) and the magnetic field no current (mfnc). The mf describes the quasi-static magnetic field system for conducting, magnetic and dielectric materials. This feature is used for easy excitation of coils and other conducting structures. The dependent variable in this application mode is the vector magnetic potential in the Cartesian coordinate (A_r, A_{phi} and A_z) and electric current can be used as input in the model subdomain setting. The Lorentz force and other magnetic parameters are calculated from the vector magnetic potential.

To simulate the effect of the bias magnetic field generated by the permanent magnet, the application mode; magnetic field no current (mfnc) was employed. It describes the magnetostatics of conducting and magnetic material. The dependent variable in this application mode is the magnetic scalar potential (V_m).

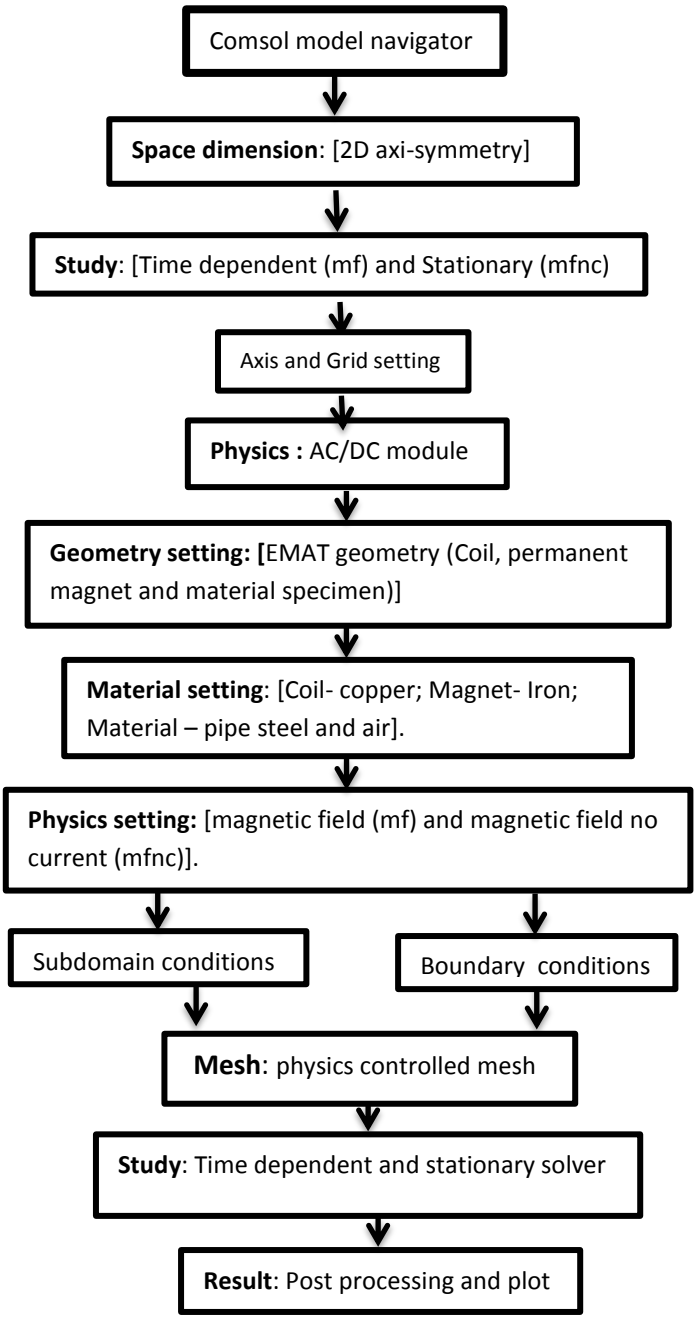

Fig 4.1 Block diagram showing the steps involved in FE modelling of the generation Eddy current and Lorentz by the novel KT- EMAT configuration.

4.3 Comparative study Of EMAT coil configurations

This research compares the induced current density and Lorentz force generated by two commonly used conventional EMAT coil configurations on one hand and the key type configuration on the other hand, on CS70 grade of steel used in the construction of oil and gas pipelines. The most important disadvantage of the conventional EMAT coil configurations (i.e. circular spiral and meander line coil) is the fabrication complexity regarding electric connection from the middle end of the coils. To overcome this problem, a novel design known as the Key-Type coil is proposed (see Fig.4.2C) for use in EMATs. The novel design combines the structural property of a planar spiral coil (Fig.4.2B) and the current path of a meander-line coil (Fig.4.2A) to generate radially polarised Rayleigh and bulk wave. In the novel KT coil, the coil patterning and the electric connections can be made in the same layer making it very easy to fabricate and stacked in layers to generate greater Eddy current and Lorentz force densities. The electrical and magnetic property of this pipe steel is given in table 4.1.

Table 4.1: Measured Electromagnetic properties of pipe steel material [90]

Designation of pipe steel	Conductivity σ [S/m]	Relative permeability μ_r
CS70	3.77×10^6	59

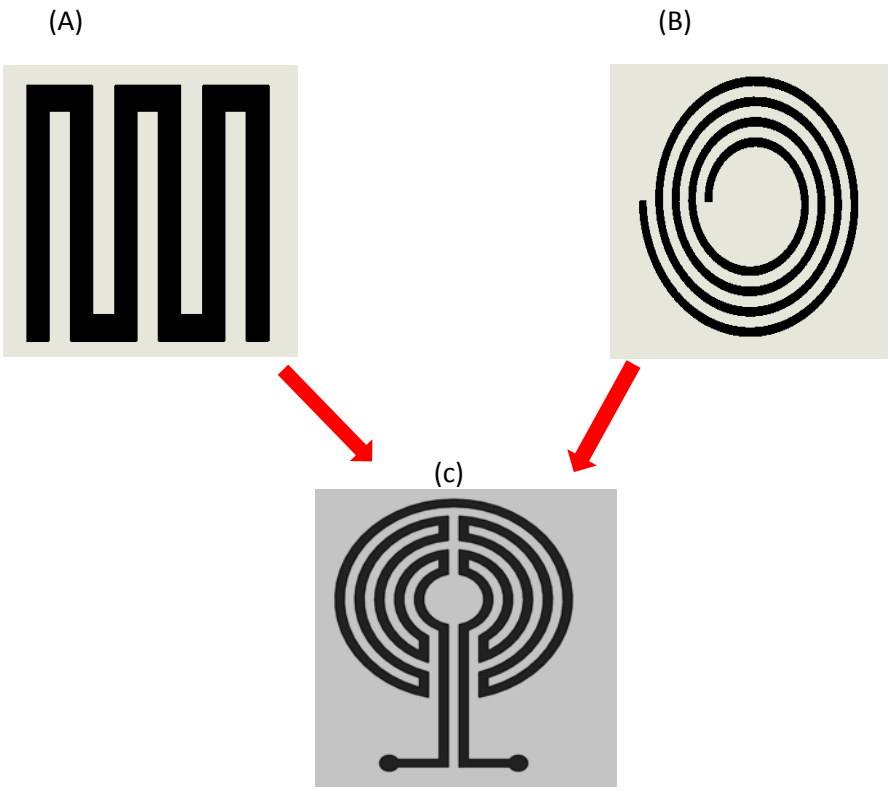

Fig. 4.2 Schematic of EMAT coil configurations.(A) Meander-line coil, (B) Spiral coil, (C) Proposed Key-Type coil. A Combination of the current path of (A) with the structural configuration of (B) gives a novel coil configuration (c).

The cross sectional view and the structural parameters of the EMAT configurations under investigation is given in Fig.4.3 (A, B and C) and Table 4.2 respectively. It consists of a static magnetic field, a steel plate used as the test specimen and a coil. The transient magnetic field for the transmitting EMAT is expressed in terms of magnetic vector potential (MVP) A, and source current density (SCD). If we assume that the test material is infinitely long, the current densities j_{sk} and MVP have only longitudinal, and z-component [160-162] and is represented by the differential equation given in equation (3.25).

Table 4.2 Parameters used in the simulation of various EMATs configurations

s/n	**Parameter name**	**Abbreviation**	**size**
1	Permanent magnet	NbFeb	5x12mm
2	Steel plate	CS70	6x18mm
3	Coil thickness	t_c	0.2mm
4	Coil width	c_w	1.5mm
5	Coil distance	c_s	1mm
6	Lift off distance	H	0.5mm
7	Internal diameter	d_{in}	4mm

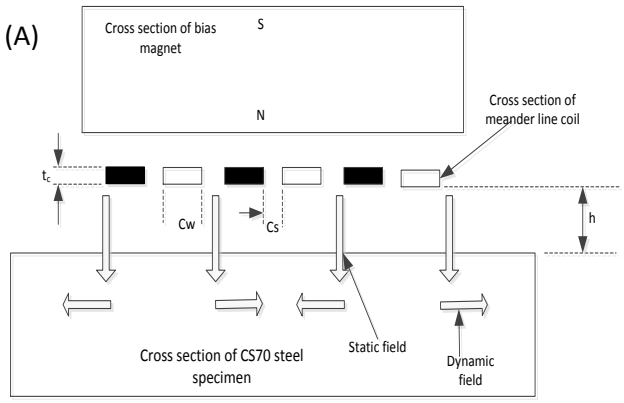

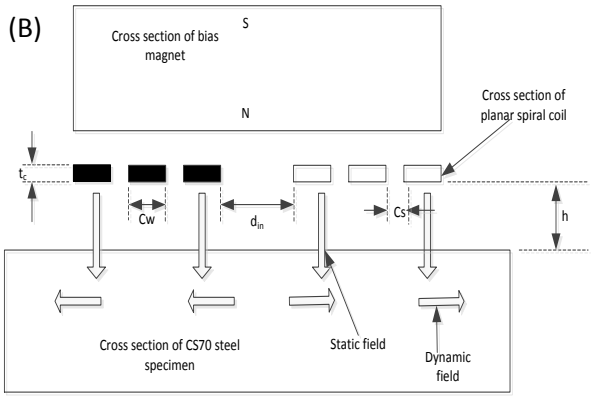

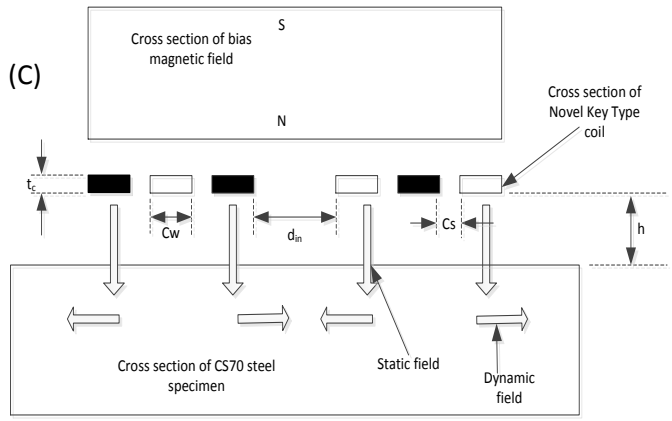

Fig.4.3 Cross sectional view of EMAT structure with dynamic field, static field, effective magnetic field and current path shown. (A) Meander-line coil over pipe steel specimen. (B) Planar spiral coil over pipe steel specimen. (C) Proposed Key-Type coil over pipe steel specimen. Figure not drawn with scale. ■ *represents the in-plane current, while* ▭ represents the out-plane current.

For time varying magnetic field analysis, the source current density is expressed as [162].

$$j_{sk} = \frac{i_k(t)}{s_k} \tag{4.1}$$

Where $i_k(t)$ and s_k are total current and cross-sectional area of the Kth coil conductor. Applying the integral form of Maxwell's equation, it is possible to include the effect of the dynamic field generated by the excited coils into the expression. Thus, the expression for the source current density J_{sk} in the z direction is given in equation (3.24)

The source current density is a function of both the total current flowing through the conductor and the time derivative of the surface integral of the magnetic vector potential [162] and is given in the equation (3.25)

Equation (3.25) takes into account the magnetic field generated by the coil and is a more accurate equation for modelling the scenario under consideration.

The analysis in this section is based solely on the Lorentz force ($\vec{F}_L$) mechanism. Lorentz force is generated as a result of the interaction between the static magnetic

field $\vec{B}_o$ produced by a permanent magnet or an electromagnet, and the eddy current density $\vec{J}_e$ induced by a coil excited with a sinusoidal current. The Lorentz force causes the vibration of the atomic structure of the material, which then leads to the generation of acoustic wave inside the conducting material. The direction and density of the Lorentz force has been described in section (2.2). The acoustic field equation can therefore, be stated in terms of the particle displacement vector $\vec{u}$ and the Lorentz force as:

$$\mu\nabla \times \nabla \times \vec{u} - (\tau+2\mu)\nabla\nabla.\vec{u} + \rho\frac{\partial^2\vec{u}}{\partial t^2} = \vec{F}_L \quad (4.2)$$

Where ρ is mass volume density and τ and μ are Lam*é* constants.

4.3.1 Finite element formulation

The simulation of the coupling of both the magnetostatics, electromagnetic and mechanical/elastic analysis of EMAT shown in Fig.4.1 is presented in the following stages:

Stage1: Calculation of the static magnetic field ($\vec{B}_0$) to solve the differential equation in (4.3). Static analysis is employed to calculate the magnetic scalar potential V_m, which leads to the calculation of static magnetic field;

$$\vec{B}_0 = -\nabla V_m \quad (4.3)$$

In this model, $\vec{B}_0$ is calculated using the magnetic field no current (mfnc) mode of the AC/DC module in COMSOL multiphysics and is assumed to be perpendicular to the current induced in the material specimen as seen in Fig.4.3.

Stage 2: Transient analysis which employed mf mode of the AC/DC module is used to calculate the induced current (J_e), which is time dependent. The coil is excited with a time varying sinusoidal current source $i_k(t)$ and the static magnetic field $\vec{B}_0$ calculated in stage 1, is coupled to the mf mode in the subdomain. The result of the simulation obtained at the surface of the material within the skin depth is the induced current density ($\vec{J}_e$) described in equation (3.17).

It is assumed that the material specimen is infinitely long; hence $\vec{J}_e$ has only one component in the z direction as depicted in equations (3.22 and 3.23).

Stage 3: To calculate the Lorentz force (F_l), the cross product of the induced current density ($\vec{J}_e$) and the static magnetic field $\vec{B}_0$ is obtained, leading to the force component as described in equation (3.31). The direction of the force is also determined by equation (3.31). Due to the fact that the model is in 2D, the static field $\vec{B}_0$ has x and y components, while the induced current ($\vec{J}_e$) has only one component in the z direction. This gives rise to two force components in x and y direction.

4.3.2 Finite element mesh

The finite element model in Fig. 4.4 was obtained by discretising the physical model in to numerous second order quadratic triangular elements consisting of 65454 elements for the ML EMAT, SP EMAT and KT EMAT. The mesh element was refined at about 0.1mm around the skin depth surface of the steel material. This refinement of the model significantly improves its accuracy, though the number of elements as well as the solution time was greatly increased. The refinement is achieved by continuously comparing the calculated result at different degree of refinement until the result hardly changes with refinement.

The time steps, relative tolerance and the absolute tolerance were adjusted for a more accurate calculation.

To obtain an accurate record of the time variation of the extracted data from the simulation, the point probe was placed underneath the first turn of the meander-line, spiral, KT coil configurations respectively.

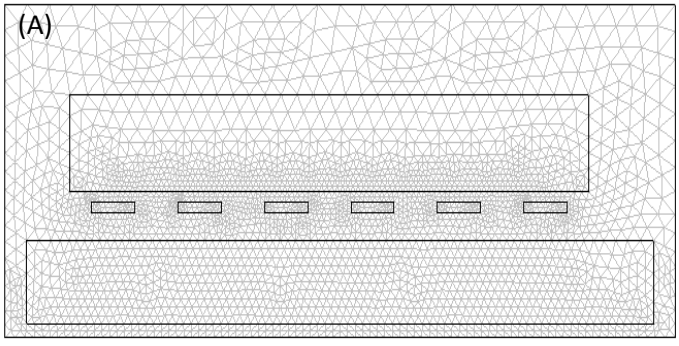

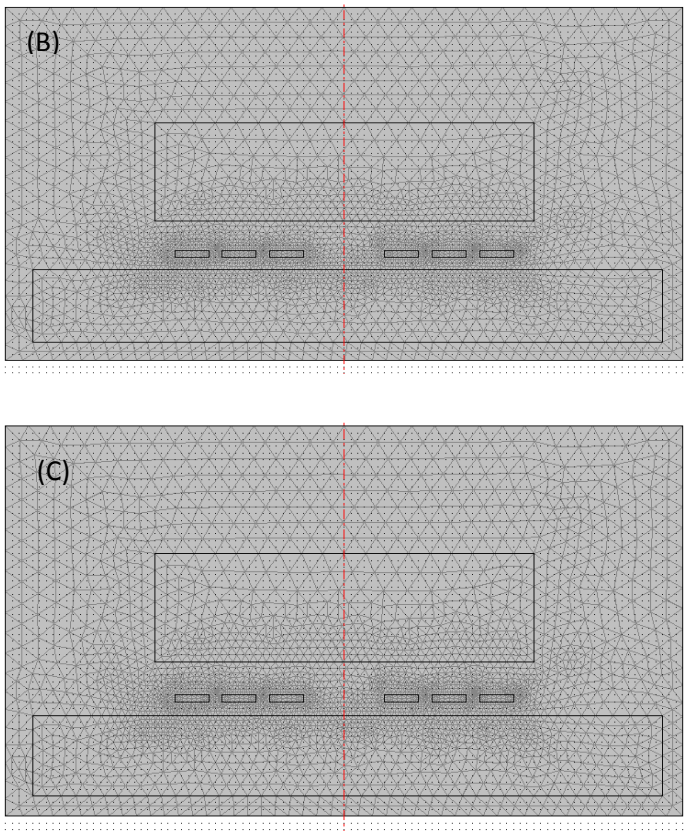

Fig. 4.4 *FE mesh; (A) meander- line coil EMAT, (B) Spiral coil EMAT, (C) KT coil EMAT*.

4.3.3 Simulation and analysis

The driving current applied to the EMAT coil is a two cycle tone burst pulse signal (see equation 3.26). In a 2D scenario, the driving current is converted to current density by dividing the magnitude of the current by the cross sectional area of the coil (i.e. $\frac{I_0}{A}$). The plot of the external source current density employed in the simulation is given in Fig.4.5.

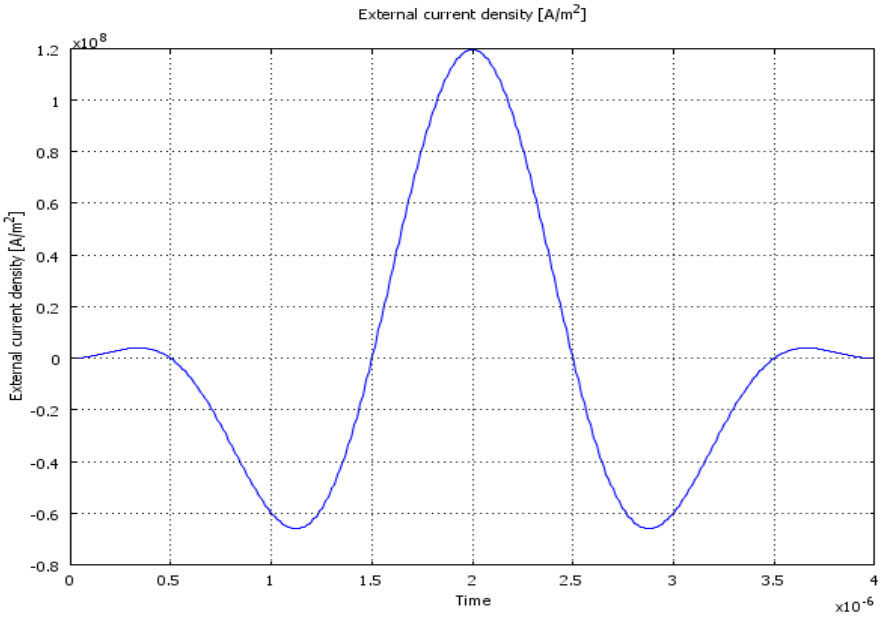

Fig. 4.5 Time history of the External current density for ML, SP and KT EMAT.

Applying the external source current and the static magnetic field in the finite element model, equations (3.25 and 3.31) are solved to obtain the induced current and Lorentz force density respectively, within the skin depth of the CS70 grade of pipe steel. A point plot of the induced current and Lorentz force density is obtained close to the surface of the steel material for the ML, SP, single layer KT EMAT and multi- layer KT-EMAT respectively as shown in figures (4.14 and 4.15).

4.3.3.1 Meanderline coil EMAT configuration

Fig.4.6 shows the surface plot of the dynamic magnetic fields and the Eddy current density induced in the material when a meanderline coil EMAT configuration is employed. Turns 1, 2 and 5 represents the in-plane current while turns 2, 4 and 6 represents the out-plane current. The implication of this configuration is that the dynamic magnetic field due to turns 2, 3, 4 and 5, tends to interfere with each other destructively thereby reducing the strength of the field and consequently reducing the density of the Eddy current generated by the central turns. However, the turns at the edge (i.e. turns 1 and 6) does not experience much of the destructive interference, hence the relative increase in the density of Eddy current experienced at the edges (Edge effect). The same phenomenon is observed with the Lorentz force generated on the material as shown in Fig.4.7.

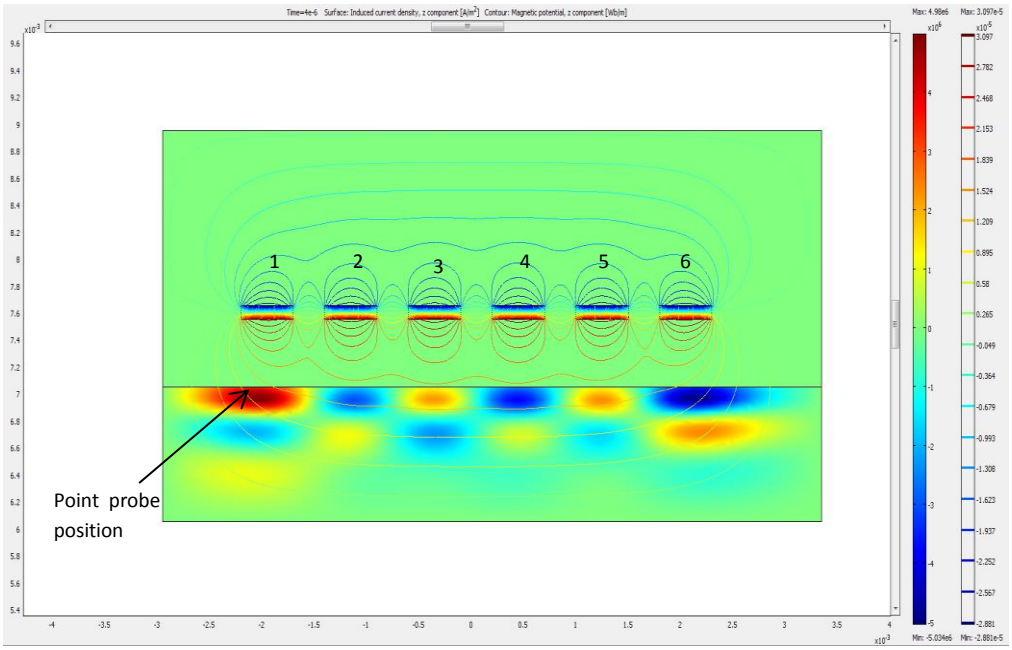

Fig.4.6 Surface and contour plot of the induced current density and magnetic vector potential respectively for a mender-line coil EMAT acting on a CS70 pipe steel plate of 6mm thickness.

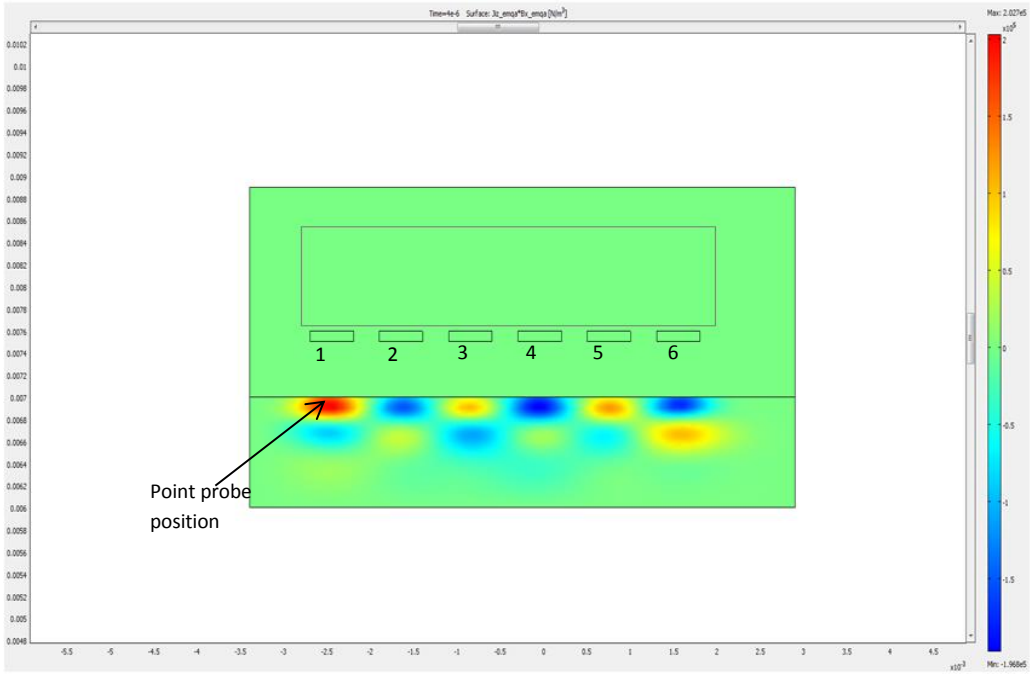

Fig.4.7: Surface plot of the Lorentz force density for a meander-line coil EMAT acting on a CS70 pipe steel plate of 6mm thickness.

4.3.3.2 Spiral coil EMAT configuration

Fig.4.8 depicts the dynamic magnetic field and Eddy current induced in the test material when a spiral coil EMAT configuration is employed in the generation of acoustic wave. Turns 1, 2 and 3 indicates the in-plane current while turns 4, 5 and 6 indicates the out-plane current. The advantage of this configuration is that the destructive interference of the magnetic field is very minimal, hence the induced Eddy current is evenly distributed in the material thereby eliminating the edge effect observed with the meanderline coil EMAT configuration. Also, the gap between turns 3 and 4 (coil inner diameter) contributes to the reduced effect of dynamic magnetic field cancellation, hence there is observed increase in Eddy current density when compared to the meanderline coil EMAT. The same phenomenon is also observed with the Lorentz force surface plot in Fig.4.9.

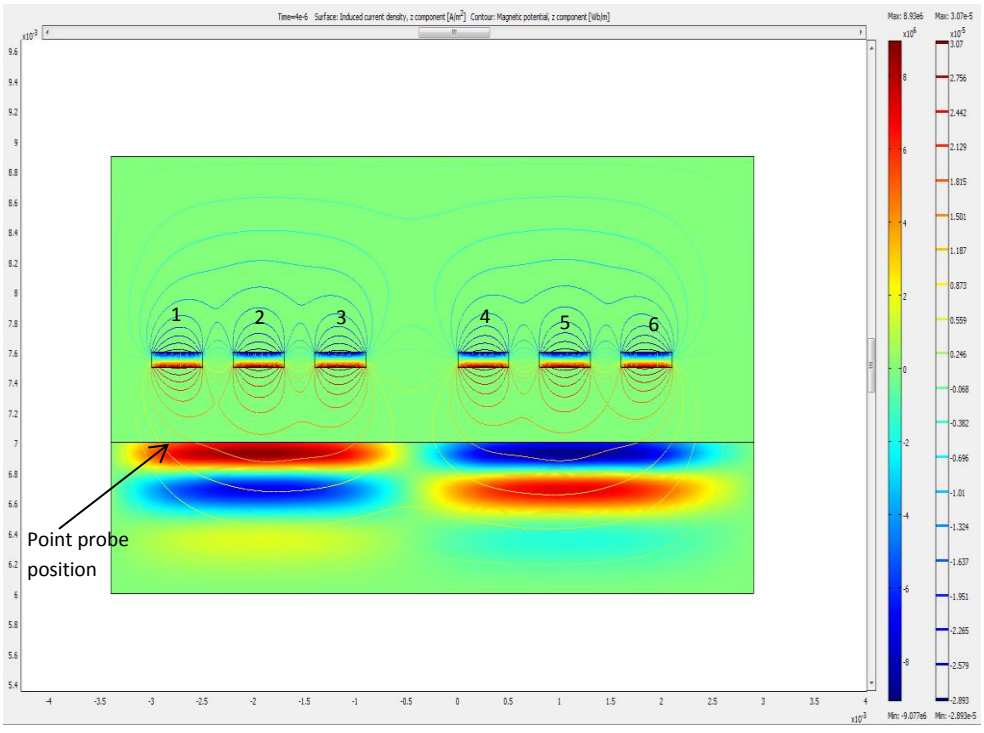

Fig.4.8 Surface and contour plot of the induced current density and magnetic vector potential respectively for a spiral coil EMAT acting on a CS70 pipe steel plate of 6mm thickness.

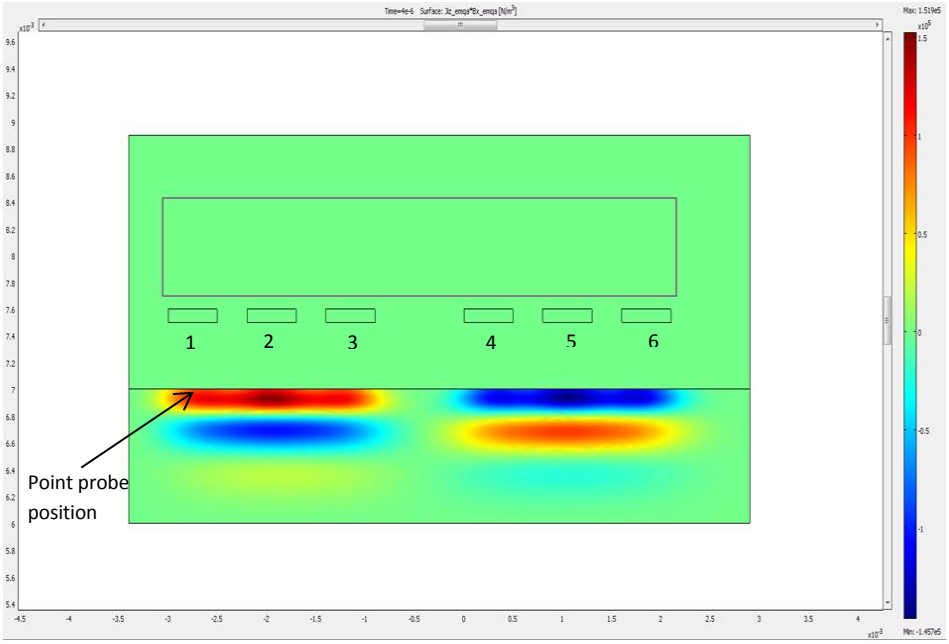

Fig.4.9: Surface plot of the Lorentz force density for a spiral coil EMAT acting on a CS70 pipe steel plate of 6mm thickness.

4.3.3.3 Novel Key Type EMAT configuration

As already discussed in section (4.3), the novel KT coil EMAT combines the structural characteristics of the spiral coil EMAT and current part of the meanderline coil EMAT. This feature is visualised in the surface plot presented in Figs.(4.10 and 4.11). In the KT coil EMAT configuration, the in-plane current flows through turns 1, 3 and 5 while the out-plane current flows through turns 2, 4 and 6 like the meanderline coil EMAT configuration. However, due to the cancellation of the dynamic magnetic fields around turns 1 and 3, and turns 4 and 6; a reduction of the Eddy current and Lorentz force density is observed around turns 2 and 5 while an increase is observed around turns 1 and 6 (Edge effect). Furthermore, by introducing air gap (coil internal diameter) between turns 3 and 4 the density of Eddy current and Lorentz force was also observed to increase around turns 3 and 4. The significance of this phenomenon is that the overall Eddy current induced in the material and the Lorentz force generated by the novel KT coil EMAT is observed to be higher than that generated by the meanderline coil EMAT, but not as high as that generated by the spiral coil

EMAT. The reduced Eddy current can be compensated when the novel KT coils are are stacked in layers and connected in series (see Figs.4.12-4.15).

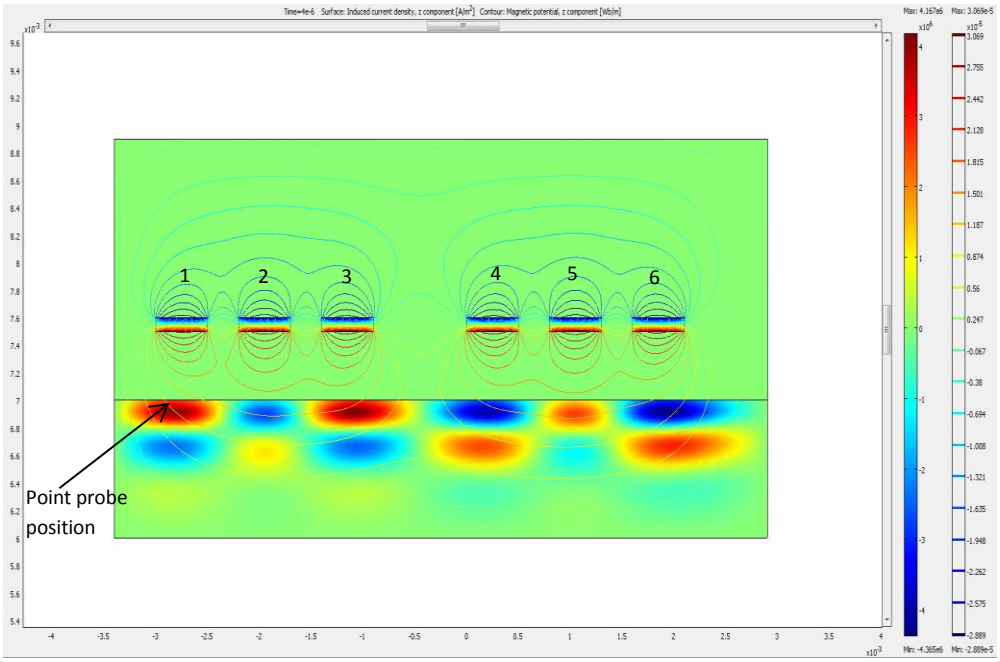

Fig.4.10: Surface and contour plot of the induced current density and magnetic vector potential respectively for a KT coil EMAT acting on a CS70 pipe steel plate of 6mm thickness.

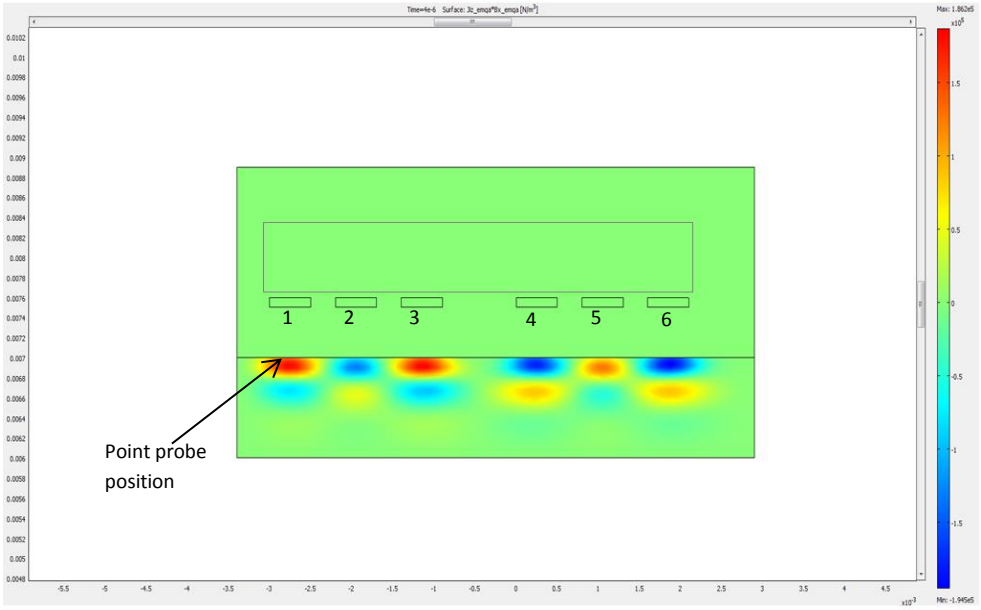

Fig.4.11: Surface plot of the Lorentz force density for a KT coil EMAT acting on a CS70 pipe steel plate of 6mm thickness.

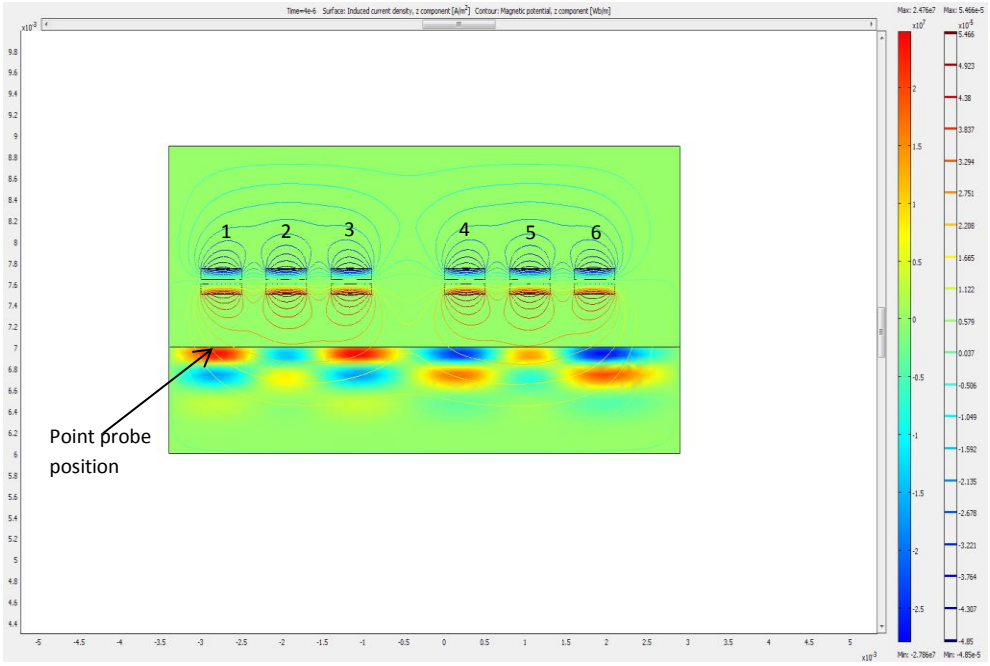

Fig.4.12: Surface and contour plot of the induced current density and magnetic vector potential respectively for a double layer KT coil EMAT acting on a CS70 pipe steel plate of 6mm thickness.

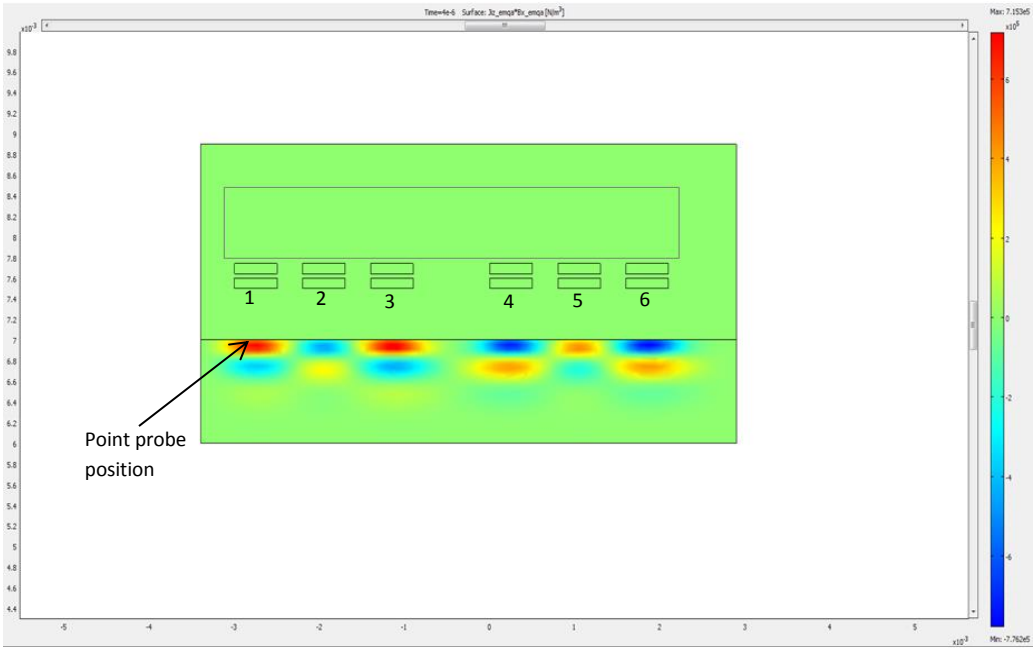

Fig.4.13: Surface plot of the Lorentz force density for a double layer KT coil EMAT acting on a CS70 pipe steel plate of 6mm thickness.

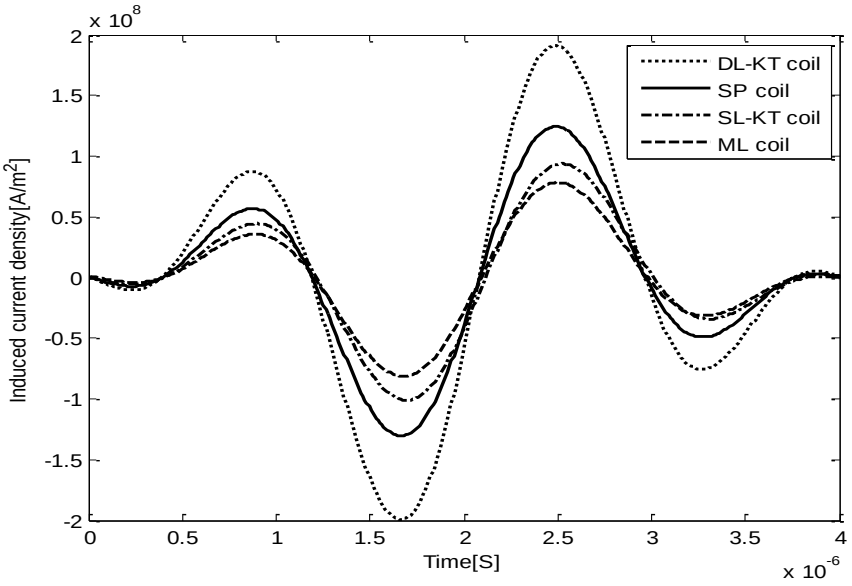

Fig.4.14: Comparison of the FEM result for induced current density generated by ML, SP, single layer KT and double layer KT coil EMAT acting on a CS70 pipe steel plate of 6mm thickness. The plot was extracted from the surface of the material underneath the first coil turn.

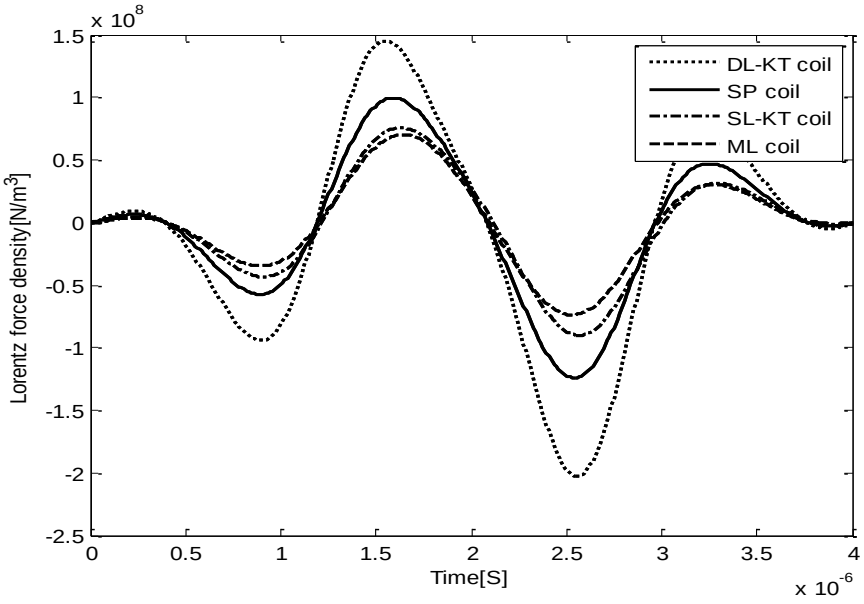

Fig.4.15: Comparison of the FEM result for the Lorentz force density generated by ML, SP, and single layer KT and double layer KT coil EMAT acting on a CS70 pipe steel plate of 6mm thickness. The plot was extracted from the surface of the material underneath the first coil turn.

Futhermore, the result in figures (4.14) and (4.15) shows that there is a correlation between the source excitation current, the induced current and the Lorentz force density respectively. This phenomenon is expected as the induced current is due to the source excitation current and the Lorentz force depends on the induced current as expressed in equations (3.17) and (3.32). The difference observed in the value of amplitude of the source excitation current, induced current and Lorentz force is due to the energy lost during electromagnetic energy conversion. This result is in good agreement with published work [163].

4.4 Investigation of the performance of novel KT-EMAT configuration

Several methods of optimising the performance of EMAT system have been proposed by various researchers [80, 81, 95, 129, 163-166] . One of the methods used to improve the strength of acoustic wave generated by any EMAT system is by improving the density of Eddy current generated, which translate to higher Lorentz force density.

This section studies the response of the KT EMAT to variation of various key EMAT parameters with a view of improving the Lorentz force density generated. The key EMAT parameters studied includes: the influence of the lift-off distance, the influence of coil stacking or layering, the influence of coil internal diameter, the influence of static flux density, the influence of insulation layer thickness, the influence of period of excitation current, the influence of the excitation frequency and influence coil dimension on the Lorentz force density.

4.4.1 The influence of coil dimension on the Lorentz force density

The effect of coil width on the density of Lorentz force generated by KT EMAT coil configuration was investigated. The Lorentz force density was calculated at fixed current amplitude of 20A, static magnetic flux (B_0) of 1.2T, coil thickness of t_c of 0.5mm and an excitation frequency of 500KHz. The value of K-factor (the ratio of coil width (C_w) to coil thickness (t_c)) is calculated and presented in Table 4.3.
Different simulations were carried out by varying the coil width using the K-factor and the result obtained is shown in Figs.(4.16) and (4.17).

Table4.3: Ratio of coil width to coil thickness.

Coil width (w_c)	Coil Thickness (t_c)	K-factor ($\frac{wc}{tc}$)
1mm	0.5mm	2
1.5mm	0.5mm	3
2mm	0.5mm	4
2.5mm	0.5mm	5
3mm	0.5mm	6
3.5mm	0.5mm	7
4mm	0.5mm	8
4.5mm	0.5mm	9
5mm	0.5mm	10

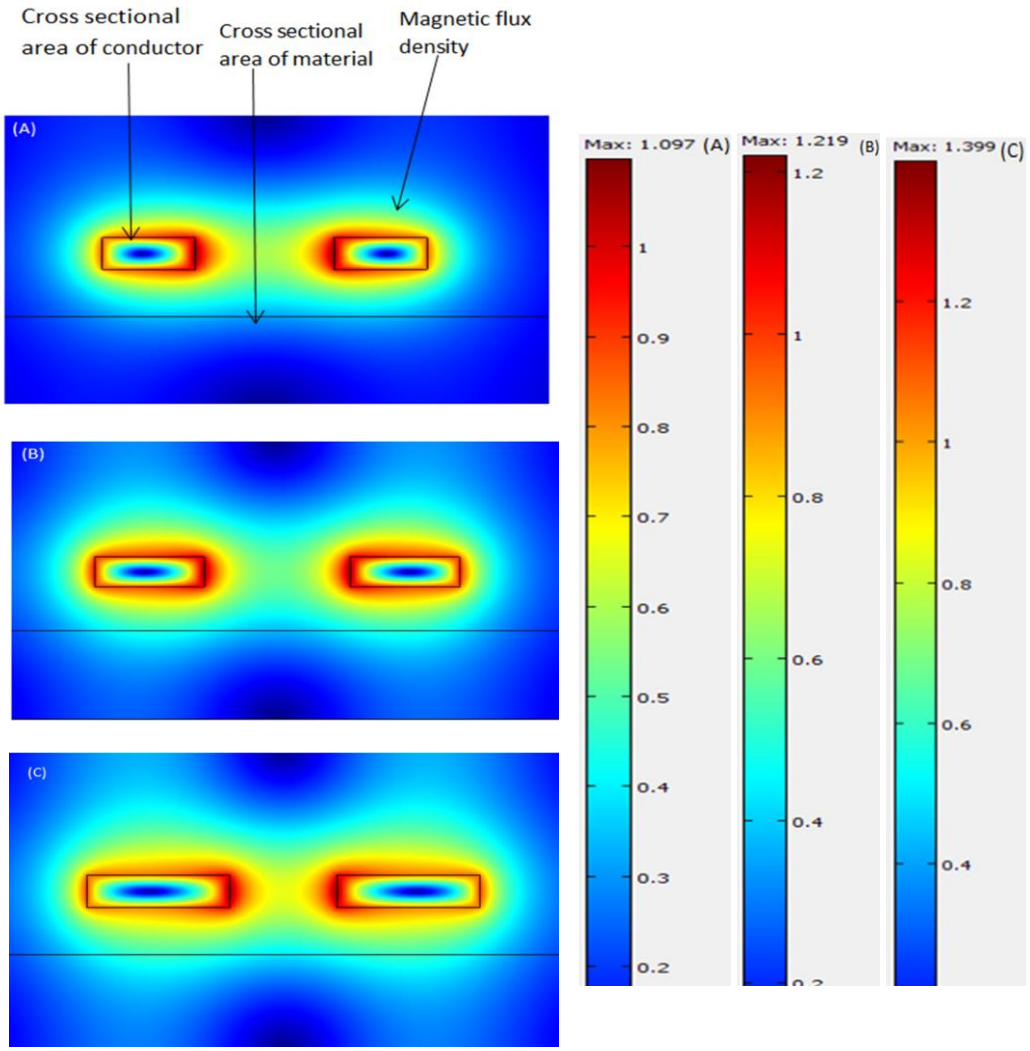

Fig.4.16: Visualisation of the magnetic flux density at K factor (A) 2, (B) 3 and (C) 4.

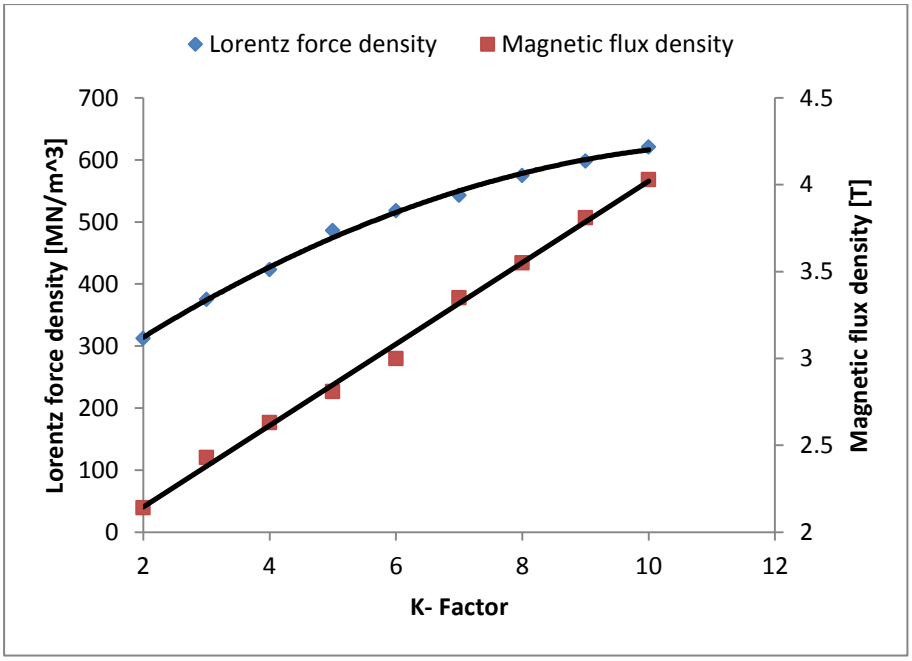

Fig.4.17: Plot of the variation of the K-factor on the Lorentz force and magnetic flux density respectively.

The result in Fig.(4.17) shows that as the value of the K-factor is increased, the Lorentz force and magnetic flux density also increases. This is expected because when the coil dimension is increased while the current density is fixed, the total current is increased and this gives rise to a stronger magnetic flux at the surface of the material.

4.4.2 The influence of lift-off distance on the Lorentz force density

The performance of the three EMATs coil structure on CS70 grade of pipe steel was investigated by varying the lift-off distance from 0.5mm to 8mm above the surface of the steel specimen. The measurement of Lorentz force density was extracted at 0.1mm below the surface of the material specimen around the first turn of the coil. The results shown in Fig.(4.18) indicates that the Lorentz force density decreases exponentially with the lift-off distance, with the four layered KT-EMAT configuration having the best lift off characteristics, followed by the three, two and one layered configuration. This observation is in good agreement with work carried out by [19 80, 167]. In general, the result further indicates that the improvement in the lift-off characteristics is a function of the Lorentz force density, which depends on the number of layers of coil employed.

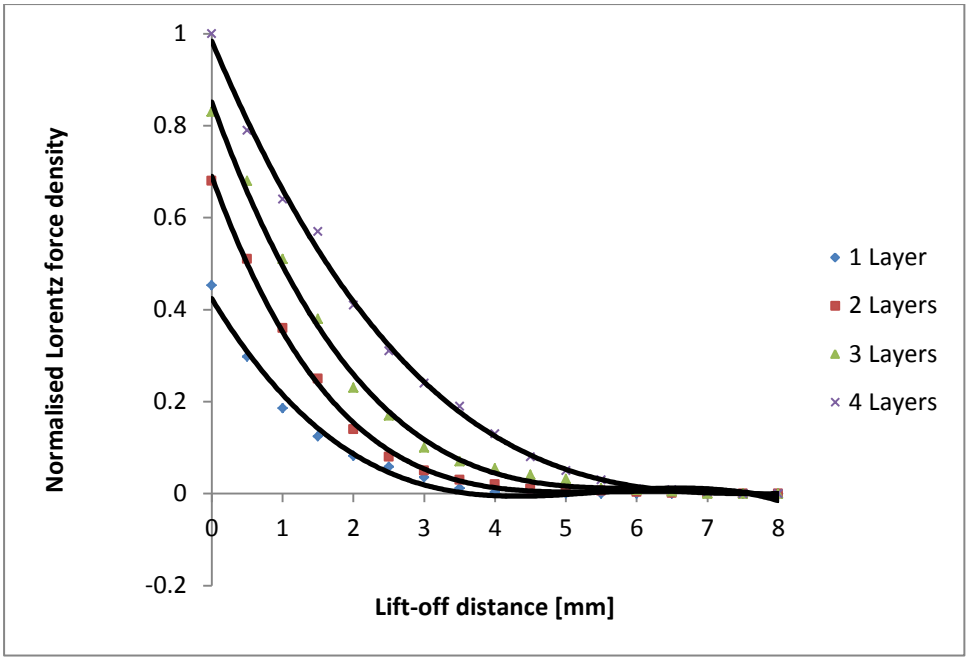

Fig.4.18 Plot of the influence of lift off distance for 1 to 4 layer KT coil structure on CS70 grade of pipe steel.

4.4.3 The influence of coil stacking on the Lorentz force density

The most important disadvantage of planar spiral coil used in EMAT is the fabrication complexity regarding the electrical connection from the middle end of the spiral. This in effect makes it very difficult and expensive to have more than one coil on a planer surface. This draw-back is eliminated by modifying the spiral coil to a novel KT coil (see Fig.4.2C in section 4.2), which is a novel coil combining the structural configuration of a planar spiral coil and the current part of a meander-line coil. The KT is easy and less expensive to fabricate and allows the coils to be stacked one on top of the other using a suitable insulation in-between each stack.

Fig.(4.19), shows the value of the density of Lorentz force for various numbers of coils in a stack. The plot shows that density of the Lorentz force in the materials increases exponentially with the increase in the number of layers of coils and saturates when the number of coils increases beyond ten coils per layer. Any further increment beyond this point does not yield any significant increase in the result. This is expected since an increase in the number of layers of coils, translates to an increase in the total dynamic magnetic flux. This gives rise to an increase in the induced current and Lorentz force densities respectively in the material specimen.

Also, it is worthy to note that the KT coil configuration performs optimally when the number of coil layers does not exceed twelve. This is as a result of the reduced effect of the magnetic field of the additional coil.

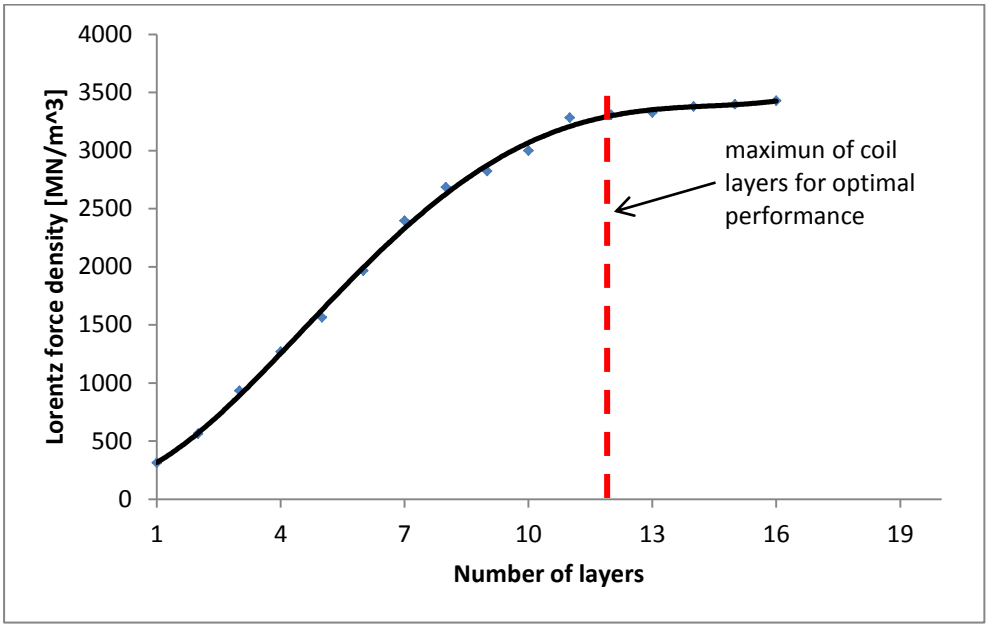

Fig. 4.19: Plot of the influence of coil layers on the Lorentz force generated by the novel KT EMAT configuration.

4.4.4 The influence of coil internal diameter (d_{in}) on the Lorentz force density

Figure (4.20) shows a relationship between the internal diameter and Lorentz force density generated by a KT EMAT. As the internal diameter is increased the Lorentz force also increases up to about 16mm, where any further increment has a negligible effect on the Lorentz force density. This is due to the fact that as the internal diameter is increased, the interaction between opposing dynamic magnetic field created by the opposing current direction in the inner coil turns is reduced. This continues up to a point where there will be little or no effect of the opposing field. Therefore, for optimal performance of this coil configuration, the internal diameter must not be less than 15mm.

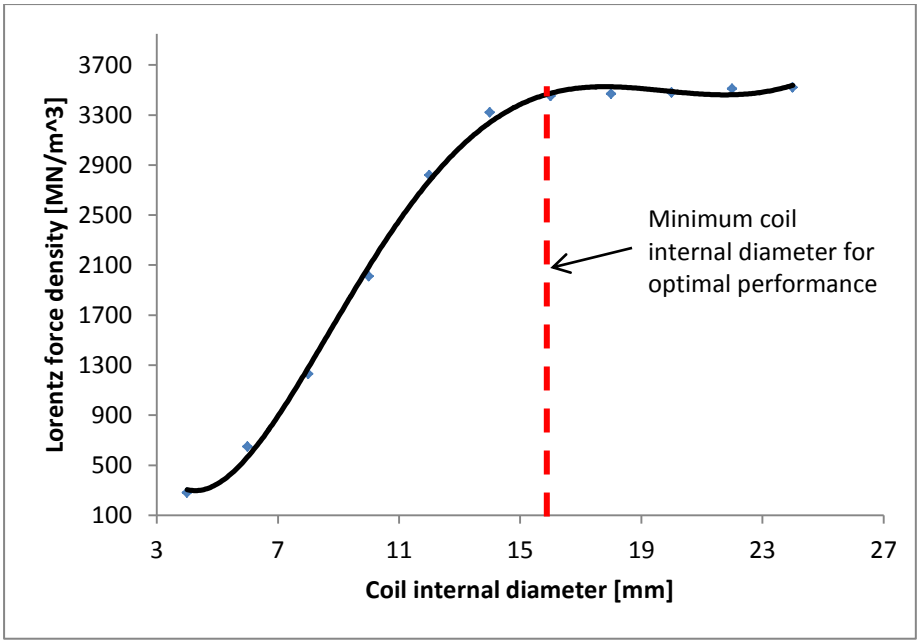

Fig.4.20: Plot of the influence of coil internal diameter on the Lorentz force density generated by the novel KT EMAT configuration.

4.4.5 The influence of the static flux (B_0) on the Lorentz force density

As shown in equations (3.8), (3.18) and (3.31); the static flux is an important factor that influence the density of Lorentz force, hence the need to investigate its effect on the Lorentz force generated on the material specimen.

Fig.(4.21) shows the result of the simulation obtained by varying the static magnetic field from 0.5T to 2.0T. As expected, the result shows that by increasing the static magnetic flux, the Lorentz force generated in the material specimen also increases and vice versa. At 0.5T, the peak to peak value of the Lorentz force is 1.2×10^9 N/m^3 while the value of 2.0T produced the highest LF of 2.7×10^9 N/m^3. The result is in good agreement with published work of [80, 84].

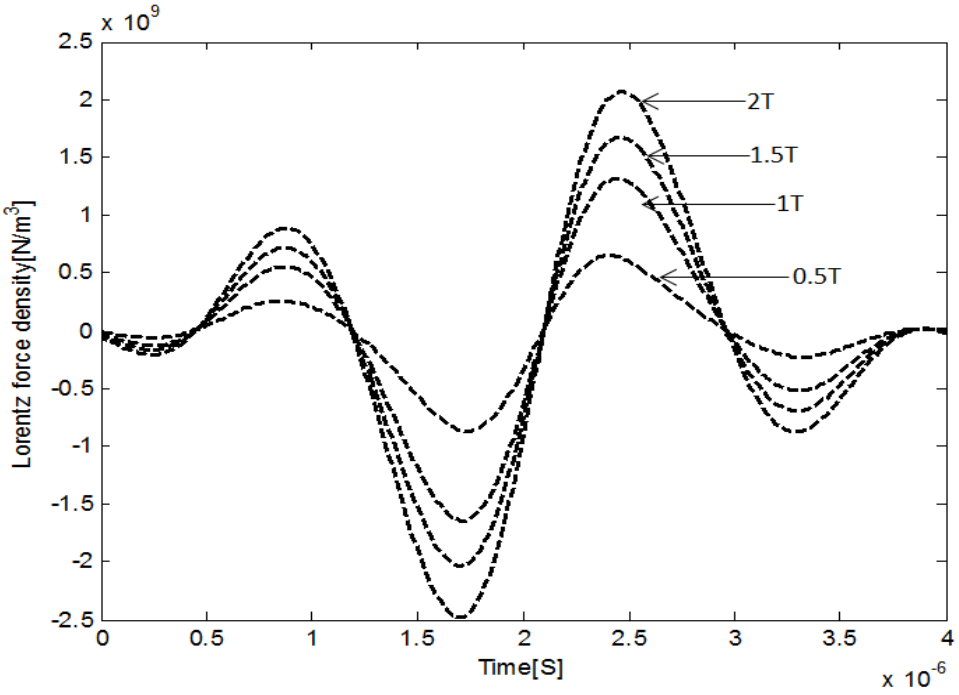

Fig.4.21: Time history of the influence of static magnetic field on the Lorentz force generated on the material by the novel EMAT configuration.

4.4.6 The influence of insulation layer thickness (T_{in}) on the Lorentz force density

As mentioned in section (4.2), one of the major advantages of the key type coil is that it allows coils to be stacked on one another. To prevent short circuiting and increase adhesion, the coils are bathed in an insulation material. The insulation material used in this simulation is Z1258 anti-rust silicone baffle paint. The performance index of Z1258 insulation material is listed in Table 4.4 and has the following properties [168];

(i) Good heat resistance

(ii) Firm adhesion

(iii) Short drying period

(iv) High dielectric strength of $30x10^6$ Vm^{-1}.

Fig.4.22 shows the result of the simulation. The result implies that, the Lorentz force density decreases exponentially with increasing insulation thickness. The highest value of Lorentz force density of $5.2x10^9$ Nm^{-3} was obtained at insulation thickness of 0.1 mm while the least value of $1.3x10^9$ Nm^{-3} was obtained at a thickness of 3 mm.

Therefore, for optimal performance of the KT coil, the insulation thickness must not exceed 1mm.

Table 4.4: Performance index of Z1258 anti rust silicone baffle paint [168]

No	Index name	Unit	Index
1	Appearance		The film becomes bright after drying
2	Viscosity	cP	≥40
3	Content of solid (10g paint, (23 ± 2^{0}C/h)	%	55±5
4	Drying time under room temperature	H	≤24
5	Dielectric strength	MVm^{-1}	≥30
6	Volume resistivity	Ω-m	≥ $1x10^{8}$
7	Fineness(scrapper fineness meter	μm	≤45
8	Adhesion coil	grade	1~2

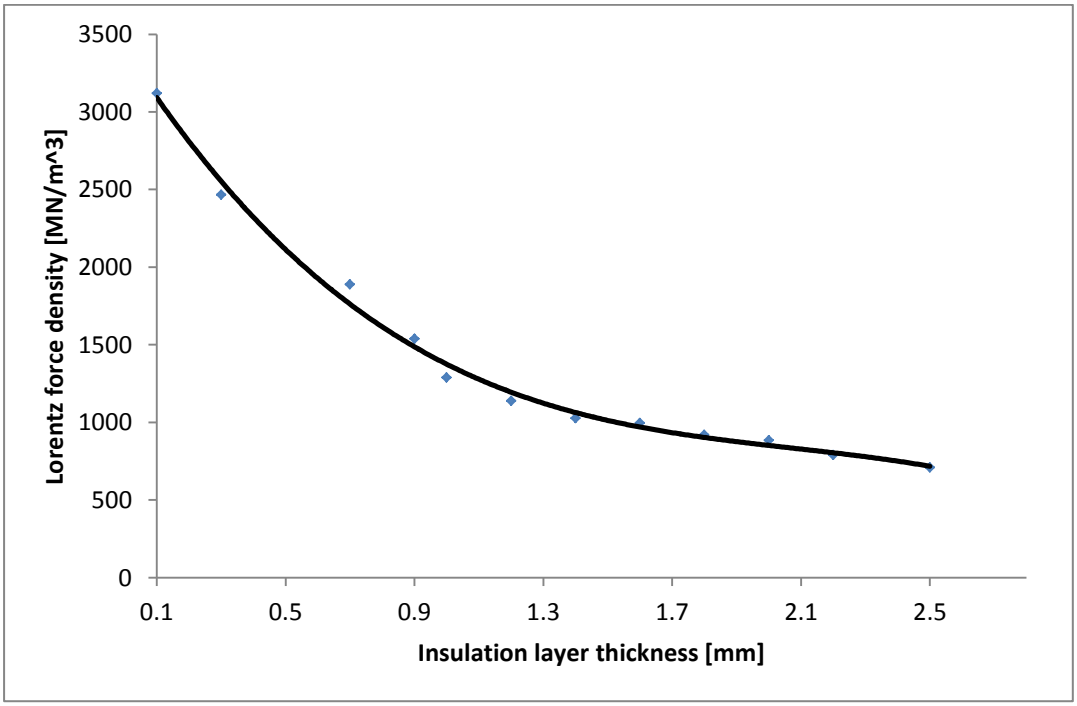

Fig.4.22: Plot of the influence of insulation layer thickness on the Lorentz force density generated by the novel KT EMAT configuration.

4.4.7 The influence of the period of the excitation current on the Lorentz force density

The period number of a tone burst signal determines the quantity of energy transferred from the power source to the coil [167]. This has a direct effect on the Lorentz force density and mechanical energy generated by the EMAT. Consequently, more period number gives rise to more excitation energy and excitation time. In the previous results, the coils were excited with a two period tone burst signal (see Fig.4.5). To understand the impact of period number on the Lorentz force generated by the KT-EMAT configuration under an excitation current amplitude and frequency of 20A and 500 KHz respectively, the period number of the tone burst signal was varied in the following sequence (2, 3, 4, 5 and 6) with all other EMAT parameters remaining unchanged. The result shows that an increase in the period, leads to an increase in the width of the Lorentz force wave packet (see Fig.4.23). Analysing the result further, a quadratic relationship was established between the Lorentz force density and the number of periods of the excitation signal as shown in Fig.(4.24).

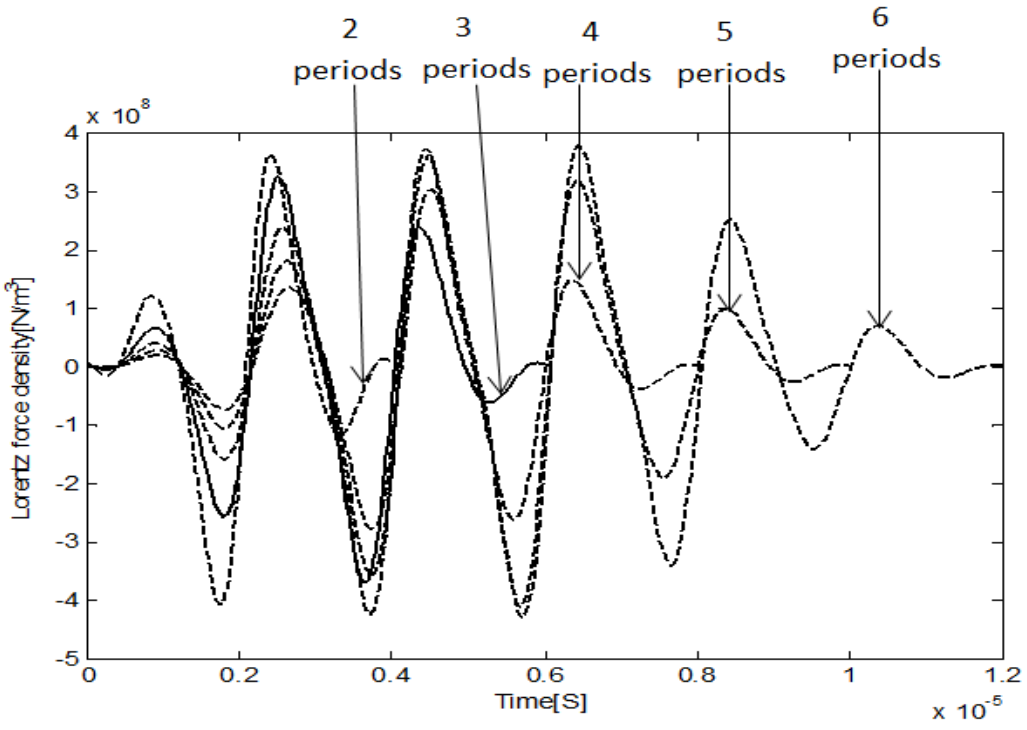

Fig. 4.23: Time history of the influence period number on the Lorentz force density generated by the novel KT EMAT configuration.

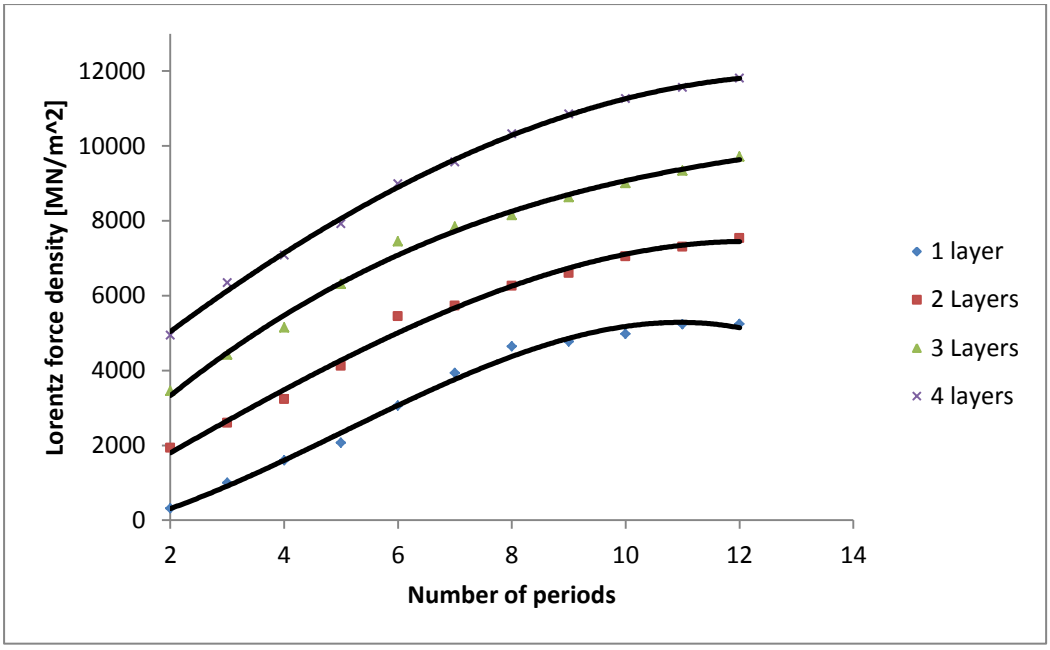

Fig.4.24: Plot of the influence of period number for 1 to 4 layers KT EMAT coil on the Lorentz force density generated on the test material.

4.4.8: The influence of excitation current frequency on the Lorentz force density

To investigate the influence of excitation frequency on the density of the Lorentz force generated by the proposed KT-EMAT configuration, the static field and the excitation current amplitude were maintained at 1.2T and 20A respectively.

The excitation frequency was varied from 500 KHz to 8MHz, and the corresponding change in Lorentz force generated in the material specimen was calculated. Fig.(4.25) shows that the Lorentz force density increases as the excitation frequency is varied from 0.5MHz and peaked at about 6.5MHz, thereafter it decreases sharply. This implies that any increase in frequency beyond 6.5MHz has a negative effect on the density of the Lorentz force generated in the material specimen. Hence for optimal performance of this EMAT configuration, the right excitation frequency required is between 0.5 and 6.5MHz. This result is in good agreement with work published by [167].

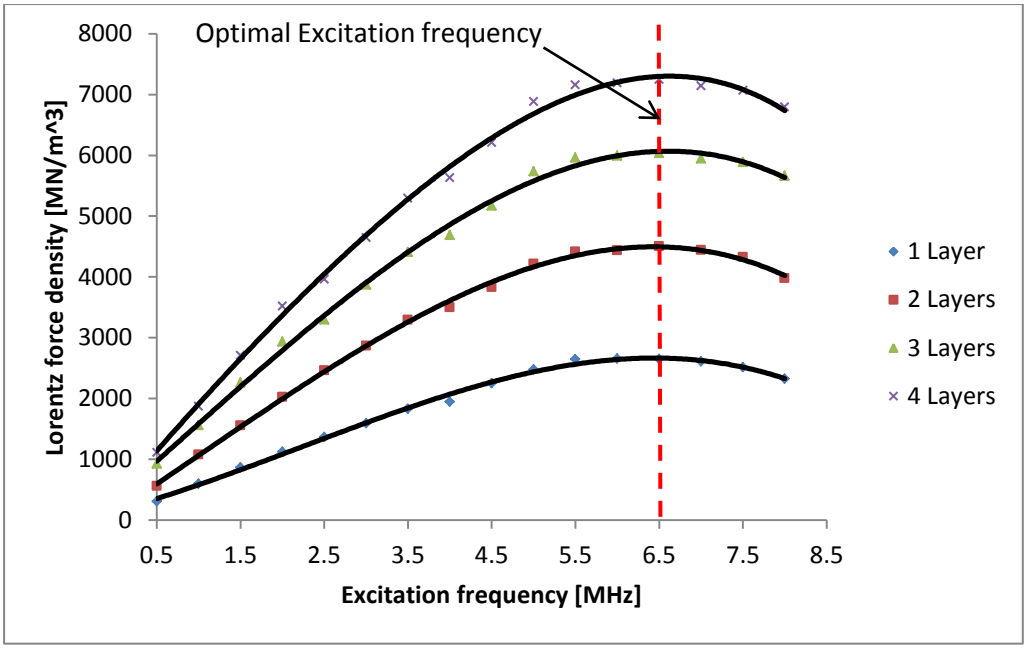

Fig.4.25: *Plot of the influence of the excitation frequency for 1 to 4 layers KT EMAT coil on the Lorentz force density generated on the test material.*

4.5 Summary

A finite element model in the time domain has been successfully developed and used to study and compare two commercially available EMAT coil structures (the spiral and meander-line EMAT coil configurations) and a novel KT EMAT coil configuration. The study was carried out in three stages: the first stage involves calculating the induced current and Lorentz force density respectively generated by the three EMAT configurations on CS70 grade of pipe steel plate of 6mm thick. The result is then compared to ascertain the configuration that generates the greatest induced current and Lorentz force density respectively on the pipe steel plate. As expected the result showed that the KT coil when stacked in layers generated greater Eddy current and Lorentz force density, followed by the spiral coil EMAT while the meander-line coil generated the least.

The second stage of the study investigated the robustness and efficiency of the novel KT EMAT configuration. The parameters investigated includes: Lift-off distance, coil stacking in layers, coil internal diameter, static flux density, insulation layer thickness, excitation current period, excitation current frequency and coil dimension. The result of the investigation gave a benchmark for optimizing the Lorentz force

density and consequently the strength of acoustic wave generated by the KT EMAT configuration.

Finally, this chapter has demonstrated that the KT EMAT configuration has a great potential for use in long range ultrasonic testing due to the high Lorentz force density it can generate especially when the coils are stacked in layers.

CHAPTER 5

DEVELOPMENT AND VALIDATION OF COUPLED FINITE ELEMENT MODEL FOR THE NOVEL KEY-TYPE (KT) EMAT CONFIGURATION.

5.1 Introduction

This chapter will develop a comprehensive finite element model to study the generation, propagation and detection of acoustic wave by the novel EMAT configuration. The couple mechanical model will be developed by coupling the magnetostatic model to the electrodynamic model in time domain to generate body forces which gives rise to acoustic wave generation (see Fig.1.11). The model will also detect acoustic waves by exploiting the 'Valerie' effect. Furthermore, the validity of the developed coupled mechanical model will be investigated by comparing its predictions with analytical and experimental results.

5.2 Modelling of novel KT- EMAT configuration as an acoustic wave transmitter and detector

A 2D cross- sectional representation of EMAT transmitter and receiver model is shown in Fig. (5.1), the model consists of a complete EMAT system acting as the acoustic wave generator/transmitter and same EMAT system acting as the acoustic wave detector. Both transmitter and receiver EMATs are placed in close proximity (lift off of 0.5mm) to a CS70 grade of pipe steel plate of thickness 3mm. The transmitting EMAT generates acoustic waves as described in section (3.4). The generated wave propagates along the material and can be detected by the receiver EMAT.

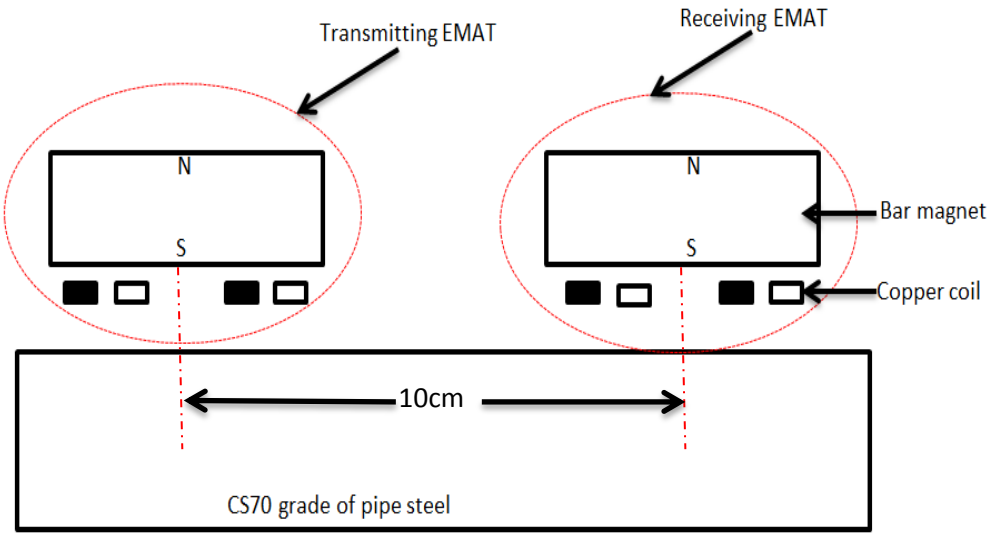

Fig. 5.1: Cross sectional representation of the transmitter and receiver EMAT system employed in the model.

Before proceeding to the analysis of wave generation, propagation and detection in the transmitter and receiver EMAT, a convergence test of the computational model was carried out to minimise errors due to size of the mesh. The next stage of the analysis is the calculation of transient magnetic fields around the coils, followed by the calculation of shear stress and transient particle displacement in the pipe steel material. This gives rise to the calculation of the acoustic wave generated and propagated within the pipe steel material and the induced voltage around the open circuited receiver coil.

5.2.1 Model setup

The EMAT transmitter and receiver model consist of KT coils with four turns each, immersed in a magnetic field of 1.2T generated by an NbFeB bar magnet. The setup on the left hand side is the transmitting EMAT while the setup on the right hand side is the receiver EMAT. The parameters used to create this model are as follows:

(a) Coil width (C_w) = 1.5mm

(b) Coil thickness (t_c) = 5µm

(c) Distance between coil or coil spacing (C_s) = 1mm

(d) Internal diameter (d_{in}) = 8mm.

(e) Distance between coil and material or lift off (h) = 1mm

(f) Centre to centre distance between the transmitter EMAT and the receiver EMAT is 10cm

The coils are excited with a 20A, 8 cycle tone burst current oscillating at 1.8MHz. The frequency of the excitation current was chosen arbitrary since UT use of frequencies between 500 kHz and 50 MHz with majority of industrial UT testing performed between a frequency of 1MHz and 10MHz. The physical quantities displayed in the material as depicted in the surface plots are: the dynamic magnetic field and the magnetic vector potential (MVP) shown in Fig.(5.2), the shear stress and the transient particle displacement as shown in Fig.(5.3) and the electric field around the transmitting and receiving EMAT as shown in Fig. (5.4).The surface plot shows a high concentration of the quantities around the transmitting section and a low concentration around the receiving section of the model. This is expected as the amplitude of the shear stress and particle displacement attenuates as the wave propagates along the material.

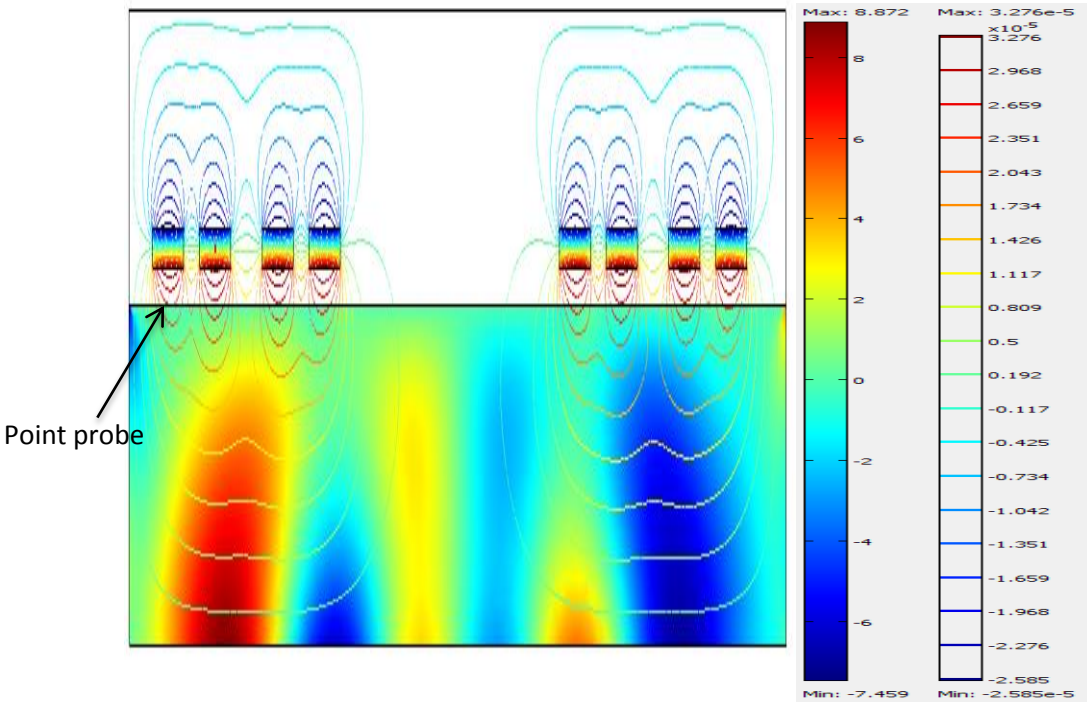

Fig. 5.2: Contour and surface plot showing the dynamic magnetic fields and the magnetic vector potential respectively of the transmitting and receiving coils with the bar magnet hidden. The position of the point probe is indicated with a dark arrow.

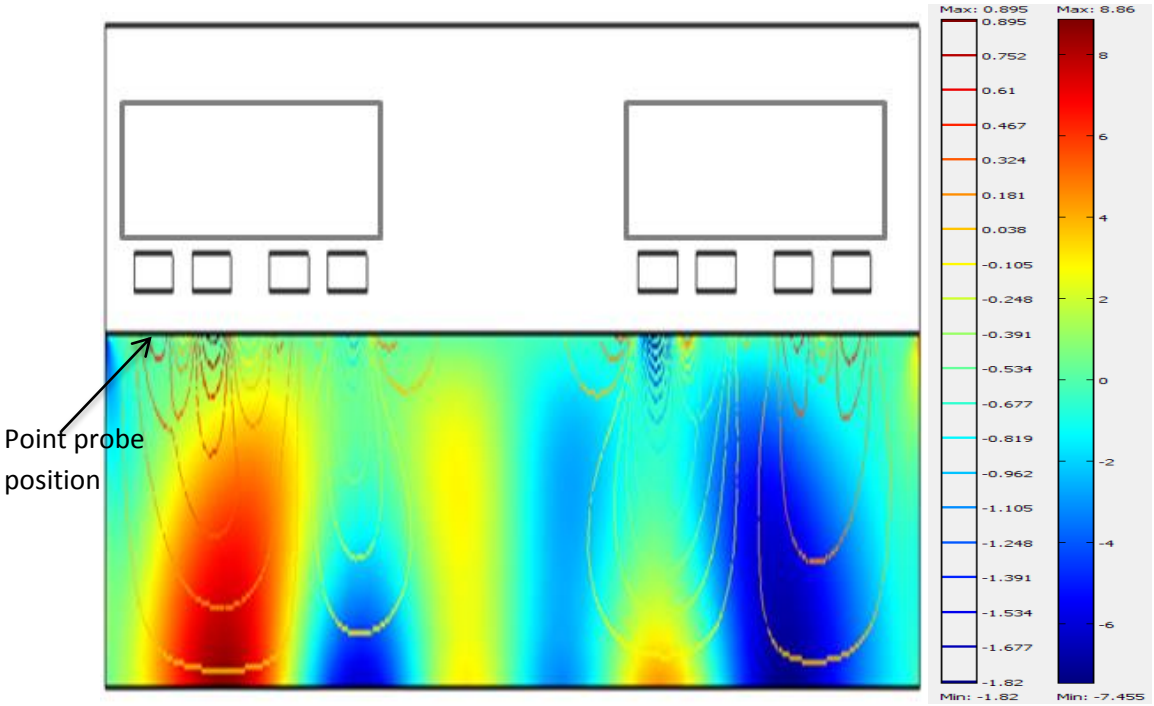

Fig. 5.3: Surface and contour plot showing particle displacement and shear stress at the surface of the transmitting and receiving EMAT. The point position is indicated with a dark arrow.

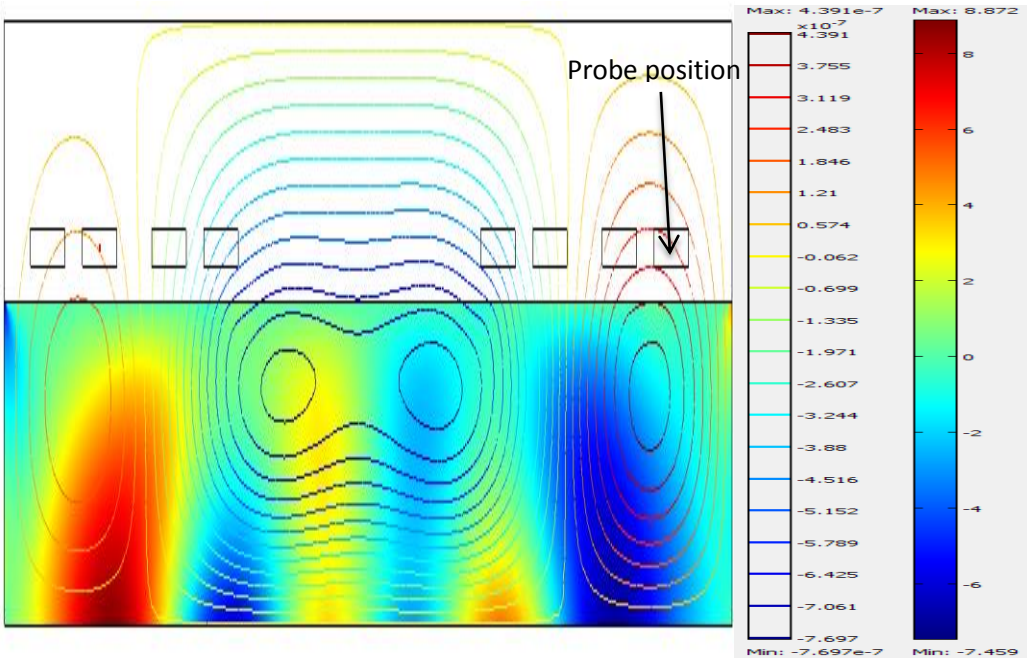

Fig. 5.4: Contour plot of the electric field around the EMAT transmitter and receiver showing the point probe position with the bar magnet hidden. The position of the point probe is indicated with a dark arrow.

5.2.2 Convergence test

Fig.5.5 shows the finite element mesh of the EMAT model used to study the generation, propagation and detection of acoustic wave. The mesh consists of 9534 second order quadratic triangular elements and refined around the skin depth of the material below the transmitting and receiving EMAT coil. The refinement is necessary to enhance accuracy since the result will be extracted from this region. The mesh density of the model will be varied to obtain the best result without necessarily increasing the computation time.

The convergence of the numerical model is investigated by varying the triangular element size to determine the convergence of the Von Mises stress; this will also ensure the convergence of all other physical quantities. The mesh is then refined from 1000 to 18000 elements at interval of 3000 and for a time step of 0.01μs. To obtain the result, a point probe was placed almost at the surface of the material (skin depth) underneath the transmitting EMAT. The result in Fig. (5.6) shows how the Von Mises stress reaches its convergence from 10000 elements, which indicates that all simulations can be run with this amount of triangular elements without affecting the accuracy of the simulation result. The result further indicates that increasing the number of elements beyond 10000 elements does not have commensurate increase in the amplitude of Von Mises stress generated as the computation time and computer memory is increased.

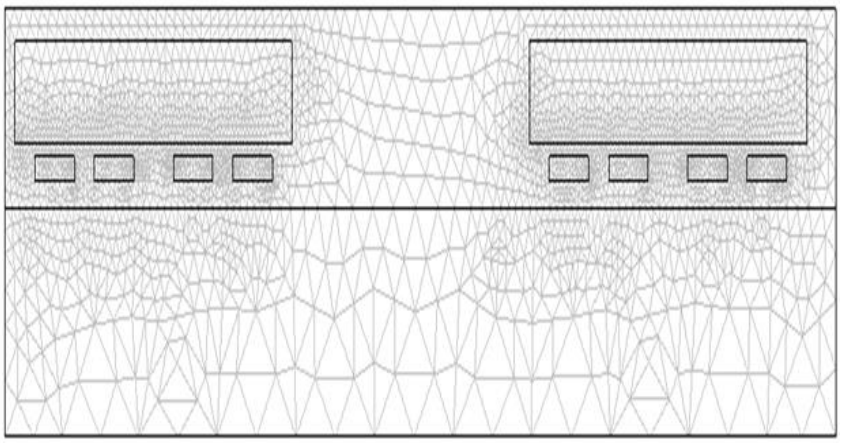

Fig. 5.5: Finite element mesh of the transmitter and receiver EMAT. The mesh consists of 9534 second order quadratic triangular elements.

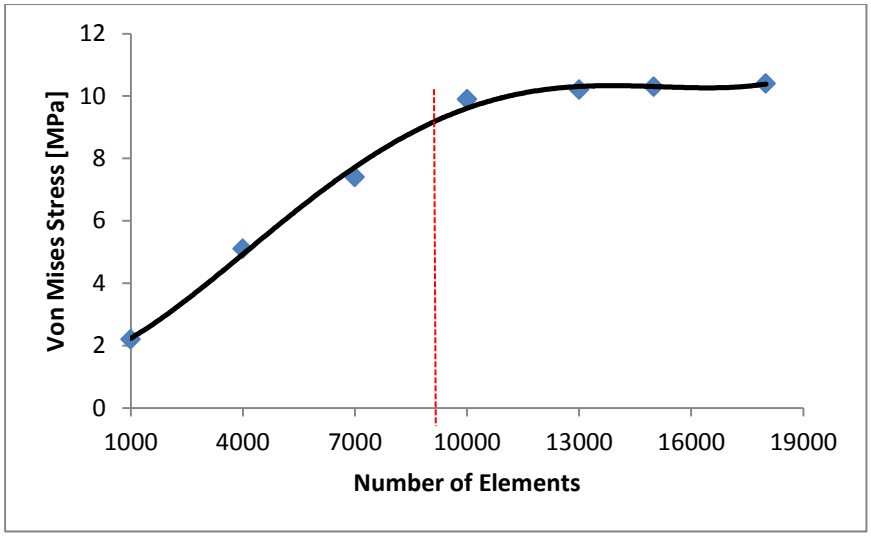

Fig.5.6: Variation of finite element triangular mesh from coarse mesh (1000 elements) to Extra fine meshes (18000 elements). The red line indicates the number of elements adopted in Fig.5.5.

5.2.3 Calculation of external current density

In the transmitting EMAT, the external current density in the coils can be calculated by applying the excitation source current of 8 cycle tone burst signal with a centre frequency of 1.8MHz and excitation current amplitude of 20A. The transient excitation current in the coil is given as:

$$J_{exc} = I_0(sin\omega t)\left[0.5\left(1 + cos(\omega t)\right)\right] \text{ for } 0 \leq t \leq 4.5\ \mu s \qquad (5.1)$$

Where I_0 is the excitation current amplitude, ω = 2πf is the angular centre frequency. The coil is immersed in a constant magnetic field of 1.2T generated by a permanent magnet. To obtain the external current density, the point probe is place at the centre of the first coil turn in the transmitting EMAT. The result in Figure 5.7 with a peak to peak value of 2.4×10^{8} (Am^{-2}) is the external current density obtained after the excitation current has been applied. The result shows a similarity with the 8 cycle tone burst source current in equation (5.1).

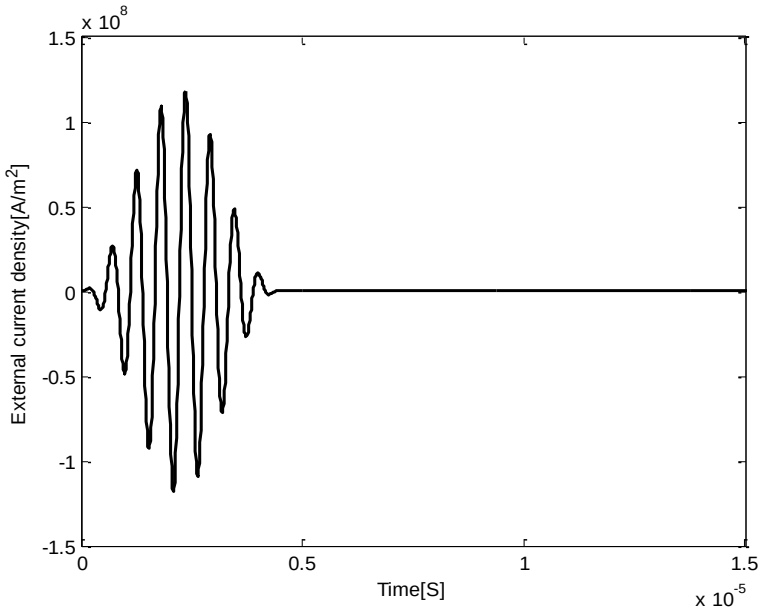

Fig. 5.7: Time history of the external current density at the transmitting coil.

5.2.4 Calculation of induced current density

Figure 5.8 shows the time history plot of the z component of the induced current density on the material with a peak to peak value of 1.2×10^{8} (Am^{-2}). The plot is obtained by placing the point probe within the skin depth of the material underneath the first turn of the transmitting coil as shown in Fig. (5.2). There is a great similarity between the shape of the induced current density and external current. This is expected as the induced current density is as a result of the external current density. However, some differences were observed; the orientation of the induced current plot is opposite to that of the external current density, this is expected since the induced current density is a mirror image of the excitation current [33, 88]. Also, the peak to peak amplitude of the induced current density is less than that of the excitation current. The difference stems from the transduction energy loss during the electromagnetic conversion which is a function of the lift-off and other coil parameters such as coil impedance.

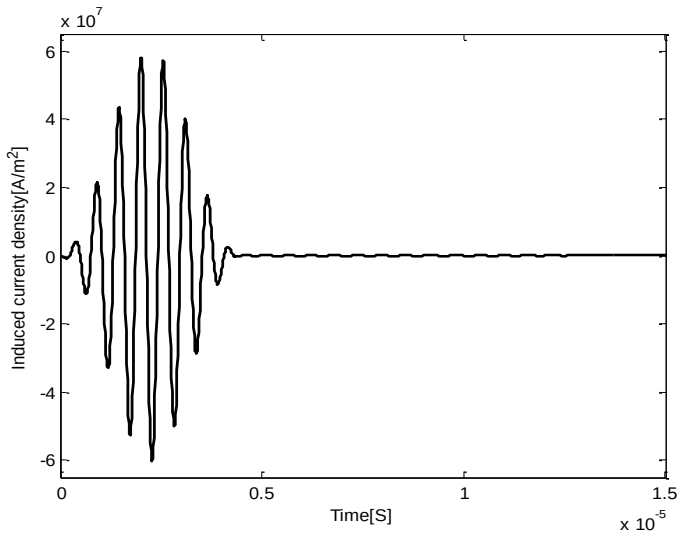

Fig.5.8: Time history of the induced current density in the material under the transmitting EMAT coil.

5.2.5: Calculation of Particle Displacement

The particle displacement at the surface of the material under the transmitter and the receiver EMAT is calculated based on the constitutive equation described in section (3.4). The coupled electromagnetic and mechanical model was run and the result extracted by placing the point probe at the skin depth surface of the pipe steel plate material (about 0.05mm) underneath the first turn of the transmitting and receiving EMAT as shown in Fig.(5.3). The result in Figs.(5.9) and(5.10) shows that there is a reduction of the peak to peak amplitude of the particle displacement from 9.4nm at the transmitting EMAT to 3.3nm at the receiving EMAT. The reduction in displacement amplitude is as a result of damping and scattering of the wave signal in the material.

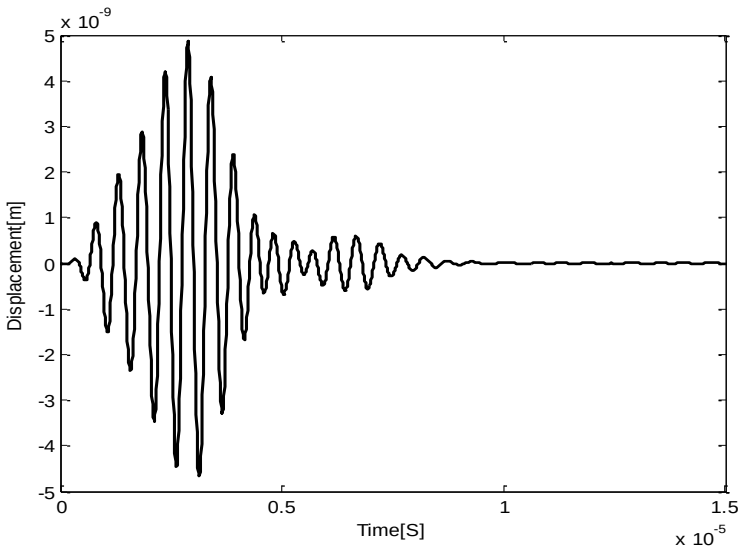

Fig.5.9: Time history of the displacement at the surface of transmitting EMAT.

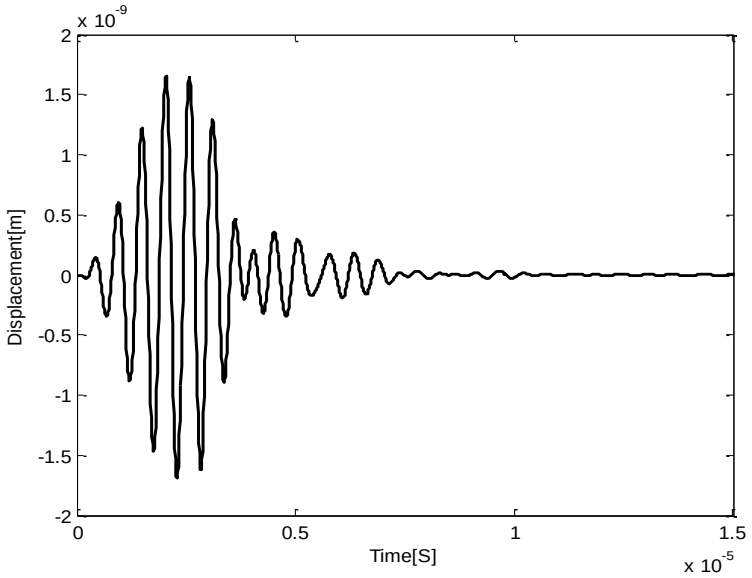

Fig.5.10: Time history of the displacement at the surface of material under receiver EMAT coil.

5.2.6 Calculation of shear stress

To calculate the amount of shear stress generated when particles are displaced in the material, a post processing tool inbuilt in the structural mechanics module of Comsol multiphysics allows the particle velocity due to the body forces to be converted to shear stress. The plot in Figures (5.11) and (5.12) shows the time

history of the vertical shear stress at the surface of the material due the transmitter and receiver EMAT respectively.

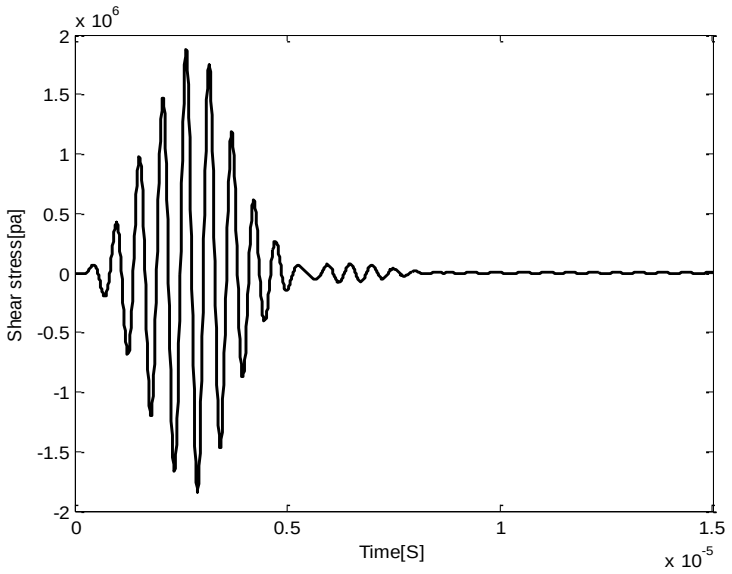

Fig.5.11: Time history of the shear stress at surface of material under the transmitter EMAT.

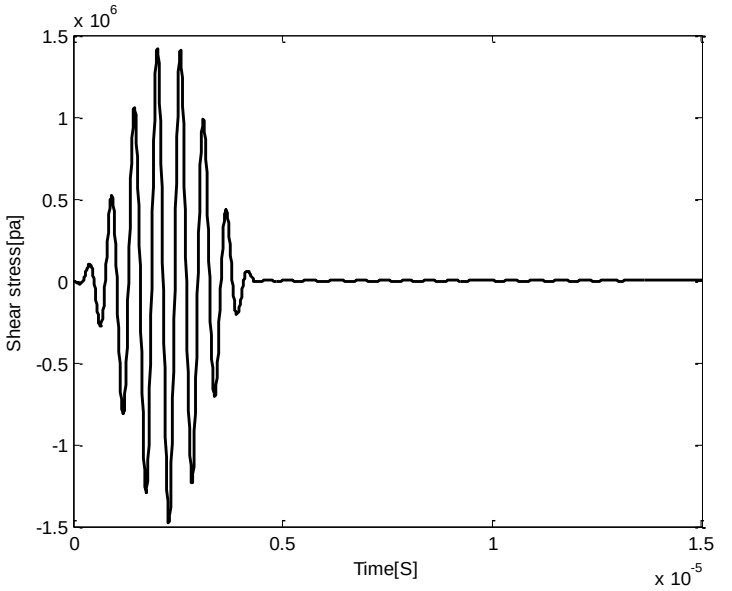

Fig.5.12: Time history of shear stress at surface of material under the receiver EMAT.

5.2.7 Calculation of magnetic vector potential (MVP)

Following the calculation of the particle displacement and shear stress in the material beneath the receiver EMAT, the next physical quantity to be calculated is the magnetic vector potential around the receiver coil. By placing the point probe

under the coil of the receiver EMAT model and employing a special post processing tool in the AC/DC module of Comsol multiphysics, the magnetic potential in Wb/m can be calculated. Fig.(5.13) shows the time history of the magnetic potential around the coil of the receiver EMAT. The result shows that the shape of the wave form is similar to that of the excitation current, the particle displacement and shear stress. This proves that the MVP is as a result of the particle displacement and shear stress in the material.

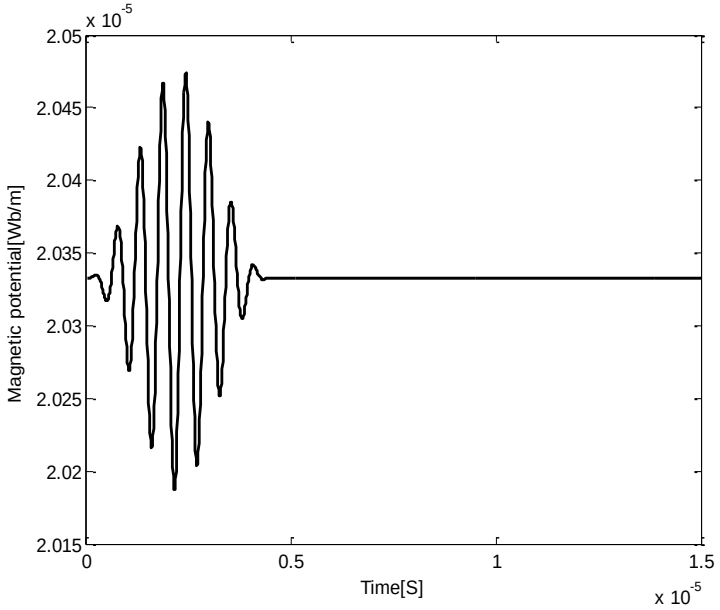

Fig.5.13: Time history of the magnetic potential at surface of material underneath the receiver EMAT coil.

5.2.8 Calculation of open circuit voltage at the receiver end of EMAT

The acoustic wave generated by the interaction of the static magnetic field $B_0(y,z)$ and the induced eddy current J_{ez} arrives at the receiver. If ϑ(y,z,t) is the particle velocity and σ is the conductivity of the material, a free conducting current density distribution J is formed at the surface of the specimen under the receiving EMAT. This is due to the interaction of acoustic vibration in the material and the static magnetic field generated by the permanent magnet as illustrated in equation (5.2) [33, 169].

$$J = \sigma \vartheta \times B_0 \qquad (5.2)$$

This phenomenon gives rise to a time varying MVP A(y,z,t) in and around the material specimen as calculated in section (5.2.7), which can be detected as an open circuit voltage in the receiver EMAT coil as shown in Fig.(5.14).

The first step in calculating the open circuit receiver voltage is to calculate the transient particle displacement (previously explained in section 5.2.5) in the material, then the result is used as a source term to calculate the magnetic vector potential (A_z) around the receiver coil. This leads to the calculation of the induced emf in the coil based on the evaluation of Faraday's law, which relates the induced emf to the flux density(B_0).

According to [169], the induced voltage at the receiver coil can be defined as:

$$V_R(t) = \frac{\iint V_p(y,z,t) d_y d_z}{\iint d_y d_z} \tag{5.3}$$

Where, $V_p(y,z,t)$ is the induced voltage due to a point is receiver coil and is defined as:

$$V_p(y,z,t) = -\frac{\partial}{\partial t} \iint B.dS = -\frac{\partial}{\partial t} \iint (\nabla \times A).dS = -\int_c \frac{\partial A}{\partial t}.dL. \tag{5.4}$$

The block diagram in Fig.(5.15) summarises the numerical processes involved in the analysis of the generation, propagation and detection of acoustic wave using the novel EMAT configuration.

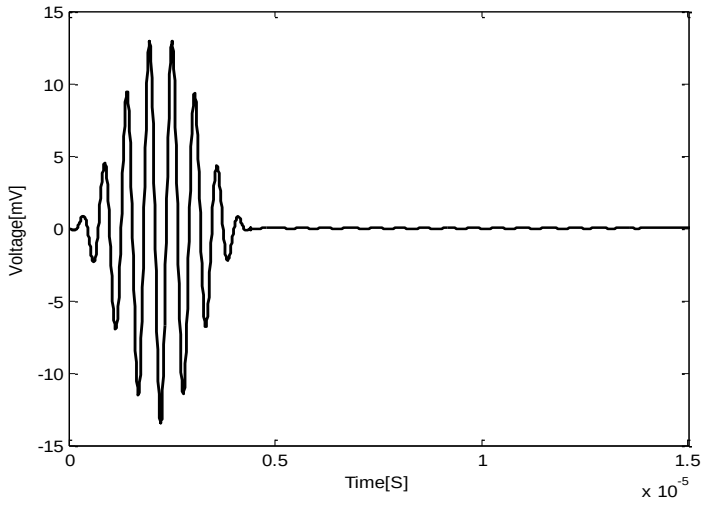

Fig.5.14: Time history of the open circuit voltage at receiver coil.

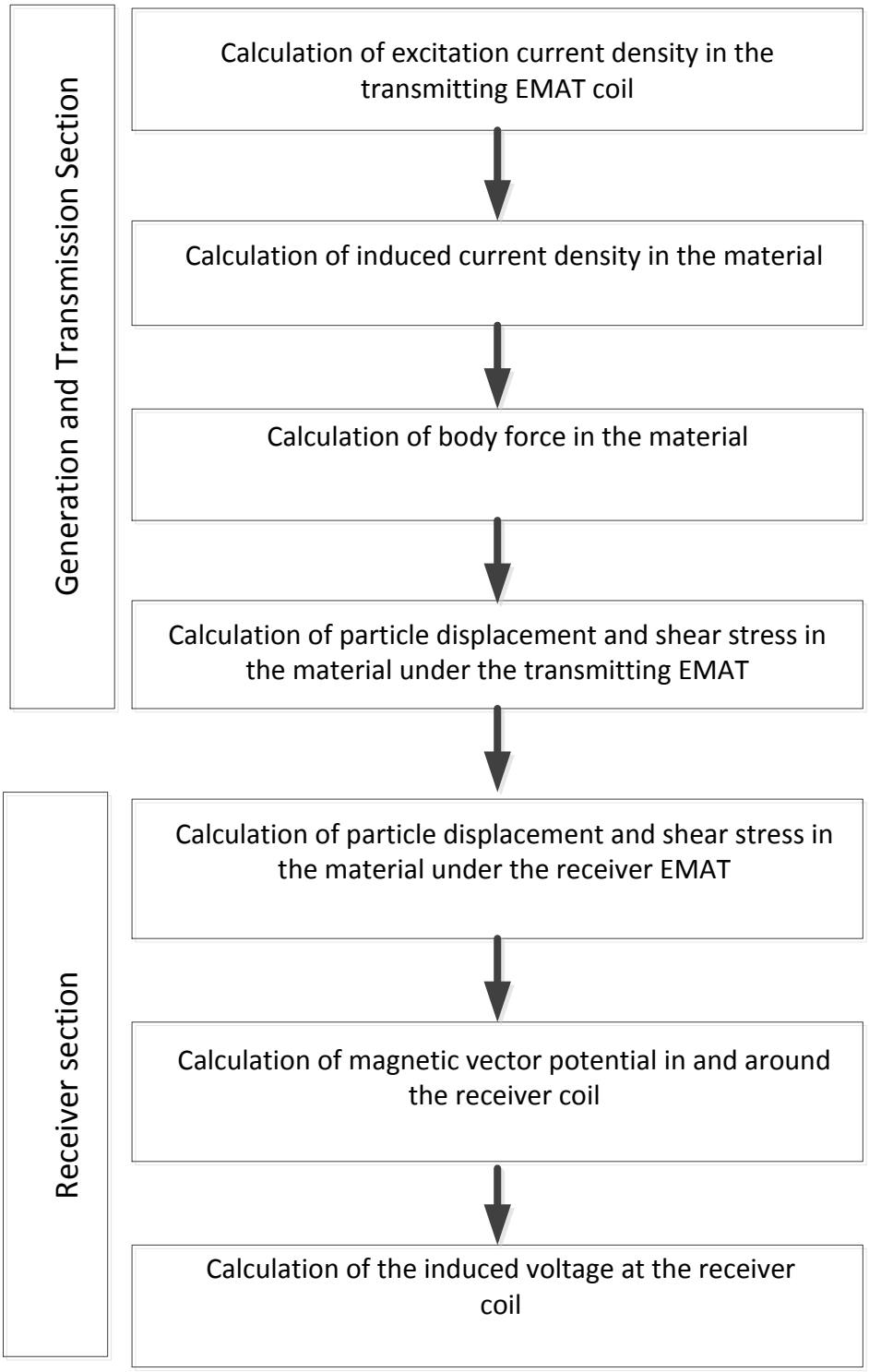

Fig5.15: Illustration of the processes carried out in the analysis of the generation, propagation and detection of acoustic wave using the novel EMAT configuration

5.2.9 The influence of number of coil layers and lift- off distance on the received voltage.

A major goal of the design of any EMAT configuration is to boost the generated and detected amplitude of the ultrasonic signal without a corresponding increase in the system noise. The signal to noise ratio (SNR) can be optimised by effectively increasing the received signal amplitude of the EMAT system. One of the key parameters that affect the received signal amplitude is the lift-off distance (h) between the coil and the test material. It is well established that the combined amplitude of the received signal increases with each additional coil layers as shown in Fig.(5.16), but the received signal of individual coil layers (V_{rec}) decreases due to the increase lift-off (h) and the relationship is expressed as [170]:

$$V_{rec} = V_0 e^{\left(-2\pi h / d_c\right)} \tag{5.5}$$

Where d_c is the coil spacing and V_0 is the amplitude of the received voltage when $h = 0$.

Fig.4.43 shows the relationship between the lift off distance (h) and the normalised received voltage for various layers of coil. The received voltage decreases exponentially to zero as the lift-off increases.

It has been theoretically established in [170] that an additional coil layer will increase the amplitude of the received signal. However, in practice this is not the case; additional layers will increase lift-off distance, hence reducing the amplitude of the received voltage. To overcome this problem, the KT coil configuration is stacked with a thin layer of Z1258 insulation of about 0.01mm (see section 4.4.5 for more details) and connected in series. This yields a multi-layered KT coil EMAT configuration that minimises the effect of lift-off distance and maximises the received signal amplitude. The result in Fig.5.16 shows that the received signal amplitude increases with increase in the number of coil layers. This trend is observed to continue to about the 11^{th} coil layer, beyond this point it is observed that there is no significant increase in the amplitude of the received voltage as the coil layer is increase. Hence, for better efficiency when KT coil is used as an acoustic wave receiver, the number of layers of

coils should be limited to a maximum of 10 coil layers per stack. The result also shows that when the coils are stacked in layers, there is a significant improvement in the lift-off characteristic of the KT EMAT as the number of layers is increased (see Table. 5.1, extracted from Figs. (4.16) and (5.17).

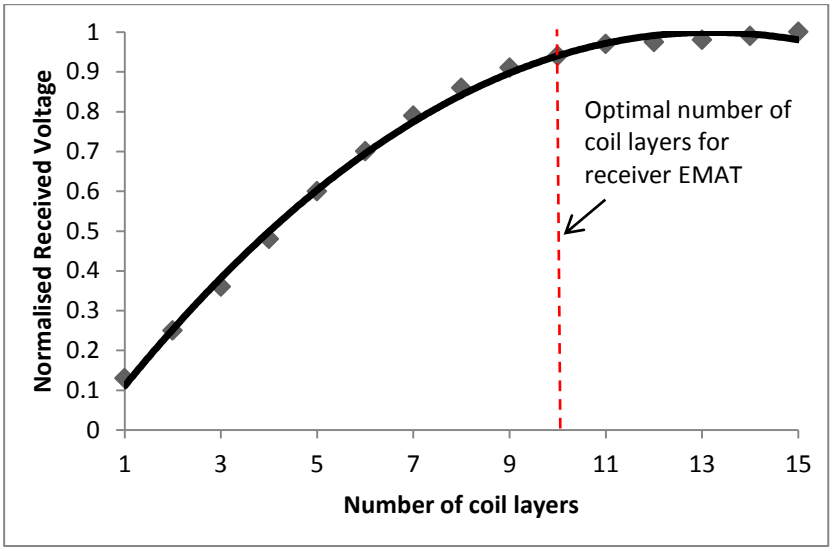

Fig.5.16: Plot of the relationship between received voltage at the pick-up coil and the number of layer of coil.

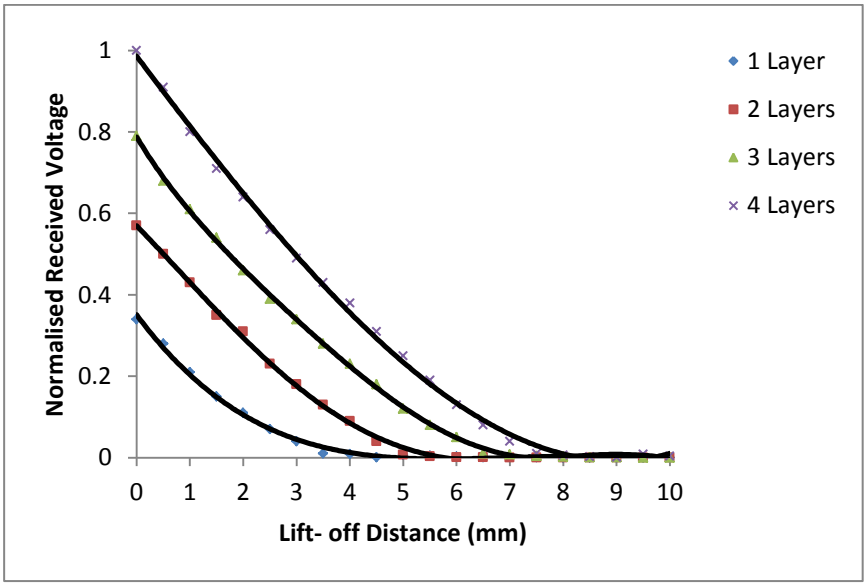

Fig.5.17: Plot of the relationship between received voltage for various layers of the pick-up coil and the lift off distance (h).

Table.5.1: Comparison of the lift-off characteristics of the stacked KT coil as an acoustic wave generator and receiver.

Number of coil layers	Significant lift-off distance for generator KT EMAT (mm)	Significant lift-off distance for Receiver KT EMAT (mm)
1 layer	0 - 3	0 – 4
2 layers	0 - 4.5	0 – 5.5
3 layers	0 – 5.5	0 – 6.5
4 layers	0 – 6.0	0 -7.5

5.3 Validation of coupled finite element model

5.3.1 Introduction

This section investigates the validity of the coupled finite element models developed in section 5.2, by comparing its predictions with analytical and experimental results. First, the single modules (electromagnetic and ultrasonic modules) were bench marked against known analytical solutions. The induced Eddy current when a time varying current is applied to an EMAT coil, the magnetic field due to a permanent magnet and the ultrasonic field generated as a result of the interaction of the eddy current with the bias magnetic field was modelled and the numerical results compared with the analytical results. This is followed by the validation of the fully coupled multiphysics numerical model against experimental results. The experimental validation involves numerically computing the particle velocity dependence on important EMAT parameters such as the bias field, the driving current amplitude and the excitation frequency. The validated model was carried out on CS70 grade of pipe steel plate and can be extended to design EMAT for any desired application.

5.3.2 Analytical validation

To ensure the reliability of the software (Comsol multiphysics) the single modules that accounts for the static magnetic field, the induced Eddy and the ultrasonic field respectively, was compared with known analytical solutions. In section (5.3.2.1 and 5.3.2.2), simple electromagnetic models to address the static field (created by the permanent magnet) and the induced Eddy current (produced by a time dependent current) were developed and validated against analytical solution. While in section (5.3.2.3) a simple mechanical model to address the ultrasonic field was developed and also validated against an analytical model (the piston source model proposed by Kawashima).

5.3.2.1 Static magnetic field

The magnetic flux density along the axis of a cylindrical rare earth (NbFeB) magnet, at distance *x* from its pole is given as [171]:

$$B_x = \frac{B_r}{2}\left(\frac{L+x}{\sqrt{(R^2+(L+x)^2)}} - \frac{x}{\sqrt{(R^2+x^2)}}\right) \quad (5.6)$$

where L and R are the length and radius respectively while B_r is the remnant flux of the magnet, which is the flux density when the magnetic field is null, that is (B_r= B_H= 0). This relationship is only available and implementable for simple geometries as seen in Fig.5.18. A finite element model using Comsol multyphysics has been developed to compare the numerical results against the results obtained using equation (5.6). The numerical model was implemented using the magnetic field no current mode available in the AC/DC module of Comsol multiphysics. This solves the magnetostics problem by neglecting the field at the exterior boundaries of the computational domain. The equation in (5.6) is only used to verify the performance of the software as it does not hold when a ferromagnetic material is placed very close to the magnet. A 2D axisymmetric geometry shown in Fig.(5.18) is employed in the model and is expressed in {r,z,Ø} cylindrical co-ordinates. The constitutive equation employed within the domain of the magnetic for the analysis is:

$$B=\mu_0\mu_r H+B_r \quad (5.7)$$

Which combines the relationship between the magnetic flux density and magnetic field together with the equation ($\nabla.B=0$), to obtain an equation for the scalar magnetic potential V_m given as;

$$-\nabla\cdot(\mu_0\nabla V_m-\mu_0 M_0)=0 \quad (5.8)$$

The model applies equation (5.8) by selecting magnetic field no current (mfnc) physics in Comsol and is solved using static analysis, since no time dependent phenomenon is involved.

In the model, the magnet is surrounded by air, and the model assumes the continuity relations at the boundaries.

For both the numerical and static analysis, a rare earth magnet (NbFeB) was used with magnetization of 750 kA/m along the along the x axis. The dimensions of the magnet are 20mm radius and 12 mm thick. A comparison of the result of the analytical formula in equation (5.6) and the Finite Element simulation is given in Fig. (5.19), and shows good agreement.

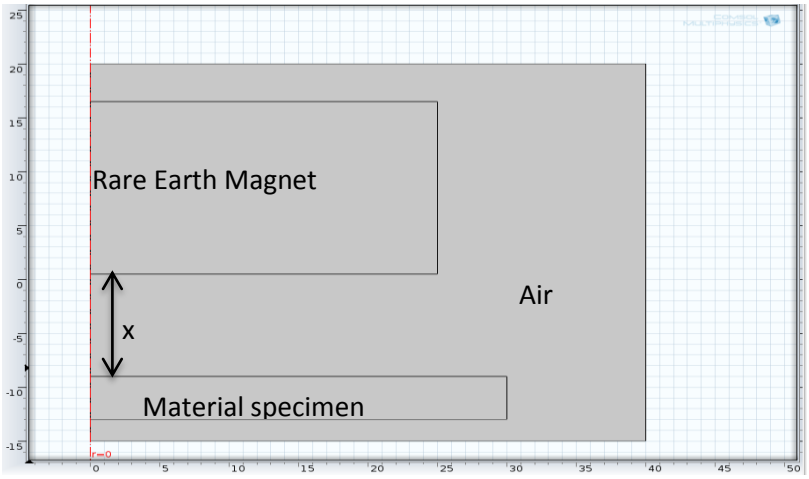

Fig.5.18: 2D axial symmetry representation of a cylindrical rare earth magnet in Comsol at a distance x from the pole surface (where X>0) on the magnet's centre line.

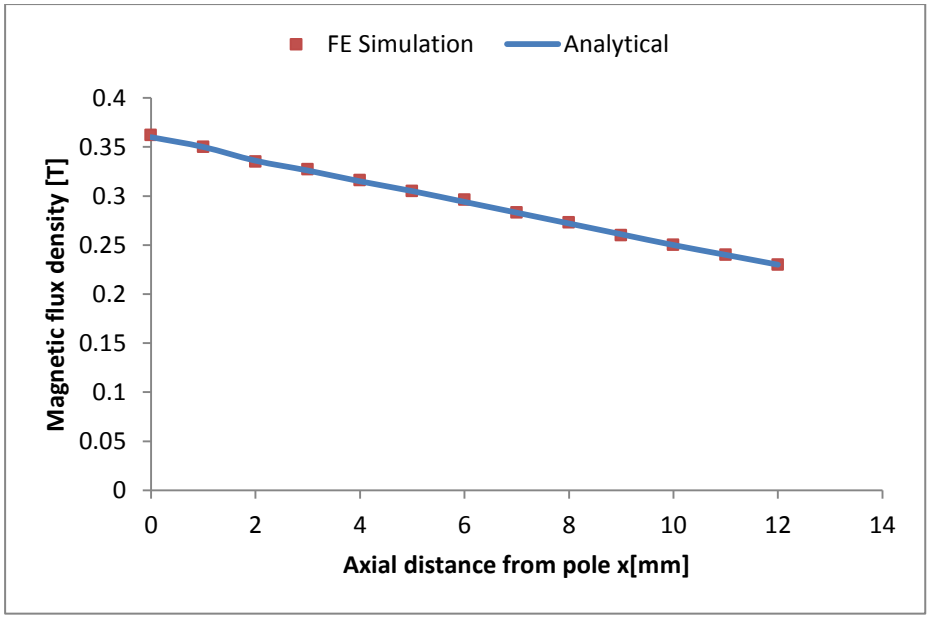

Fig.5.19: Comparison of the FE simulation and analytical result of the magnetic flux density produced by a cylindrical rare earth magnet.

5.3.2.2 Eddy current

The bench mark model for the generation of Eddy current employs the classical Dodd's and Deed's model [125] for a circular coil placed above a conductive medium. The coil is modelled as a thin current sheet parallel to the surface of the material and placed at a distance h, known as the lift off (see Fig. 5.20). The model assumes an asymmetrical geometry and is expressed in cylindrical co-ordinates {r,z,Ø}. The driving current is sinusoidal and has only a circumferential component $J_{ø}$, thus simplifying the problem to a single differential equation with the circumferential component of the magnetic vector potential $A_{ø}$(r,z) as the unknown.

The dependent variable in this application is the azimuthal component of magnetic vector potential A, which obeys the relation;

$$(j\omega\sigma - \omega^2\epsilon)A_{ø} + \nabla \times (\mu^{-1}\nabla \times A_{ø}) = j_{ø}^{e} \quad (5.9)$$

where ω, σ, μ and ϵ are the angular frequency, conductivity, permeability and permittivity respectively. $j_{ø}^{e}$ denotes external current density.

The induced eddy current on the infinite material was computed using the formula;

$$j_e = -j\omega\sigma A_{ø}, \quad (5.10)$$

Kawashima [128] , proposed an analytical solution to this problem by employing the classical Dodd's and Deed's formula for a geometrical parameter and material property of a coil with inner radius (r_1) of 3mm, outer radius (r_2) of 17mm, lift off (h) of 0.5mm and a driving current of 1A at a frequency of 1×10^6 Hz acting on an infinite half space with conductivity (σ_1) of 36.5×10^6 S/m and relative permeability (μ_1) of 1.

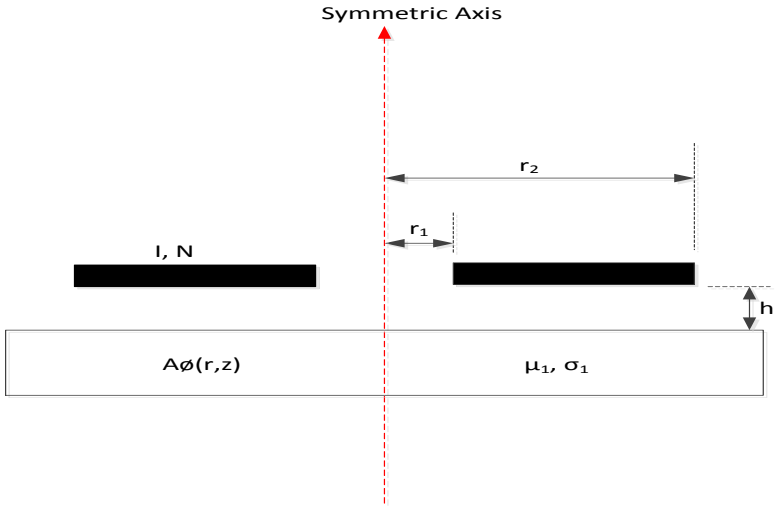

Fig.5.20: Analytical model of a flat pancake coil and a conducting half space used by to calculate electromagnetic vector potential, adapted from Kawashima [128].

The numerical model used to compare the theoretical model, was implemented using Comsol Multiphysics, the model employed the 2D axisymmetric magnetic field (mf) mode available in the AC/DC module with time harmonic analysis. The time harmonic analysis assumes that all variation in time occurs as sinusoidal signal. The numerical model solves the same differential equation solved analytically by Dodd's and Deed's using the same parameters as the analytical model, but with one main difference, the coil in the numerical model has a finite thickness. The numerical model assumes the conductivity of copper coil to be zero, to reproduce the homogeneous current sheet assumed in the theoretical model. The boundary condition employs the continuity of the tangential component of the magnetic field across different regions. The model was solved by means of an iterative algorithm and comprises of 14500 triangular elements. The result of the computation shows the radial distribution of modulus of the magnetic vector potential generated on the

metal surface (z=0). The discrepancy between the FE and the analytical result from Dodd's and Deed's is shown in Fig. (5.21) and is approximated to be 4.9%.

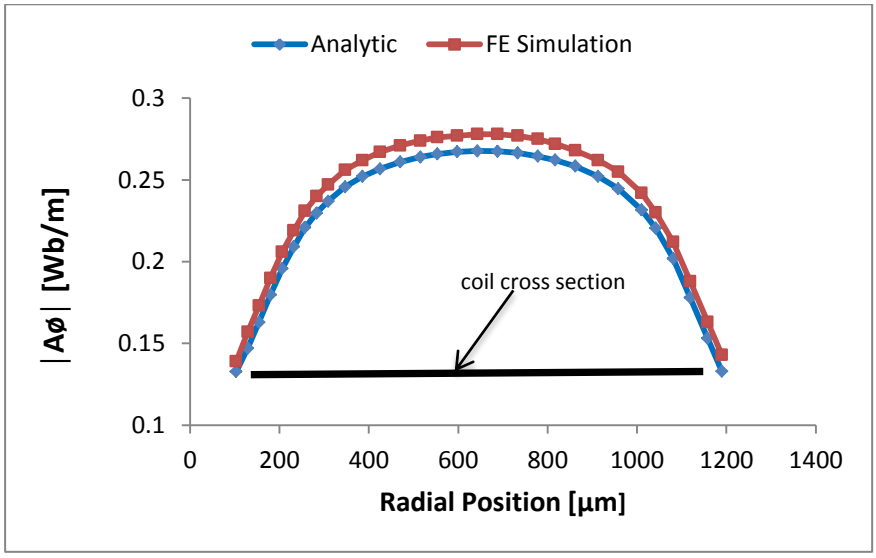

Fig. 5.21: Comparison of finite element simulation and analytical calculation [128] *of the radial distribution of the magnetic vector potential* $\{A_{\emptyset}(r,0)\}$ *on the surface of an aluminium sample.*

5.3.2.3 Ultrasonic field

The numerical calculations for elastic wave produced by time varying vertical surface forces acting on the vertical surface and the radial horizontal surface force is summarised in [87];

$$U_{zz} = \frac{a_1}{\mu}\int_0^{\infty}\frac{\alpha_1}{f_0(\alpha)}[(k^2-2\alpha^2)exp(-\alpha_1 z)+2\alpha^2 exp(-\alpha_k z)]\times J_0(\alpha r)J_1(\alpha a_1)d\alpha$$

(5.11)

$$U_{rz} = \frac{a_1}{\mu}\int_0^{\infty}\frac{\alpha}{f_0(\alpha)}[(k^2-2\alpha^2)exp(-\alpha_1 z)+2\alpha_1\alpha_k exp(-\alpha_k z)]J_1(\alpha a_1)da \qquad (5.12)$$

Where $f_{0(\alpha)} = (2\alpha^2-k^2)^2 - 4\alpha^2\alpha_1\alpha_k$, $\alpha_1 = \sqrt{(\alpha^2-1)}$, $\alpha_k = \sqrt{(\alpha^2-k^2)}$ and

$k^2 = \frac{k_s^2}{k_c^2}$. J_0 *and* J_1 are the Bessel function of the first and second kind respectively, α is the radius of disk

Equations (5.11) and (5.12) are the same ones derived by Miller and Pursey [126] to solve cylindrical problems. Its numerical counterpart was implemented in COMSOL multiphysics using the structural mechanics module with axial symmetry, stress strain application mode. This module solves the Navier Stokes equation for isotropic elastic medium in cylindrical coordinate form {r, z, Ø}. This assumes that the displacement in the circumferential direction is zero and the loads are only in r and z direction and is independent of Ø. The model was implemented as an elastic half space with uniform time dependent stress applied over a circular area on its surface, in the direction normal to it. This model can describe the sound field due to a cylindrical piezoelectric transducer applying a force in the normal direction to the sample.

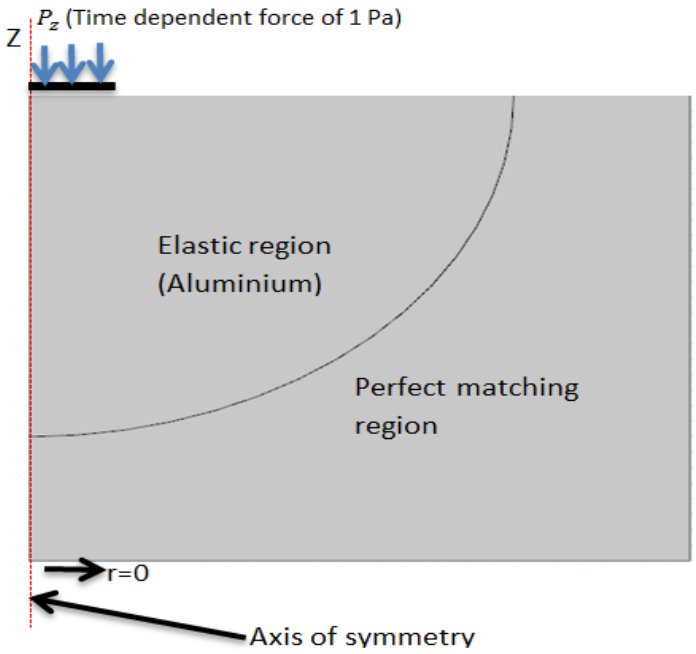

Fig.5.22: Geometry of the piston source model on a half space showing the elastic and perfect matching region in Comsol multiphysics.

In the calculation, a surface pressure with amplitude of 1 Pa is applied on a circular area of 10mm and a frequency of 1MHz as shown in Fig. (5.22). The material used is aluminium with Young modulus of 69GPa, Poisson's ration of 0.33 and density of 2700kgm^{-3}. In the numerical model, the semi-infinite model employed in the analytical counterpart cannot be implemented, hence a perfect matching region

[172-174] is introduced around the edge of the elastic region to prevent reflections from the boundaries. Figures (5.23) and (5.24) show the result of the computation of the amplitude of both the normal (Uzz) and the radial (Urz) respectively, plotted against the angle of symmetry on a hemisphere of 70mm radius. The result is consistent with the analytical solution found in Kawashima [87] .

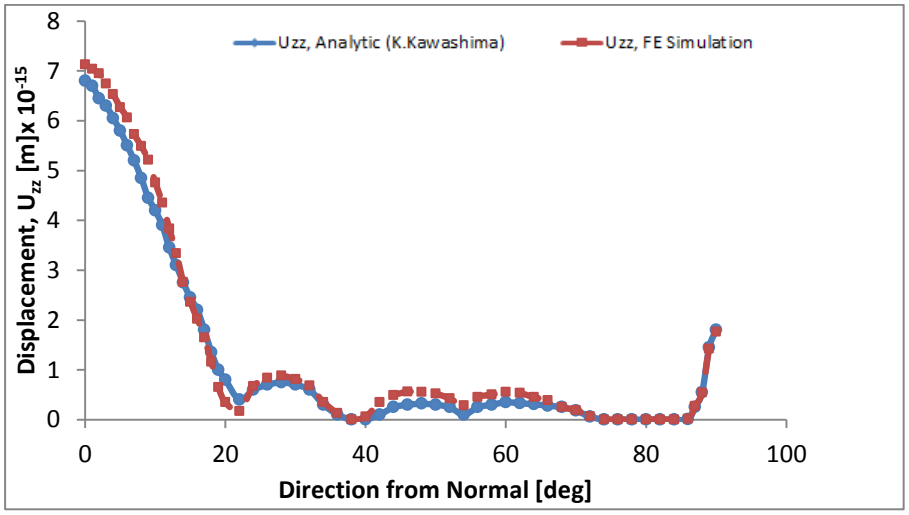

Fig.5.23: FE simulation and analytical calculation of the normal displacement vector (U_{zz}) on a hemisphere of 70mm radius exerted by a vertical surface force uniformly distributed over a circular area of 10mm radius, this is known as the Piston Source model first proposed by Kawashima [87].

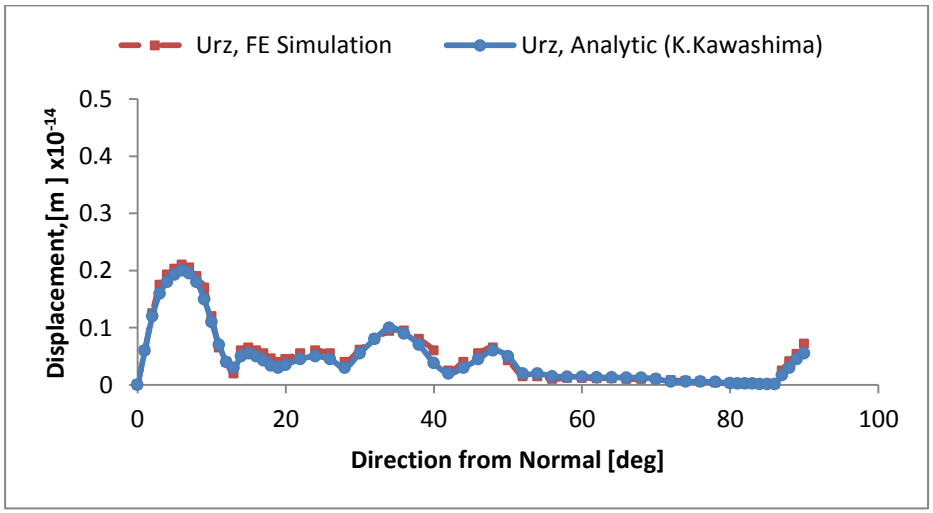

Fig.5.24: FE simulation and analytical calculation of the normal displacement vector (U_{rz}) on a hemisphere of 70mm radius exerted by a vertical surface force uniformly

distributed over a circular area of 10mm radius, this is known as the Piston Source model first proposed by Kawashima [87].

5.3.3 Experimental validation

Due to the complexity of the physics involved in EMAT's operation, there is no known single analytical method that can account for the multiphysics phenomenon. Hence the multiphysics model (which couples the complex electromagnetic and elastic phenomena in EMAT) developed in Chapter IV is validated using experimental methods.

The first stage in the experimental validation involves the fabrication of KT coil. This is followed by the actual experiments where some key EMAT parameters (such as excitation current, excitation current frequency and bias or static magnetic field) are varied and the resultant particle velocity is detected, recorded and used to compare against the result from the FE numerical model. Section (5.3.3.1 to 5.3.3.3.1) describes in detail the experimental methods used in the model validation.

5.3.3.1 Coil fabrication

The Novel KT EMAT coil used in this experiment was fabricated in-house by employing a simple and cost effective process proposed by Branson et al [175]. Here a double sided Bungard FR4 photoresist flexible board from Rapid Electronics was used. The thickness of the board, thickness of copper, thermal expansion, dielectric brake-down, volume resistivity are 0.125µm, 5µm, 5×10^{-5}, >60kV, 5×10^{8} - 5×10^{9} respectively. Other materials required for the fabrication are LaserJet printer, double sided UV exposure unit, NaOH solution,$(NH_4)_2S_2O_8$ solution and acetone. The following steps shown in Fig.(5.25) were taken to fabricate the coils.

Step A: A Print masks of the coil was made at high resolution on drafting paper using a LaserJet printer as shown in Fig. (5.6).

Step B: The double layer photoresist board comprising of the photoresist, copper and FR4 layers respectively, was exposed to ultra-violet (UV) light for about 100s on both sides using the UV exposure unit.

Step C: The UV exposed photoresist board was then immersed in a solution of 1.5g NaOH in 150ml DI H_2O. This procedure removes the photoresist exposing the copper layer.

Step D: The board was immersed in a solution of 33g of ammonium persulphate ($(NH_4)_2S_2O_8$) in 100ml DI H_2O at 38^oC for about 20 minutes with gentle agitation. This removes the copper layer exposing the FR4. The board was rinsed in DI H_20 to remove the excess ammonium persulphate.

Step E: Finally, the board was rinsed in a solution of acetone to remove the unexposed photoresist and then rinsed again in a DI H_2O before drying for about 10 minutes in an oven at 50^0C. The finished double layer KT coil (Figs. 5.27 and 5.28) is bathed with silicone baffle paint for proper insulation. All chemicals used were purchased from Sigma Aldrich.

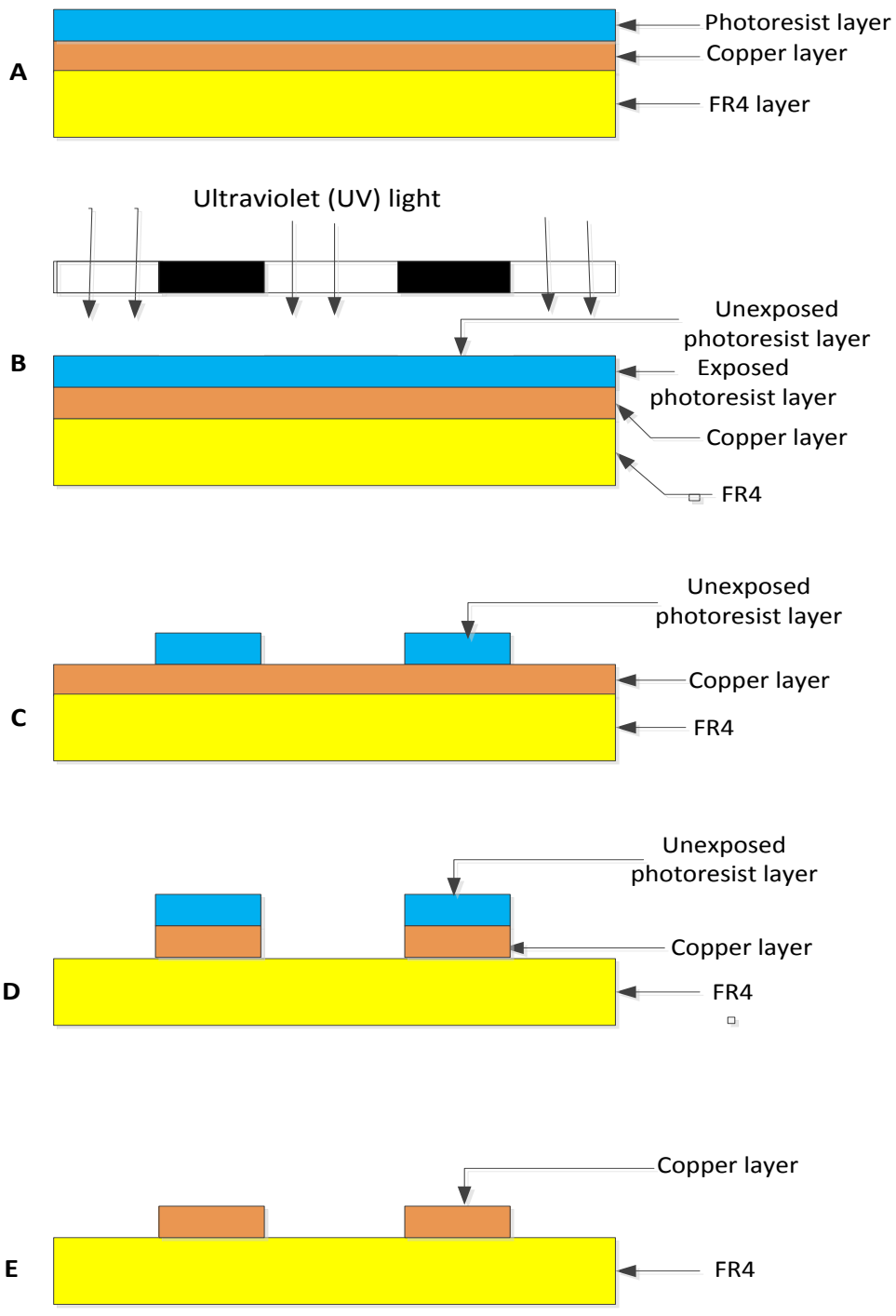

Fig.5.25: Schematic representation of the processes involved in the manufacture of the KT coil used in the experimental validation of the model.

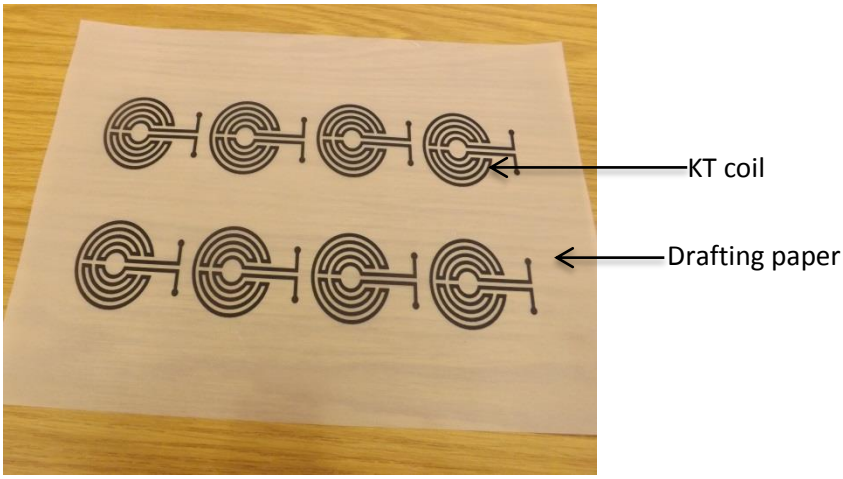

Fig.5.26: Print mask of KT coils on drafting paper.

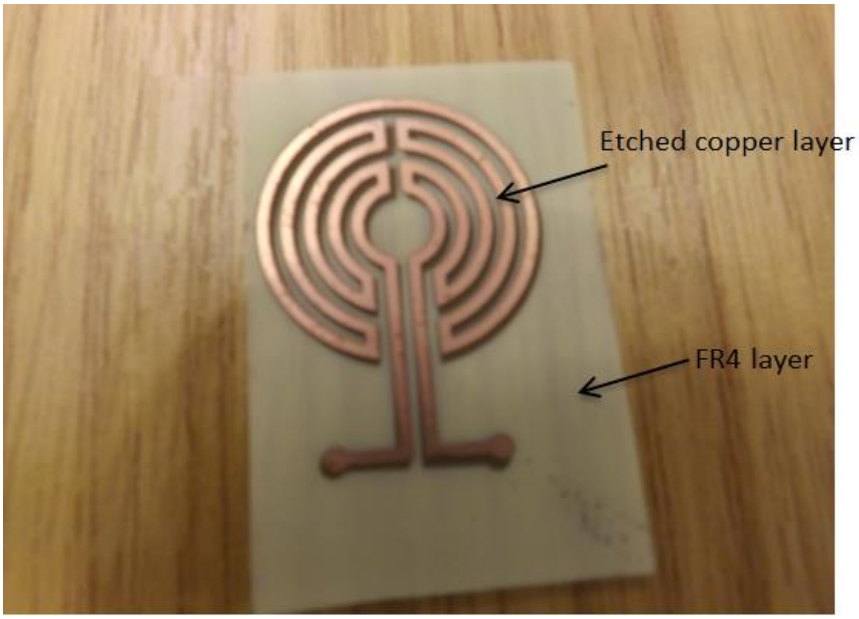

Fig. 5.27: Finished double layer KT coil after copper etching and photoresist clean up.

The KT coil employs the structure of planner spiral coil but with a current orientation of the meander-line coil.

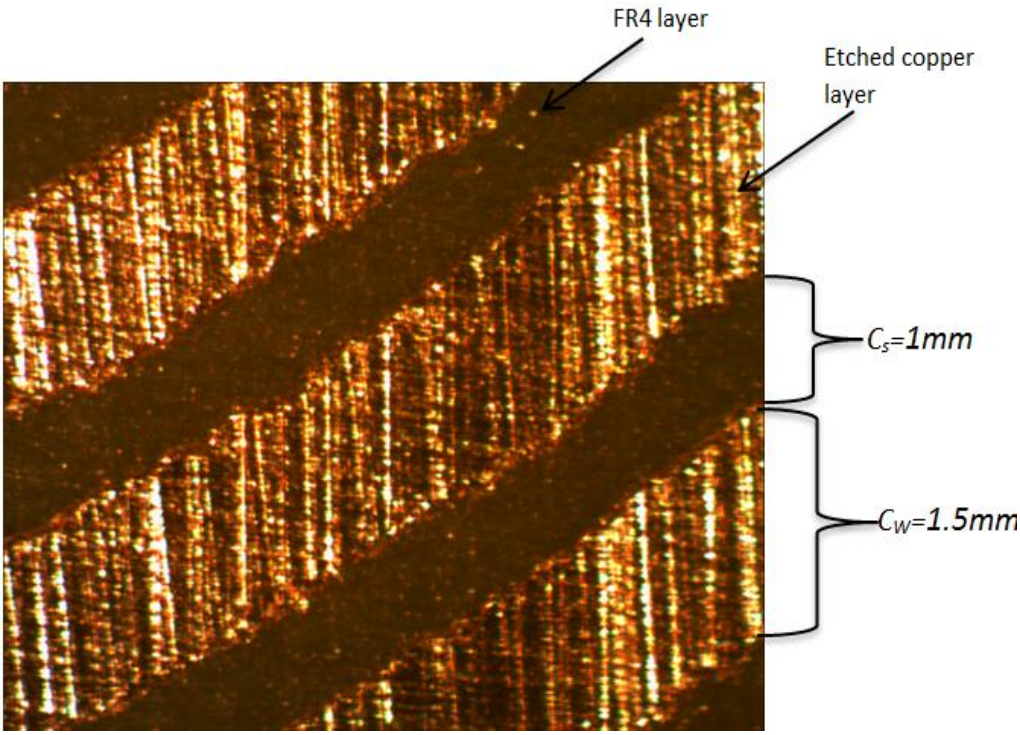

Fig.5.28: Close-up view of the finished double layer KT coil with copper width (C_w) of 1.5mm and coil spacing (C_s) of 1mm.

5.3.3.2 Experimental setup

The experimental validation of the model developed in Chapter IV was carried out in TWI Cambridge. The set up for this experiment consist of an EMAT system made up of a double layer KT coil fabricated in-house and reported in [96], a 24V DC electromagnet (Isliker magnets UK), a Teletest mark III pulser/receiver system (plant Integrity Cambridge), a magnetometer manufactured by AlphaLab Inc. USA, a laser Doppler vibrometer manufactured by Polytec Ltd UK, a resistor circuit (manufactured in-house) and a CS70 grade of pipe steel plate as the test specimen as shown in Fig.5.29 (A) and (B).

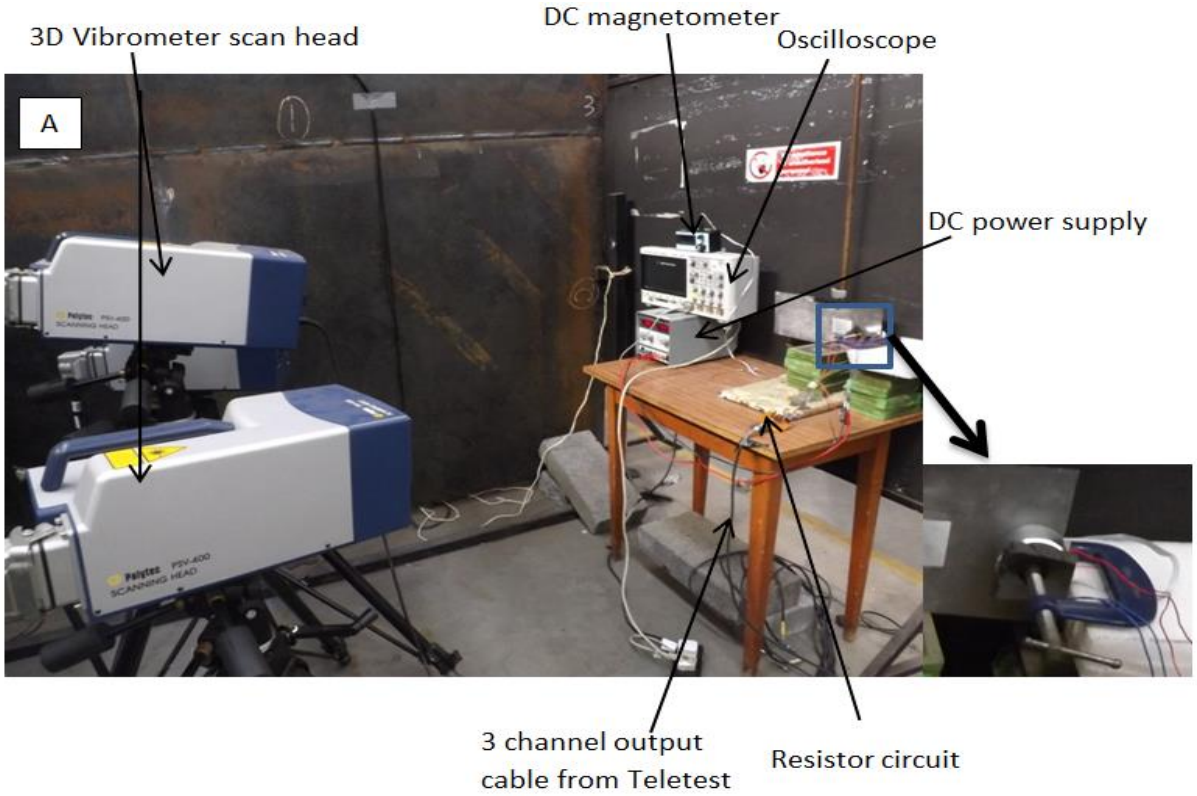

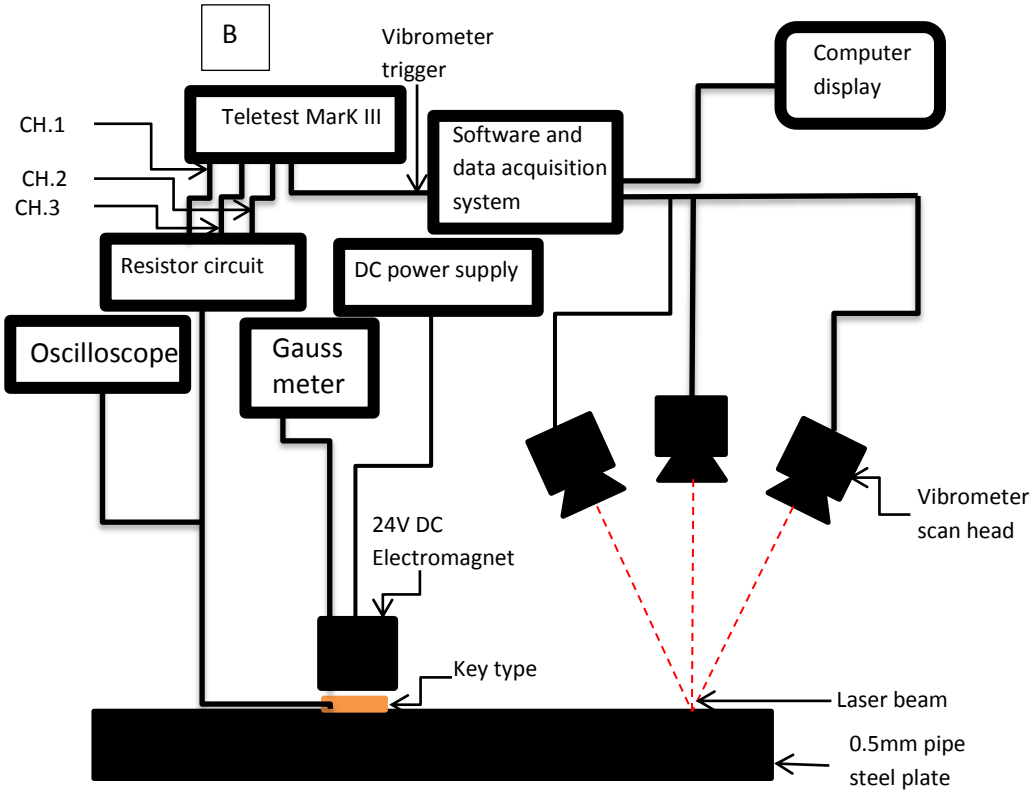

Fig 5.29: (A) Experimental setup used for model validation showing close up view of EMAT system comprising DC electromagnet, a KT copper coil sandwiched between the electromagnet and the pipe steel plate. (B) Schematic of the experimental setup.

5.3.3.2.1 EMAT setup

The EMAT consist of a double layer KT copper coil (with internal diameter (d_{in}) of 8mm, Outer diameter (O_D) of 20mm, Coil width (C_w) of 1.5mm and coil spacing (C_s) of 1m), a ø 40× 12mm DC ferrite electromagnet (with a rated voltage and maximum holding force of 24V and 400N respectively) and a CS70 grade of pipe steel plate of size 320×160×0.5mm as shown in Fig. (5.30). The KT coil is coated with Z1258 silicon baffle paint for electrical insulation and firm adhesion as described in section (4.4.5). The lift off of 0.5mm was used (this is the thicknesses of the silicon baffle paint insulating the coil from sample surface).

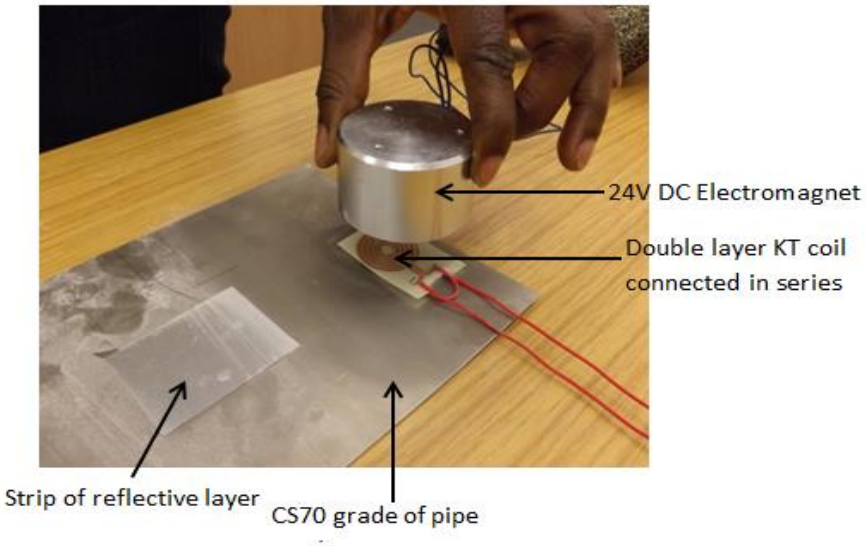

Fig.5.30: Pictorial representation of the KT-EMAT configuration used in the experiment, showing the double layer KT coil connected in series, the electromagnet and the CS70 steel plate with a strip of reflective layer attached to its surface to reduce reflection and scattering of the laser beam.

5.3.3.2.2 Teletest Mark III pulser / receiver unit

The Teletest mark III pulser-receiver system shown in Fig. (5.31) is originally used for long range guided wave ultrasonics and consists of 24 fully independent transmit and receive channels with a maximum output of 150V peak to peak per channel. The system is fully backed with tooling wave scan software [32].

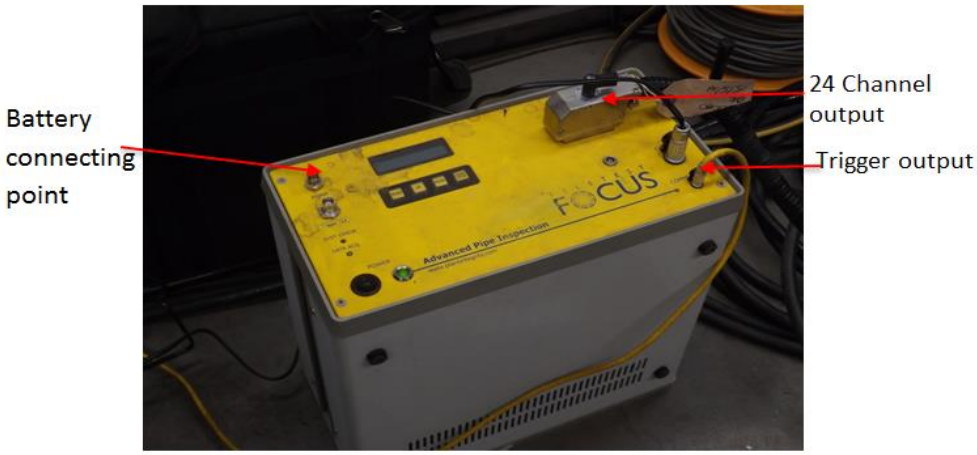

Fig.5.31: Pictorial representation of the teletest focus mark III pulser/receiver system showing the 24 channel output and the trigger output to the vibrometer unit [32].

5.3.3.2.3 Laser doppler vibrometer

The Polytec 3D scanning vibrometer provides 3-dimensional measurement, imaging and analysis of structural vibrations at acoustic frequencies [176]. The system consists of three scan heads made up of the geometry scan unit for 3-D measurements, the vibrometer controller for each scan head (remotely controlled by the data management system), a junction box that provides the interface between the three vibrometer controllers and the data management system, a tripod for positioning the scan head and a data management system (consisting of a PC mounted on a wheeled cabinet with cards to provide 3-channel signal generation, 4 channel data acquisition and a system control function) as shown in Fig.(5.32). The vibrometer uses a class II He-Ne laser, 633nm (red) and 1mW per sensor [176].

Fig.5.32: Pictorial representation of the PSV-400-3D scanning vibrometer used in the model validation experiment [176].

5.3.3.2.4 High power resistor circuit

The high power resistor bank in Fig.(5.33A) consists basically of three 40Ω, 25w resistors connected in parallel as shown in Fig.(5.33B). The aim is to regulate the peak to peak amplitude of the current at each channel to 2.6A since the maximum voltage obtainable at each channel is 150V at 500 kHz. Combining the current at each of the three channels, a maximum current of up to 7.8A can be obtained to drive the KT coil in the experiment. This technique is further explained in section 5.3.3.3.

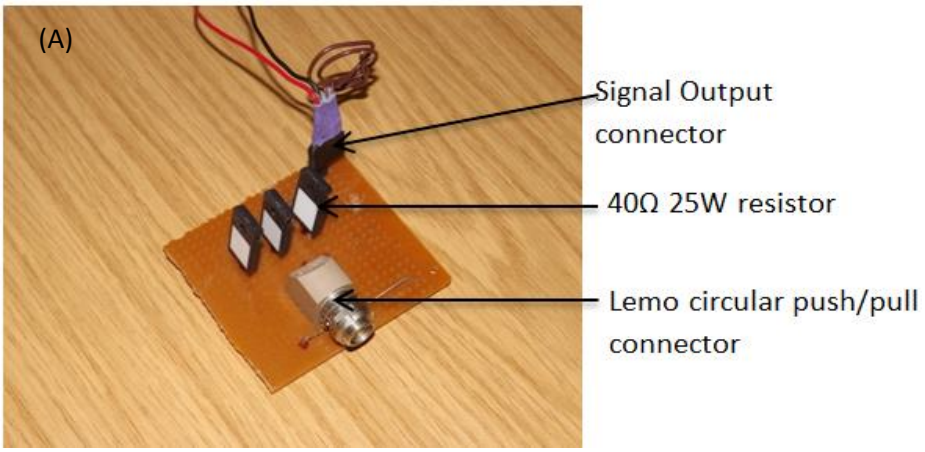

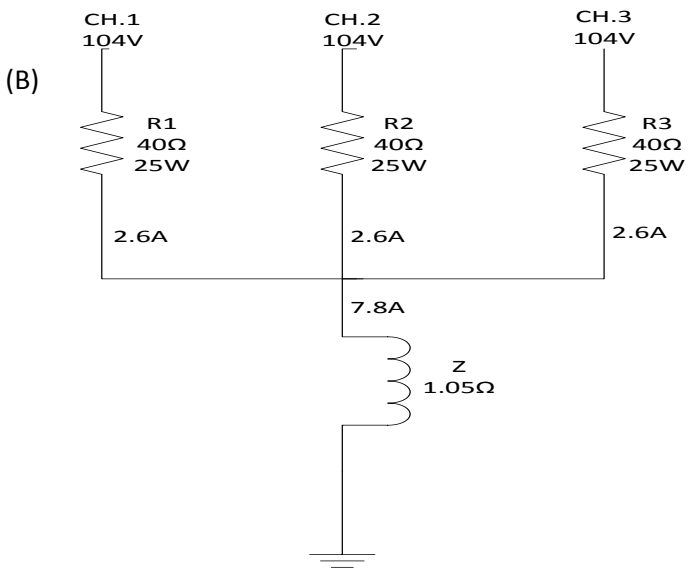

Fig.5.33: Special in-house resistor bank used for impedance matching and to combine the current from each of the three channels of the Teletest® equipment. (A) Pictorial representation,(B) Circuit diagram.

5.3.3.3 Experimental measurements

In the experiment, the KT coil is sandwiched between the test specimen and the electromagnet. The electromagnet generates the bias field when driven with a 24V DC supply. The excitation current required to drive the KT coil is obtained by combining the three channels of the Teletest equipment and monitored using an oscilloscope. The bias field generated by the electromagnet is monitored via a magnetometer. The LDV being a particle velocity sensor [177], and triggered by the Teletest Focus Mark III equipment detects the particle velocity of acoustic signal generated on the pipe steel specimen.

The coil was driven by a tone burst excitation produced by Mark III Teletest equipment. For this experiment, only three channels out of the 24 channels were utilised with each channel generating a maximum pulse of 150V and 3.8 A at 500 KHz. The Teletest equipment has high impedance and operates at high voltage with low current while the coil has very low impedance, but operates at a high current and low voltage. To drive the coil with a current of up to 8.0A, a special high power resistor circuit (see Fig. 5.33) was developed and connected between the coil and the Teletest equipment. This serves two main purposes; it acts as a matching circuit

to protect the equipment from over current and combines the individual currents of the channels to a single output of up to 7.8A while maintaining the voltage at 104V. More current can be obtained by combining more of the channels. Before performing the experiment, the Polytec-420 LDV was first calibrated and the test sample (CS70 grade of pipe steel plate) was coated with a reflective layer to reduce interference and reflection.

5.3.3.3.1 The influence of excitation current on particle velocity

To verify the effect of varying the driving current on the amplitude of the particle velocity, the scale factor in the software platform of the Teletest equipment was adjusted from 0.3 t0 0.9 at 500kHz. This procedure varies the driving current from 3.15A to 7.80A (see Table 5.2). A constant bias magnetic flux (B^{air}) of 2500 Gauss (0.25T) was generated by driving the electromagnet with a DC current of 2.5A while a centre frequency of 500 KHz was maintained throughout the experiment. It is assumed that due to boundary conditions, the magnetic field within the thin pipe steel (CS70) plate is approximately the same as the magnetic field measured in air, (that is $H^{air} = H^{CS70}$) and the magnetic field in air is computed as $H^{air} = \frac{B^{air}}{\mu_0}$. This approximation has been verified numerically by Ribichini [90] with an error margin of less than 5%.

Table 5.2: Teletest software platform voltage adjustment to produce the excitation current.

Scale factor	CH.1 (Voltage)	CH.2 (Voltage)	CH.3 (Voltage)	CH.1 (Current)	CH.2 (Current)	CH.3 (Current)	Total Current
0.3	42 V	42V	42V	1.05A	1.05A	1.05A	3.15A
0.4	53V	53V	53V	1.33A	1.33A	1.33A	3.98A
0.5	62V	62V	62V	1.55A	1.55A	1.55A	4.65A
0.6	71V	71V	71V	1.78A	1.78A	1.78A	5.33A
0.7	83V	83V	83V	2.08A	2.08A	2.08A	6.24A
0.8	92V	92V	92V	2.30A	2.30A	2.30A	6.90A
0.9	104V	104V	104V	2.60A	2.60A	2.60A	7.80A

To take measurement, the excitation current was varied and the amplitude of the particle velocity signal detected by the LDV was averaged and Fourier transformed. The ratio between the velocity and the excitation current spectra at the centre frequency gives the experimental particle velocity per unit current. The numerical particle velocity computed using Comsol multiphysics is in good agreement with the experimental result with an average discrepancy of 8.8% as seen in Fig. 5.34. Shown in Figures (A.2.1-A.2.7) are the raw traces of the captured experimental particle velocity signal when the excitation current was varied from 3.15A to 7.8A.

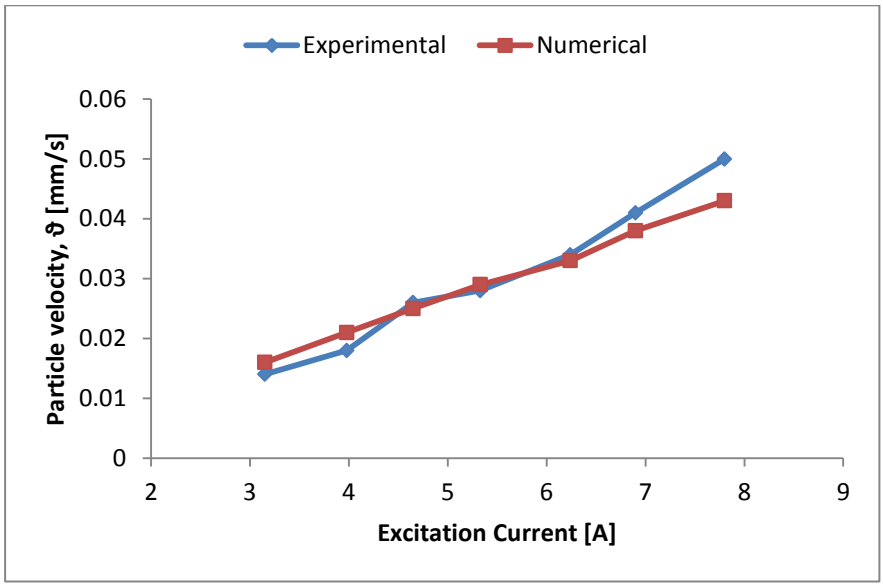

Fig 5.34: Comparison between calculated and measured particle velocity along sound beam when the excitation current is varied from 3.15A-7.80A.

5.3.3.3.2 The influence of excitation frequency on particle velocity

In order to further validate the model used in this study, the particle velocity signal obtained when the excitation frequency is varied from 200 KHz to 500 KHz, is compared with numerical simulation result. A fixed value of excitation current and bias magnetic field of 7.8A and 2500 Gauss (0.25T) respectively were employed for both the experimental and numerical study.

The set up for the experiment is as described in section (5.3.3.2). The excitation frequency was varied via the Teletest Focus Mark III software platform. The particle velocity signal detected by the LDV was obtained and the result averaged and Fourier transformed. To obtain the particle velocity at each frequency, the spectrum of the measured velocity was divided by the spectrum of the excitation current. This process is very necessary since the FE model was carried out in frequency domain. The amplitude of the measured particle velocity was compared with numerical result as shown in Fig.5.35. The results show good agreement with an average discrepancy of 11.3%. Figures (A.3.1-A.3.7) shows the raw traces of the captured experimental particle velocity signal when the excitation frequency was varied from 200 kHz to 500 kHz.

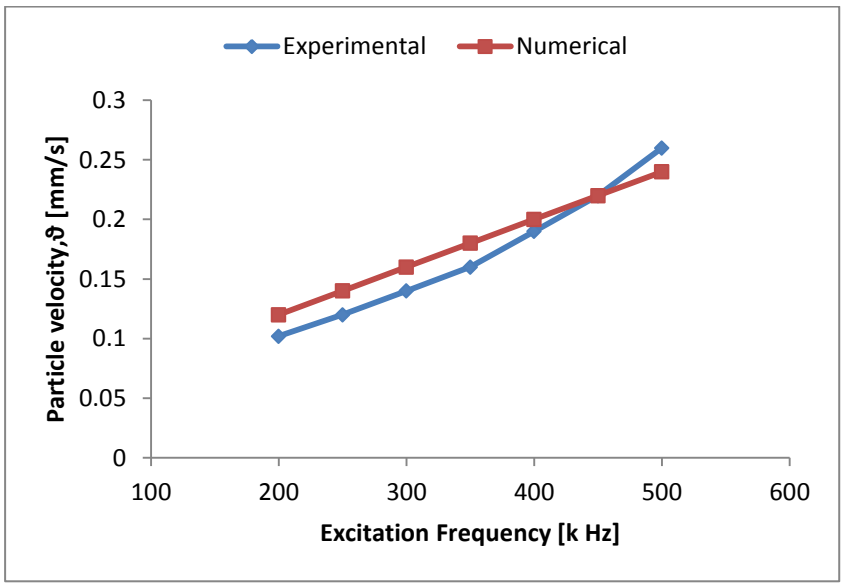

Fig.5.35: *Comparison between numerical and experimental particle velocity along sound beam when the excitation frequency is varied from 200 KHz-500 KHz.*

5.3.3.3.3 The influence of static (bias) magnetic field on particle velocity

The set up for this investigation is as outlined in section (5.3.3.2). The excitation current and frequency were maintained at 7.8A and 500 KHz respectively. This investigation is very important for the validation of the model as it has been reported in [33, 87, 89] that the bias magnetic field contribute significantly to the amplitude of the acoustic wave. It is well known that the driving current (direct

current) fed to the electromagnet is proportional to the static magnetic field produced; hence, the bias magnetic field was varied by changing the driving current of the electromagnet producing the field. Also, as explained in section (5.3.3.3.1), the magnetic flux in air (B^{air}) is a product of the magnetic field in air (H^{air}) and the permeability of free space (μ_0) and it is assumed that the magnetic field in air is proportional to the field in the pipe steel material used in this study.

To obtain measurement in the experiment, the bias field was varied by adjusting the driving current of the Electromagnet and the particle velocity signal was captured by the LVD. Figures (A.4.1-A.4.7) shows the raw traces of the captured experimental particle velocity signal when the bias field was varied from 0.15T to 0.25T. The signal detected was averaged, Fourier transformed and the final result was used to compare the numerical prediction. The experimental result was observed to be consistent with the numerical prediction (see Fig.5.36) with an average discrepancy of 5.6%.

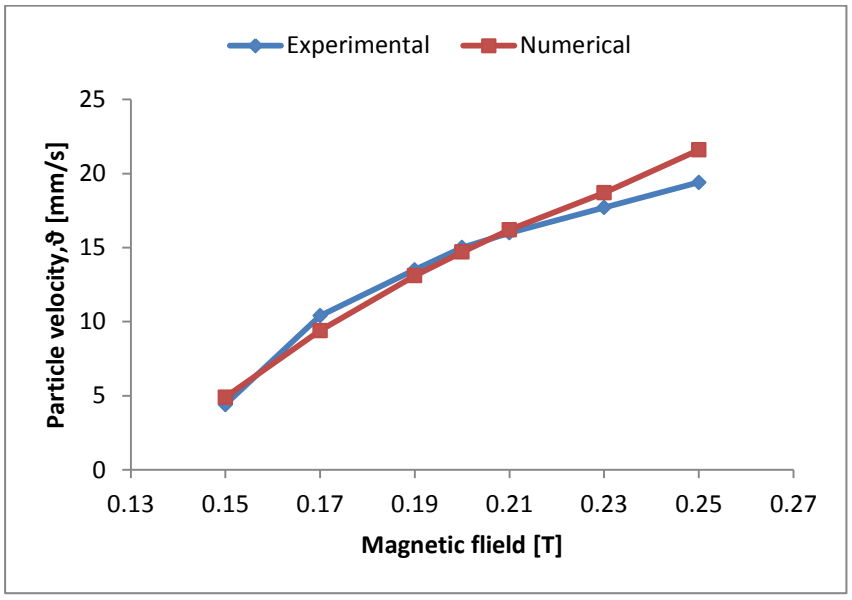

Fig.5.36: *Comparison between numerical and experimental particle velocity along sound beam when the bias magnetic field is varied from 0.15 [T] to 0.25T [T].*

5.4 Reasons for the discrepancy observed in the result

(i) One of the reasons for the observed discrepancy in the result is due to errors due to environmental noise and or as a result of vibration due to increase in temperature from the heating of the electromagnet during measurement.

(ii) Another most common sources of errors in modelling are the computational limitations. The model is extremely demanding, the number of element used was limited by the available computer memory. It is well known that the more the number of element used in the finite element mesh, the more accurate the result becomes and also the more computer memory required to run the simulation. A trade-off is required between the number of element used and the resolution of the skin depth and the wave length in the elastic region respectively. Four elements through the skin depth and 15 elements per wavelength were employed. This gives rise to a small but non-negligible error in the numerical results.

(iii) Physical variability of the magnetic properties of ferromagnetic materials is another common source of error in the model. From Eddy current inspection, flawless and apparently homogeneous ferromagnetic materials show significant variability when spatial scans are performed on them [178]. This is attributed to the spatial variation of the magnetic permeability caused by different surface conditions, residual stress, magnetic histories and aging effect [178]. The implication of this is that the validity of the physical model of a perfectly homogenous ferromagnetic specimen used in the simulation is in context. For instance, it has been proposed that a thin surface layer (known as dead layer) between 10-100μm whose permeability is significantly lower than the bulk of the material exist in ferromagnetic materials [179].

(iv) Another source of error in the model is related to the frequency dependence of the magnetic properties of ferromagnetic materials. In the model a constant magnetic permeability was used throughout the study, while in reality, the magnetic permeability varies with frequency. Experimental investigations with different methods like inductance measurement [180] and potential drop measurement [181]

have shown that the relative permeability of pure iron exhibits significant dependence on frequency.

The issues enumerated above show that most errors in the simulation are due to insufficient knowledge on the behaviour of ferromagnetic media on the variation of some physical parameters.

5.5 Summary

The FE model used in this study has been successfully validated by comparing its predictions with analytical and experimental results. Overall, the validation has demonstrated that the physics of the transduction mechanism involved in EMATs operation is well represented by the model. The FE model results (single bench mark and multiphysics models) when compared to both the analytical and experimental results yielded an average discrepancy less than 9%. The FE model was carried out on pipe steel plate, this can be extended to pipes by creating a ring of equally spaced KT EMAT probes supported by a collar wrapped around the pipe as can be seen in Chapter VI of this theses. Finally the validated FE model will be used in the next Chapter to study the transduction mechanisms involved in the operation of two major EMAT configurations (the MS EMAT and NB EMAT).

CHAPTER 6[2]

A NEW STUDY OF THE TRANSDUCTION MECHANISMS OF A NOVEL KEY-TYPE (KT) EMAT CONFIGURATION ON VARIOUS GRADES OF PIPE STEEL MATERIALS.

6.1 Introduction

This Chapter will develop a coupled magnetostrictive model which consists of the validated coupled mechanical model discussed in Chapter 5 with some modifications to account for magnetostriction (see Fig.1.11). The coupled magnetostrictive model will give a comprehensive picture of the mechanism of operation of EMAT when used on Ferro-magnetic materials. Also a novel algorithm will be developed in conjunction with the coupled magnetostrictive model to decouple and quantify the transduction forces (MF, DLF and SLF) operating simultaneously at various excitation current when NB and MS EMAT configurations are deployed on pipe steel materials. The chemical and electromagnetic properties of these grades of pipe steel are shown in Table 6.1.

Table 6.1: Measured electromagnetic properties of Pipe steel material and their constituent elements. The electromagnetic properties were measured via an alternating current potential drop (ACPD) technique [90].

Material	Carbon (%)	Other Elements (%)	Relative Permeability (μ_r)	Conductivity, σ [Sm^{-1}]
CS70	0.65-0.75	0.7 Mn	59	$3.77x10^6$
J55	0.40-0.50	1.00 Mn, 0.17Cr, 0.09 Cu, Mo, Ni	137	$4.06x10^6$
TN80Cr3	0.25-0.30	Mo, Cr, Ti	86	$2.61x10^6$
L80SS	0.25-0.30	Mo, Cr, Ti	67	$4.19x10^6$
L80A	0.25-0.30	1.0 Mn, 0.12Cu, Mo, Cr, Ti	70	$4.54x10^6$

[2] A substantial part of this chapter has been published by the author in [97, 98]

6.2 Theoretical background

A unified electromagnetic formulation describing the electro-acoustic transduction process governing an EMAT involves combining the momentum conservation form of Maxwell's equation in the quasi-static limit, and Cauchy's law of motion. This method creates separate subsystem for the electrical, mechanical and material phenomenon, where the mutual coupling between the systems is facilitated through force densities [91]. This approach inspired by Chu [182] and Engel [183], achieves the coupling of the field tensors as part of an additional material subsystem instead of the conventional technique of accounting for the electromagnetic material interaction by direct combination of mechanical stress and magnetic flux by means of their constitutive relation.

This mathematical formulation established by Ludwig [92], accounts for both the magnetostrictive force, Lorentz force due to the static field, Lorentz force due to the dynamic magnetic field and Magnetization. A typical schematic of a normally biased (NB) and Magnetostrive (MS) EMATs using a Key-Type (KT) coil is depicted in Figures 6.1 (A and B).

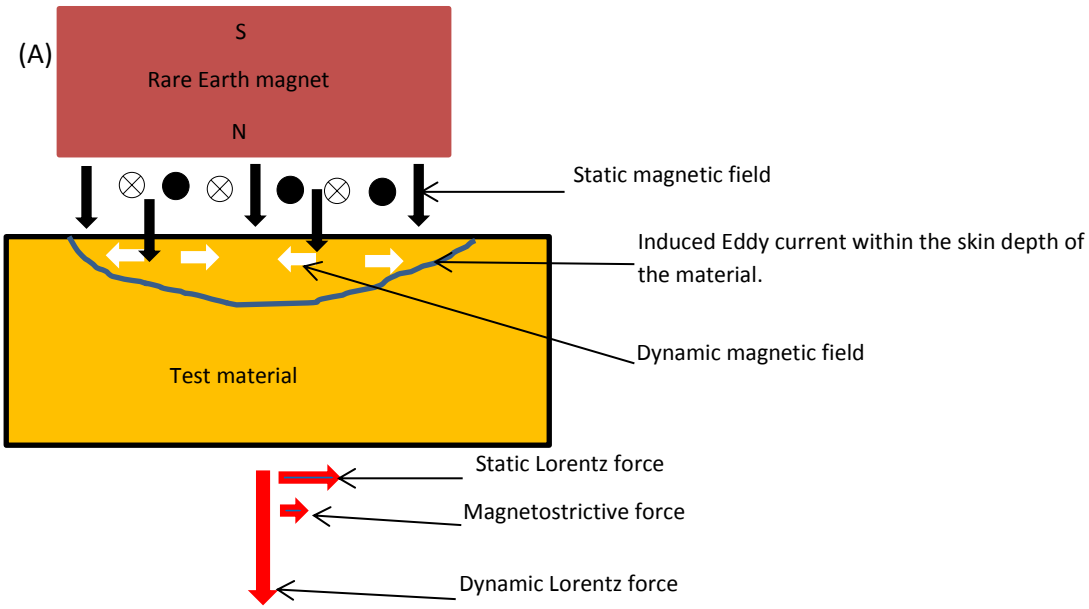

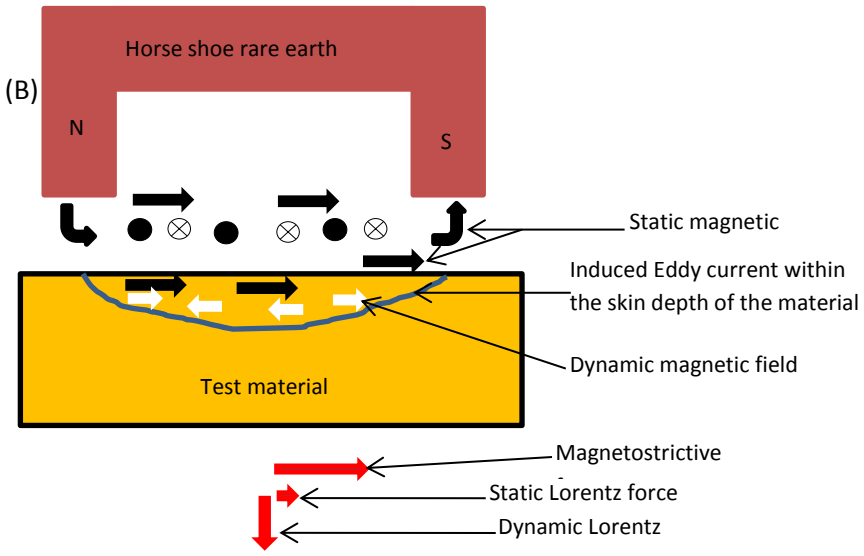

Fig.6.1: Schematic of a typical EMAT showing the orientation of the Magnetostrictive strain, dynamic Lorentz force and Static Lorentz force due to the magnetostriction, dynamic magnetic field and static magnetic field respectively. (A) Normally biased EMAT configuration with bias magnetic field normal to the surface of the test material. (B) Magnetostrictive EMAT configuration with the bias magnetic field parallel to the surface of the test material.

Conservation of momentum law of electromagnetic radiation states that: the total generated electromagnetic force is equal to the sum of the work done and the energy density [111]. This is expressed in the form of;

$$\int_s (T.da)da = \int f dv + \frac{\partial}{\partial t}\int_v \frac{S}{C^2} dv \qquad (6.1).$$

where T , f, C and S are the Maxwell's stress tensor, force density, speed of light and the Poynting vector respectively. $\frac{S}{C^2}$ represents the momentum density. For simplicity, the physical model in Figs.6.1 (A and B) is divided into three mutually coupled sub-system; the electrical, the mechanical and the material subsystem formulation.

6.2.1 Electrical subsystem formulation

Faraday's and Ampere's equation which forms part of Maxwell's equation within the quazi-static field limit is of the form [92]:

$$\nabla\times \mathrm{E} = -\mu_0 \frac{\partial H}{\partial t} - J_m \tag{6.2}$$

$$\nabla\times \mathrm{H} = J_f \tag{6.3}$$

$$\nabla.\mathrm{H} = -\nabla.\mathrm{M} \tag{6.4}$$

Where the magnetic source density J_m can be expressed in terms of magnetization and mechanical particle velocity through;

$$J_m = \mu_0 \frac{\partial M}{\partial t} + \mu_0\nabla\times\left(M \times \frac{\partial u}{\partial t}\right) \tag{6.5}$$

Where μ_0 and u are absolute permeability and particle displacement respectively.

The total free conducting current density J_f is given as:

$$J_f = \sigma \mathrm{E} + \mu_0 \sigma\frac{\partial u}{\partial t}\times(H + M) + J_s \tag{6.6}$$

with σ and J_s denoting material conductivity and source current density respectively.

The electromagnetic field equation in (6.2) and (6.3) can be expressed in the form;

$$\nabla.T_e + \frac{\partial G}{\partial t} = f_e \tag{6.7}.$$

Equation (6.7) is analogous to the mechanical momentum conservation equation, where the negative part of the Maxwell's stress tensor is given as:

$$T_e = \frac{1}{2}\mu_0|H|^2\mathrm{I} \tag{6.8}$$

Assuming that the electromagnetic moment of momentum due to the quasi-static field is zero, that is

$$\frac{\partial G}{\partial t} = \varepsilon_0\mu_0 \frac{(E\times H)}{\partial t} = 0 \tag{6.9},$$

Combining equations (6.7) and (6.9) yields

$$f_e = \nabla . T_e \tag{6.10}$$

Substituting equations (6.8) and (6.10) yields the electromagnetic force density given as:

$$f_e = - J_e \times \mu_0 \mathrm{H} + \mathrm{H}\left(\nabla . (\mu_0 M)\right) \tag{6.11}$$

with J_e and M denoting the induced eddy current density and magnetization respectively in the material under investigation.

In EMAT's operation, it is well-known that two types of magnetic fields cause stress on the material. The fields are: the static magnetic field due to the bias magnetic and dynamic magnetic field due to the sinusoidal excitation of the coils. The effective field on the material is given as:

$$\mathrm{H} = H_s + H_d \tag{6.12}$$

where H_s and H_d denotes the static and dynamic field respectively. Substituting equation (6.12) in (6.11) yields:

$$f_e = - J_e \times \mu_0 (H_s + H_d) + (H_s + H_d)\ (\nabla . \mu_0 M) \tag{6.13}.$$

6.2.2 Mechanical subsystem formulation

When an ultrasonic wave propagates within a metal, it does not obey 'Hooke's law' as a result of the strain generated in the metal [184]. A nonlinear approximation based on Cauchy's first law of motion is employed to account for the acoustic wave propagating in the metal. In the propagation of elastic waves nonlinear effects may arise from many different sources, i.e. when the amplitude of an elastic wave becomes sufficiently large as to generate a finite strain on the material. The relationship between Cauchy's stress tensor and the finite strain tensor gives the elastic properties of nonlinear materials and can be derived by invoking Cauchy's law of motion [92]:

$$\nabla . (C : \nabla_u) + f_k = \rho \frac{\partial^2 u}{\partial t^2} \tag{6.14}$$

where ρ is the density and f_k is the source term which must be determined as a result of the magnetic field distribution. In the momentum conservation form, equation (6.14) becomes:

$$\nabla.T_k + \frac{\partial G_k}{\partial t} = f_k \tag{6.15}$$

where the negative kinetic stress tensor T_k is defined by the linearized form of Hooke's law:

$$T_k = -c:\nabla_u \tag{6.16}$$

and the momentum density is given as

$$G_k = \rho \frac{\partial u}{\partial t} \tag{6.17}$$

The unified conservation law description of EMAT has been numerically implemented by Ludwig in [91].

6.2.3 Material subsystem formulation

The material subsystem accounts for the coupling between the electrical and mechanical subsystem. The outflow of electromechanical energy from the transducer into the material and its subsequent conversion into acoustic energy depends on the geometry of the coil, the coil lift off, the properties of the material and the material coupling factor. Applying the conservation law (which takes into account all the parameters involved in acoustic wave generation and propagation), the material subsystem tensor is introduced as [92];

$$\nabla.T_m + \frac{\partial G_m}{\partial t} = f_m \tag{6.18}$$

Where G_m is the material momentum density and is equal to zero (G_m) , T_m is the material tensor while f_m is the material dependent force. T_m is created as part of a general power series expansion T_g with expansion coefficient α^{pq} in the form;

$$T_g = \sum_{p,q\geq 0} \alpha^{pq} (\nabla_u)^p H^q \tag{6.19}$$

To convert equation (6.19) to index notation and account for the magnetised state of the material medium an additional tensor contribution (-$\mu_0 MH$) is included, transforming the material subsystem tensor to;

$$T_m = \sum_{p,q\geq 0} \alpha^{pq} (\nabla_u)^p H^q - \mu_0 MH + \alpha^{10} : \nabla_u \quad (6.20)$$

Taking the divergence of (6.20) yields the material dependent force density;

$$f_m = \nabla . T_m = - \alpha^{01} . \nabla H - \alpha^{02} H_s . \nabla H - \mu_0 M . (\nabla H) \quad (6.21)$$

6.2.4 Subsystem combination

The momentum conservation law can be employed to construct a unified formula to account for acoustic wave generation by EMAT. The unified formula must account for the three subsystems involved in the generation of acoustic wave in the transducer. A mutually coupled EMAT system has no additional external force operating on it, hence the total force densities add up to zero;

$$f_m + f_e + f_k = \nabla . (T_m + T_e + T_k) - \frac{\partial}{\partial t} (G_m + G_e + G_k) = 0 \quad (6.22)$$

In the form of (6.16), equation (6.22) becomes;

$$f_k = -\nabla . (T_m + T_e) - \frac{\partial}{\partial t} (G_m + G_e) \quad (6.23)$$

Linearizing equation (6.20) and expanding to its first three terms, equation (6.23) becomes;

$$f_k = \alpha^{01} \alpha^{01} . \nabla H + \alpha^{02} . H_d : \nabla H + J_e \times \mu_0 H + \mu_0 M . (\nabla H) \quad (6.24)$$

If the third rank magnetostrictive tensor defined as [185];

$$-e^T = \alpha^{01} + \alpha^{01} . H_s \quad (6.25)$$

is invoked (where the superscript T denote transpose), equation (6.24), yields the four force mechanism in operation when EMAT is employed in a ferromagnetic material. Thus, equation (6.24) becomes;

$$f_k = J_e \times \mu_0 H_s + J_e \times \mu_0 H_d - e^T . \nabla H + \mu_0 M . (\nabla H) \quad (6.26)$$

Where the first term represents the Lorentz density due to the static magnetic field, the second term is the Lorentz force density due to the dynamic magnetic field, the third term is the magnetostrictive force density while the last term is the magnetization force density. Equation (6.26) can be used in equation (6.14) to resolve completely the problem of acoustic wave propagation in ferromagnetic material. It has been reported in [89, 114, 142, 186, 187] that for an EMAT configuration where the bias field is tangential to the sample as seen in NB and MS EMATs, the contribution of the magnetization force to acoustic wave generation is very small and can be neglected. This is because the components of the Lorentz and magnetization force in the direction normal to the sample have similar amplitude but are out of phase; hence the two forces cancel each other.

6.3 Determination of experimental parameters for simulation

The aim of the experiment is to obtain a magnetostrictive curve (magnetostrive strain versus magnetic field strength) for five grade of pipe steel plate shown in Table 6.1. The magnetostrictive parameter subsequently obtained from the magnetostrictive curve is fed into the numerical model to account for magnetostriction in EMATs. Fig.6.2 (A),(B) and (C) shows a close up view of the magnetic circuit and the block diagram respectively of the setup used for the experiment. Four Kyowa strain gauges (Sensor UK) with a gauge factor of 2.1 were connected in a bridge form (for optimal sensitivity) and mounted on the pipe steel plate using M-Bond 200 and AE-10 adhessive systems (HBM UK) [188], the strain gauges were placed between two 24V, 500N ferrite electromagnet of diameter 50mm and height 30mm that generates the static field. Each of the electromagnets were connected to a dual mode adjustable DC power supply (RACAL DANA 9232) and then placed on a pipe steel plate of (320 × 120 × 0.5mm) to form a magnetic circuit. The sensor tip of a DC magnetometer (Alpha Lab, USA) was placed underneath the electromagnet to measure the magnetic flux density generated on the surface of the material. The terminals of the bridge strain gauge were connected to a channel of strain measurement bridge amplifier instrument (Tinsley Sovereign). The strain measurement equipment provides the excitation voltage and amplifies

the output signal of the strian gauge, since the magnetostrictive strain (ε) caused by the magnetic field on the plate is very small (in micro strain).

The magnetic field strength inside the steel material can be calculated by assuming that $H^{air} = H^{steel}$ and the boundary condition for the magnetic field strength (H) sets the continuity of the tangential component at the boundary between two media [90], hence

$$H^{air} = \frac{B^{air}}{\mu_0} \tag{6.27}$$

To be sure that the strain gauge is measuring the strain on the steel material and not the magnetic field on the surface of the steel material, the same experiment was conducted, but this time with a non-magnetic material (aluminum). The measurement on the strain measuring equipment was observed to be zero. This indicates that the strain gauge was unable to detect any variation of the magnetic field on the surface of the material.

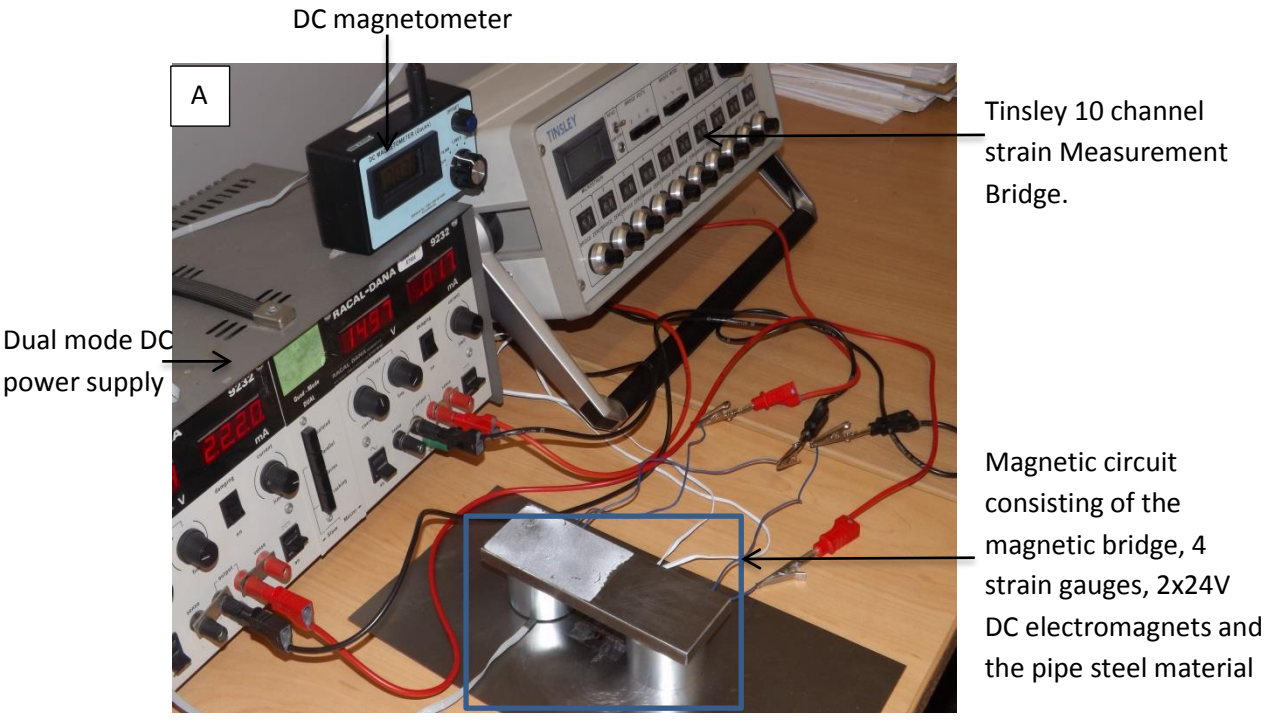

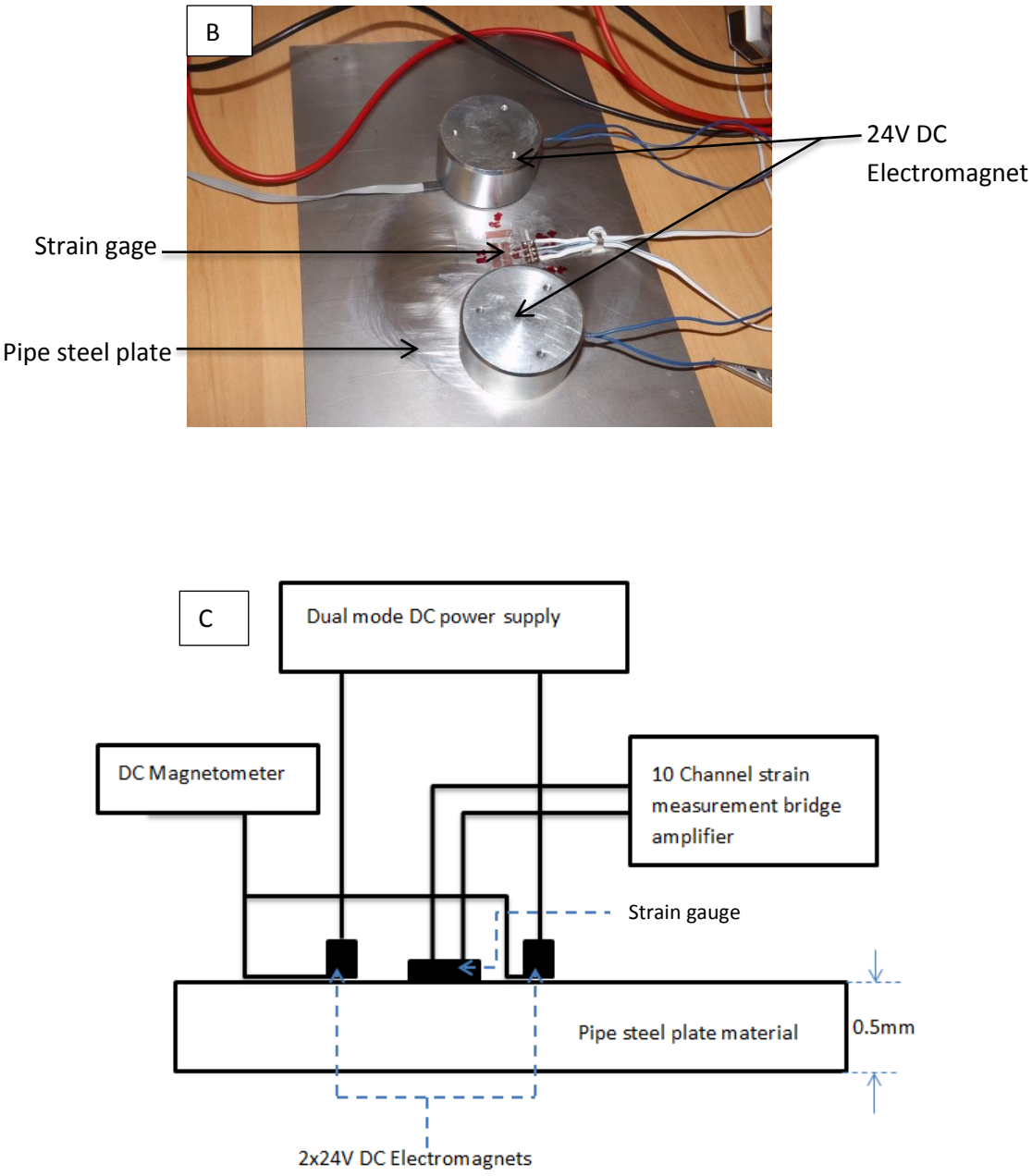

Fig.6.2 (A) Pictoral view of the experimental setup to measure Magnetostrictive strain on pipe steel grade of materials. (B) Closeup view of the experimental setup showing the bridge strain gage circuit. (C) Block diagram of the experimental setup to measure magnetostrictive strain on pipe steel grade of materials.

The magnetostrictive curve in Fig.(6.3) shows that on application of the magnetic field, the pipe steel sample expands causing positive strain along the direction of the field where H<10 kA/m. Between 10 kA/m and 15 kA/m the magnetostrictive strain peaks (maxima) for all steel grades while compression sets in when H>15 kA/m. This result is consistent with work done by other researchers [88, 90, 112, 189, 190].

Furthermore, it is observed that although the shapes of the curves are similar, the position of the maxima (for which piezo magnetic strain equalls zero) differs significantly for each grade of pipe steal studied as shown in Fig.(6.3)

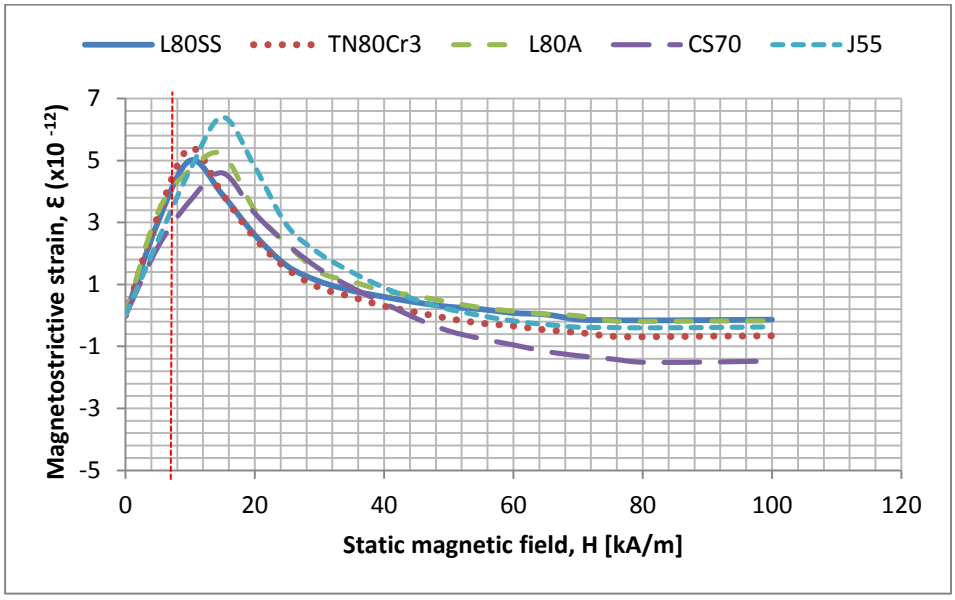

Fig.6.3: Experimental magnetostrictive curve of five grade commonly used pipe steel materials.

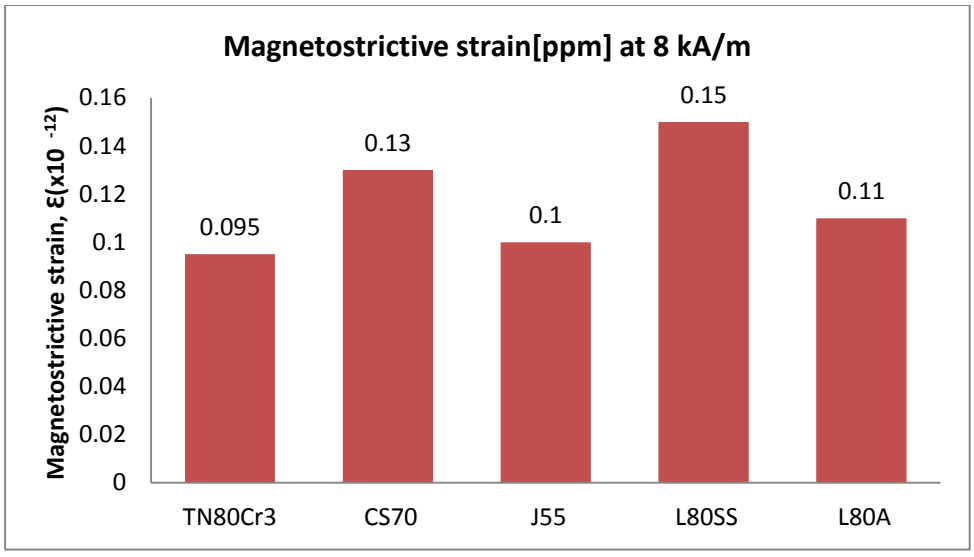

Fig.6.4: Chart of magnetostrictive strain obtained from the slope of each magnetostriction curve at H =8 kA/m for five grades of pipe steel. The slope of the curve deffer slighly due to the different relative permaeability of the samples.

6.3.1 Finite element modelling

A numerical modelling technique using finite element commercial software (COMSOL multi-physics) is proposed. The technique involves creating a Whole EMAT model (WEM) that accounts for the DLF and SLF, a magnetostrictive model (MEM), that accounts for MF, DLF and SLF and a dynamic model that accounts for only the DLF, see Table (6.2).

Table 6.2: Illustration of the composition of the proposed models.

Whole EMAT model (WEM)	Full EMAT model comprising of a static magnet that generates the static magnetic field or bias field, a copper coil that generates the dynamic magnetic field and the pipe steel material specimen.
Magnetostrictive EMAT model (MEM)	This includes every component of the whole model plus the magnetostrictive parameters. It describes the complete working of EMAT on ferromagnetic material.
Dynamic EMAT model (DEM)	This is the whole model without the permanent magnet. That is, the model consists of only the copper coil and the pipe steel material specimen.

The model solves simultaneously, the electrodynamics problems which account for the Eddy current induction and elastic phenomenon that gives rise to wave generation. The magneto-mechanical coupling is achieved by the influence of the total Lorentz force (F_T) and magnetostrictive force. The total Lorentz force (F_T) is implemented as a sum of the dynamic and static Lorentz forces. The dynamic Lorentz force (DLF) is the vector product of the induced eddy current (J_e) and the dynamic magnetic field, while the static Lorentz force (SLF) is the vector product of the induced Eddy current (J_e) and static magnetic field as reported in equation (6.26).

In the case of magnetostriction, the constitutive equation is modified in such a way analogous to piezoelectricity;

$$\begin{cases} \varepsilon = s\sigma + DH_d \\ B = D^T\sigma + \mu H_d \end{cases} \quad (6.28)$$

where ε, σ, H_d, B, s, D and μ represents strain tensor, stress tensor, magnetic field, magnetic flux density, compliance matrix, piezomagnetic strain coefficient and magnetic permeability respectively.

To make it easier to represent in the Comsol multiphysics equation (6.28) becomes;

$$\begin{cases} \sigma = C_{mod}\varepsilon + \sigma_0 \\ B = \mu H_d + B_r \end{cases} \quad (6.29)$$

where $\sigma_0 = \beta B$, $B_r = D^T\sigma$ and C_{mod} denotes the effective initial stress, the effective remnant flux density and the effective stiffness coefficient respectively.

In (6.29), the first equation represents the 'Joule effect' or direct magnetostriction which occurs when magnetostrictive materials are strained as a result of exposure to a magnetic field, while the second equation known as 'Villari' effect is employed in the detection process when a mechanical stress changes the magnetization or magnetic flux density of the material in the presence of a bias magnetic field.

Here,

$$C_{mod} = (I - cD\mu^{-1}D^T)^{-1}c \quad (6.30)$$

where c = s^{-1} and I = 6×6 Identity matrix.

The piezomagnetic stress coefficient (β) is given as

$$\beta = -(I - cD\mu^{-1}D^T)^{-1}cD\mu^{-1} \quad (6.31)$$

which transforms to

$$\beta = C_{mod}D\mu^{-1} \quad (6.32)$$

The peizomagnetic strain coefficient (D), is given as [33];

$$D = \begin{bmatrix} 0 & 0 & \frac{-m}{2} \\ 0 & 0 & \frac{-m}{2} \\ 0 & 0 & m \\ 0 & 0 & 0 \\ 0 & 0 & n \\ n & 0 & 0 \end{bmatrix} \quad (6.33)$$

for a normally biased EMAT

$$D = \begin{bmatrix} 0 & \frac{-m}{2} & 0 \\ 0 & m & 0 \\ 0 & \frac{-m}{2} & 0 \\ 0 & 0 & n \\ 0 & 0 & 0 \\ n & 0 & 0 \end{bmatrix} \quad (6.34)$$

for a magnetostrictive EMAT

Where $m = d_{22} = \left[\frac{\partial \varepsilon}{\partial H}\right]_{H_s}$ and $n = d_{61} = \frac{3\varepsilon}{H}$

Where m and n represents the two independent components of the piezomagnetic coefficients d_{22} and d_{61} respectively. d_{22} is related to the changing magnitude of strain while d_{61} relates to the changing orientation. The bias magnetic field generates the magnetic strain to a certain extent while the dynamic field makes the strain to oscillate around the static magnetostrictive strain. The two independent components of the piezomagnetic coefficient (*D*) to be fed into the model can be obtained as the slope of the experimental magnetostrictive strain curve. In calculating the stiffness coefficient to be imputed into the model reference compliance matrix (s) for structural steel was assumed [191].

6.3.2 Model implementation

The model was implemented using the AC/DC and structural mechanics module. A 2D axisymmetric model was obtain by discretising the model into 10353 triangular elements for NB EMAT and 10126 triangular elements for MS-EAMT as shown in Figs.6.7 (A and B) respectively, the strength of the field generated by the permanent magnet (NbFeB) employed is 750kAm^{-1}, the width and length of the pipe steel material are 0.5mm and 10mm respectively, the distance between the coil and the material (lift-off) is 0.5mm. An 8 cycle tone burst current shown in Fig.(6.5), with

centre frequency of 2MHz and peak to peak current amplitude ranging from 20-400A was used to drive the coil. The elastic properties used were the same for all grades of pipe steel employed; Young modulus 200 GPa, Poisson's ratio 0.33 and density 7850 Kgm^{-3}.

In the material domain within the skin depth, full magnetostrictive and Lorentz constitutive equation was employed to simulate the transduction process. An absorbing region with finite damping constant surrounds the elastic domain to avoid back scatter reflections from the boundary of the model.

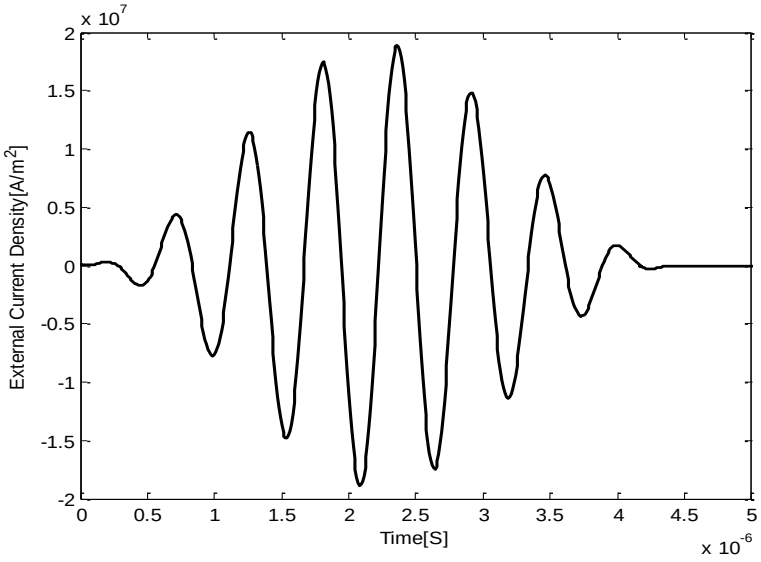

Fig.6.5: Time history of 8 cycle tone burst excitation current with centre frequency 2MHz.

The algorithm in Fig.(6.6) depicts how the model was implemented in COMSOL multiphysics. The model assumes that:

(a) The excitation coil is a homogenous current carrying domain where the individual wires are not resolved.
(b) The strain in the material is relatively small.
(c) The material properties of individual samples are isotropic.
(d) All material properties are constant over the operating range of magnetic field and stress.
(e) Effects of increase in temperature due to Joule heating are not included.

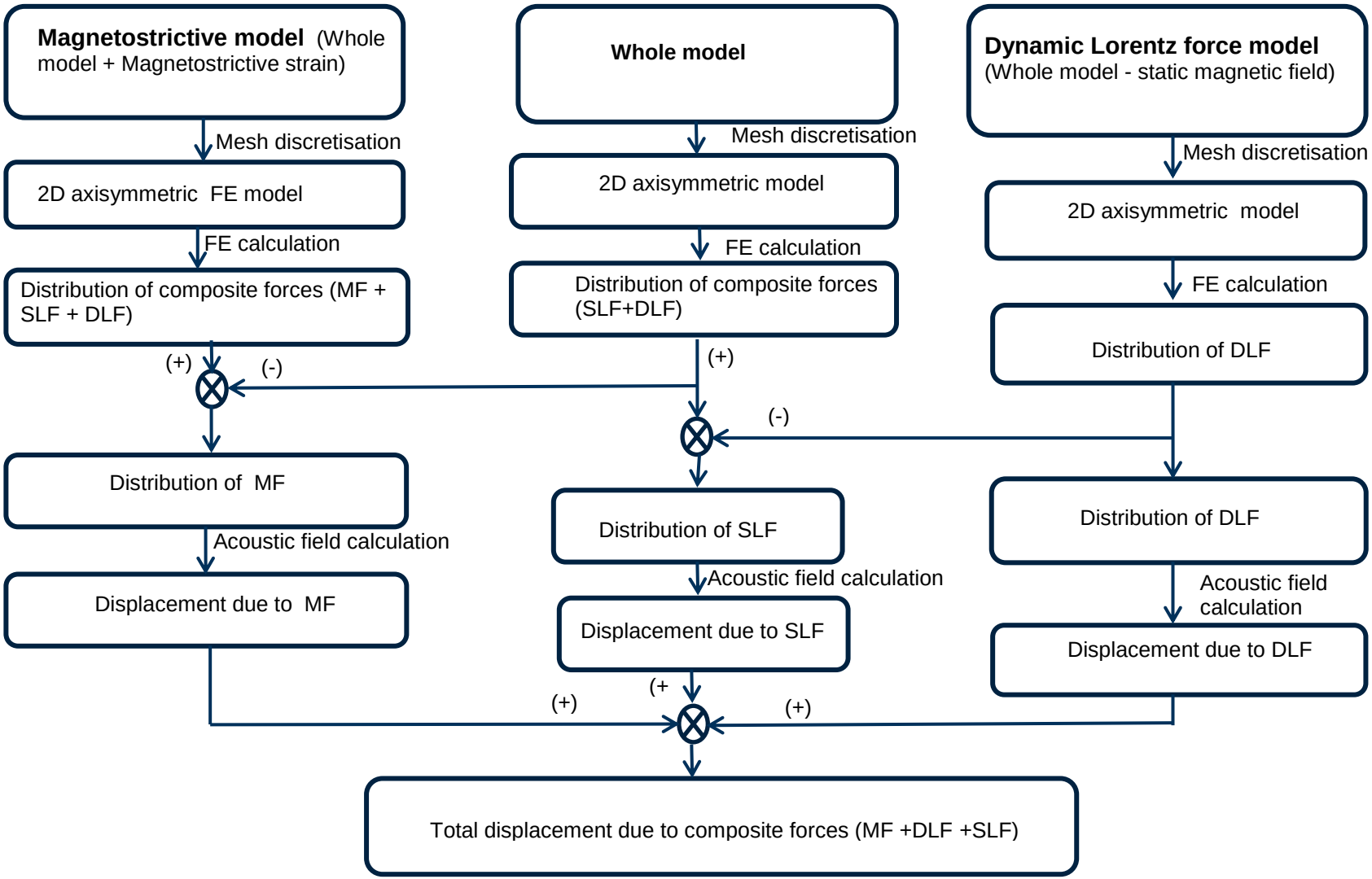

Fig.6.6 Novel modelling technique to decouple and quantify particle displacement due to various transduction forces.

To obtain the distribution of the transduction mechanism at various excitation current for NB and MS EMATs, the following steps (depicted in Fig.6.6) were carried out:

STEP 1:

(a) Run the MS and NB models with full magnetostriction and Lorentz parameters using a driving current ranging from 20-400A for all five grades of pipe steel.
(b) Obtain the particle displacement due to the combined transduction mechanism using the point probe plot parameter in Comsol multiphysics.
(c) Obtain the peak-peak value of the displacement amplitude for the conditions in step 1(a). The result gives the particle displacement due to magnetostrictive force (MF), SLF and DLF for the EMAT configuration under investigation.

STEP 2:

Repeat the procedure in step 1 but this time disabling the magnetostrictive parameters in the structural mechanics model. The result gives the value of the displacement amplitude due to the SLF and DLF alone.

STEP 3:

Repeat the procedure in step 2 but with the permanent magnet domain in the magnetic field module disabled. The result obtained gives the value of the displacement amplitude due to DLF.

Likewise the difference between the value of the displacement amplitude obtained in step 1 and step 2 gives the value of the particle velocity due to MF.

The difference between the values of the displacement amplitude between step 2 and 3 gives the value of particle displacement due to SLF. Step 3 gives the value of the particle displacement due to DLF.

The result of a typical finite element simulation for both (MS and NB) EMAT configuration is shown in Figures 6.8 (A and B). The value of the displacement

amplitude produced by each of the models on the pipe steel material was obtained by means of a point probe tool incorporated in the software. Figures 6.9 (A) and (B) shows an example of the value of the displacement amplitude for an NB and MS EMATs respectively at 20A excitation current. These values are plotted against various excitation currents to obtain the CEC for both the NB and MS EMAT configurations under investigation.

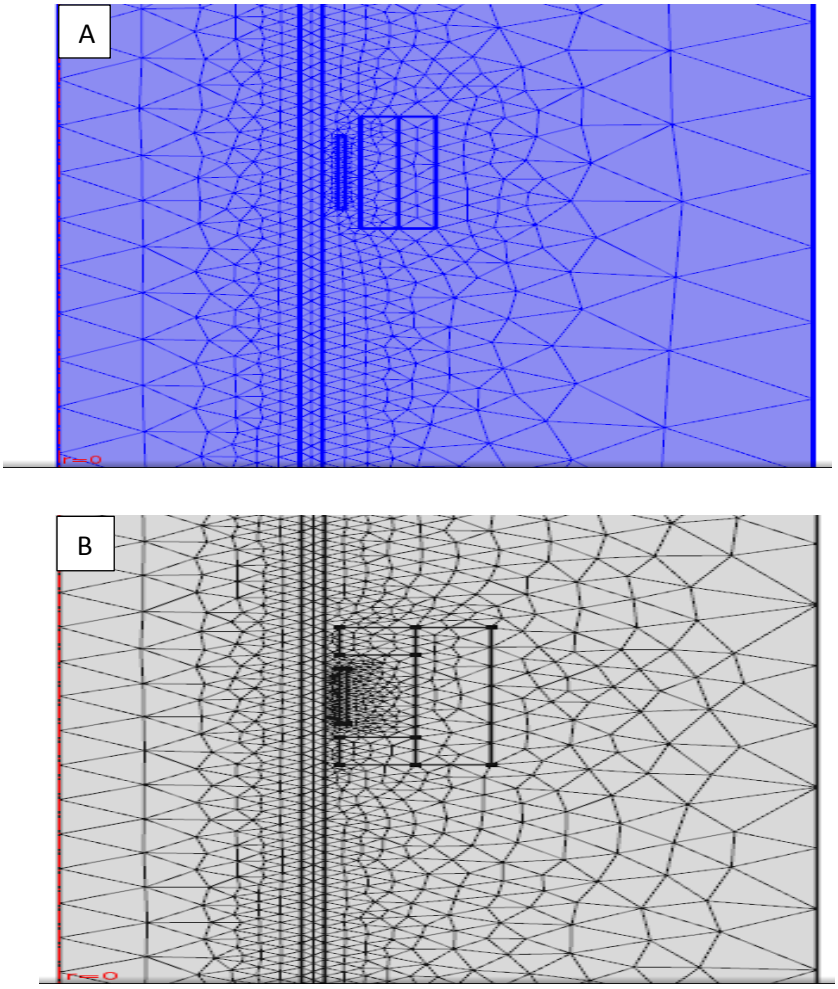

Fig.6.7: Finite Element mesh (A) Normally biased model with 10353 triangular elements. (B) Magnetostrictive EMAT model with 10126 triangular elements

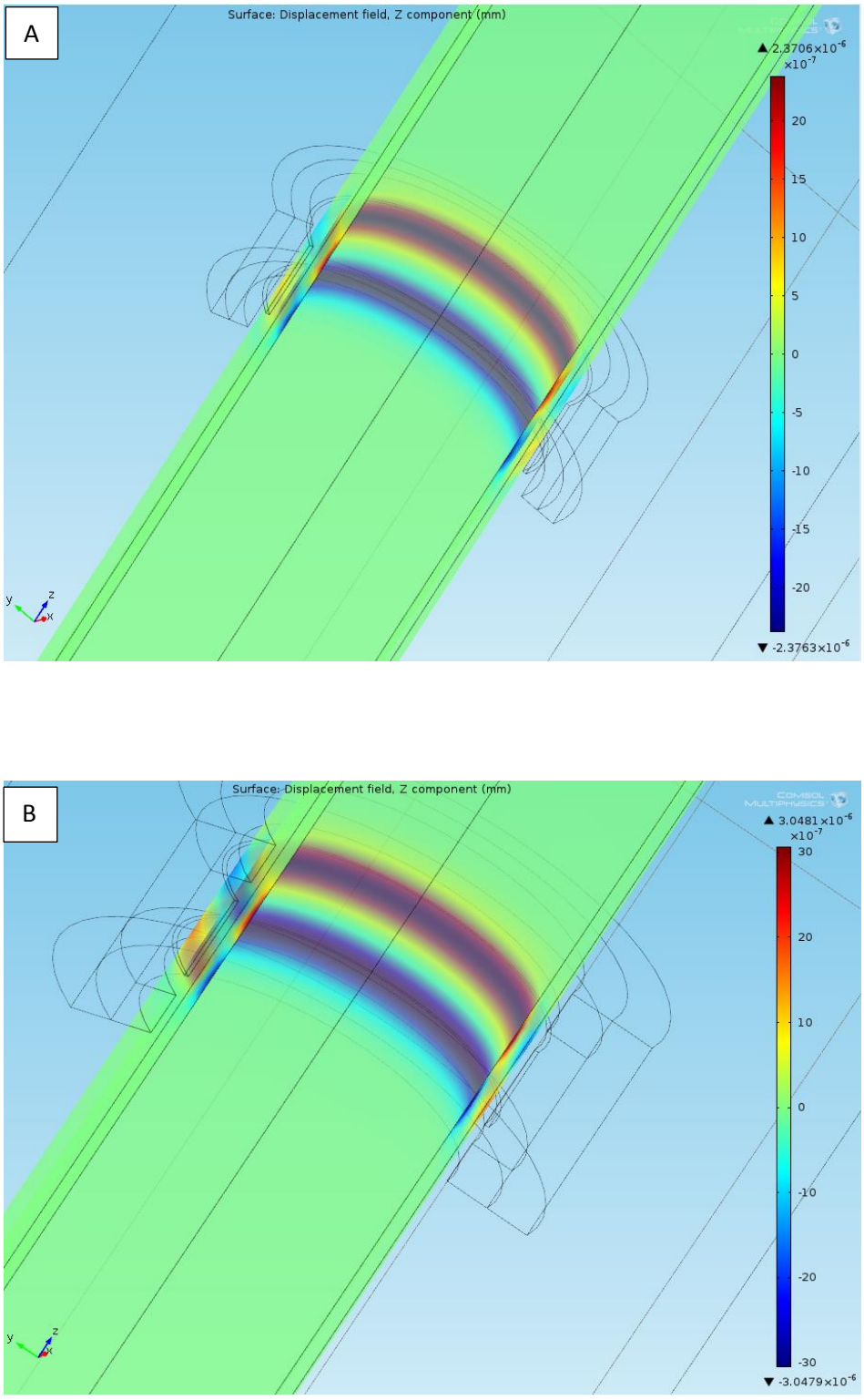

Fig.6.8: Surface plot of the z component of the displacement field on pipe steel (CS70 grade). (A) NB-EMAT and (B) MS-EMAT.

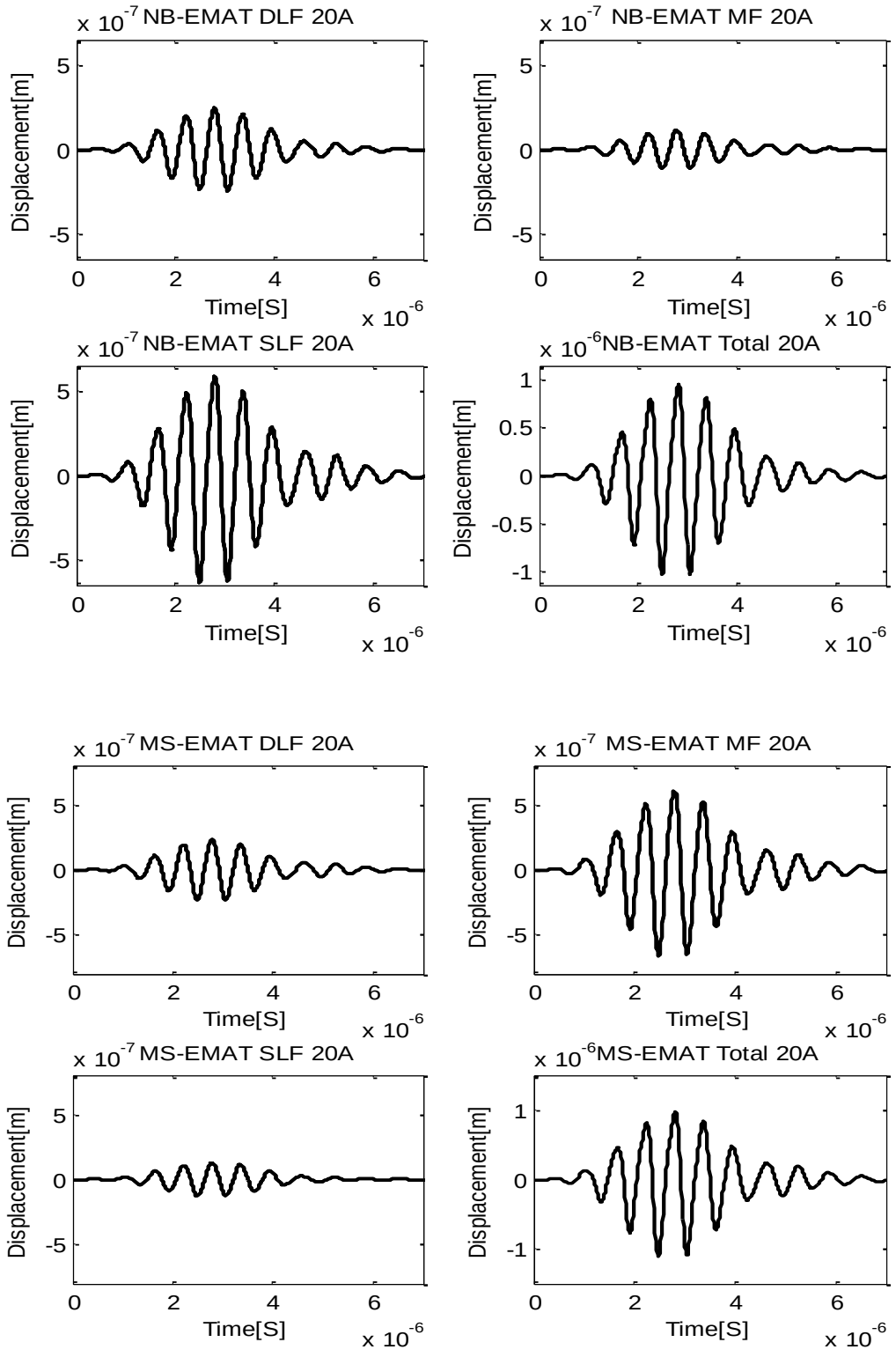

Fig.6.9: Time history of the transduction mechanisms at 20A on a CS70 grade of pipe steel. (A) *NB-EMAT, (B) MS-EMAT. The plot depicts the peak to peak value employed to compute the distribution of the transduction meachanisms*.

6.4 Results and Discussions

This section presents and intepret the distribution of transduction forces and the effect of Joule heating at elevated excitation current in the numerical model implemented in sections (6.3.1 and 6.3.2) for both the NB and MS EMATs.

6.4.1 Distribution of transduction forces in NB-EMAT

A typical plot of the particle displacement due to the transduction mechanisms with variation of excitation current from 20-400A for five grades of commonly used pipe steel is shown in Figs.(6.10-6.14). In the entire steel sample studied, prior to attaining critical excitation current as summarised in Table 6.3, SLF appears to be dominant, followed by the DLF while magnetostriction appears to be the least. This trend continues until at a certain excitation current, and it was observed that the DLF equals and becomes greater than the SLF. Also, a slight increase in the magnetostrictive force is observed, this is due to the effect of the radial component of the dynamic magnetic field. The current at which the particle displacement due to DLF equals that due to SLF for the purpose of the research is known as CEC.

Microscopically speaking, when the coil of the NB-EMAT is excited, the Eddy current is induced within the skin depth of the steel material, the dynamic and static field interacts with the Eddy current to generate the static and dynamic Lorentz force respectively. The third force involved in the generation of sound wave is the magnetostriction which is due to the tiny radial component (r) of the dynamic field [101].

$$\varepsilon_{rz} \propto \frac{3\varepsilon}{H_s} H_{dr} \tag{6.35}$$

Wang et al [82] also corroborated this fact when they observed that the x component of the dynamic magnetic field in a 3D EMAT simulation is very small compared to the z component. As the current is increased the z and r components of the dynamic magnetic field also increases proportionally, hence the observed slight increase in magnetostriction. The increase in the SLF observed even when the static

field is constant is due to the fact that the SLF is a vector product of the Eddy current and static magnetic field;

$$f_{s=} J_e \times H_s \tag{6.36}$$

Hence as the excitation current increases, the Eddy current induced in the material increases, thus the SLF increases proportionally.

The DLF is seen to increase exponentially, this due to the fact that it is a vector product of the dynamic field and the Eddy current;

$$f_{d=} J_e \times H_d \tag{6.37}$$

Therefore, any increase in the excitation current increases both the induced Eddy current in the material and also the dynamic magnetic field. Consequently, the frequency of the DLF is twice that of the SLF [82]. The percentage distribution of transduction mechanism of the NB EMAT on five grades of pipe steel is shown in Table (6.4).

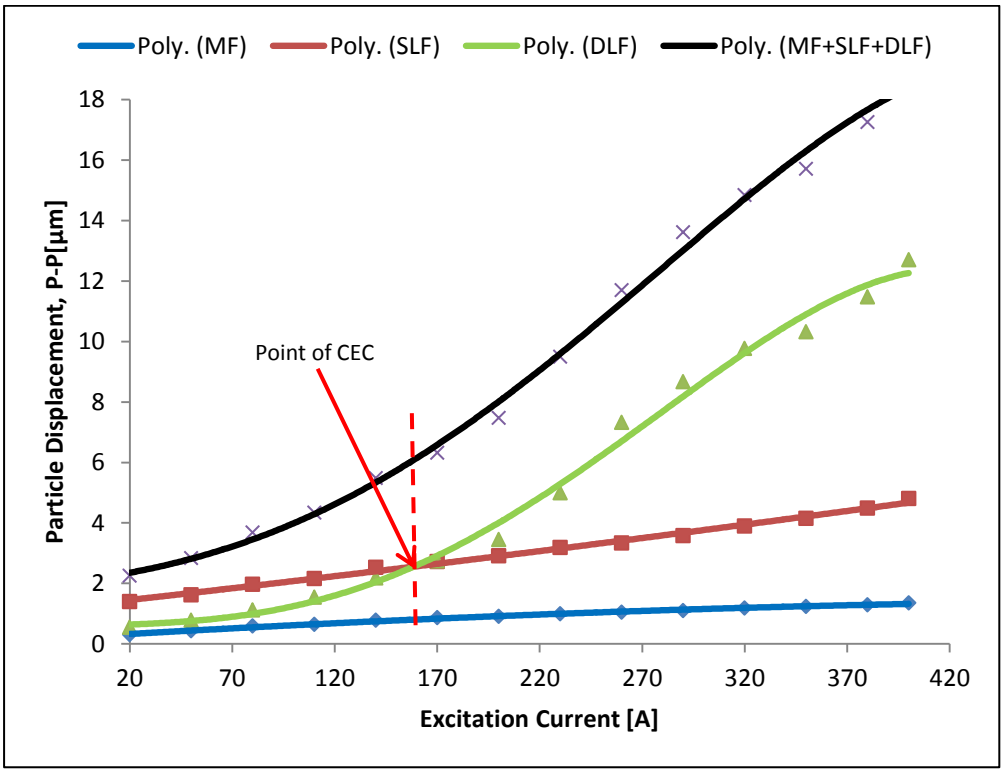

Fig.6.10: Distribution of the transduction forces of NB EMAT on TN80Cr3 grade of pipe steel.

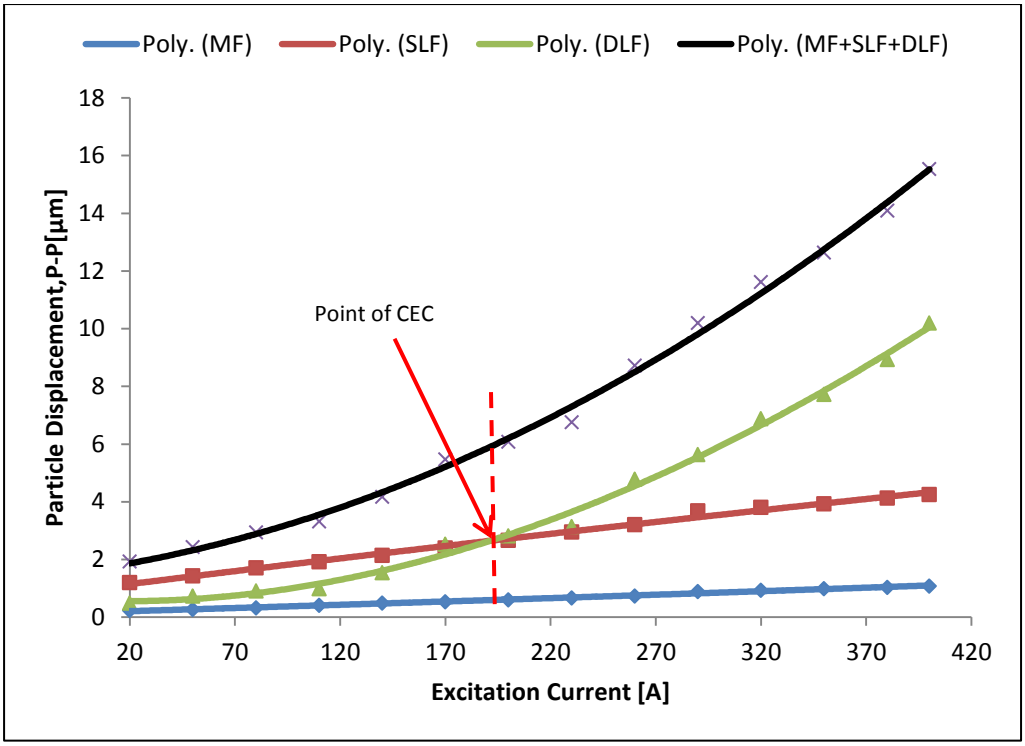

Fig.6.11:Distribution of the transduction forces of NB EMAT on CS70 grade of pipe steel.

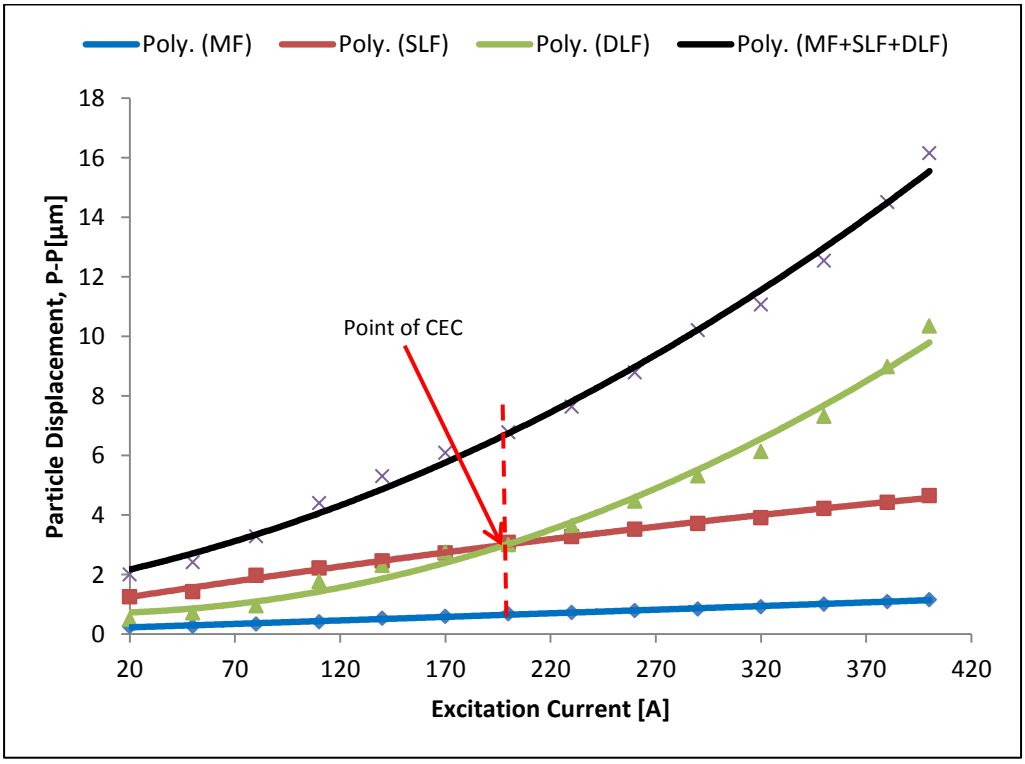

Fig.6.12: Distribution of the transduction forces of NB EMAT on J55 grade of pipe steel.

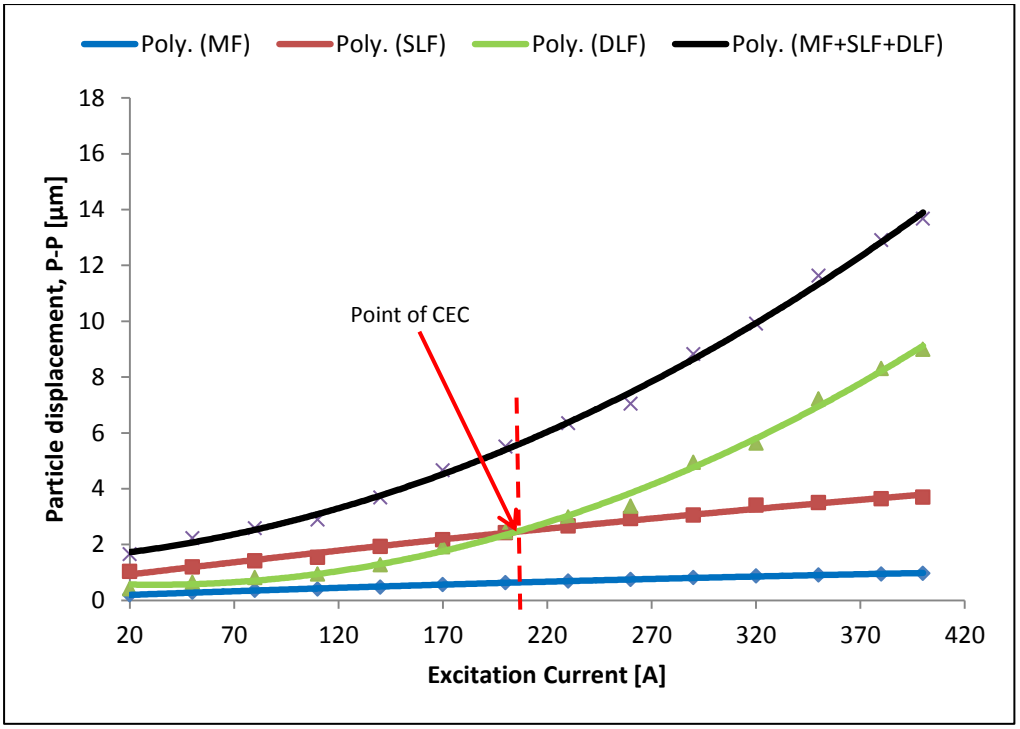

Fig.6.13: *Distribution of the transduction forces of NB EMAT on L80SS grade of pipe steel.*

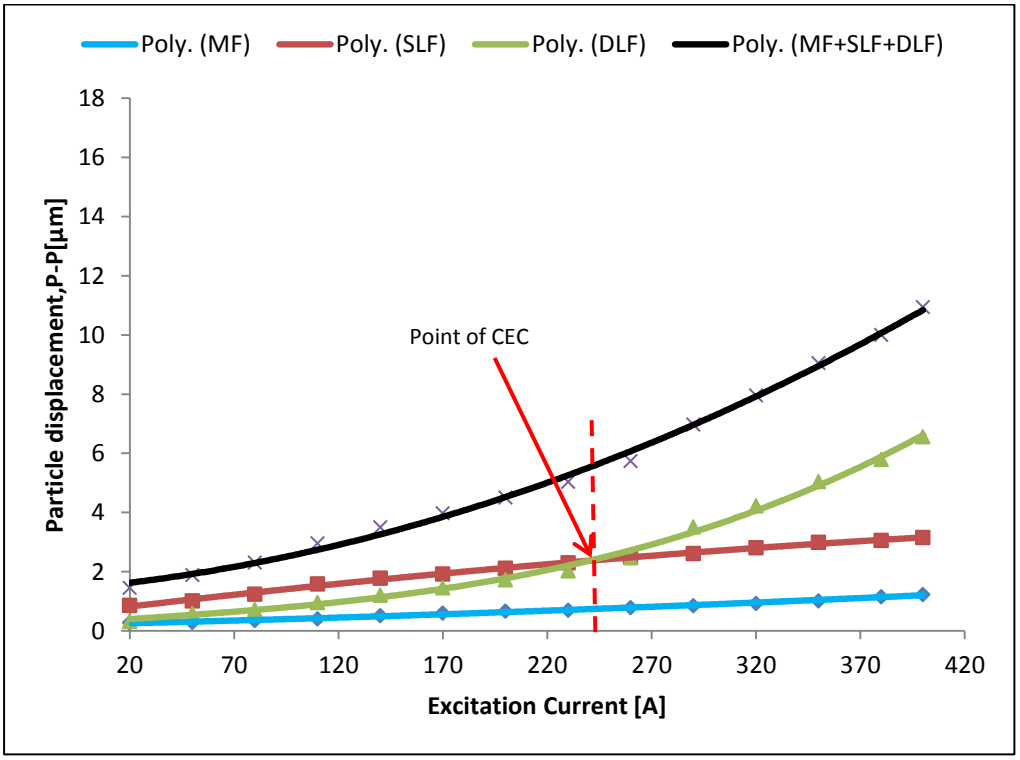

Fig.6.14: *Distribution of the transduction forces of NB EMAT on L80A grade of pipe steel.*

6.4.2 Distribution of transduction forces in MS- EMAT

As shown in Fig.(6.1B), the bias field in an MS EMAT is parallel to the surface of the material specimen; hence its mode of operation is slightly different from that of the NB-EMAT. The particle displacement plot for five grades of pipe steel (CS70, TN80Cr3, L80SS, L80A and J55) shown in Figs.(6.15-6.19),indicates clearly that prior to attaining critical excitation current, the magnetostrictive effect is dominant followed by the DLF and the least is the SLF. As the current is increased the dynamic magnetic field increases also, leading initially to positive strain on the material along the direction of the field. The deformation reaches a maximum and turns into a compressional strain and remains fairly constant at higher excitation current. The strain generated by the fields as shown in equation (6.35), vibrates the material causing the generation of sound wave. The particle displacement obtained in Fig.(6. 15-6.19) due to magnetostrictive strain is consistent with earlier work done by Thompson [88].

The particle displacement due to the DLF is seen to increase exponentially, this is due to the fact that it is a vector product of the dynamic field and the Eddy current as seen in equation (6.37); the increase continues until it becomes the dominant transduction mechanism beyond the critical excitation current.

The SLF shows a linear increase as the excitation current is increased, in all the pipe steel material studied even as the bias field is constant at 750 kAm^{-1}. This is due to the influence of the Eddy current. As the excitation current varies the eddy current also varies proportionally and since the SLF is a vector product of the Eddy current and the static field as shown in equation (6.36), a linear increase in the particle displacement due to SLF is observed. Table 6.3 shows the critical excitation current of both EMAT configurations.

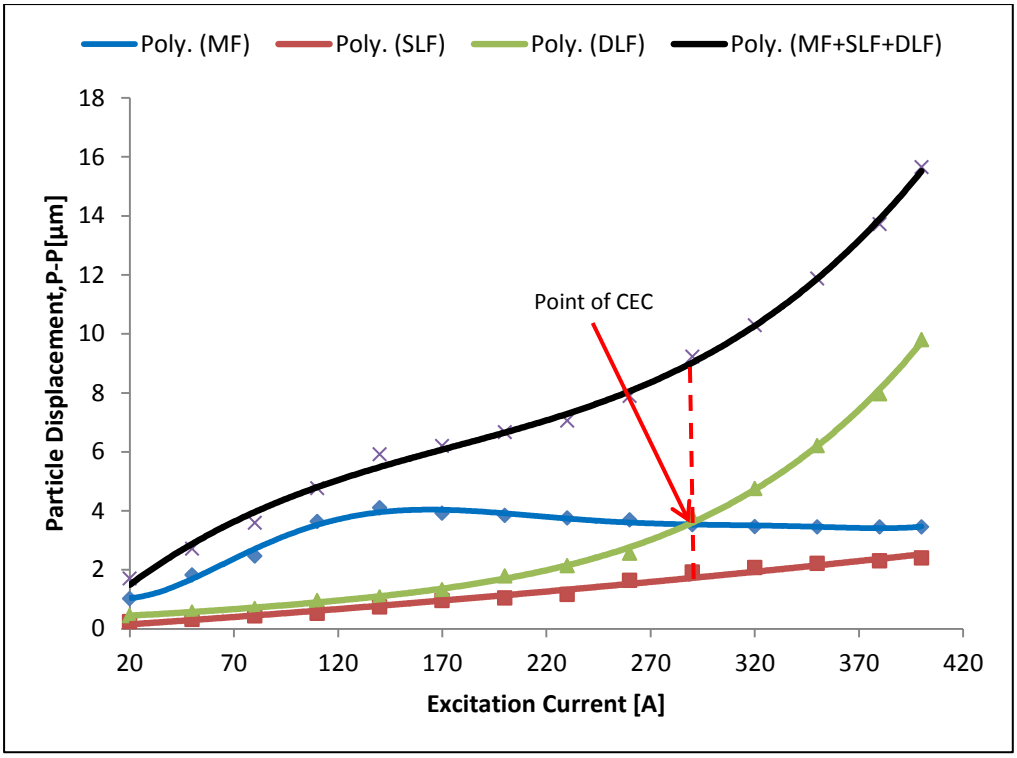

Fig.6.15: *Distribution of the transduction forces of MS-EMAT on TN80Cr3 grade of pipe steel.*

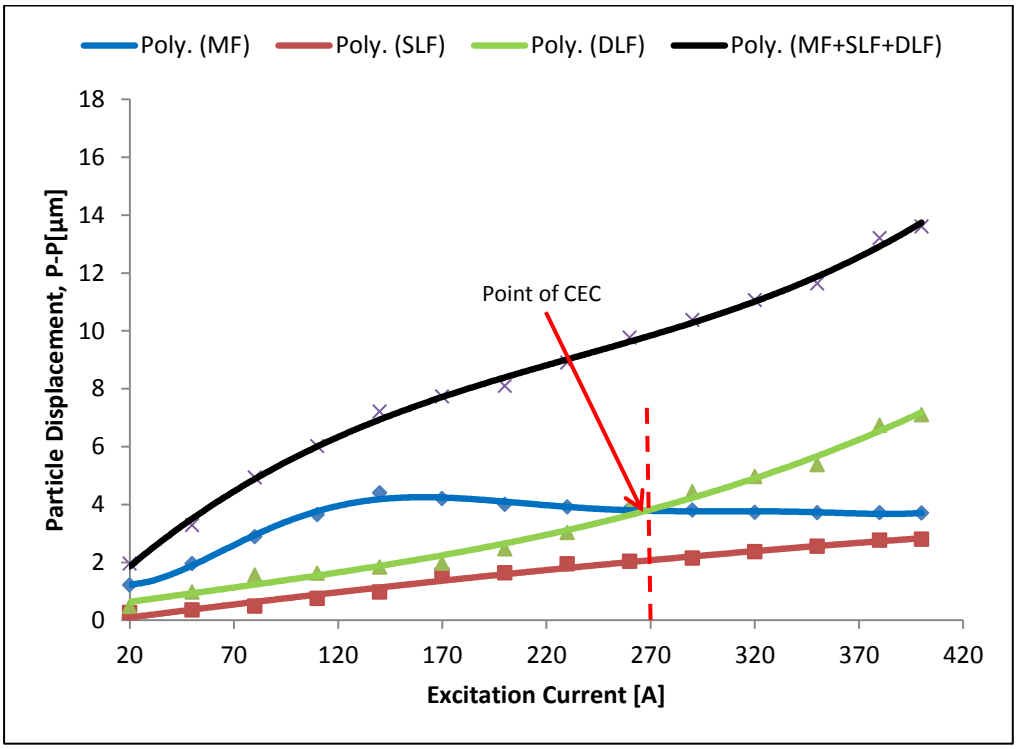

Fig.6.16: *Distribution of the transduction forces of MS-EMAT on CS70 grade of pipe steel.*

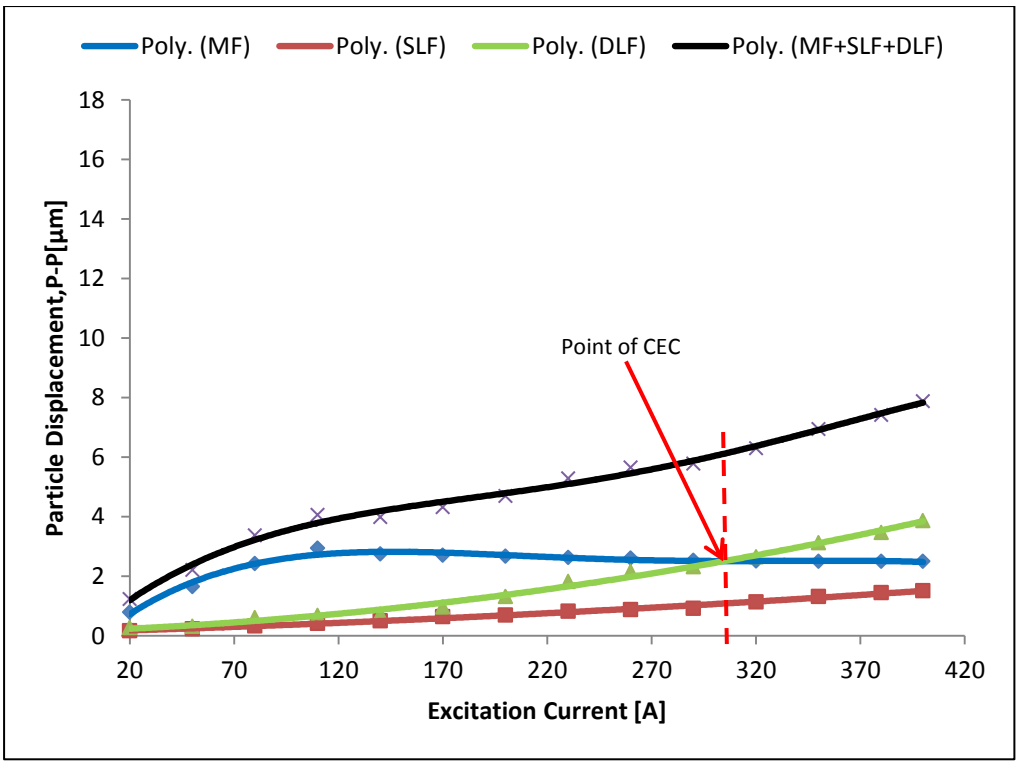

Fig.6.17: *Distribution of the transduction forces of MS-EMAT on J55 grade of pipe steel.*

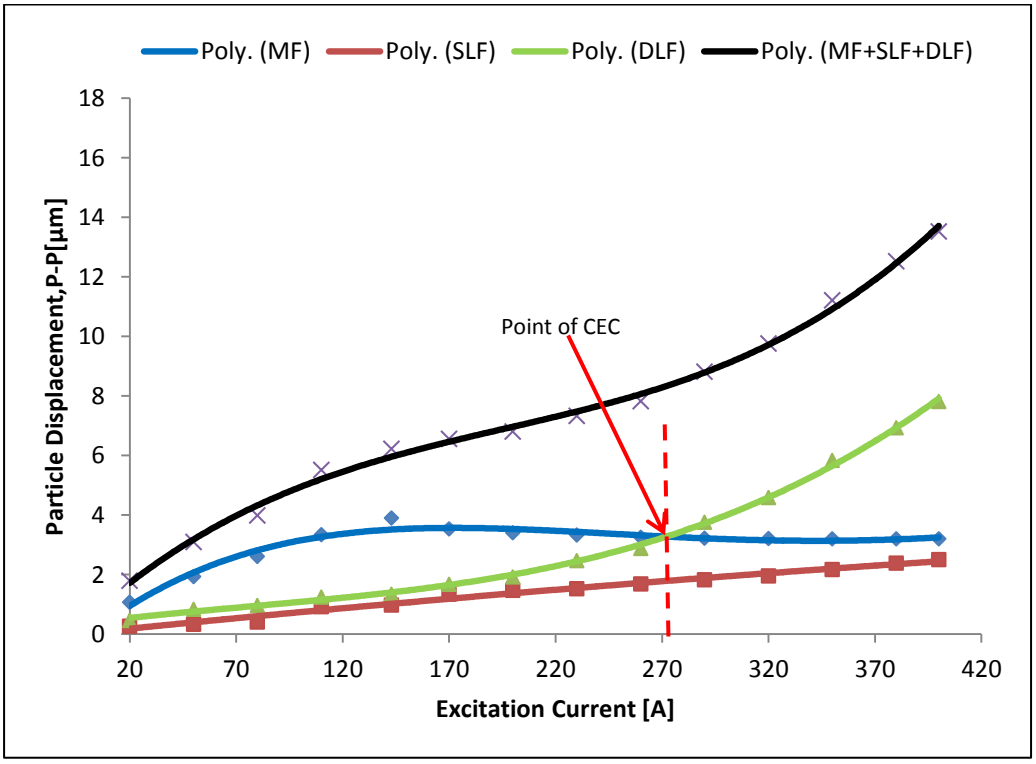

Fig.6.18: *Distribution of the transduction forces of MS-EMAT on L80SS grade of pipe steel.*

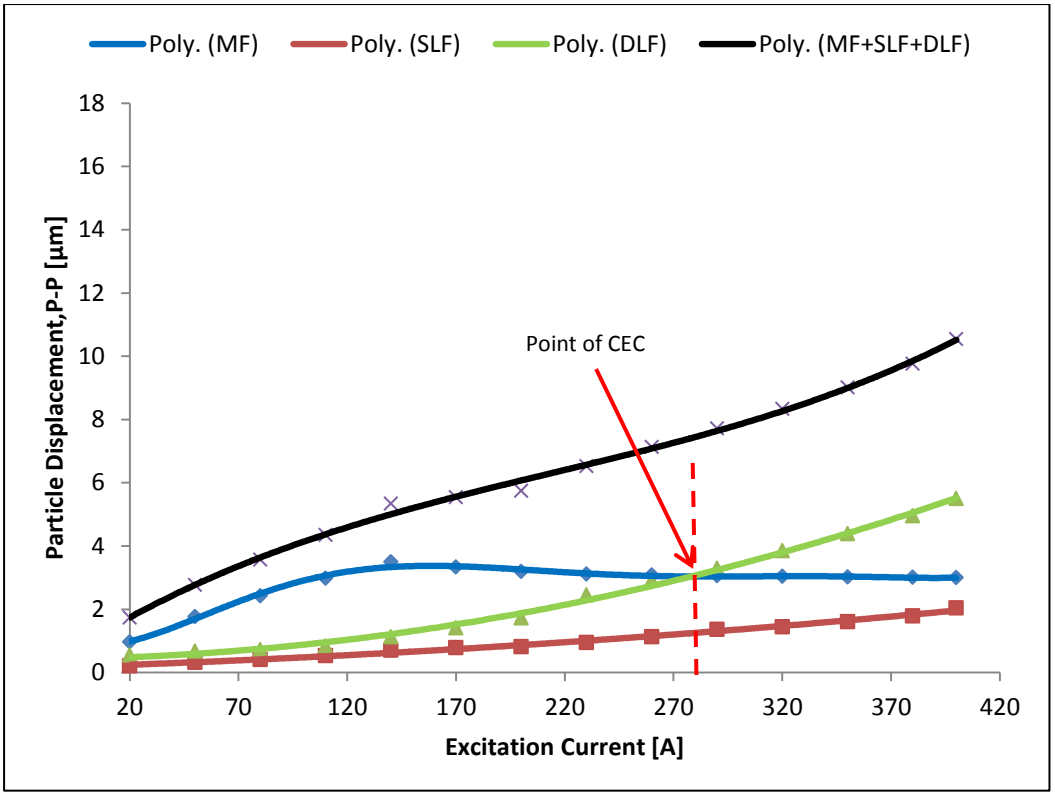

Fig.6.19: *Distribution of the transduction forces of MS-EMAT on L80A grade of pipe steel.*

Table 6.3: Relationship between relative permeability, conductivity and critical excitation current for NB and MS EMAT.

Pipe steel material	Relative permeability	Conductivity (Sm^{-1})	Critical Excitation Current (A)	
			MS EMAT	NB EMAT
CS70	59	3.77×10^{6}	268	190
L80SS	67	4.19×10^{6}	274	205
L80A	70	4.54×10^{6}	279	240
TN80Cr3	87	2.61×10^{6}	290	160
J55	137	4.06×10^{6}	305	200

6.4.3 Comparison of the CEC for MS and NB EMAT configurations

The result, in Fig.(6.20) shows the comparison of the minimum electrical energy required by both EMAT configurations to generate sound waves efficiently using solely the DLF mechanism for five grades of pipe steel. It is observed that more current or energy is required by the MS-EMAT to attain the critical excitation current, hence the NB-EMAT is more efficient in generating sound wave solely by the dynamic Lorentz force mechanism.

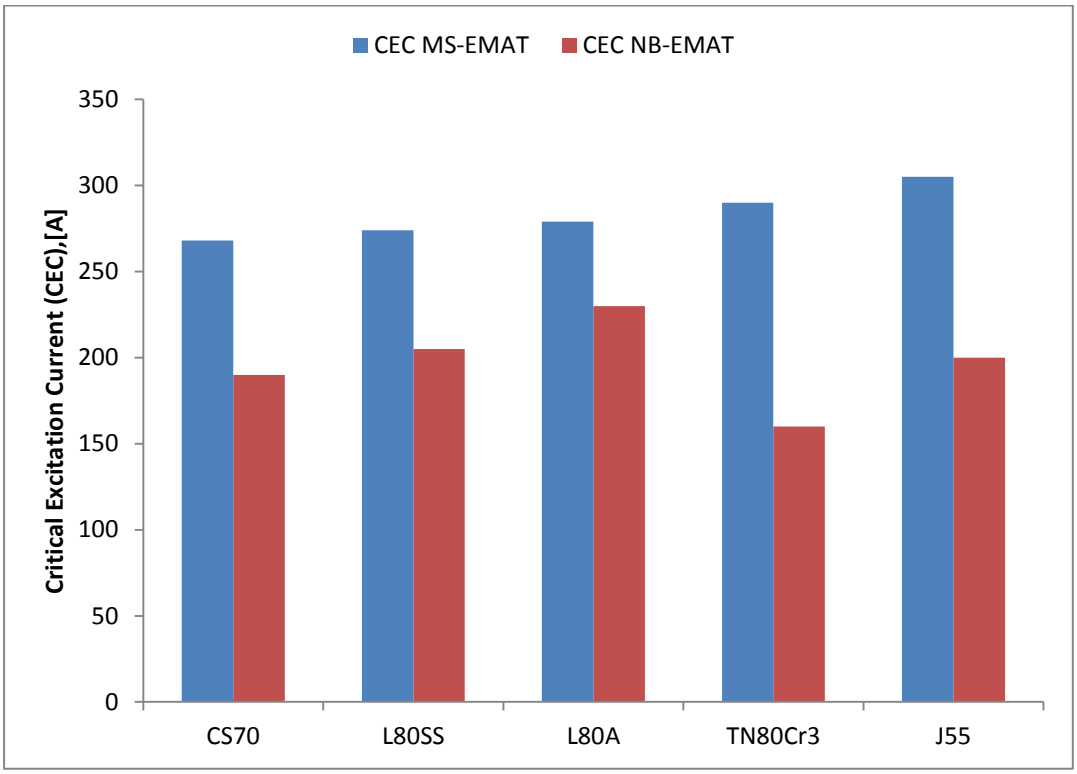

Fig.6.20: Comparison of the Critical Excitation Current (CEC) for MS and NB-EMATs.

Table 6.4: Percentage contribution of the transduction forces to acoustic wave generation at various excitation current on five grades of pipe steel materials for both NB and MS EMAT configurations.

		PERCENTAGE PARTICLE DISPLACEMENT					
		MAGNETOSTRICTIVE FORCE (MF)		DYNAMIC LORENTZ FORCE (DLF)		STATIC LORENTZ FORCE (SLF)	
		NB- EMAT	MS-EMAT	NB-EMAT	MS-EMAT	NB- EMAT	MS- EMAT
EXCITATION CURRENT (20A)	CS70	12.2	62.4	25.5	24.0	62.3	13.6
	L80SS	12.1	59.4	25.3	25.6	62.7	15.0
	L80A	19.0	55.9	22.1	31.7	59.0	12.4
	TN80Cr3	13.3	59.7	24.1	26.3	62.2	14.0
	J55	12.7	63.7	24.8	22.6	62.5	13.7
EXCITATION CURRENT (140A)	CS70	11.8	61.1	36.9	25.5	51.3	13.5
	L80SS	13.0	62.7	34.7	21.5	52.3	15.8
	L80A	14.6	65.5	34.6	21.2	50.8	13.3
	TN80Cr3	14.2	69.3	39.7	18.2	46.1	12.5
	J55	10.1	68.9	43.5	18.3	46.4	12.8
EXCITATION CURRENT (260A)	CS70	8.4	39.4	54.8	39.8	36.8	20.8
	L80SS	10.6	41.6	47.8	36.8	41.6	21.6
	L80A	13.7	43.2	43.1	41.0	43.2	15.9
	TN80Cr3	8.9	46.8	62.6	32.5	28.5	20.8
	J55	9.1	46.2	50.8	38.2	40.1	15.6
EXCITATION CURRENT (400A)	CS70	7.0	27.2	65.7	52.2	27.4	20.6
	L80SS	27.1	23.7	65.8	57.8	27.1	18.5
	L80A	11.2	28.5	60.0	52.2	28.8	19.4
	TN80Cr3	7.2	22.1	67.4	62.6	25.5	15.3
	J55	7.2	31.7	64.1	49.1	28.8	19.2

6.4.4: The Effect of Joule heating on the excitation coil at elevated excitation current.

The temperature profile of the EMAT coil driven with an excitation pulse ranging from 100–500A and at a duration of up to 10µs is shown in Fig.6.21. The result was obtained using the Joule Heating module of Comsol multiphysics. As observed in the plot, with reference temperature of 293^0K the maximum temperature rise at 500A is 0.9^0K. This implies that due to the short pulse duration, very small amount of energy is consumed, even at high current. Transmitting power circuits working in parallel and with the improvement in semiconductors, the amplitude of the excitation current can be increased. An excitation current of 300A at 500 KHz has been demonstrated in [82] by applying a tone burst signal on a narrow band meander line coil. Higher current amplitude up to 500A can also be achieved using single pulse excitation.

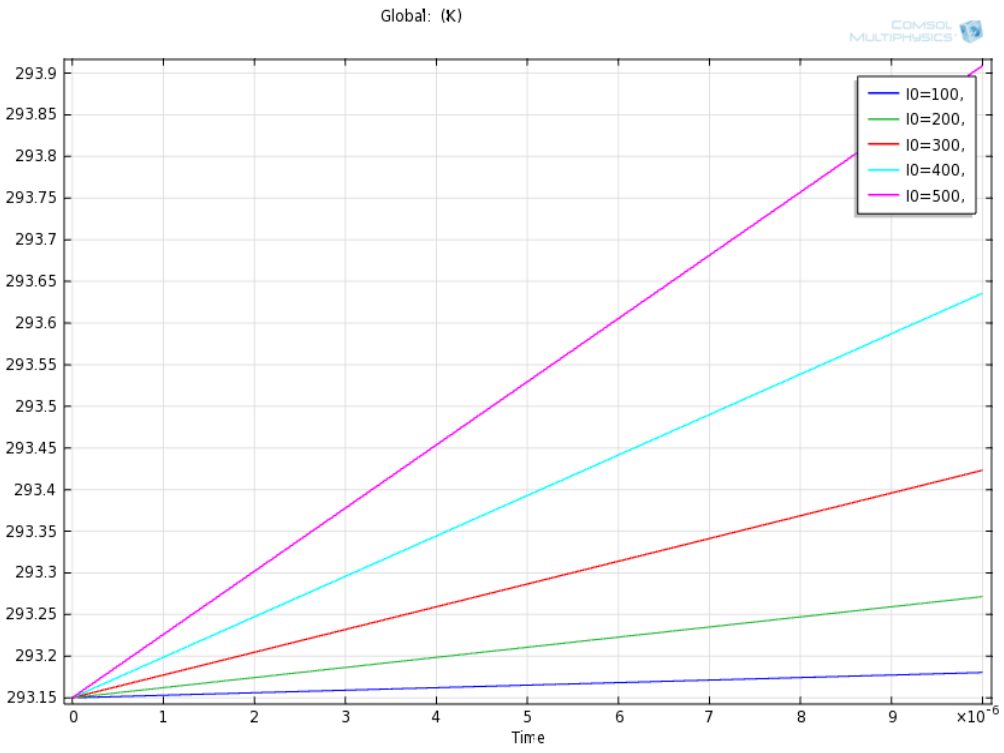

Fig.6.21: Time history of the heat flux (in Kelvin) generated by the KT EMAT coils at a peak to peak pulse excitation current ranging from 100-500A.

6.5 Summary

This research has established that when NB EMATs are used on pipe steel material, the transduction mechanisms in operation are the MF, SLF and DLF. In all the pipe steel material investigated, the SLF was found to be dominant prior to attaining the CEC, while the DLF was the dominant mechanism afterwards as seen in Figures (6.10 – 6.19). In MS EMAT, the dominant transduction mechanism prior to attaining the CEC is the MF, while the DLF became the dominant mechanism afterwards. Table 6.4, also shows the percentage particle displacement due to the three transduction mechanisms on the various pipe steel materials at a peak to peak pulse driving currents of 20A, 140A, 260A and 400A.

The overall implication of this work is that beyond the CEC where the DLF dominates, EMATs can operates solely on coils eliminating the problem of using magnets on steel materials and also the structure of EMAT can be miniaturised and made more compact and robust for measurement in difficult and high temperature environment.

Furthermore, the research has established quantitatively for both the NB and MS EMATs configuration, the value of the minimum excitation current required to generate acoustic wave efficiently by employing only the dynamic Lorentz force mechanism, on five grades of pipe steel.

In general, the research has established that, the NB EMAT require less current (electrical energy) to reach its CEC than the MS EMAT. This can be interpreted to mean that at higher excitation current, the NB EMAT tends to be more efficient than the MS EMAT in generating acoustic wave on steel material.

CHAPTER 7

CONCLUSION AND FUTURE WORK

7.1 Thesis review

In this research, the general operation of EMAT has been investigated through the development of numerical models. Chapter 1 gave a brief overview of some popular NDT methods used in the industries. This was followed by a comprehensive review of previous work done in the field of EMATs (the main subject of this Thesis) in Chapter 2. The review showed that the field of EMAT is an active research area as much research has been carried out in the modelling and optimization of the transducer. Most research on EMAT focused on the Lorentz force mechanisms while other important transduction phenomena like magnetostriction were only included in the ideal analytical models. Furthermore, the review showed that most research carried out on EMAT (Ribichini et.al. and Dixon et.al) lumped the Lorentz forces (DLF and SLF) together for easy analysis. This is not correct as in the ideal case the two Lorentz forces are produced by different mechanisms and they play different roles in the generation of acoustic waves by EMATs. This observation led to the development of a numerical model implemented in COMSOL Multiphysics and used as a prediction tool for arbitrary EMAT configurations. The theoretical basis for this model was described in Chapter 3, where the relevant equations that describe the physics of the transduction mechanisms involved in the process of generating, transmitting and reception of acoustic waves by EMAT were presented. The actual implementation of the governing electrodynamic equations in COMSOL Multiphysics was described in Chapter 4. Here the 2D model was used to study and compare the Lorentz force and Eddy current density generated by various EMAT coil configurations (i.e. ML, SP and a novel KT coil). The model was also used in section 4.4 to study performance of the novel KT EMAT on CS70 grade of pipe steel material by varying some key EMAT parameters and observing the density of Lorentz force generated. This was followed by the study of the generation, propagation and detection of acoustic wave by the KT EMAT configuration using coupled mechanical model in Chapter 5. The

effectiveness of the coupled mechanical model was also confirmed by comparing its predictions with the results from analytical (bench mark) models and experimental tests. The predictions of single numerical models such as Eddy current, static magnet field and ultrasonic models respectively were compared with the results of the analytical models, whilst the predictions of the coupled multiphysics model was compared with experimental results (particle velocity of the acoustic wave) by varying some key EMAT parameters such as excitation current, excitation frequency and static magnetic field. The analytical and experimental results show good agreement with the numerical result with an average discrepancy less than 9%.

The validated model was used with relevant modification in Chapter 6 to study the transduction mechanisms (SLF, DLF and MF) of both NB and Ms EMAT configuration for five grades of pipe steel material. This was achieved by introducing the effect of magnetostriction in the model and developing a special algorithm (see section 6.3.2) to decouple and quantify the various transduction forces that gives rise to the generation of acoustic wave in EMAT. The magnetostrictive parameters were obtained experimentally (see section 6.3) and used as an input in the model to account for the magnetostrictive force.

Furthermore, in comparison to other researches carried out in this field especially the research conducted by Remo Ribichini at Imperial College, this research:

(a) Developed and studied numerically a novel KT EMAT configuration that combines the structure of a spiral coil and the current part of a meanderline coil EMAT configurations respectively to generate high amplitude of radially polarised Rayleigh and bulk waves.
(b) Developed a comprehensive numerical EMAT model for the NB and MS EMAT that incorporated magnetostrictive effect inherent when EMAT is used on pipe steel. The model use to study characterise the transduction mechanisms of various EMAT configuration
(c) Developed a novel algorithm to decouple the major transduction forces in operation when NB EMATs and MS EMATs are used on various grades of pipe steel materials.

(d) Numerically characterise the transduction forces when both NB and MS EMATs respectively are driven with higher excitation current ranging from 20-400A on pipe steel materials.

(e) The experimental work in this research was used to validate the numerical model developed to study the generation, transmission and detection of ultrasonic waves on CS70 grade of pipe steel material.

Finally, one weakness of this research in comparison to others in this field is that the research is centred on numerical modelling with the only experimental work being model validation and determination of the magnetostrictive parameters used as input in the coupled magnetostrictive model. Whilst other works especially the work of Remo Ribichini; apart from also developing a numerical model and validating it experimentally, investigated and compared qualitatively, the performance of some EMATs configuration for shear horizontal wave and bulk shear wave generation like the Periodic Permanent Magnet and nickel strip bonded/unbonded magnetostrictive EMATs respectively, on some structural steel materials (EN32B, EN3, BO1 and EN24). The author had private communication with Dr. Ribichini to access his model for comparison with the model presented in this thesis but unfortunately it was not available due to commercial confidentiality.

7.2 Suggestions for future work

The FE model developed in this thesis can only solve EMAT problems in 2D; this was due to the limitations of the computer processor and the commercial software COMSOL multiphysics. The 2D model has 9000 to 11000 triangular elements, which is close to the limit of 8 Giga-bytes RAM. With the availability of high processing computers (grid computing), a more realistic 3D model of EMAT can be achieved with a different commercial software known as FLUX™ developed by Cedrat of Grenoble, France. The 3D model has the capacity to provide more accurate results and increase the understanding of EMAT system, though with a risk of increasing the complexity of the EMAT model which will include all the components of a practical EMAT such as the magnet, coils, back plate and casing. The 3D model if successfully

developed can be extended to study the transduction efficiency of other EMAT configurations.

With the improvement of power electronics, a more robust pulser/receiver power supply can be developed to harness the advantage of EMAT generating acoustic wave more efficiently at higher excitation current (see section 6.4.1 to 6.4.4). At present the conventional EMAT system is driven by RYTEC pulser/receiver unit that can give up to 50A peak to peak tone burst supply. This research has shown that at high current of about 150-400A peak to peak, EMAT generates acoustic wave by DLF mechanism more efficiently and not much energy is consumed by the system since the duration of the excitation current is in micro seconds (see section 6.4.5). Presently, the amplitude of the driving current is enhanced by connecting the transmitting circuits in parallel.

Further investigation should be conducted to ascertain the relationship between the CEC and the electrical and magnetic properties of pipe steel materials. This should be extended to other ferromagnetic materials.

There is also a need to investigate and develop a miniaturised KT EMAT using MEMS technology to be used in a novel integrated metrology instrument to detect defects and measure the thickness of conducting fibres when coating hundreds of metres of fibre used in the manufacture of superconductors for energy storage. The miniaturised KT EMAT system will use a non-contact transduction mechanism to probe the thickness of the deposited layers and detect defects such as bubbles, cracks and beads. This will ensure that the super-capacitors are manufactured with uniform layer thickness and free of defects in order to predict the performance of the energy storage and to reduce material wastage.

The need to develop a miniaturised EMAT that can be used in a high temperature environment which does not require the use of permanent magnet cannot be overemphasized. The KT EMAT configuration presents a good start in this direction since it can be easily stacked in layers to produce higher amplitude of acoustic wave and by exploiting the DLF mechanism which the KT EMATs configuration produce more efficiently at high excitation current. An EMAT system that does not incorporate a permanent magnet eliminates the problem of mobility when they are

used on ferromagnetic materials and can be used in an environment with temperature higher than the Curie temperature of rare earth magnets (i.e. greater than 400^0C).

Finally, further research should be carried out to adapt the KT EMAT for measurements on circular structures like pipes. This can be achieved by creating an array of KT EMATs in ring form around the pipe structure to generate torsional wave mode that can propagate circumferentially along the pipe.

APPENDIX A.1

Derivation of equation for the magnetic vector potential (MVP)

A detailed derivation of the MVP equation as a function of current densities is presented. The current densities are defined as a function of the displacement vector.

Substituting equation 3.14 into 3.13, we obtain

$$S = \begin{bmatrix} S_1 \\ S_2 \\ S_3 \\ S_4 \\ S_5 \\ S_6 \end{bmatrix} = \begin{bmatrix} \frac{\partial}{\partial x} & 0 & 0 \\ 0 & \frac{\partial}{\partial y} & 0 \\ 0 & 0 & \frac{\partial}{\partial z} \\ 0 & \frac{\partial}{\partial z} & \frac{\partial}{\partial y} \\ \frac{\partial}{\partial z} & 0 & \frac{\partial}{\partial x} \\ \frac{\partial}{\partial y} & \frac{\partial}{\partial x} & 0 \end{bmatrix} \begin{bmatrix} u_x \\ u_y \\ u_z \end{bmatrix} = \begin{bmatrix} \frac{\partial u_x}{\partial_x} \\ \frac{\partial u_y}{\partial_y} \\ \frac{\partial u_z}{\partial_z} \\ \frac{\partial u_y}{\partial_z} + \frac{\partial u_z}{\partial_y} \\ \frac{\partial u_x}{\partial_z} + \frac{\partial u_z}{\partial_x} \\ \frac{\partial u_x}{\partial_y} + \frac{\partial u_y}{\partial_x} \end{bmatrix} \quad \text{(A.1.1)}$$

Let the magnetostrictive field intensity vector be given as

$$\vec{H}_{MS} = \overrightarrow{vB}_{MS} \quad \text{(A.1.2)}$$

Multiplying both sides of equation 3.9 by $v = \frac{1}{\mu}$ gives

$$\vec{H}_d = v\vec{B}_d + \vec{M}_0 \nabla.\vec{u} - \vec{H}_{MS} \quad \text{(A.1.3)}$$

Where v is the inverse of the permeability matrix μ.

Taking the curl of both sides of (A.1.3) yields

$$\nabla \times \vec{H}_d = \nabla \times \overrightarrow{vB}_d + \nabla \times (\vec{M}_0 \nabla.\vec{u}) - \nabla \times \vec{H}_{MS} \quad \text{(A.1.4)}$$

Substitute equation (3.15) into the right side of equation (A.1.4) and combining it with equation (3.6) to give

$$\nabla\times(v\nabla\times\vec{A})+\nabla\times(\vec{M}_0\nabla.\vec{u})-\nabla\times\vec{H}_{MS}=\vec{J} \quad \text{(A.1.5)}$$

Substituting equation (3.15) into equation (3.2) and cancelling the curl operator yields

$$\vec{E}=-\frac{\partial\vec{A}}{\partial t}+\vec{E}_s \quad \text{(A.1.6)}$$

Where $\vec{E}_s$ is an unknown constant which can be computed as a function of the MVP.

Substituting equation (A.1.6) into equation (2.8) yields

$$\vec{J}=-\sigma\frac{\partial\vec{A}}{\partial t}+\vec{J}_s+\sigma\frac{\partial\vec{u}}{\partial t}\times\vec{B}_0 \quad \text{(A.1.7)}$$

$\vec{J}_s=\sigma\vec{E}_s$ and is known as the source current density (SCD).

Substituting the expression $\vec{E}_s=\frac{1}{\sigma}\vec{J}_s$ into equation (A.1.6) yields

$$\vec{E}=-\frac{\partial\vec{A}}{\partial t}+\frac{1}{\sigma}\vec{J}_s \quad \text{(A.1.8)}$$

Substituting equation (A.7) into equation (A.5) gives

$$\nabla\times(v\nabla\times\vec{A})=-\sigma\frac{\partial\vec{A}}{\partial t}+\vec{J}_s+\sigma\frac{\partial\vec{u}}{\partial t}\times\vec{B}_0-\nabla\times(\vec{M}_0\nabla.\vec{u})+\nabla\times\vec{H}_{MS} \quad \text{(A.1.9)}$$

The Eddy current density, $\vec{J}_e$, Lorentz current density, $\vec{J}_L$, magnetisation current density, $\vec{J}_M$, and magnetostrictive current density, $\vec{J}_{MS}$ for a 2D EMAT model can be defined as:

$$\vec{J}_e=-\sigma\frac{\partial\vec{A}}{\partial t} \quad \text{(A.1.10)}$$

$$\vec{J}_L=\sigma\frac{\partial\vec{u}}{\partial t}\times\vec{B}_0 \quad \text{(A.1.11)}$$

$$\vec{J}_M=-\nabla\times(\vec{M}_0\nabla.\vec{u}) \quad \text{(A.1.12)}$$

$$\vec{J}_{MS}=\nabla\times\vec{H}_{MS} \quad \text{(A.1.13)}$$

Substituting equations (A.1.10, A.1.11, A.1.12 and A.1.13) into (A.1.9) yields

$$\nabla\times (v\nabla \times \vec{A}) = -\sigma\frac{\partial \vec{A}}{\partial t} + \vec{J}_s + \vec{J}_L + \vec{J}_M + \vec{J}_{MS} \quad \text{(A.1.14)}$$

In a 2D model focused on the xy plane, the MVP is directed toward the z- axis, thus

$$\vec{A} = A_z a_z \quad \text{(A.1.15)}$$

Substituting equation (A.15) into (A.14) yields

$$\nabla\times (v\nabla \times A_z) = -\sigma\frac{\partial A_z}{\partial t} + \vec{J}_{sz} + \vec{J}_{Lz} + \vec{J}_{Mz} + \vec{J}_{MSz} \quad \text{(A.1.16)}$$

By assuming that v does not depend on position and $\nabla.A_z$ = 0, equation (A.1.16) becomes

$$-v\nabla^2 A_z + \sigma\frac{\partial A_z}{\partial t} = \vec{J}_{sz} + \vec{J}_{Lz} + \vec{J}_{Mz} + \vec{J}_{MSz} \quad \text{(A.1.17)}$$

In the transmitting mode, the terms involving $\vec{u}$ and S are very compared to other terms in equation (3.8) and (3.9), hence are considered only when EMAT is used as an acoustic wave detector [99]. $\vec{J}_{Lz}$, $\vec{J}_{Mz}$ and $\vec{J}_{MSz}$ are neglected since they contain terms in $\vec{u}$ and S. therefore, equation (A.17) becomes

$$-v\nabla^2 A_z + \sigma\frac{\partial A_z}{\partial t} = \vec{J}_{sz} \quad \text{(A.1.18)}$$

Also since there is no acoustic wave in the EMAT coil, the displacement is assumed to be zero (i.e. $\sigma \frac{\partial \vec{u}}{\partial t} \times \vec{B}_0 = 0$) at the surface of the coil, hence equation (A.1.7) becomes

$$\vec{J} = -\sigma \frac{\partial \vec{A}}{\partial t} + \vec{J}_s \quad \text{(A.1.19)}$$

In integral form, Equation (3.6) can be expressed as:

$$\iint_R (\nabla \times \vec{H}).\overrightarrow{ds} = \iint_R \vec{J}.\overrightarrow{ds} = i(t) \quad \text{(A.1.20)}$$

By assuming that $\vec{J}_s$ is constant along the source conductor (A.1.19) and (A.1.20) for the k^{th} coil source conductor yields

$$\iint_{Rk} J_z ds = J_{sz} \iint_{Rk} ds - \sigma \frac{\partial}{\partial t} \iint_{Rk} A_z ds = i_k(t) \quad \text{(A.1.21)}$$

Where J_{sz} is the constant SCD of the k^{th} conductor in the z direction. The SCD (J_{sz}) can also be expressed in terms of the total current of the k^{th} conductor, $i_k(t)$, and A_z as

$$J_{sz}(t) = \frac{i_k(t)}{S_k} + \frac{\sigma}{S_k}\frac{\partial}{\partial t}\iint_{Rk} A_z ds \qquad \text{(A.1.22)}$$

Where $S_k = \iint_{Rk} ds$ is the cross-sectional area of the k^{th} conductor.

Substituting equation (A.22) into (A.18) yields

$$-v\nabla^2 A_z + \sigma\frac{\partial A_z}{\partial t} - \frac{\sigma}{S_k}\frac{\partial}{\partial t}\iint_{Rk} A_z ds = \frac{i_k(t)}{S_k} \qquad \text{(A.1.23)}$$

Appendix A.2

Experimental traces of particle velocity at various excitation currents

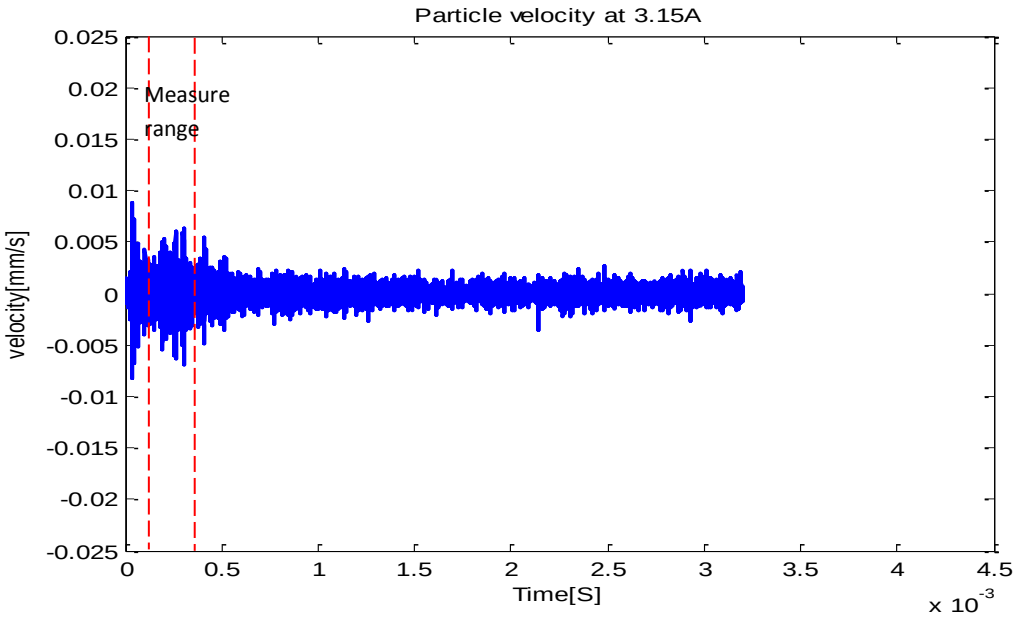

F.g.A.2.1: Experimental time history of particle velocity at 3.15A

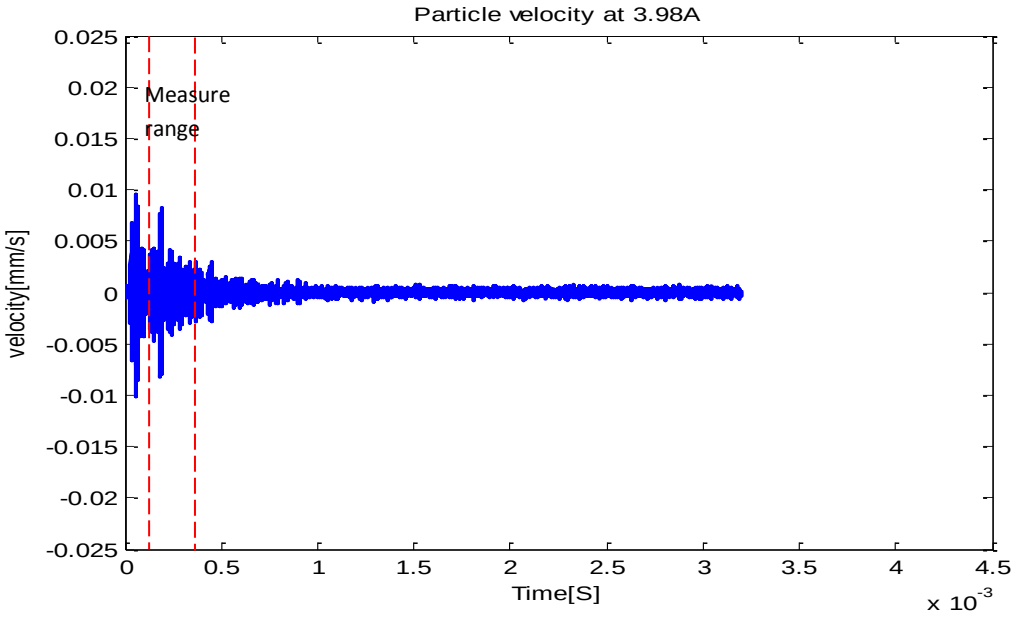

Fig.A.2.2: Experimental time history of particle velocity at 3.98A

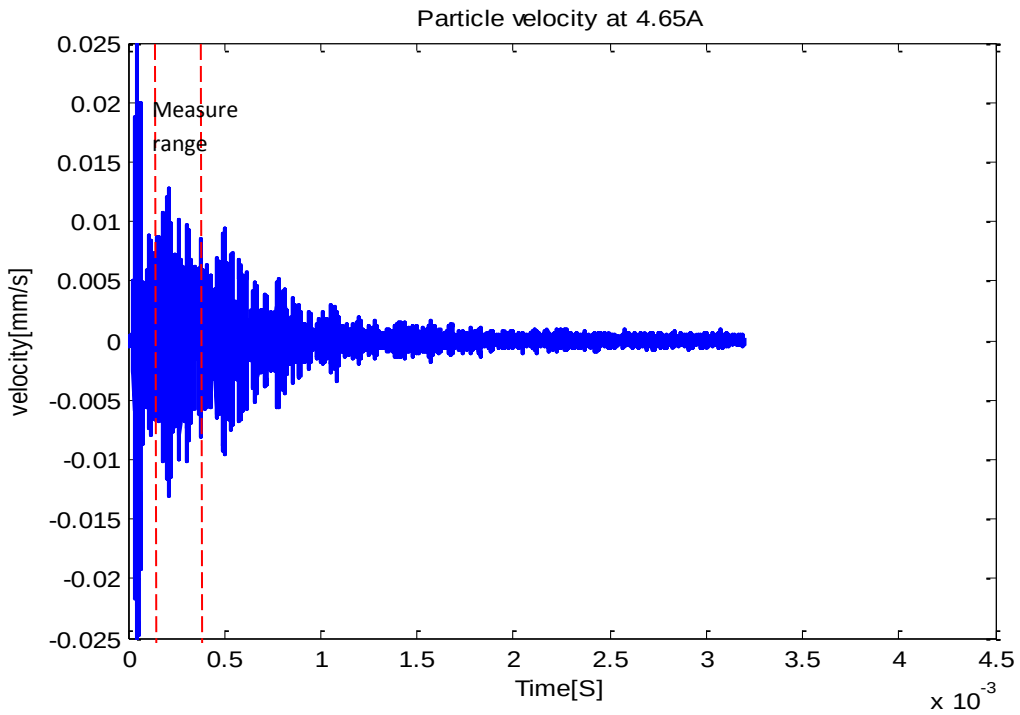

Fig.A.2.3: Experimental time history of particle velocity at 4.65A

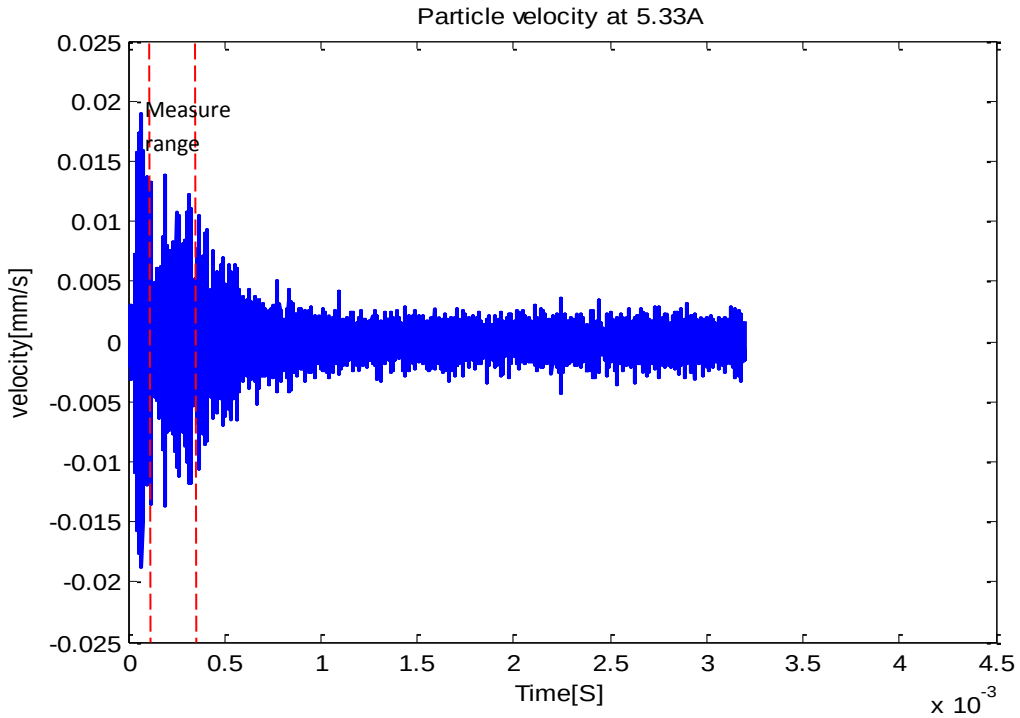

Fig.A.2.4: Experimental time history of particle velocity at 5.33A

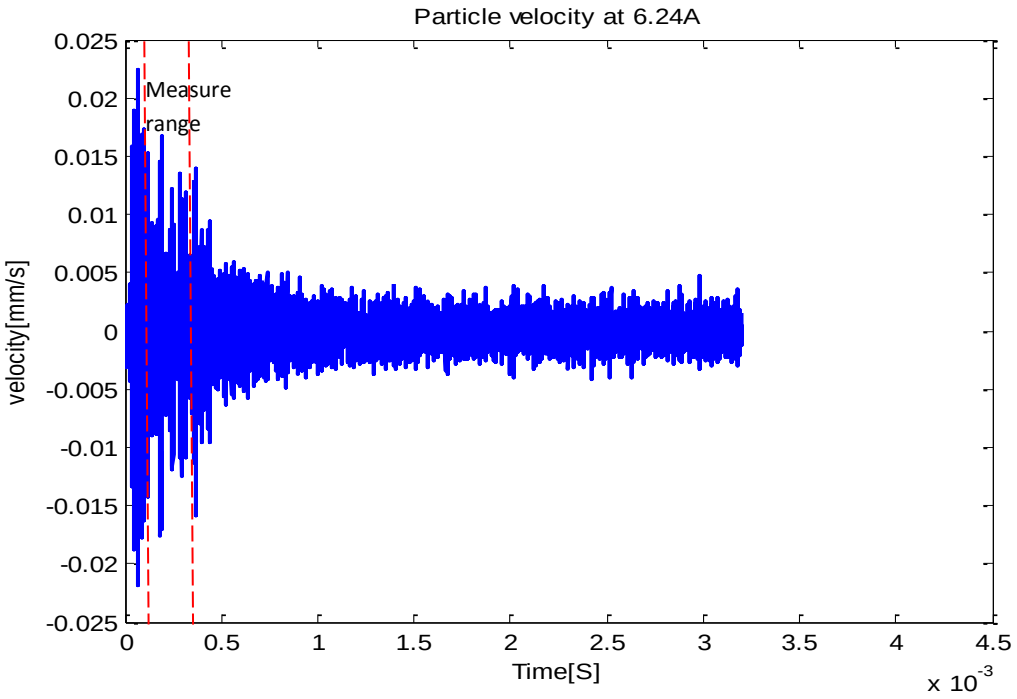

Fig.A.2.5: Experimental time history of particle velocity at 6.24A

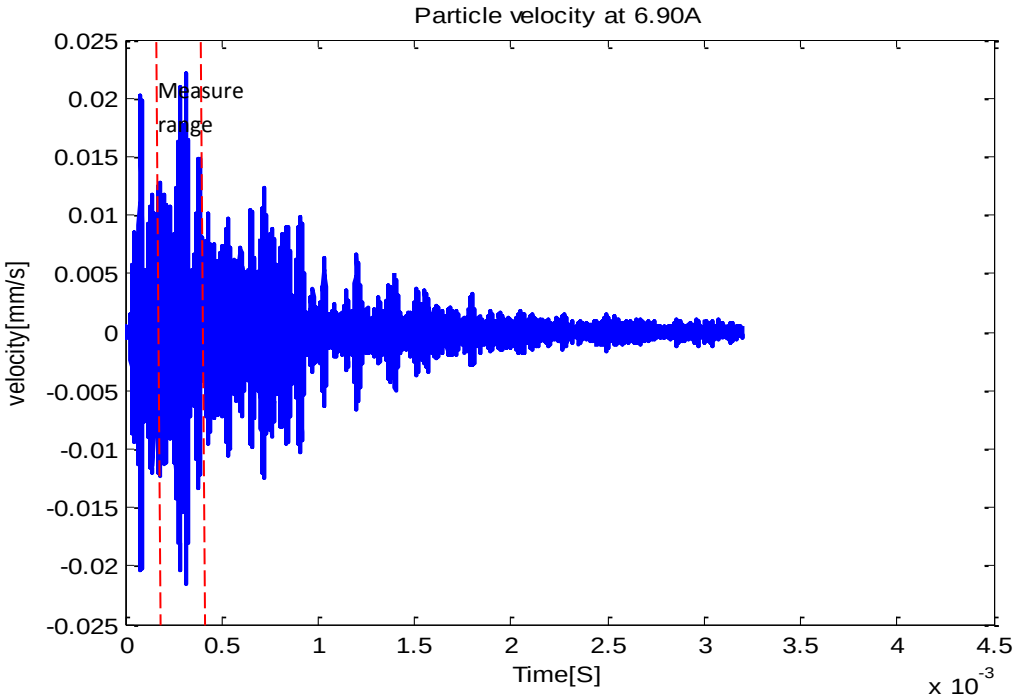

Fig.A.2.6: Experimental time history of particle velocity at 6.90A

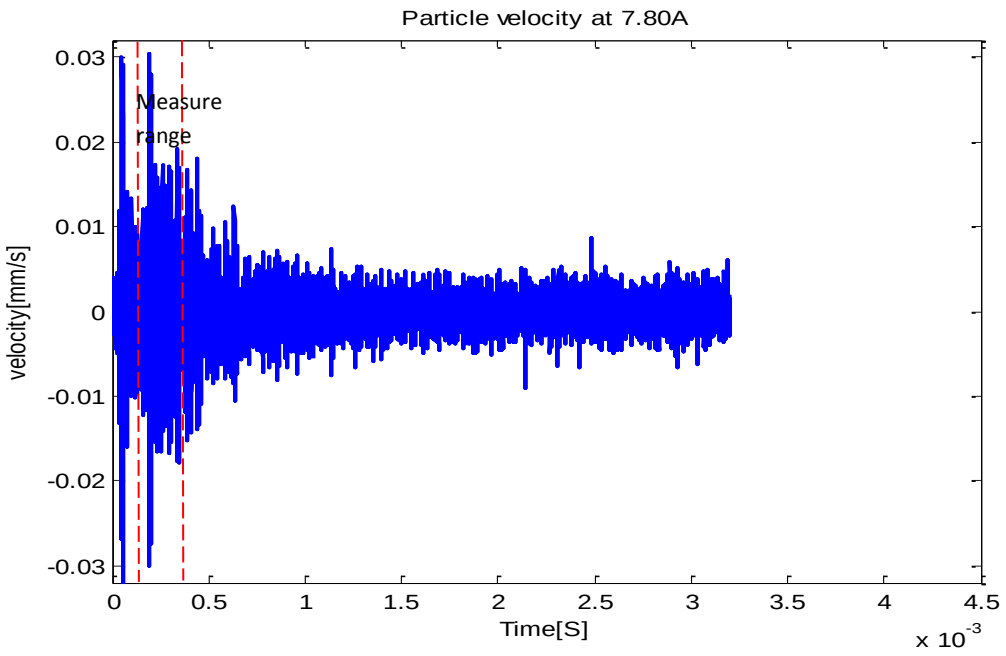

Fig.A.2.7: Experimental time history of particle velocity at 7.80A

APPENDIX A.3

Experimental traces of particle velocity at various excitation frequencies

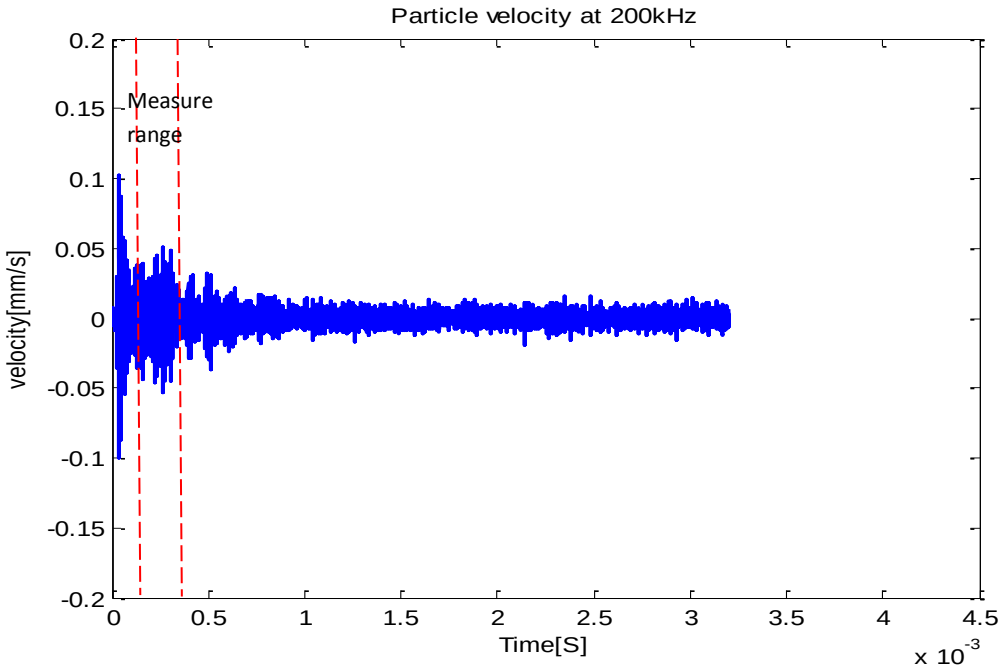

Fig.A.3.1: Experimental time history of particle velocity at 200 kHz.

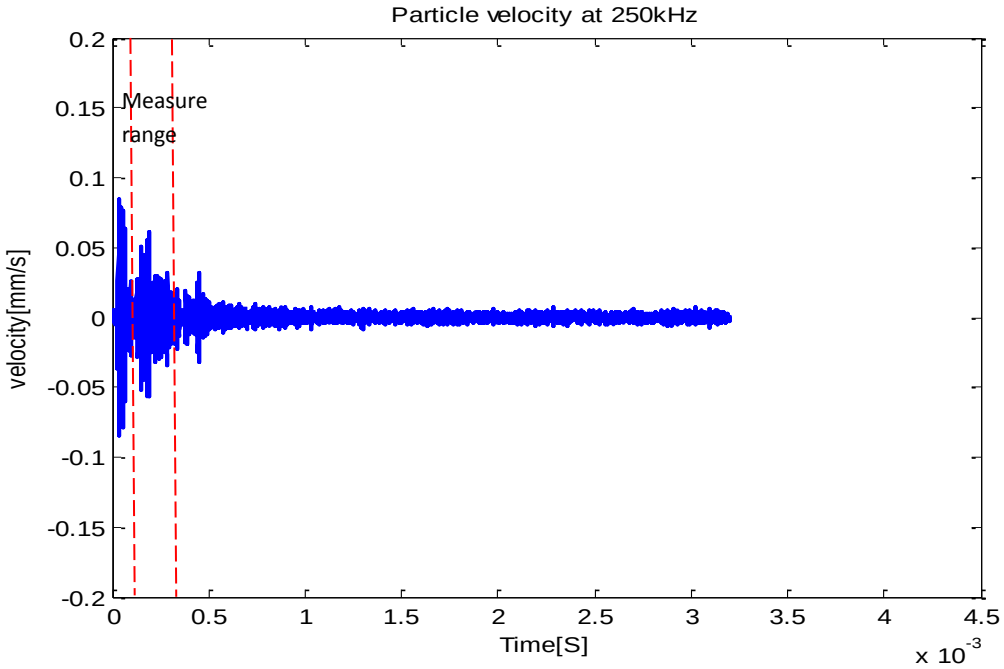

Fig.A.3.2: Experimental time history of particle velocity at 250 kHz

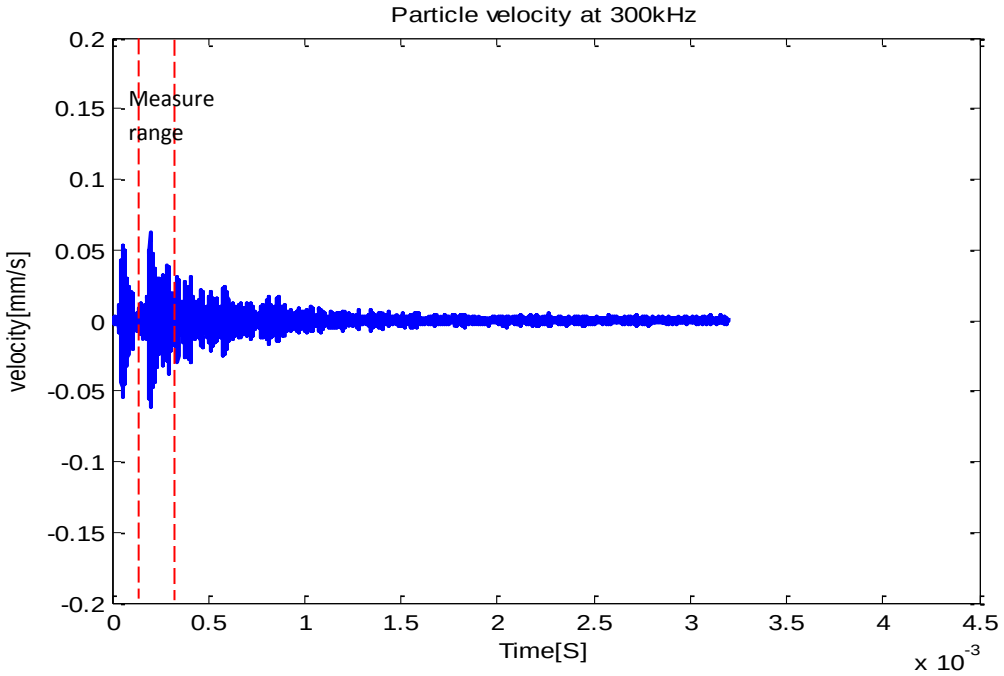

Fig.A.3.3: Experimental time history of particle velocity at 300 kHz

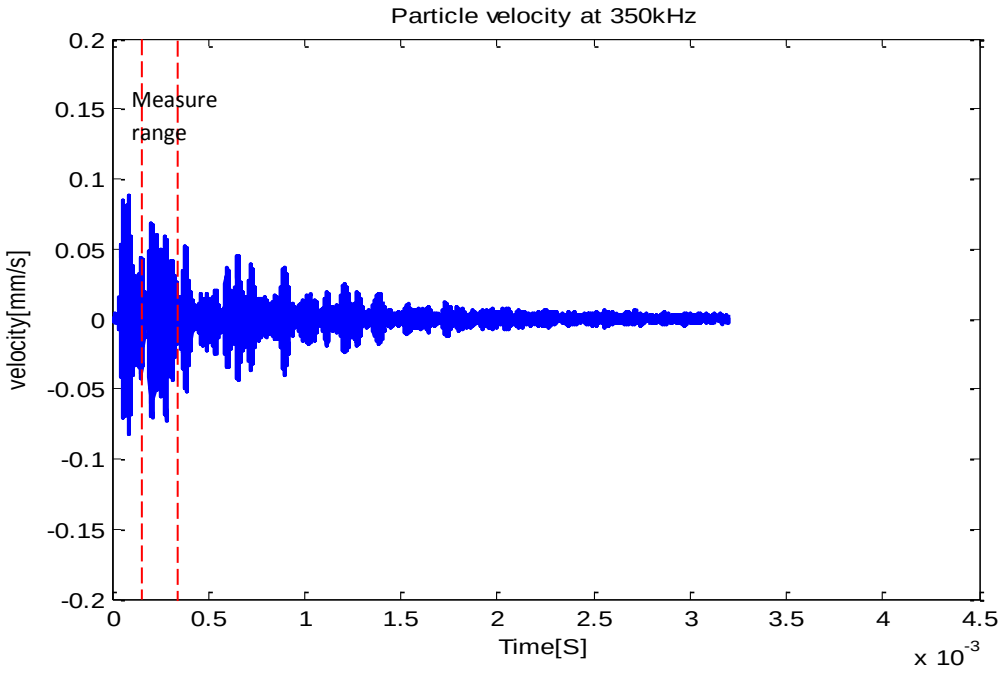

Fig.A.3.4: Experimental time history of particle velocity at 350 kHz

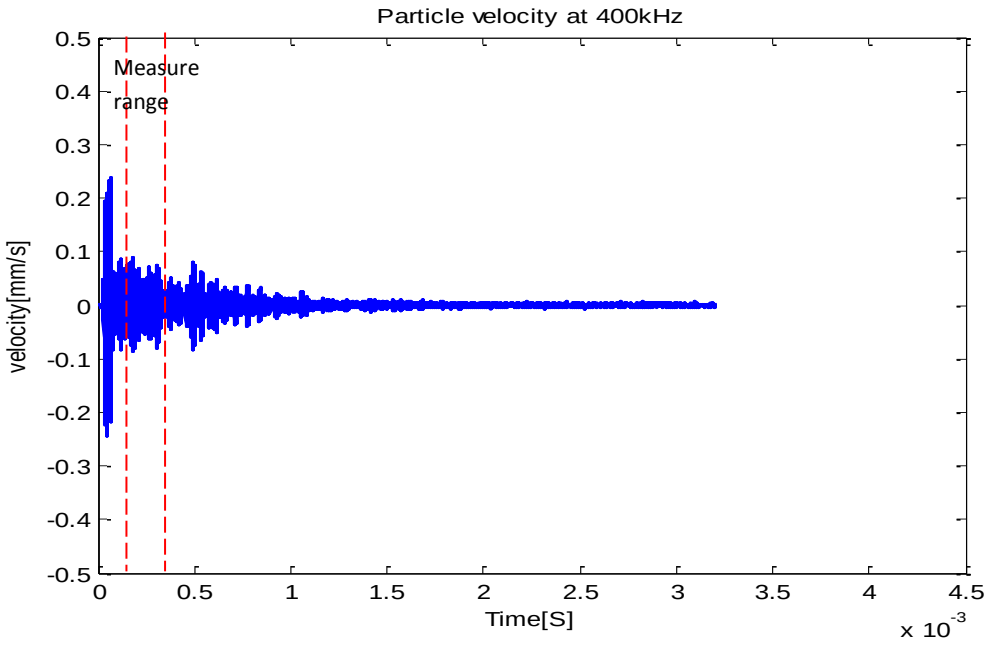

Fig.A.3.5: Experimental time history of particle velocity at 400 kHz

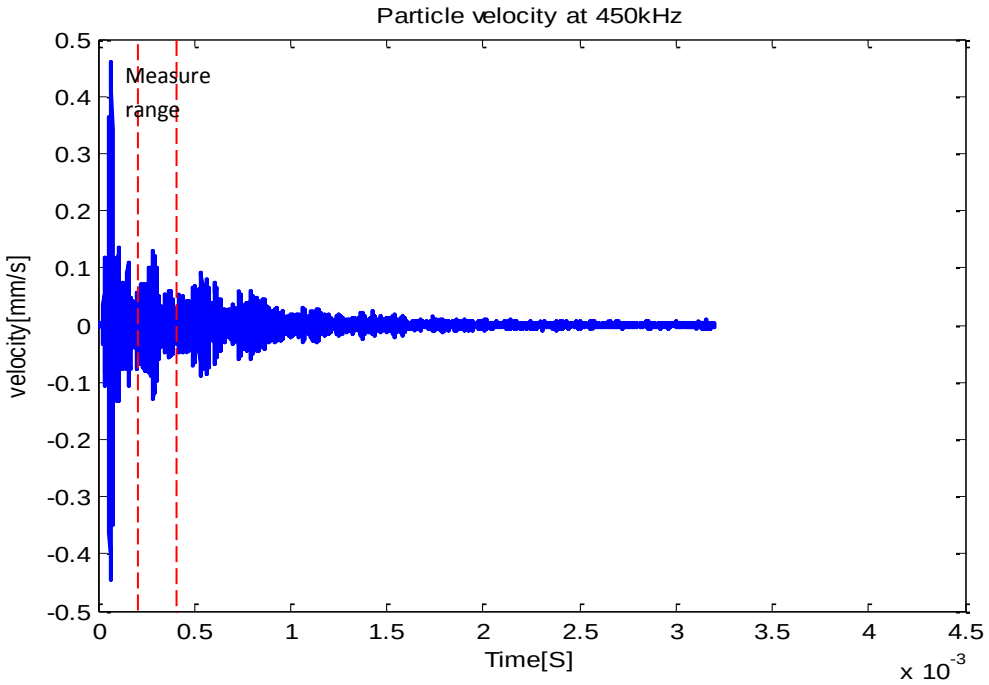

Fig.A.3.6: Experimental time history of particle velocity at 450 kHz

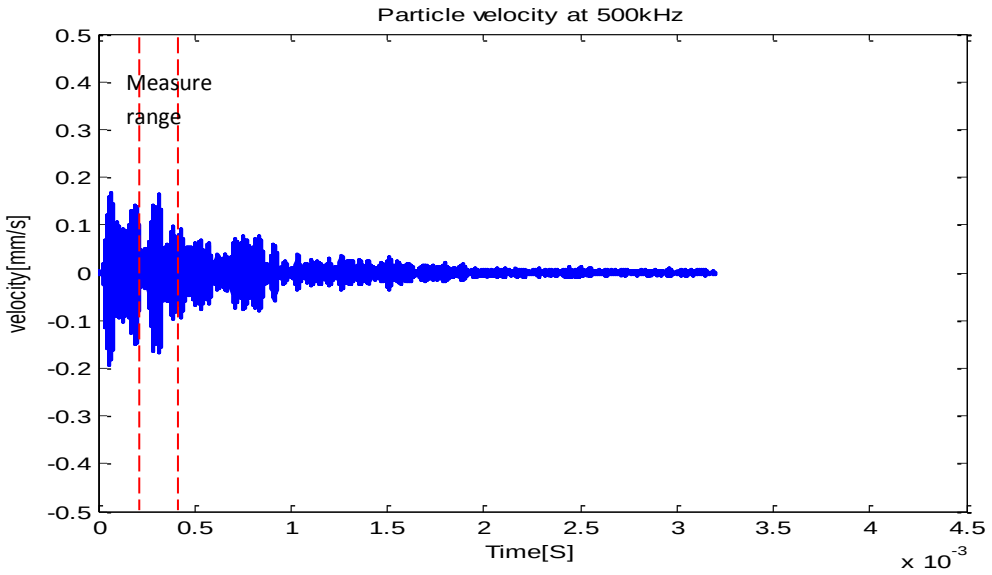

Fig.A.3.7: Experimental time history of particle velocity at 500 kHz

APPENDIX A.4

Experimental traces of particle velocity at various static magnetic fields

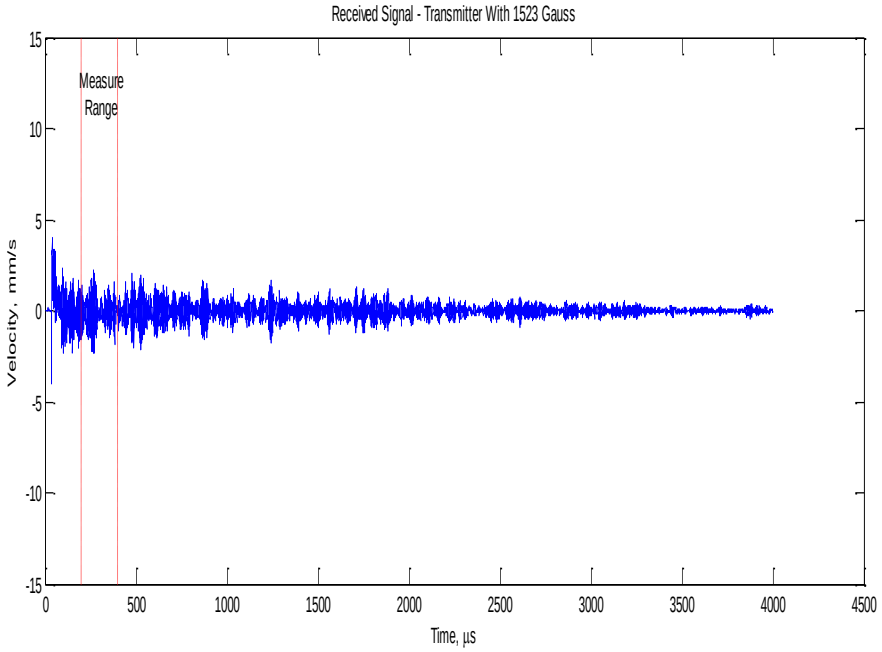

Fig.A.4.1: Experimental time history of particle velocity at 0.15T.

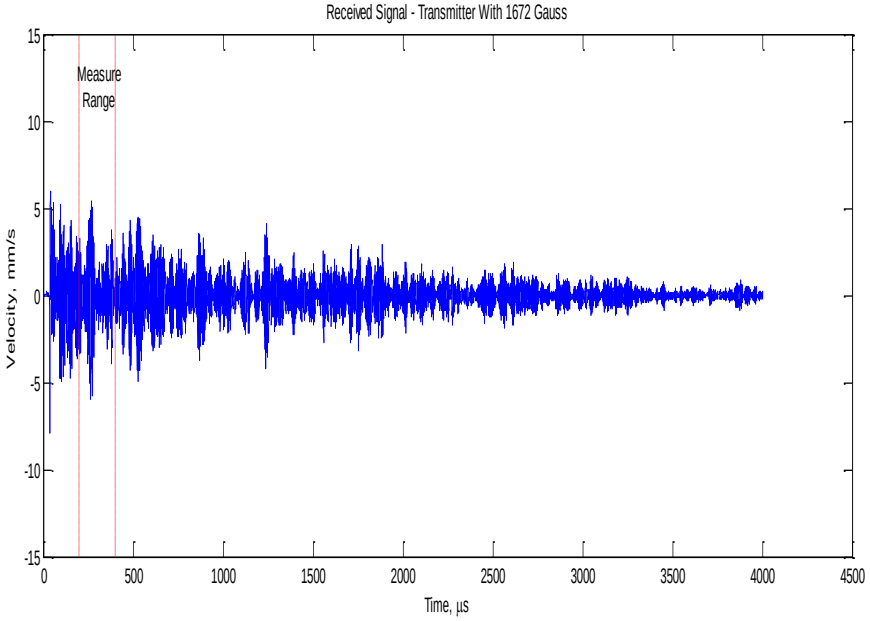

Fig.A.4.2: Experimental time history of particle velocity at 0.17T

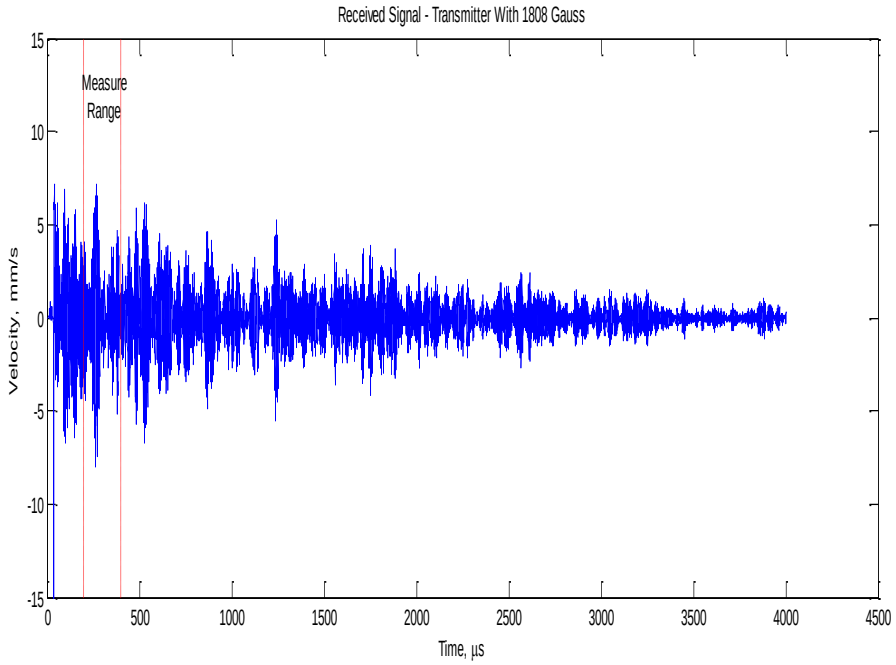

Fig.A.4.3: Experimental time history of particle velocity at 0.19T.

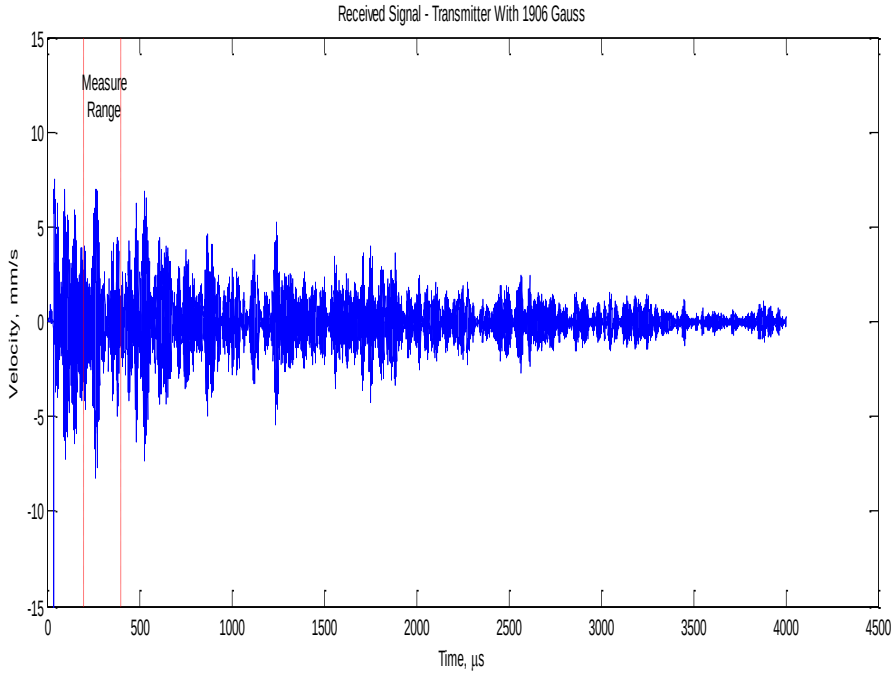

Fig.A.4.4: Experimental time history of particle velocity at 0.2T

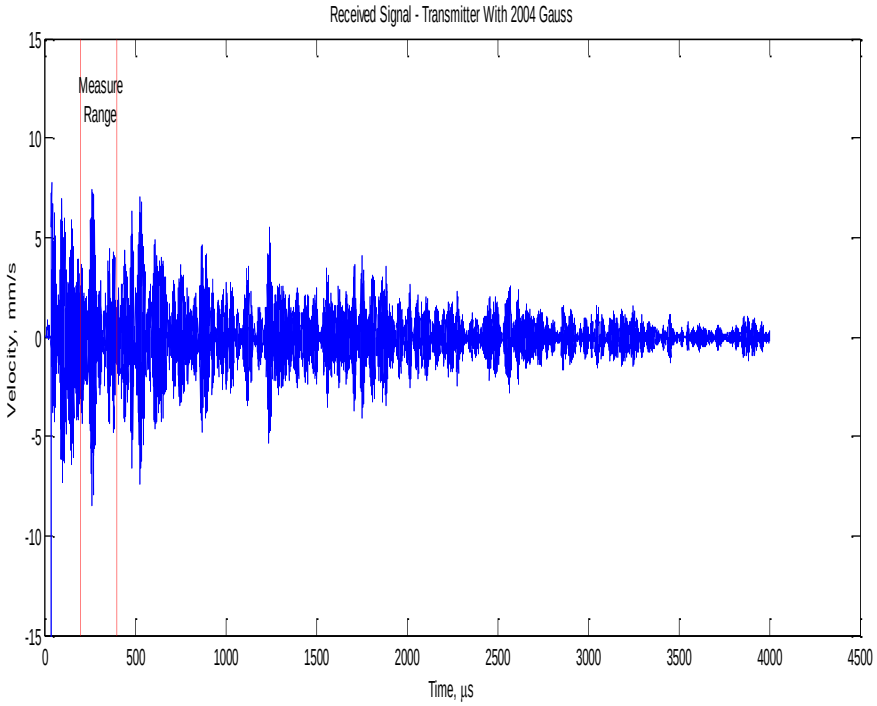

Fig.A.4.5: Experimental time history of particle velocity at 0.21T

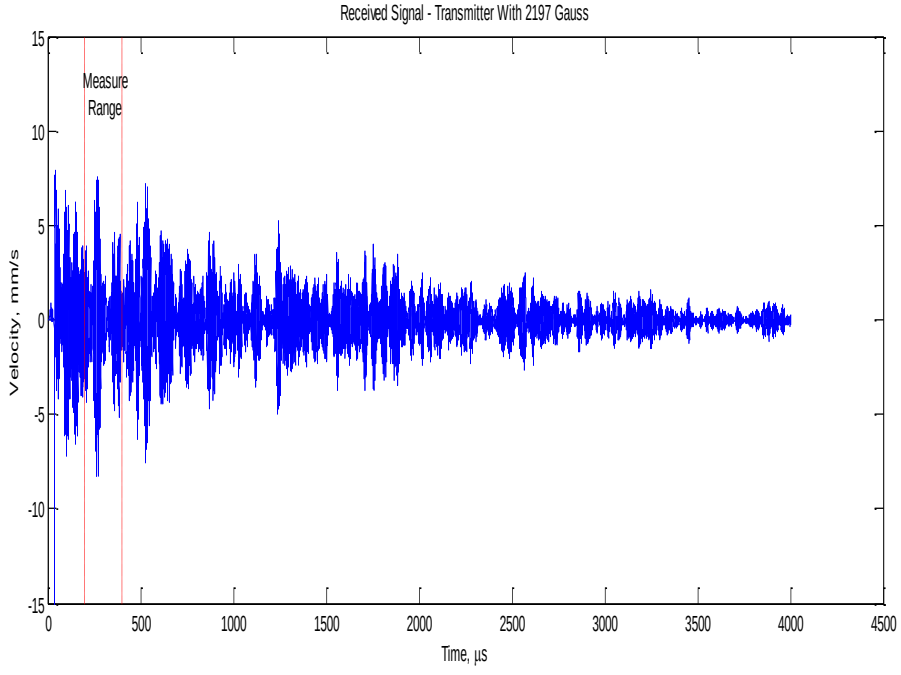

Fig.A.4.6: Experimental time history of particle velocity at 0.23T

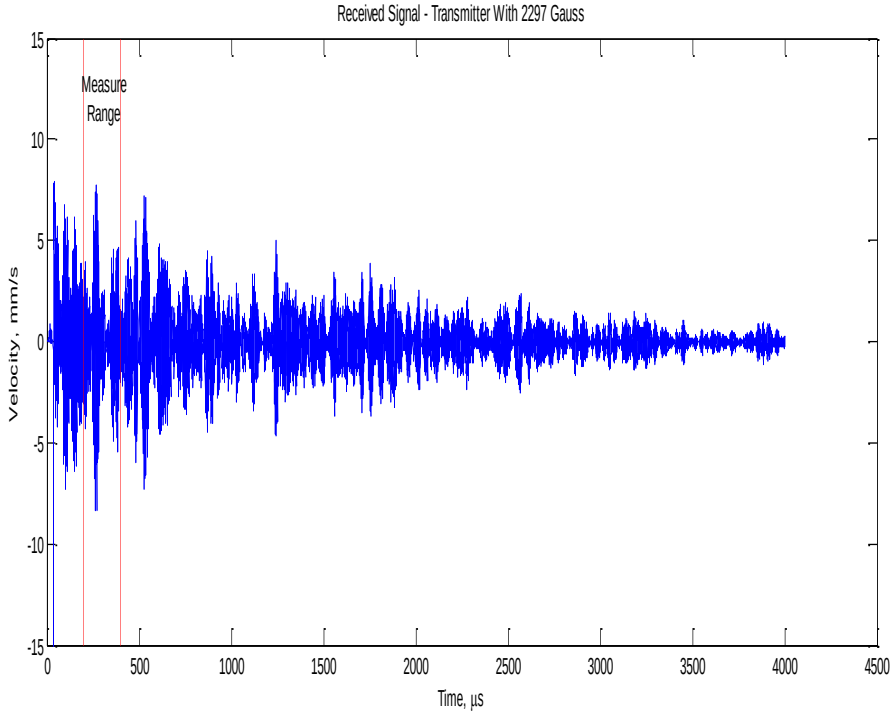

Fig.A.4.7: Experimental time history of particle velocity at 0.25T.

REFERENCES

[1] *Industrial NDT-Summit*. Available: http://industrialndt.com/index.html.

[2] International Atomic Energy Agency (IAEA), "Non-destructive testing of plant life assessment, Training course series 26," 2005.

[3] (2002). *Inspection method(radiographic testing)* [Centre for Aviation System Reliability]. Available: www.asnt.org.

[4] D. Jaffray, J. Battista, A. Fenster and P. Munro, "X-ray scatter in megavoltage transmission radiography: Physical characteristics and influence on image quality," *Med. Phys.,* vol. 21, pp. 45-60, 1994.

[5] G. Harding and J. Kosanetzky, "Scattered X-ray beam nondestructive testing," *Nuclear Instruments and Methods in Physics Research Section A: Accelerators, Spectrometers, Detectors and Associated Equipment,* vol. 280, pp. 517-528, 1989.

[6] T. Matsumoto and H. Mimura, "Point x-ray source using graphite nanofibers and its application to x-ray radiography," *Appl. Phys. Lett.,* vol. 82, pp. 1637-1639, 2003.

[7] P. Cloetens, M. Pateyron-Salomé, J. Buffiere, G. Peix, J. Baruchel, F. Peyrin and M. Schlenker, "Observation of microstructure and damage in materials by phase sensitive radiography and tomography," *J. Appl. Phys.,* vol. 81, pp. 5878-5886, 1997.

[8] P. J. SHULL, "Nondestructive evaluation: theory, techniques, and applications/." M*echanical Engieering: 142).,* 2002.

[9] Eric Lifshin, Ed., *X-Ray Characteristics of Materials.* Weinheim, Germany: WILEY-VCH Verlag GmbH, 1999.

[10] Clay Olaf Ruud and Robert E.Green,Jr., Ed., *Nondestructive Methods for Material Property Determination.* New York: Plenum Press, 1984.

[11] D.E. Bray and D. McBride, Ed., *Nondestructive Testing Techniques. New Dimensions in Engineering.* JohnWiley & Sons, Inc, 1992.

[12] A. Bieberle, D. Hoppe, E. Schleicher and U. Hampel, "Void measurement using high-resolution gamma-ray computed tomography," *Nucl. Eng. Des.,* vol. 241, pp. 2086-2092, 2011.

[13] M.S. Rapaport and A. Gayer, "Application of gamma ray computed tomography to nondestructive testing." *NDT & E International,* vol. 24, pp. 141-144, 1989.

[14] R. Halmshaw, "BS-EN-444-1994-Nondestructive testing. general principles for radio graphic examination on metallic materials by x-ray and gamma rays." *Insight,* vol. 36, pp. 618-619, 1994.

[15] C. Dragnea, "The use of selenium-75 gamma-rays for the radiography of polyethylene material used for natural gas and water distribution," *Insight,* vol. 43, pp. 418-420, 2001.

[16] J. Brenizer, B. Hosticka, H. Berger and G. Gillies, "The use of contrast agents to enhance crack detection via neutron radiography," *NDT E Int.,* vol. 32, pp. 37-42, 1999.

[17] F. Fiori, A. Hilger, N. Kardjilov and G. Albertini, "Crack detection in Al alloy using phase-contrast neutron radiography and tomography," *Measurement Science and Technology,* vol. 17, pp. 2479, 2006.

[18] H. Berger and F. Iddings, *Neutron Radiography,* 1998.

[19] R. Adams and P. Cawley, "A review of defect types and nondestructive testing techniques for composites and bonded joints," *NDT International,* vol. 21, pp. 208-222, 1988.

[20] M. Michaloudaki, E. Lehmann and D. Kosteas, "Neutron imaging as a tool for the non-destructive evaluation of adhesive joints in aluminium," *Int J Adhes Adhes,* vol. 25, pp. 257-267, 2005.

[21] J.Blitz and G. Simpson, Ed., *Ultrasonic Methods of Non-Destructive Testing.* Uk: Champman & Hall, 1996.

[22] B. A. Auld, *Acoustic Fields and Waves in Solids.* Wiley New York, 1973.

[23] J. Krautkramer and H. Krautkrâmer, *Ultrasonic Testing of Materials,* 1990.

[24] J. L. Rose, "A baseline and vision of ultrasonic guided wave inspection potential," *Journal of Pressure Vessel Technology,* vol. 124, pp. 273-282, 2002.

[25] J. L. Rose, *Ultrasonic Waves in Solid Media.* Cambridge university press, 2004.

[26] D. E. Chimenti, *Review of Progress in Quantitative Nondestructive Evaluation.* Springer, 1995.

[27] J. Achenbach, "Quantitative nondestructive evaluation," *Int. J. Solids Structures,* vol. 37, pp. 13-27, 2000.

[28] *Principle of operation of ultrasonic transducers*. Available: www.ndt.net.

[29] Lei Zhang, "EPGA Embedded System for Ultrasonic Non-Destructive Testing," pp. 3-4, PhD Theses, Brunel University London,2011.

[30] Philip Peter Catton, "The Use of Ultrasonic Guided Waves for the In Situ Inspection of industrial Pipelines for Corrosion Damage," PhD Theses at Brunel University London, 2008.

[31] P.catton, PJ Mudge, D. D'Zurko, and J. Rose, "Improved methodology for guided wave inspection of pipelines," *Pipeline and Gas Journal,* vol. 1, pp. 36-44, 2008.

[32] *Teletest Focus*. Available: www.plantintegrity.com.

[33] M. Hirao and H. Ogi, *EMATs for Science and Industry: Noncontacting Ultrasonic Measurements.* Springer, 2003.

[34] T. Kundu, "Ultrasonic nondestructive evaluation: engineering and biological material characterization. CRC press LLC Florida, USA 2004," .

[35] B. Maxfield and C. Fortunko, "The design and use of Electromagnetic Acoustic Wave Transducers(EMATs)," *Mater. Eval.,* vol. 41, pp. 1399-1408, 1983.

[36] *Resonant Acoustic NDT Technologies*. Available: www.resonic.com.

[37] S. J. Robinson, R. Goff and A. G. Sherwin, "Water based penetrants: Advantages and limitations," *Mater. Eval.,* vol. 57, pp. 893-897, 1999.

[38] David Lovejoy, Ed., *Penetrant Testing: A Practical Guide.* Great Britain: Chapman & Hall, 1991.

[39] P. Prokhorenko, A. Sekerin and A. Klornev, "a Quantitative Estimation of Penetrant Systems," *Nondestr. Test. Eval.,* vol. 13, pp. 325-345, 1997.

[40] A. Sherwin, "Still a good rule: visible penetrant inspection not to precede fluorescent," *Mater. Eval.,* vol. 48, pp. 1456-1457, 1990.

[41] B. Larson, *Study of the Factors Affecting the Sensitivity of Liquid Penetrant Inspections: Review of Literature Published from 1970 to 1998,* 2002.

[42] *Inspection method (Liquid penetrant testing)* [Amarican society for Non-destructive Testing]. Available: www.asnt.org.

[43] C. E. Betz, *Principles of Magnetic Particle Testing.* Magnaflux Corporation Chicago, 1967.

[44] P. E. Mix, "Magnetic Particle Testing," *Introduction to Nondestructive Testing: A Training Guide, Second Edition,* pp. 247-299, .

[45] David Lovejoy, Ed., *Magnetic Particle Inspection: A Practical Guide.* Great Britain: Chapman & Hall, 1993.

[46] *Magnetic Particle Inspection* . Available: www.Industrialndt.com.

[47] D. E. Bray and R. K. Stanley, *Nondestructive Evaluation: A Tool in Design, Manufacturing and Service.* CRC press, 1996.

[48] J. David, "Introduction to Magnetism and Magnetic Materials," *Chapman & Hall,* 1998.

[49] J. Blitz, *Electrical and Magnetic Methods of Non-Destructive Testing.* Springer, 1997.

[50] *Flux Leakage Test*. Available: www.Independencetube.com.

[51] A. Sophian, G. Y. Tian, D. Taylor and J. Rudlin, "A feature extraction technique based on principal component analysis for pulsed Eddy current NDT," *NDT E Int.,* vol. 36, pp. 37-41, 2003.

[52] T. Chen, G. Y. Tian, A. Sophian and P. W. Que, "Feature extraction and selection for defect classification of pulsed eddy current NDT," *NDT E Int.,* vol. 41, pp. 467-476, 2008.

[53] J. Bowler and M. Johnson, "Pulsed eddy-current response to a conducting half-space," *Magnetics, IEEE Transactions on,* vol. 33, pp. 2258-2264, 1997.

[54] J. R. Bowler, "Eddy current calculations using half-space Green's functions," *J. Appl. Phys.,* vol. 61, pp. 833-839, 1987.

[55] R. Ludwig and X. Dai, "Numerical and analytical modeling of pulsed eddy currents in a conducting half-space," *Magnetics, IEEE Transactions on,* vol. 26, pp. 299-307, 1990.

[56] *Eddy Current Test*. Available: www.microwavesoft.com.

[57] G. A. MATZKANIN, "Selecting a Nondestructive Testing Method: Visual Inspection," .

[58] F. A. Iddings, "The basics of visual testing," *Mater. Eval.,* vol. 62, pp. 500-501, 2004.

[59] M. W. Allgaier and S. Ness., Ed., *Nondestructive Testing Hansbook: Visual and Optical Testing.* Columbus, Ohio: American Society for Nondestructive Testing, 1993.

[60] R. Ambu, F. Aymerich, F. Ginesu and P. Priolo, "Assessment of NDT interferometric techniques for impact damage detection in composite laminates," *Composites Sci. Technol.,* vol. 66, pp. 199-205, 2006.

[61] Y. Hung, "Shearography: a new optical method for strain measurement and nondestructive testing," *Optical Engineering,* vol. 21, pp. 213391-213391-, 1982.

[62] Y. Hung and H. Ho, "Shearography: An optical measurement technique and applications," *Materials Science and Engineering: R: Reports,* vol. 49, pp. 61-87, 2005.

[63] Y. Hung, "Applications of digital shearography for testing of composite structures," *Composites Part B: Engineering,* vol. 30, pp. 765-773, 1999.

[64] Y. Zhu, G. Tian, R. Lu and H. Zhang, "A review of optical NDT technologies," *Sensors,* vol. 11, pp. 7773-7798, 2011.

[65] J. Butters and J. Leendertz, "Speckle pattern and holographic techniques in engineering metrology," *Optics & Laser Technology,* vol. 3, pp. 26-30, 1971.

[66] Y. Hung and C. Liang, "Image-shearing camera for direct measurement of surface strains," *Appl. Opt.,* vol. 18, pp. 1046-1051, 1979.

[67] Vest.C.M, Ed., *Holographic Interferometry.* New York: John Wiley & Sons, 1979.

[68] L. Bruno and A. Poggialini, "Back to the future: From speckle to holography," *Optics and Lasers in Engineering,* vol. 45, pp. 538-549, 2007.

[69] S. Kleven and L. Hyvaerinen, "Vision testing requirements for industry," *Mater. Eval.,* vol. 57, pp. 797-803, 1999.

[70] (2014). *Remote Visual Inspection Tecnique*. Available: www.sgswaney.com.

[71] *Speckle Pattern Inteferometer*. Available: www.ndt.uct.ac.za.

[72] Š. Kočiš and Z. Figura, *Ultrasonic Measurements and Technologies.* Chapman & Hall, 1996.

[73] C. Chen, *Ultrasonic and Advanced Methods for Nondestructive Testing and Material Characterization.* World Scientific, 2007.

[74] J. Szilard, "Ultrasonic testing: Non-conventional testing techniques." *JOHN WILEY & SONS, INC., 605 THIRD AVE., NEW YORK, NY 10158, 1982, 640,* 1982.

[75] G. Workman, D. Kishoni and P. Moore, "Nondestructive Testing Handbook, Vol. 7–Ultrasonic Testing," *American Society for Nondestructive Testing, Columbus,* 2007.

[76] L. W. Schmerr, *Fundamentals of Ultrasonic Nondestructive Evaluation: A Modeling Approach.* Plenum Press New York, 1998.

[77] D.C.Jiles, Ed., *Introduction to the Principles of Material Evaluation.* Boca Raton: CRC Press, 2008.

[78] R. B. Thompson, "Physical principles of measurements with EMAT transducers," *Physical Acoustics,* vol. 19, pp. 157-200, 1990.

[79] D. MacLauchlan, S. Clark, B. Cox, T. Doyle, B. Grimmett, J. Hancock, K. Hour and C. Rutherford, "Recent advancements in the application of EMATs to NDE," in *16th World Conference on NDT,* 2004, .

[80] M. Kaltenbacher, R. Lerch, H. Landes, K. Ettinger and B. Tittmann, "Computer optimization of electromagnetic acoustic transducers," in *Ultrasonics Symposium, 1998. Proceedings., 1998 IEEE,* 1998, pp. 1029-1034.

[81] R. Jafari-Shapoorabadi, A. Konrad and A. Sinclair, "Improved finite element method for EMAT analysis and design," *Magnetics, IEEE Transactions on,* vol. 37, pp. 2821-2823, 2001.

[82] S. Wang, L. Kang, Z. Li, G. Zhai and L. Zhang, "3-D modeling and analysis of meander-line-coil surface wave EMATs," *Mechatronics,* vol. 22, pp. 653-660, 9, 2012.

[83] R. Ludwig and X. W. Dai, "Numerical simulation of electromagnetic acoustic transducer in the time domain," *J. Appl. Phys.,* vol. 69, pp. 89-98, 1991.

[84] X. Jian, S. Dixon and R. S. Edwards, "Ultrasonic generation and optimization for EMAT," in *AIP Conference Proceedings,* 2005, pp. 1041.

[85] X. Jian and S. Dixon, "Enhancement of EMAT and eddy current using a ferrite back-plate," *Sensors and Actuators A: Physical,* vol. 136, pp. 132-136, 5/1, 2007.

[86] L. Kang, S. Wang, Z. Li and G. Zhai, "Optimal design of surface wave emats for enhancing their ultrasonic signal strength," *J. Acoust. Soc. Am.,* vol. 131, pp. 3466-3466, 2012.

[87] K. Kawashima, "Theory and numerical calculation of the acoustic field produced in metal by an electromagnetic ultrasonic transducer," *J. Acoust. Soc. Am.,* vol. 60, pp. 1089, 1976.

[88] R. B. Thompson, "Mechanisms of electromagnetic generation and detection of ultrasonic Lamb waves in iron-nickel alloy polycrystals," *J. Appl. Phys.,* vol. 48, pp. 4942-4950, 1977.

[89] R. B. Thompson, "A model for the electromagnetic generation and detection of Rayleigh and Lamb waves," *Sonics and Ultrasonics, IEEE Transactions on,* vol. 20, pp. 340-346, 1973.

[90] R. Ribichini, F. Cegla, P. Nagy and P. Cawley, "Experimental and numerical evaluation of electromagnetic acoustic transducer performance on steel materials," *NDT E Int.,* vol. 45, pp. 32-38, 2012.

[91] R. Ludwig, "Numerical implementation and model predictions of a unified conservation law description of the electromagnetic acoustic transduction process," *Ultrasonics, Ferroelectrics and Frequency Control, IEEE Transactions on,* vol. 39, pp. 481-488, 1992.

[92] R. Ludwig, "Theoretical basis for a unified conservation law description of the electromagnetic acoustic transduction process," *Ultrasonics, Ferroelectrics and Frequency Control, IEEE Transactions on,* vol. 39, pp. 476-480, 1992.

[93] E. Ashigwuike, W. Balachandran, S. Thomas and R. Mackay, "Numerical Study of EMAT Coil Structure based on Finite Element Method," *Petroleum Technology Development Journal,* vol. 3, pp. 8-24, January, 2013.

[94] E. C. Ashigwuike, W. Balachandran and S. Thomas, "Simulation based comparative study of EMATs' coil structure for long-range ultrasonic testing." in *The British Institute of Non-Destructive Testing (NDT 2012), Conference and Exhibition,* Northamptonshire, United Kingdom, 2012, pp. 15.

[95] E. Ashigwuike, W. Balachandran, S. Thomas, N. Manivannan and R. Mackay, "Improving the Lorentz Force Amplitude of an EMAT Using Stacked Coil Configuration," *Sensors and Transducers,* vol. 155, pp. 262-270, August, 2013.

[96] C. E. Ashigwuike, W. Balachandran, S. Thomas, N. Manivannan and R. Mackay, "Comparative study of a conventional SP-EMAT coil and a novel KT-EMAT coil based on lorentz force mechanism." in *The 12th International Conference of the Slovenian Society for Non-Destructive Testing*
'' Application of Contemporary Non-Destructive Testing in Engineering'', Ljubljana, Slovenia, 2013, pp. 87.

[97] Evans Chinemezu Ashigwuike, Wamadeva Balachandran, Rajagopal Nilavalan, "Study of the transduction mechanisms of magnetostrictive EMAT on pipe steel materials," in *School of Engineering and Design Research Student Conference (RESCON),* Brunel University London., 2014, .

[98] Evans Chinemezu Ashigwuike, Wamadeva Balachandran, Sadiq Thomas, Rajagopal Nilavalan, "Comprehensive study of the transduction mechanisms of normall biased (NB) EMAT configuration operating on ferromagnetic materials." in *European Conference on Nondestructive Testing,* Prague, Czech Republic, 2014, .

[99] H. Ogi, "Field dependence of coupling efficiency between electromagnetic field and ultrasonic bulk waves," *J. Appl. Phys.,* vol. 82, pp. 3940-3949, 1997.

[100] R. B. Thompson, "A model for the electromagnetic generation of ultrasonic guided waves in ferromagnetic metal polycrystals," *Sonics and Ultrasonics, IEEE Transactions on,* vol. 25, pp. 7-15, 1978.

[101] R. Ribichini, P. Nagy and H. Ogi, "The impact of magnetostriction on the transduction of normal bias field EMATs," *NDT E Int.,* 2012.

[102] Evans Chinemezu Ashigwuike, Rajagopal Nilavalan, Wamadeva Balachandran, "Non-destructive testing of pipeline corrosion using electromagnetic acoustic transducer system (EMATS)." in *School of Engineering and Design Research Student Conference (RESCON),* Brunel University, London, 2012, .

[103] S. Thomas, E. Ashigwuike, W. Balachandran and S. Obayya, "Characterization of Defects in Non-ferromagnetic Material Using an Electromagnetic Acoustic transducer." *Sensors and Transducers,* vol. 151, pp. 70-77, April, 2013.

[104] S. Thomas, W. Balachandran, E. Ashigwuike and E. O. Ezugwu, "Characterization of electromagnetic acoustic transducer using finite element method," in *The British Institute of Non-Destructive Testing (NDT 2012), Conference and Exhibition,* Northamptonshire, United Kingdom, 2012, pp. 21.

[105] S. Thomas, C. E. Ashigwuike and Ubadike Osichinaka, "Comparison of defect detection in aluminium and steel plates using an electromagnetic acoustic transducer." in *The 12th International Conference of the Slovenian Society for Non-Destructive Testing*
'' Application of Contemporary Non-Destructive Testing in Engineering''. Ljubljana-Slovenia, 2013, pp. 113-120.

[106] I. Boldea and S. A. Nasar, *The Induction Machine Handbook.* CRC press, 2002.

[107] R. Dhayalan and K. Balasubramaniam, "A hybrid finite element model for simulation of electromagnetic acoustic transducer (EMAT) based plate waves," *NDT E Int.,* vol. 43, pp. 519-526, 2010.

[108] I. D. Mayergoyz and G. Engdahl, *Handbook of Giant Magnetostrictive Materials.* Elsevier, 1999.

[109] E. Dobbs, "Electromagnetic generation of ultrasonic waves," *Physical Acoustics,* vol. 10, pp. 127-189, 1973.

[110] A. Wilbrand, "Quantitative modeling and experimental analysis of the physical properties of electromagnetic-ultrasonic transducers," *Review of Progress in Quantitative Nondestructive Evaluation,* vol. 7, pp. 671-678, 1987.

[111] A. Doniavi and M. Eskandarzade, "A model for Rayleigh wave propagation in the EMAT systems," 2006.

[112] H. Ogi, M. Hirao and T. Ohtani, "Flaw detection by line-focusing electromagnetic acoustic transducers," in *Ultrasonics Symposium, 1997. Proceedings., 1997 IEEE,* 1997, pp. 653-656.

[113] A. Wilbrand, "Emus-probes for bulk waves and Rayleigh waves. Model for sound field and efficiency calculations," *New Procedures in Nondestructive Testing,* pp. 71-82, 1983.

[114] S. Lee and B. Ahn, "Emat Application at High Temperature," *Nondestr. Test. Eval.,* vol. 7, pp. 253-261, 1992.

[115] Comsol Multiphysics, "Mathematical Modelling and Simulation of Magnetostrictive Materials," .

[116] D. Jiles, "Theory of the magnetomechanical effect," *J. Phys. D,* vol. 28, pp. 1537, 1999.

[117] J. P. Joule, "XVII. On the effects of magnetism upon the dimensions of iron and steel bars," *The London, Edinburgh, and Dublin Philosophical Magazine and Journal of Science,* vol. 30, pp. 76-87, 1847.

[118] J. C. Maxwell, "LI. On physical lines of force," *The London, Edinburgh, and Dublin Philosophical Magazine and Journal of Science,* vol. 21, pp. 338-348, 1861.

[119] R. Randall, F. Rose and C. Zener, "Intercrystalline thermal currents as a source of internal friction," *Physical Review,* vol. 56, pp. 343, 1939.

[120] D. O. Thompson and D. K. Holmes, "Effects of neutron irradiation upon the Young's modulus and internal friction of copper single crystals," *J. Appl. Phys.,* vol. 27, pp. 713-723, 1956.

[121] C. Grimes and S. Buchsbaum, "Interaction Between Helicon Waves and Sound Waves in Potassium," *Phys. Rev. Lett.,* vol. 12, pp. 357, 1964.

[122] M. Gaerttner, W. Wallace and B. Maxfield, "Experiments relating to the theory of magnetic direct generation of ultrasound in metals," *Physical Review,* vol. 184, pp. 702-704, 1969.

[123] C. Vasile and R. Thompson, "Excitation of horizontally polarized shear elastic waves by electromagnetic transducers with periodic permanent magnets," *J. Appl. Phys.,* vol. 50, pp. 2583-2588, 1979.

[124] W. Mohr, H. Licht and P. HOELLER, "The inspection of thin-walled pipes with the aid of guided ultrasonic waves," *Deutsche Gesellschaft Fuer Zerstoerungsfreie Pruefverfahren, Vortragstagung Ueber Zerstoerungsfreie Materialpruefung, Berlin, West Germany, may 5-7, 1975.) Materialpruefung,* vol. 17, pp. 240, 1975.

[125] C. Dodd and W. Deeds, "Analytical Solutions to Eddy-Current Probe-Coil Problems," *J. Appl. Phys.,* vol. 39, pp. 2829-2838, 1968.

[126] G. Miller and H. Pursey, "The field and radiation impedance of mechanical radiators on the free surface of a semi-infinite isotropic solid," *Proceedings of the*

Royal Society of London.Series A.Mathematical and Physical Sciences, vol. 223, pp. 521-541, 1954.

[127] G. Miller and H. Pursey, "On the partition of energy between elastic waves in a semi-infinite solid," *Proceedings of the Royal Society of London.Series A.Mathematical and Physical Sciences,* vol. 233, pp. 55-69, 1955.

[128] K. Kawashima, "Quantitative calculation and measurement of longitudinal and transverse ultrasonic wave pulses in solid," *IEEE Transactions on Sonics and Ultrasonics,* vol. 31, pp. 83-94, 1984.

[129] K. Mirkhani, C. Chaggares, C. Masterson, M. Jastrzebski, T. Dusatko, A. Sinclair, R. J. Shapoorabadi, A. Konrad and M. Papini, "Optimal design of EMAT transmitters," *NDT E Int.,* vol. 37, pp. 181-193, 2004.

[130] P. D. Wilcox, M. J. S. Lowe and P. Cawley, "The excitation and detection of lamb waves with planar coil electromagnetic acoustic transducers," *Ultrasonics, Ferroelectrics and Frequency Control, IEEE Transactions on,* vol. 52, pp. 2370-2383, 2005.

[131] X. Jian, S. Dixon, K. Grattan and R. S. Edwards, "A model for pulsed Rayleigh wave and optimal EMAT design," *Sensors and Actuators A: Physical,* vol. 128, pp. 296-304, 2006.

[132] J. O. Fava, L. Lanzani and M. C. Ruch, "Multilayer planar rectangular coils for eddy current testing: Design considerations," *NDT E Int.,* vol. 42, pp. 713-720, 2009.

[133] S. Wang, P. Xin, L. Kang and G. Zhai, "Research on influence of lorentz force mechanism on EMAT's transduction efficiency in steel plate," in *Industrial Electronics and Applications (ICIEA), 2010 the 5th IEEE Conference on,* 2010, pp. 196-201.

[134] H. Ogi, M. Hirao and T. Ohtani, "Line-focusing electromagnetic acoustic transducers for the detection of slit defects," *Ultrasonics, Ferroelectrics and Frequency Control, IEEE Transactions on,* vol. 46, pp. 341-346, 1999.

[135] H. Ogi, M. Hirao and T. Ohtani, "Line-focusing of ultrasonic SV wave by electromagnetic acoustic transducer," *J. Acoust. Soc. Am.,* vol. 103, pp. 2411-2415, 1998.

[136] X. Jian, S. Dixon, K. Quirk and K. Grattan, "Electromagnetic acoustic transducers for in-and out-of plane ultrasonic wave detection," *Sensors and Actuators A: Physical,* vol. 148, pp. 51-56, 2008.

[137] X. Jian, S. Dixon, R. Edwards and J. Reed, "Coupling mechanism of electromagnetic acoustical transducers for ultrasonic generation," *J. Acoust. Soc. Am.,* vol. 119, pp. 2693, 2006.

[138] L. Kang, S. Dixon, K. Wang and J. Dai, "Enhancement of signal amplitude of surface wave EMATs based on 3-D simulation analysis and orthogonal test method," *NDT E Int.,* vol. 59, pp. 11-17, 2013.

[139] P. Petcher, M. Potter and S. Dixon, "A new electromagnetic acoustic transducer (EMAT) design for operation on rail," *NDT E Int.,* vol. 65, pp. 1-7, 2014.

[140] R. Ribichini, F. Cegla, P. B. Nagy and P. Cawley, "Quantitative modeling of the transduction of electromagnetic acoustic transducers operating on ferromagnetic media," *Ultrasonics, Ferroelectrics and Frequency Control, IEEE Transactions on,* vol. 57, pp. 2808-2817, 2010.

[141] R. Ribichini, F. Cegla, P. Nagy and P. Cawley, "Modellingof electromagnetic acoustic transducers operatingon ferromagnetic materials," in *AIP Conference Proceedings,* 2010, pp. 964.

[142] H. Ogi, E. Goda and M. Hirao, "Increase of efficiency of magnetostriction SH-wave electromagnetic acoustic transducer by angled bias field: Piezomagnetic theory and measurement," *Japanese Journal of Applied Physics,* vol. 42, pp. 3020, 2003.

[143] R. Ribichini, F. Cegla, P. Nagy and P. Cawley, "Assessment of the performance of different EMAT configurations for shear horizontal and torsional waves," in *review of progress in quantitative nondestructive evaluation: Volume 31,* 2012, pp. 955-962.

[144] T. Yamasaki, S. Tamai and M. Hirao, "Arrayed-coil EMAT for longitudinal wave in steel wires," in *Ultrasonics Symposium, 1998. Proceedings., 1998 IEEE,* 1998, pp. 789-792.

[145] M. Hirao and H. Ogi, "An SH-wave EMAT technique for gas pipeline inspection," *NDT E Int.,* vol. 32, pp. 127-132, 1999.

[146] R. B. Thompson, "Generation of horizontally polarized shear waves in ferromagnetic materials using magnetostrictively coupled meander-coil electromagnetic transducers," *Appl. Phys. Lett.,* vol. 34, pp. 175-177, 2008.

[147] W. Johnson, B. A. Auld and G. A. Alers, "Spectroscopy of resonant torsional modes in cylindrical rods using electromagnetic-acoustic transduction," *J. Acoust. Soc. Am.,* vol. 95, pp. 1413-1418, 1994.

[148] M. Hirao and H. Ogi, "Electromagnetic acoustic resonance and materials characterization," *Ultrasonics,* vol. 35, pp. 413-421, 1997.

[149] M. Hirao, H. Ogi and H. Yasui, "Contactless measurement of bolt axial stress using a shear-wave electromagnetic acoustic transducer," *NDT E Int.,* vol. 34, pp. 179-183, 2001.

[150] H. Kwun and C. M. Teller, "Magnetostrictive generation and detection of longitudinal, torsional, and flexural waves in a steel rod," *J. Acoust. Soc. Am.,* vol. 96, pp. 1202, 1994.

[151] H. Kwun and K. Bartels, "Magnetostrictive sensor technology and its applications," *Ultrasonics,* vol. 36, pp. 171-178, 1998.

[152] W. P. Mason, *Physical Acoustics and the Properties of Solids.* Van Nostrand Reinhold Princeton:, 1958.

[153] R. B. Thompson, S. Lee and J. Smith, "Angular dependence of ultrasonic wave propagation in a stressed, orthorhombic continuum: theory and application to the measurement of stress and texture," *J. Acoust. Soc. Am.,* vol. 80, pp. 921, 1986.

[154] R. Thompson, S. Lee and J. Smith, "Relative anisotropies of plane waves and guided modes in thin orthorhombic plates: implication for texture characterization," *Ultrasonics,* vol. 25, pp. 133-137, 1987.

[155] M. G. Silk, "Ultrasonic transducers for nondestructive testing," 1984.

[156] I. ILIN and A. Kharitonov, "Theory of The EMA Method of Detecting Rayleigh-Waves for Ferromagnetic and Ferrimagnetic Materials," *Soviet Journal Of Nondestructive Testing-USSR,* vol. 16, pp. 549-554, 1980.

[157] R. Jafari-Shapoorabadi, A. Konrad and A. Sinclair, "The governing electrodynamic equations of electromagnetic acoustic transducers," *J. Appl. Phys.,* vol. 97, pp. 10E102-10E102-3, 2005.

[158] W. H. Hayt and J. A. Buck, *Engineering Electromagnetics.* McGraw-Hill New York, 2001.

[159] W. B. Zimmerman, "Multiphysics Modeling With Finite Element Methods (Series On Stability, Vibration And Control Of Systems, Serie)(Series," 2006.

[160] R. J. Shapoorabadi, A. Konrad and A. Sinclair, "Computation of current densities in the receiving mode of electromagnetic acoustic transducers," *J. Appl. Phys.,* vol. 97, pp. 10Q106, 2005.

[161] S. Thomas, S. Obayya, R. Taneja and W. Balachandran, "A Coupled Electromagnetic and Mechanical Analysis of Electromagnetic Acoustic Transducers," *International Journal for Computational Methods in Engineering Science and Mechanics,* vol. 10, pp. 124-133, 2009.

[162] R. Jafari-Shapoorabadi, A. Sinclair and A. Konrad, "Finite element determination of the absolute magnitude of an ultrasonic pulse produced by an EMAT," in *Ultrasonics Symposium, 2000 IEEE,* 2000, pp. 737-741.

[163] R. S. Edwards, X. Jian, Y. Fan and S. Dixon, "Signal enhancement of the in-plane and out-of-plane Rayleigh wave components," *Appl. Phys. Lett.,* vol. 87, pp. 194104-194104-3, 2005.

[164] R. Dhayalan, V. Satya Narayana Murthy, C. Krishnamurthy and K. Balasubramaniam, "Improving the signal amplitude of meandering coil EMATs by using ribbon soft magnetic flux concentrators (MFC)," *Ultrasonics,* vol. 51, pp. 675-682, 2011.

[165] S. Dixon, C. Edwards and S. Palmer, "The optimization of lamb and rayleigh wave generation using wideband-low-frequency EMATs," in *AIP Conference Proceedings,* 2003, pp. 297.

[166] Y. Fan, S. Dixon and X. Jian, "Lift-Off Performance of Ferrite Enhanced Generation EMATs," in *AIP Conference Proceedings,* 2008, pp. 835.

[167] Hao Kuang Sheng, Huang Song Ling, Zhao Wei Wang Shen, "Multi-belt coil longitudinal guided wave magnetostrictive transducer for ferromagnetic pipes testing." *Science China Technological Science,* vol. 54, 2011.

[168] Anonymous, "Zhuzhou Insulation material Co.Ltd; transformer coil coating - technical manual," 2011.

[169] R. Ludwig, Z. You and R. Palanisamy, "Numerical simulations of an electromagnetic acoustic transducer-receiver system for NDT applications," *Magnetics, IEEE Transactions on,* vol. 29, pp. 2081-2089, 1993.

[170] E. A. Mandracchia, *Electromagnetic Acoustic Transducer,* 1996.

[171] Anil Nanji, "Magnet Sales and Manufacturing Inc. High performance magnets7," 1995.

[172] E. Bécache, S. Fauqueux and P. Joly, "Stability of perfectly matched layers, group velocities and anisotropic waves," *Journal of Computational Physics,* vol. 188, pp. 399-433, 2003.

[173] J. Berenger, "A perfectly matched layer for the absorption of electromagnetic waves," *Journal of Computational Physics,* vol. 114, pp. 185-200, 1994.

[174] COMSOL Inc, "Documentation of Comsol Multiphysics, Version 4.3b,", May 2013.

[175] J. Branson, J. Naber and G. Edelen, "A simplistic printed circuit board fabrication process for course projects," *Education, IEEE Transactions on,* vol. 43, pp. 257-261, 2000.

[176] *Polytec PSV-400-3D Scanning Vibrometer*. Available: www.polytec.com/vibrometer/PSV-400-3D.

[177] *Polytec Application Notes*. Available: www.polytec.com/usa/applications.

[178] J. C. Moulder, C. Tai, B. F. Larson and J. H. Rose, "Inductance of a coil on a thick ferromagnetic metal plate," *Magnetics, IEEE Transactions on,* vol. 34, pp. 505-514, 1998.

[179] E. Peterson and L. Wrathall, "Eddy currents in composite laminations," *Radio Engineers, Proceedings of the Institute of,* vol. 24, pp. 275-286, 1936.

[180] J. H. Rose, E. Uzal and J. C. Moulder, "Magnetic permeability and eddy-current measurements," in *Review of Progress in Quantitative Nondestructive Evaluation*Anonymous Springer, 1995, pp. 315-322.

[181] N. Bowler, "Frequency-dependence of relative permeability in steel," in *AIP Conference Proceedings,* 2006, pp. 1269.

[182] L. Chu, H. Haus and P. Penfield, "The force density in polarizable and magnetizable fluids," *Proc IEEE,* vol. 54, pp. 920-935, 1966.

[183] A. Engel and R. Friedrichs, "On the electromagnetic force on a polarizable body," *American Journal of Physics,* vol. 70, pp. 428-432, 2002.

[184] V. Chiroiu, C. Chiroiu, C. Rugina, P. Delsanto and M. Scalerandi, "Propagation of ultrasonic waves in nonlinear multilayered media," *J. Comput. Acoust.,* vol. 9, pp. 1633-1645, 2001.

[185] T&R Committee of IEEE Group on Sonics and Ultrasonics, IEEE, "Standards on Magnetostrictive Materials: Piezomagnetic nomenclature, IEEE Trans. Sonics Ultrasonics." vol. SU-20, pp. 67-76, 1973.

[186] E. W. Lee, "Magnetostriction and magnetomechanical effects," *Reports on Progress in Physics,* vol. 18, pp. 184, 2002.

[187] K. Whittington, "Ultrasonic testing at high temperatures," *Physics in Technology,* vol. 9, pp. 62, 1978.

[188] Student Instruction Bulletin, "B-127, Strain Gage installation with M-B200 Adhessive; M-Line Accessories," .

[189] D. Jiles and D. Atherton, "Theory of the magnetisation process in ferromagnets and its application to the magnetomechanical effect," *J. Phys. D,* vol. 17, pp. 1265, 2000.

[190] R. M. Bozorth, "Ferromagnetism," *Ferromagnetism, by Richard M.Bozorth, Pp.992.ISBN 0-7803-1032-2.Wiley-VCH, August 1993.,* vol. 1, 1993.

[191] G. Engdahl, *Handbook of Giant Magnetostrictive Materials.* Academic Press, 1999.